1364f

105K03/1303
UNC
VOL 1
Royal Holloway, University Of London

1993/11/01 1993/11/01

015103

nation and metamorphism of the Vangorda Pb - Zn ssive sulphide deposit, Yukon Territory, Canada.

by

Dennis Lewis Brown

A thesis submitted for the degree of

Doctor of Philosophy of the

University of London

November 1993

Royal Holloway, University of London

Department of Geology

Egham

Surrey, TW20 OEX

U.K.

1.2 Introduction

1.2.1 Preamble

The extent and geometry of many of the worlds Pb-Zn (barite) massive sulphide deposits is controlled by post-deposition regional deformation, metamorphism, mobilisation and remobilisation (e.g. Mount Isa, Australia; Sullivan, Canada; Black Angel, Greenland). Any one or any combination of these processes can affect the size of the deposit and the metallurgical response of the ores and may be the determining factor in whether or not the deposit is economic. In order to economically evaluate a deposit it is important to first understand the structural context in which it exists as well as the deformation features within, and the geometry of, the sulphide package. Geological interpretation of a mineral deposit prior to development usually relies on unoriented diamond drill core which provides limited information on the deformation of the deposit. In order to obtain an increased understanding of a deposit a direct study of it during its development is required. This thesis is concerned with the geology of the deformed and metamorphosed Vangorda Pb + Zn (barite) massive sulphide orebody which was mined as an open pit operation from 1990 to 1993.

Examination of sulphide orebodies during mine development has a two fold importance. Firstly, it provides significant data on the response of the sulphide package to the deformation and metamorphism that have affected it, many of which cannot be fully realised from drill core alone. This data can be used to infer similar responses to similar conditions both within the same mining district or outside. Secondly, it provides important information such as an understanding of the location, orientation, and expression of structures and structural elements within a deformed and metamorphosed orebody that are of interest to the mine geologists and engineers in the day to day operations of the mine. For instance, the orientation and location of features such as

Acknowledgements

A Ph.D. is an intensely personal thing and is best done with the support of ones family. The understanding and support (both financial and moral) provided by my mother, sister and brothers have never failed nor even wavered from being absolute. If this thesis can be dedicated to anyone it is dedicated to all of you and to you all I say thank-you.

Joaquina Alvarez-Marrón, my wife, is thanked for her unflagging support over several continents and oceans. Her meticulous attention to details made sure many aspects of this work are technically correct. Now we can spend less time in airports and on planes and more time doing what is important.

One cannot undertake to carry out a project such as a Ph.D., especially in a foreign country, without the help of a great many people. First I would like to thank Ken McClay for his belief in me and his help and wise advise whenever it was needed. Thanks Ken. Any project in a geology department cannot be successfully completed without the staff and technicians that make the place run. Keith Stevens, Kevin De'Souza and Neil Holloway where extremely helpful. Then there are the 'lads'. What more can be said than thank-you for the friendship, the laughs, the drinks, the Snitch Brothers and Furball.

The people at the Department of Geology, Oviedo, Spain are thanked for providing me with a friendly place to work on my many visits and for introducing me to things Spanish. They are also gratefully acknowledged for providing access to the electron microprobe.

Personal funding, in the form of scholarships, for this project was provided by the Rothemere Foundation and by the Special Scholarship for Students doing Research in Resource Development administered by Memorial University of Newfoundland. Fieldwork was supported by Curragh Inc., Department of Indian and Northern Affairs Canada (Whitehorse), Geological Survey of Canada (Vancouver), and by the Industry Association (RHUL), all of whose help are gratefully acknowledged. Gregg Jilson and Lee Pigage of Curragh Inc. are thanked for their help during the course of fieldwork. This project benefited greatly from the help of many people at the Faro mine site. I would especially like to thank Cam Reid, Bill Dunn, Mitch Wassel, Peter Ledwidge, Glen, Vicki, Deborah, Scott, Brad, and Joe. The 'Weasels' provided entertainment. The last two field seasons in Faro would not have been possible without the help of DIAND, Whitehorse. In particular, Steve Morrison is thanked for making this possible and everyone else in the Whitehorse office for being kind and helpful.

TABLE OF CONTENTS

Abstract ii

Acknowledgements iii

Table of Contents iv

List of Figures x

CHAPTER 1 Introduction 1

1.1 Purpose and Scope 1

1.2 Introduction 2

1.2.1 Preamble 2

1.2.2 The Anvil District 3

1.2.3 The Vangorda orebody 4

1.3 Methodology 5

1.4 Published results 7

CHAPTER 2 Regional Geology 8

2.1 Introduction 8

2.2 Canadian Cordillera 8

2.2.1 Tectonic framework 8

2.2.2 Selwyn Basin 11

2.2.2.1 Stratigraphy 11

2.2.2.2 Deformation and Metamorphism of Selwyn Basin 12

2.2.3 Geological Framework of the Anvil District 13

2.2.3.1 Lithostratigraphy 13

2.2.3.2 Structural geology 16

2.2.3.3 Metamorphism 17

2.3 Massive sulphide mineralisation in Selwyn Basin 20

2.3.1 Mineralisation in Selwyn Basin 20

2.3.1.1 Sulphur and lead isotopes 21
2.3.1.2 Lead isotopes 22
2.3.2 A general SEDEX model for the Selwyn Basin Pb-Zn-(Ba) deposits 23
2.3.3 Deformation and metamorphism of Selwyn Basin deposits 26
2.3.4 Anvil District mineral deposits 27
2.3.4.1 General deposit geology 27
2.3.4.2 Sulphur and lead isotopes 31
2.3.4.3 Model for formation of the Anvil District deposits 32

CHAPTER 3 Geology and lithostratigraphy of the Vangorda Orebody 34
3.1 Introduction 34
3.2 Geology of the Vangorda orebody 34
3.3 Lithostratigraphy 36
3.3.1 Host rock lithostratigraphy 36
3.3.1.1 The Mount Mye formation 36
3.3.1.2 The Vangorda formation 37
3.3.2 Ore lithofacies 39
3.3.2.1 Ribbon-banded, carbonaceous quartzite 39
3.3.2.2 Pyritic quarzite 41
3.3.2.3 Massive pyritic quartzite 41
3.3.2.4 Baritic massive sulphides 43
3.3.2.5 Pyrrhotite + sphalerite + galena massive sulphide 43
3.4 Distribution of metals in the sulphide lithofacies 44

CHAPTER 4 Structural Analysis of the Vangorda Orebody 48

4.1 Introduction 48

4.2 The Vangorda orebody 48

4.3 Structural element analysis 50

4.3.1 Pre-D_1 features 52

4.3.2 D_1 structural elements 52

4.3.2.1 S_1 cleavage 52

4.3.2.2 F_1 folds 56

4.3.3 D_2 structural elements 59

4.3.3.1 S_2 cleavage 59

4.3.3.2 F_2 folds 61

4.3.3.3 Post-F_2 faulting 64

4.3.3.4 Jointing 70

4.3.3.5 Post-F_2 thrusting 71

4.3.4 Synthesis of structural element analysis 72

4.4 D_2 deformation textures 78

4.4.1 Durchbewegung textures 78

4.4.2 Shear textures 79

4.4.3 Cataclastic textures 88

4.4.4 Syn- to post-D_2 mobilisation features 89

4.5 Diamond drill core analysis 91

CHAPTER 5 Microtextural analysis of the sulphide lithofacies in the Vangorda orebody 95

5.1 Introduction 95

5.2 Petrography of the sulphide lithofacies 95

5.2.1 Massive pyritic sulphides 95

5.2.2 Pyrrhotite + sphalerite + galena massive sulphides 98

5.2.3 Pyritic quartzite 100
5.2.4 Baritic massive sulphides 101
5.2.5 Ribbon-banded, carbonaceous quartzite 103
5.3 Deformation textures in sulphides 104
5.3.1 Pyrite textures 104
5.3.1.1 Primary textures in pyrite 104
5.3.1.2 Brittle deformation textures in pyrite 104
5.3.1.3 Plastic deformation textures in pyrite 106
5.3.1.4 Annealing and grain growth textures in pyrite 109
5.3.2 Pyrrhotite textures 110
5.3.2.1 Brittle deformation textures in pyrrhotite 110
5.3.2.2 Plastic deformation textures in pyrrhotite 111
5.3.2.3 Annealing and grain growth textures in pyrrhotite 111
5.3.3 Sphalerite textures 112
5.3.3.1 Brittle deformation textures in sphalerite 112
5.3.3.2 Plastic deformation textures in sphalerite 112
5.3.3.3 Annealing and grain growth textures in sphalerite 113
5.3.4 Galena textures 113
5.3.4.1 Brittle deformation textures in galena 113
5.3.4.2 Plastic deformation textures in galena 113
5.3.4.3 Annealing and grain growth textures in galena 114
5.4 Deformation textures in magnetite, quartz and barite 115
5.4.1 Magnetite 115
5.4.2 Quartz 116
5.4.3 Barite 116

5.5 Distribution of microtextures in the orebody 119

CHAPTER 6 Thermobarometry of the Vangorda orebody sulphide and phyllites 125

6.1 Introduction 125

6.2 Thermobarometry 126

6.2.1 Microprobe operating conditions 126

6.2.2 Chlorite thermometry 127

6.2.3 Arsenopyrite thermometry 128

6.2.4 Sphalerite, hexagonal pyrrhotite (± pyrite) barometry 131

CHAPTER 7 Discussion 136

7.1 Deformation and metamorphism of the Vangorda orebody: implications for the Anvil District 136

7.1.1 The effects of D_1 and M_1 on the orebody 137

7.1.2 The geometry and effects of D_2 on the orebody 137

7.1.2.1 Geometry of the Vangorda orebody 137

7.1.2.2 Remobilisation in the Vangorda orebody 138

7.1.2.3 Microtextures 143

7.1.3 Pressure and temperature conditions of metamorphism 145

7.2 Implications for deformation and metamorphism in the Anvil District 148

7.3 Shear textures and processes: implicstions for the deformation of massive sulphides 151

7.3.1 Significance of shear textures 151

7.3.2 Model for the development of shear zones and durchbewegung in sulphides 156

CHAPTER 8 Conclusions 160

References 164

Appendix 1 Sample locations 172

Appendix 2 Thermobarometry calculations 180

Appendix 3 Microprobe data 183

Appendix 4 Pressure and temperature data 204

LIST OF FIGURES

Figure 1.1 *Generalised geological map showing the location of the study area*.....4

Figure 1.2 *1:1000 scale map of the Vangorda mine*..... (in back pocket)

Figure 1.3 *1:1000 scale drill core cross section : 4 + 00E*..... (in back pocket)

Figure 1.4 *1:1000 scale drill core cross section : 6+ 00E*..... (in back pocket)

Figure 1.5 *1:1000 scale drill core cross section : 8 + 00E*..... (in back pocket)

Figure 1.6 *1:1000 map showing location of drill holes*..... (in back pocket)

Figure 2.1 *Tectonic assemblage map of the Canadian Cordillera*.....9

Figure 2.2 *Regional map of northern Canadian Cordillera showing location of mineral deposits*..... 10

Figure 2.3 *Geological map of Anvil District*..... 14

Figure 2.4 *Lithostratigraphy of Anvil District*..... 15

Figure 2.5 *Photographs of F_2 folds in Anvil District*..... 18

Figure 2.6 *Metamorphic map of Anvil District*..... 19

Figure 2.7 *Selwyn Basin sulphide curve*..... 21

Figure 2.8 *Pb isotope curve for Selwyn Basin*..... 23

Figure 2.9 *Model for formation of stratiform sulphide deposits*..... 24

Figure 2.10 *Geometric models for stratiform deposits*..... 25

Figure 2.11 *Metamorphic conditions of mineral deposits in Selwyn Basin*..... 26

Figure 2.12 *Anvil Cycle lithostratigraphy*..... 29

Figure 2.13 *Cross sections of Anvil Deposits*..... 30

Table 2.1 *Lithostratigraphy data for northern Canadian Cordillera*..... 12

Table 2.2 *Features of stratiform Pb - Zn deposits in Canadian Cordillera*..... 25

Table 2.3 *Tonnage and grade figures for Anvil Deposits*..... 28

Table 2.4 *$\delta^{34}S$ isotope data for Anvil District*..... 31

Table 2.5 *Pb isotope data for Anvil District*..... 32

Figure 3.1 *Geological map and cross section of the Vangorda plateau*..... 35

Figure 3.2 *Field photograph of Mt. Mye fm*..... 37

Figure 3.3 *Field photograph of Vangorda fm*..... 38

Figure 3.4 *Field photograph of ribbon-banded quartzite*..... 40

Figure 3.5 *Field photograph of pyritic quartzite*..... 40

Figure 3.6 *Field photograph of massive pyritic sulphide*..... 42

Figure 3.7 *Field photograph of baritic massive pyritic sulphide*..... 42

Figure 3.8 *Photograph of pyrrhiotite+sphalerite+galena massive sulphide*..... 44

Figure 3.9 *Grade histograms of Vangorda sulphide lithofacies.* 45
Figure 3.10 *Metal ratios in Vangorda deposit.* 47

Figure 4.1 *General geology map of Vangorda area.* 49
Figure 4.2 *Geology map of Vangorda mine.* 51
Figure 4.3 *Long section through the orebody.* 50
Figure 4.4 *Stereoplots of structural elements of each fault* .....
block and location of fault blocks. 54
Figure 4.5 *Pit wall sketchs showing $S_0/S_1/S_2$ relationships.* 55
Figure 4.6 a *Field photograph of S_1 in lithons.* 57
4.6 b *S_1 banding in sulphides.* 57
Figure 4.7 *Photograph of refolded folds.* 58
Figure 4.8 a/b *Photomicrographs of S_2* 60
Figure 4.9 a/b *Field photograph of isoclinal F_2 fold in phyllites* 62
c/d 63
Figure 4.10 *Stereoplots showing reorientation of F_2 and S_2*
in footwall of Northwest fault. 64
Figure 4.11 *Stereoplot of fault orientations* 65
Figure 4.12 *Pit wall shetch shown graben style of extensional faults* 66
Figure 4.13 *Pit wall sketckes showing NW fault* 67
Figure 4.14 a/b *Field photographs of extensional fault in sulphides.* 68
c/d 69
Figure 4.15 *Field photograph of a joint set.* 71
Figure 4.16 *Stereoplot of joint set orientations* 71
Figure 4.17 *Field sketch of post-S_2 thrust.* 72
Figure 4.18a *S_1/S_2 map of mine.* 74
4.18b *S_2 map of mine.* 75
4.18c *S_1 map of mine.* 76
Figure 4.19 *S_1/S_2 cross sections* 77
Figure 4.20 *S_2 long section.* 78
Figure 4.21 a/b *Photographss of durchbewegung* 80
c/d 81
Figure 4.22 *Kinematic reference frame for shear indicators* 82
Figure 4.23 a/b *Photographs of sheared sulphides* 84
Figure 4.24 a/b *Photographs of pressure solution and shear*
banding in sulphides 85
Figure 4.25 a/b *Photographs of tailed inclusions* 86
c/d 87
Figure 4.26 a/b *Photographs of remobilised sulphides.* 90

Figure 4.27 *Drill core cross sections.* 93
Figure 4.28 *Drill core structural elements* 94
Table 4.1 *Summary of structural elements in mine.* 53

Figure 5.1 *Photomicrographs of textures in massive pyritic sulphides* 97
Figure 5.2 *Photomicrographs of textures in pyrrhotite + sphalerite + galena massive sulphides.* 99
Figure 5.3 *Photomicrographs of textures in the pyritic quartzite.* 101
Figure 5.4 *Photomicrographs of textures in the baritic massive sulphides* 102
Figure 5.5 *Photomicrographs of textures in the ribbon-banded, carbonaceous quartzite* 104
Figure 5.6 *Deformation textures in pyrite.* 108
Figure 5.7 *Deformation textures in pyrrhotite.* 110
Figure 5.8 *Deformation textures in sphalerite* 112
Figure 5.9 *Deformation textures in galena.* 114
Figure 5.10 *Deformation textures in magnetite* 115
Figure 5.11 *Deformation textures in quartz* 117
Figure 5.12 *Deformation textures in barite.* 118
Figure 5.13 *Deformation textures in section 4+00E* 122
Figure 5.14 *Deformation textures in section 6+00E* 123
Figure 5.15 *Deformation textures in section 8+00E* 124
Figure 5.16 *Deformation gradient in baritic massive sulphides.* 120
Table 5.1 *Relative abundance of sulphide minerals* 96
Table 5.2 *Sulphide mineral assemblages* 98
Tabl3 5.3 *Deformation mechanisms and textures in sulphide in the Vangorda orebody.* 105

Figure 6.1 *Photomicrographs of textures used in thermobarometry.* 127
Figure 6.2 *Chlorite compositions.* 128
Figure 6.3 *Arsenopyrite compositions* 130
Figure 6.4a *T vs At% As in arsenopyrite* 131
6.4b *$logfS_2$ vs T in the arsenopyrite field* 131
Figure 6.5 *Mol% FeS in sphalerite* 133
Figure 6.6 *Phases diagram of coexisting pyrrhotite and sphalerite* 134
Figure 6.7 *N_{FeS} vs T and the pyrite - pyrrhotite solvus.* 135
Table 6.1 *Representative chlorite analyses and T data* 129
Table 6.2 *Representative arsenopyrite analyses and T data.* 130
Table 6.3 *Representative sphalerite inclusion in pyrite analyses and P data.* 132
Table 6.4 *Representative pyrrhotite and sphalerite analyses and P data.* 134

Figure 7.1 *Schematic block diagram of the Vangorda orebody*..... 136
Figure 7.2 *Cross sections of orebodies showing hinge zone thickening and limb thinning*..... 140
Figure 7.3 *Section and detail of Black Angel orebody showing D_2 shearing*..... 141
Figure 7.4. *Petrogenetic grid showing the metamorphic conditions of the Anvil District and the Vangorda orebody*..... 148
Figure 7.5 *Ternary plot of Cu-Pb-Zn in stratiform deposits*..... 151
Figure 7.6 *Model for the geological evolution of the Vangorda orebody*..... 152
Figure 7.7 *Mechanical behaviour for common sulphide minerals*..... 155
Figure 7.8 *Model for the development of shear zones and durchbewegung in sulphides*..... 158
Table 7.1 *Mechanisms of mobilisation/remobilisation*..... 139
Table 7.2 *Deformation mechanisms active in common sulphides*..... 144
Table 7.3 *Summary of P-T conditions conditions in Vangorda orebody*..... 146

CHAPTER 1
Introduction

1.1 Purpose and Scope

The purpose of this thesis is to document the deformational style and metamorphic imprint of the Vangorda orebody and put it in the regional context of the geology of the Anvil District, Yukon, Canada. This has involved documenting the macroscopic, mesoscopic and microscopic deformation structures and textures to determine the processes that were active within the deforming sulphide package and host rocks during the various phases of deformation and to quantify the pressure and temperature conditions of metamorphism.

The scope of this thesis is to provide a detailed structural analysis of the Vangorda orebody based on open pit mapping during the development of the orebody as a mine and diamond drill core data that was acquired during exploration. These data where used to determine the geometry of the orebody and the effects of the various episodes of deformation and metamorphism on the distribution of metals. A further scope is to evaluate the metamorphic imprint recorded by mineral assemblages, textures and composition using petrographic techniques and thermobarometry using mineral chemical data obtained by electron microprobe analysis. Finally, the significance of the deformation and metamorphic structures and textures described for the Vangorda orebody are reviewed in the context of the district-scale deposits and for stratabound massive sulphide deposits in general.

1.2 Introduction

1.2.1 Preamble

The extent and geometry of many of the worlds Pb-Zn (barite) massive sulphide deposits is controlled by post-deposition regional deformation, metamorphism, mobilisation and remobilisation (e.g. Mount Isa, Australia; Sullivan, Canada; Black Angel, Greenland). Any one or any combination of these processes can affect the size of the deposit and the metallurgical response of the ores and may be the determining factor in whether or not the deposit is economic. In order to economically evaluate a deposit it is important to first understand the structural context in which it exists as well as the deformation features within, and the geometry of, the sulphide package. Geological interpretation of a mineral deposit prior to development usually relies on unoriented diamond drill core which provides limited information on the deformation of the deposit. In order to obtain an increased understanding of a deposit a direct study of it during its development is required. This thesis is concerned with the geology of the deformed and metamorphosed Vangorda Pb + Zn (barite) massive sulphide orebody which was mined as an open pit operation from 1990 to 1993.

Examination of sulphide orebodies during mine development has a two fold importance. Firstly, it provides significant data on the response of the sulphide package to the deformation and metamorphism that have affected it, many of which cannot be fully realised from drill core alone. This data can be used to infer similar responses to similar conditions both within the same mining district or outside. Secondly, it provides important information such as an understanding of the location, orientation, and expression of structures and structural elements within a deformed and metamorphosed orebody that are of interest to the mine geologists and engineers in the day to day operations of the mine. For instance, the orientation and location of features such as

faults, joints, and various foliations provide important information that can be used to help predict and assess pit wall stability, potential problems with water, location of road access to the active mining area and to develop better loading patterns and charge of blasts. Likewise, an enhanced understanding of the location and orientation of folds and faults, which are major and which minor, are of importance in grade control during mining. By paying careful attention to these factors dilution of the ore can be significantly reduced and mine development factors can be more efficiently assessed and the costs of mine operations reduced. These and other aspects of a structural analysis of a developing mine are beyond the scope of this thesis but were an important aspect of the field work and illustrate the importance of continuous and detailed mapping during mine operation.

1.2.2 The Anvil District

The Anvil District forms part of Selwyn Basin of the northern Canadian Cordillera (Figure 1.1). The district is underlain by up to 5 km of late Precambrian to upper Paleozoic polydeformed and polymetamorphosed metasediments and metavolcanics and is intruded by mid-Cretaceous granitoids. Two major deformation events have affected the district and deformed the massive sulphide orebodies. Both deformation events were accompanied by metamorphism. The geology of the Anvil District is discussed in detail in Chapter 2.

The Anvil District is the largest Pb - Zn mining district in northern Canada with estimated geological reserves before mining of 120 million tonnes. The district hosts five stratiform Pb - Zn deposits of presumed Cambrian age. Mining operations began in the Anvil District in the late 1960's with the large Faro orebody (see Chapter 2) and continued with several interruptions until 1992.

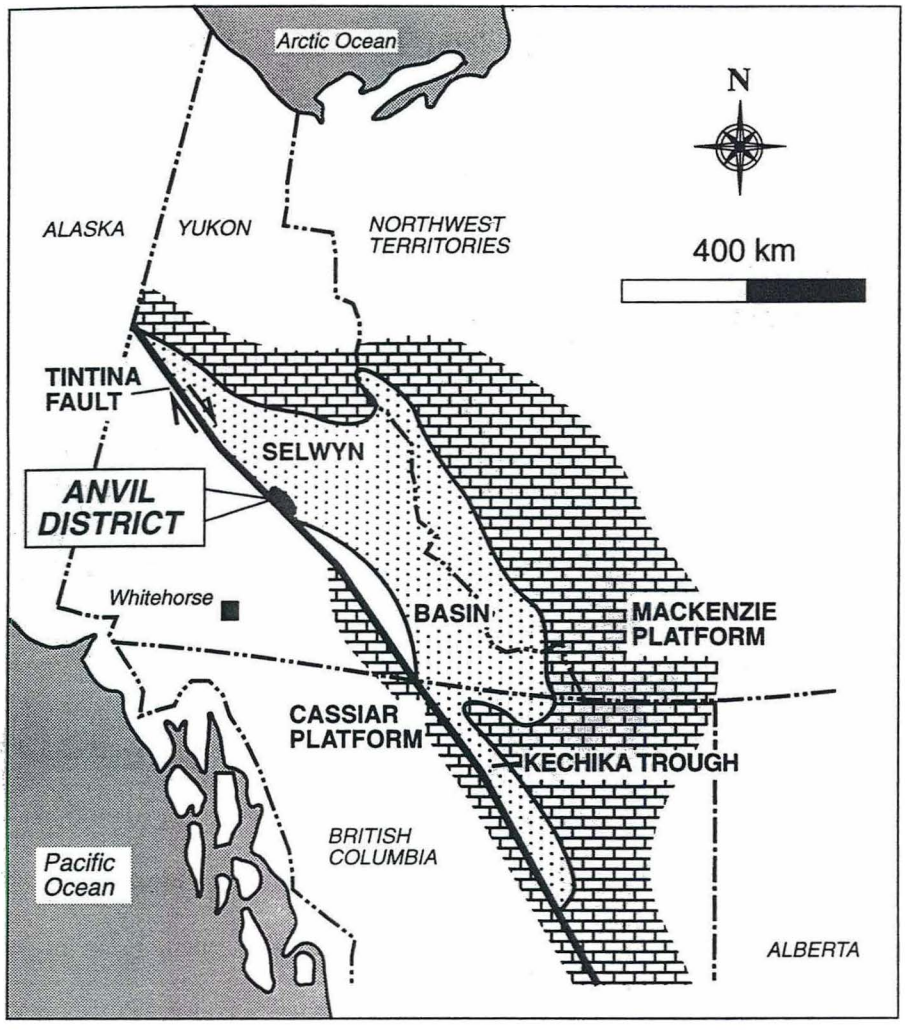

Figure 1.1. *Generalised map of the northwestern Canadian Cordillera showing the location of Selwyn Basin. The Anvil District is located on the present western margin of Selwyn Basin, adjacent to Tintina Fault.*

1.2.3 The Vangorda orebody

The Vangorda orebody was the first massive sulphide discovery in the Anvil District (Pigage 1990). It was discovered by conventional prospecting techniques and staked by Al Kulan in 1953. The property was optioned to Prospector's Airways and was extensively drilled between 1953 and 1956. However, exploitation of the orebody was not carried out at this time. The orebody passed through a succession of owners until it was acquired by Cyprus Anvil Mining Corporation who began infill diamond and rotary

drilling between 1979 and 1981. Curragh Inc. bought the Vangorda orebody in 1985 and carried out further infill diamond drilling in 1987, 1988, and 1990. It was developed as an open pit mine from 1990 to 1992 by Curragh Inc., producing approximately 13,000 tonnes of ore per day with an average combined Pb + Zn grade of 7.7% with a cut-off grade of 4.0%.

Prior to this study the geology of the Vangorda orebody was interpreted (c.f Jennings & Jilson 1986) using the regional structural style compiled from sparse outcrops in the district (there was only one exposure of Vangorda massive sulphides) and diamond drill core using techniques for structural analysis outlined by Laing (1977) and Johnston (1985). This thesis documents the geology of the orebody as revealed during mining operations. The mine is now closed and the open pit has been flooded.

1.3 Methodology

Fieldwork for this thesis began in May of 1990 and totalled eleven months until September 1992. During that time the present study was incorporated into the final phase of the exploration diamond drilling project on the Vangorda orebody in which 10,000 metres of core were drilled. Subsequently, the final cross section, long section and bench plan interpretation of the orebody were made in collaboration with the mine geologist, Cam Reid. Throughout the course of the fieldwork a close working relationship was maintained with the mine geologist, mine engineers, and grade control geologists working in the open pit and with a consultant mining engineer studying pit wall stability in the Vangorda open pit.

Much of the fieldwork emphasis was placed on detailed (1 : 200 scale) structural analysis of the developing open pit mine from which 1 : 1000 scale maps have been constructed (Figure 1.2, enclosed in the back pocket). Pit wall mapping was augmented

by incorporating blast hole lithofacies data to infill areas that were mined out. These maps were used in grade control, short term planning (e.g. road construction to the active mining face) and blast engineering by the mine geologists and engineers during mine operations. Detailed (1 : 100 scale) logging was carried out on approximately 4200 meters of Vangorda diamond drill core as well as production logging during exploration. The main emphasis of the detailed logging was placed on examination of mesoscopic structures, mineral assemblages and textures and their relationship to the larger-scale structure. As well, 34 diamond drill hole cross sections, 14 long sections, and approximately 50 mid-bench plan sections were provided by Curragh Inc. for analysis. From this information, together with drill log data for nearly 500 diamond drill holes also provided by Curragh Inc., three parallel 1 : 500 scale cross sections have been constructed through the main part of the orebody. These cross sections (8 + 00E, 6 + 00E, and 4 + 00E) (Figure 1.3, 1.4 and 1.5, respectively) are enclosed in a pocket at the back of this thesis. Approximately 10,000 chemical analysis for Pb, Zn, Fe, Ba, Ag, and Au were also made available by Curragh Inc. for analysis of the metal distribution.

Three hundred diamond drill core samples were taken form selected locations within drill core and in many cases samples were collected from each lithofacies in the drill interval. The location of each sample is given in Appendix 1 and the locations of the diamond drill holes are given on Figure 1.6 (enclosed in the back pocket). The location of the drill core logged at a 1 : 100 scale for this thesis are shown on Figure 1.6 and summary logs are given on the three drill core cross sections (Figures 1.3, 1.4 and 1.5). Samples for petrographic and petrological examination were predominantly collected from diamond drill core to insure a precise sample location. Polished blocks and thin sections were prepared from these for reflecting and transmitted light microscopy, respectively. One hundred larger samples were collected for mesoscopic structural and textural examination. These were slabbed, polished and photographed, and analysis of

structures and textures carried out.

Electron microprobe analysis was conducted on selected samples for geothermobarometry. Analyses were carried out on a Cameca SL50 at the University of Oviedo, Spain. Details of operating conditions and standards used are given in Chapter 6. Microprobe mineral composition analysis are presented in Appendix 2.

1.4 Published results

Preliminary results of field work have been published in the Geological Survey of Canada's *Current Research* (Brown & McClay 1992), and *Yukon Geology and Exploration* (Brown & McClay 1993). A manuscript on the deformation textures in pyrite in the Vangorda orebody has been published in *Mineralogical Magazine* (Brown & McClay 1993). A manuscript describing the structural style of the Vangorda orebody (Brown and McClay) is in press with *Ore Geology Reviews* and a manuscript looking at the pressure and temperature conditions of metamorphism has been accepted pending corrections (which have been submitted) with *Mineralium Deposita*. Copies of all manuscripts are provided in the back pocket.

CHAPTER 2
Regional Geology

2.1 Introduction

The Anvil District, which hosts the Vangorda orebody, occurs within Selwyn Basin of the northern Canadian Cordillera, Yukon, Canada. This chapter outlines the regional geology of the Canadian Cordillera. It discusses the depositional and tectonic history of Selwyn Basin - Kechika Trough and provides the general nature and characteristics of the main stratiform Pb - Zn deposits such as those in the Gataga District, Macmillan Pass, Howards Pass and Anvil District and the models invoked for their formation. The deposits of the Anvil District are put into the context of the general tectonic regime and models for mineralisation in the northern Canadian Cordillera.

2.2 Canadian Cordillera

2.2.1 Tectonic framework

The Northern Canadian Cordillera is a 2000 km long Mesozoic to Tertiary orogenic belt that records a long and complex history of terrane accretion, subduction, strike-slip and extensional faulting (Monger & Price 1979; Monger *et al.* 1982; Gabrielse 1985; Parrish *et al.* 1988). From east to west, the Canadian Cordillera consists of five major tectonic elements (Monger *et al.* 1982) several of which are made up of a number of allochthonous and parautochthonous terranes (Figure 2.1). From west to east these are; (1) the Foreland Thrust and Fold Belt which consists of imbricated Proterozoic to Palaeozoic North American continental margin rocks and Mesozoic to early Tertiary foreland basin sediments; (2) the Omineca Crystalline Belt consisting of

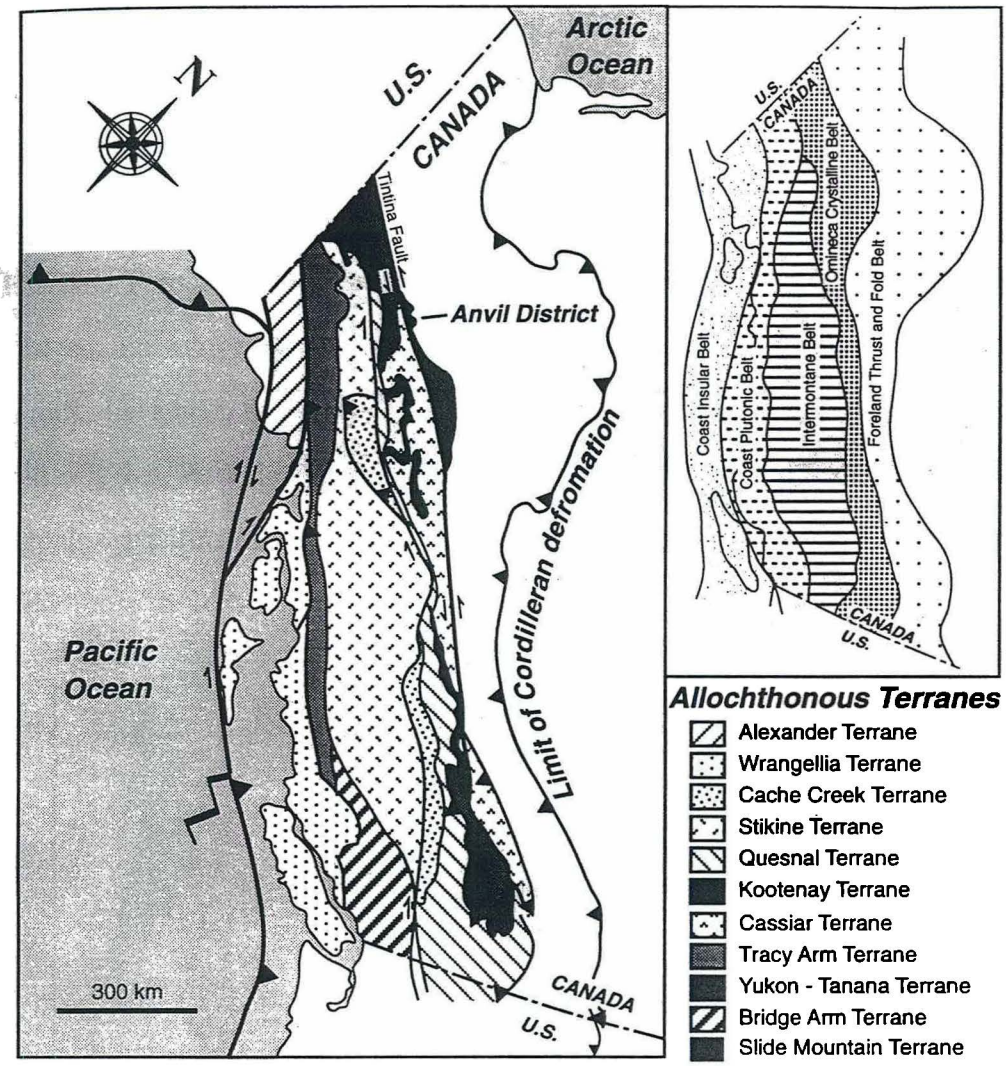

Figure 2.1. *Tectonic assemblage map of the western Canadian Cordillera showing the major allochthonous and parautochthonous terranes. The inset shows the tectonic subdivision of the Canadian Cordillera. (Redrafted from Coney 1989)*

passive margin facies rocks, high-grade metamorphic complexes, plutonic complexes and imbricated craton and klippen of accreted terranes; (3) the Intermontane Belt which consists of Palaeozoic to early Jurassic accreted oceanic arcs, subduction melange, marginal basins and flysch; (4) the Coast Belt consisting of Cretaceous to early Tertiary plutons; (5) the Insular Belt which consists of Palaeozoic to Jurassic volcanic, plutonic, metamorphic and sedimentary rocks (see Wheeler & McFeely 1991).

The four major belts west of the Foreland thrust and Fold Belt are made up of allocthonous and parautochthonous terranes (Coney *et al.* 1980) (Figure 2.1). These terranes are often thin sheets that have been thrusted towards the craton for distances of

up to several hundred kilometres (Coney 1989). Despite post-emplacement modification of these terranes by strike-slip and extensional faulting, they maintain a regional northeast (towards the carton) structural vergence.

The Foreland Thrust and Fold Belt is made up of thick sequences of late Precambrian to early Mesozoic miogeoclinal rocks (see section 2.2.2.1) and foreland basin rocks. These rocks have been thrust towards the northeast to east forming a thin-skinned thrust and fold belt (e.g. Price 1981). It is within the Foreland Thrust and Fold Belt that many of the major stratiform massive sulphide deposits of the Canadian Cordillera occur, in particular those in Selwyn Basin (Figure 2.2).

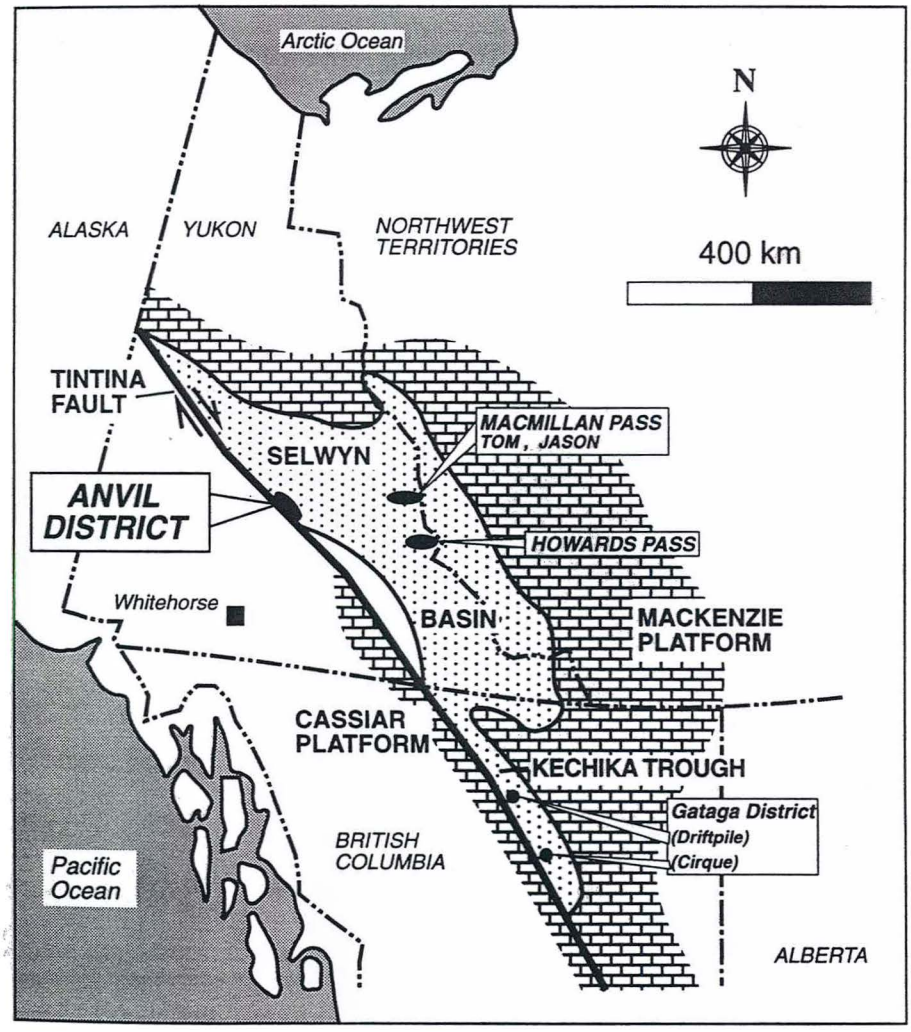

Figure 2.2. *Generalised map of northwestern Canada showing the location of the major stratiform massive sulphide deposits that occur in Selwyn Basin.*

2.2.2 Selwyn Basin

2.2.2.1 Stratigraphy

The stratigraphic record for the ancient continental margin of western North America contains evidence for four depositional megasequences that are related to rifting during the mid Proterozoic to upper Palaeozoic (Thompson *et al.* 1987). These megasequences have now largely been incorporated into the Foreland Thrust and Fold Belt. Selwyn Basin (Figure 2.2) has been defined in broad terms as an epicratonic marine basin that formed as a result of marginal rifting and rift-related subsidence during the Cambrian to upper Palaeozoic (Gabrielse 1967; Cecile 1982). Abbott *et al.* (1986) provide a comprehensive overview of the stratigraphy of Selwyn Basin and the reader is referred to these papers for a more thorough description of these rocks. It is within these rift-related sequences of Selwyn Basin that the stratiform massive sulphide deposits of the Canadian Cordillera were deposited.

Selwyn Basin (Figure 2.2) is underlain by the first megasequence of Thompson *et al.* (1987), the 1500 - 800 Ma, westward-thickening, shallow water clastics of the Wernicke, Pinguicula, and Mackenzie Mountain megasequence and by the second megasequence of 800 - 600 Ma rift-related feldspathic grits, clastics and volcanics of the Winderemere Supergroup (Eisbacher 1981; Abbott *et al.* 1986) (Table 2.1). The "Grit unit" (Eisbacher 1981), largely quartzofeldspathic turbidites, may form the upper part of the Winderemere Supergroup (Abbott *et al.* 1986). The third rifting event identified by Thompson *et al.* (1987) ranges in age from 600 to 370 Ma and marks the initiation of the development of Selwyn Basin. The third rifting event was marked by marine clastic and carbonate deposition that continued throughout the Cambrian to lower Palaeozoic, culminating in the deposition of deep water clastics and carbonates of the Rabbitkettle Formation and Road River Group (Tempelman-Kluit 1970, 1977; Gordey 1981; Abbott

et al. 1986) (Table 2.1). The fourth rifting event lasted from 379 to 180 Ma and largely resulted in deposition of black clastics, chert and chert conglomerate of the Earn Group (Gordey *et al.* 1982; Abbott *et al.* 1986) (Table 2.1).

Table 2.1. Lithostratigraphic data and location of major stratform mineral deposits of the northern Canadian Cordillera.

Age (Ma)	Stratigraphy	Lithologies	Tectonic setting	Mineral Deposits
1500-800	Wernicke, Pinguicula and Mackenzie mountain sequences	Westward thickening shallow water clastics and carbonates	———	———
800-600	Windermere supergroup	Westward thickening coarse to fine feldspathic grits and clastics. Basic volcanics and dykes at base	Newly rifted margin of western North America	———
600-370	Lower Paleozoic to Cambrian (Rabbitkettle Fm.) (Road River Group)	Shallow to deep water coarse- and fine-grained clastics and carbonates.	Cooling and subsiding rifted (rifting?) continental margin	Anvil District (Lower Cambrian) Howards Pass (Silurian)
370-80	Upper Palaeozoic - Mesozoic (Earn Group)	Transgressive, fine-grained black clastics, chert and chert conglomerates	Possible rifting, strike-slip faulting, and collisional orogenic processes	Gataga District (M.-U. Devonian) Cirque (M.-U. Devonian) Macmillan Pass (M.-U. Devonian)

-Modified from McClay (1991) with data from Abbott et al. (1986) and McIntyre (1992).

2.2.2.2 *Deformation and metamorphism of Selwyn Basin*

Selwyn Basin is situated in the western part of the Foreland Thrust and Fold Belt and is bound on the west by the Tintina Fault. Following rifting and megasequence deposition Selwyn Basin underwent inversion (e.g. McClay *et al.* 1989) and northeast-directed telescoping. Recognition of folding, thrusting and thrust sheet development is severely hampered by the extensive distribution of black shales and siltstones making recognition of thrust surfaces and repeated panels of rock very difficult. However, several southwest-dipping imbricate thrust panels have been recognised in Selwyn Basin (e.g. Gordey & Irwin 1987; McClay *et al.* 1989; Wheeler & McFeely 1991). Transport direction of these thrust sheets is predominantly towards the northeast, although in Macmillan Pass southward directed thrusting has also been recognised (Abbott 1982; Abbott & Turner 1990). Deformation in the area is considered to be late Jurassic to mid Cretaceous with cross-cutting mid Cretaceous granitoids (e.g. Pigage & Andersen 1985) providing an upper bound on the age of deformation.

Metamorphism in Selwyn Basin is dated at approximately 125 - 120 Ma (Gabrielse & Yorath 1989). Metamorphic grade is generally low to mid-greenschist facies (Large 1980; McIntyre 1979; McClay 1983, 1991) though this is locally overprinted by higher grades of metamorphism associated with intrusion of the mid Cretaceous granitoids, as in the case for the Anvil District (e.g. Tempelman-Kluit 1972, Pigage & Andersen 1985; Smith & Erdmer 1990).

2.2.3 Geological framework of the Anvil District

The Anvil District (Figure 2.3) forms part of Selwyn Basin (Tempelman-Kluit 1972; Jennings & Jilson 1986) (Figure 2.2) and rocks in the district consist of late Precambrian to upper Palaeozoic metasedimentary and metavolcanic rocks (Jennings & Jilson 1986). During the mid-Cretaceous the district was intruded by granitoids of the Anvil Plutonic Suite (Jennings & Jilson 1986; Pigage & Anderson 1985).

The district is structurally overlain by the allochthonous Yukon-Tanana terrane (Tempelman-Kluit 1979; Coney *et al.* 1980) and is adjacent to a major orogen-scale strike-slip fault, the Tintina Fault (Figure 2.3). The Tintina Fault cuts the Yukon-Tanana terrane displacing it dextrally approximately 450 km (Tempelman-Kluit 1976). Intrusion of the Anvil Plutonic Suite resulted in northwest-southeast doming of the district into a structural culmination, the Anvil Arch.

2.2.3.1 Lithostratigraphy

The Anvil District is thought to be underlain by Precambrian continental crust and the shallow marine and continental sediments of the Winderemere Supergroup. The deep water quartzofeldspathic coarse- to fine-grained clastics of the "Grit unit" may be the

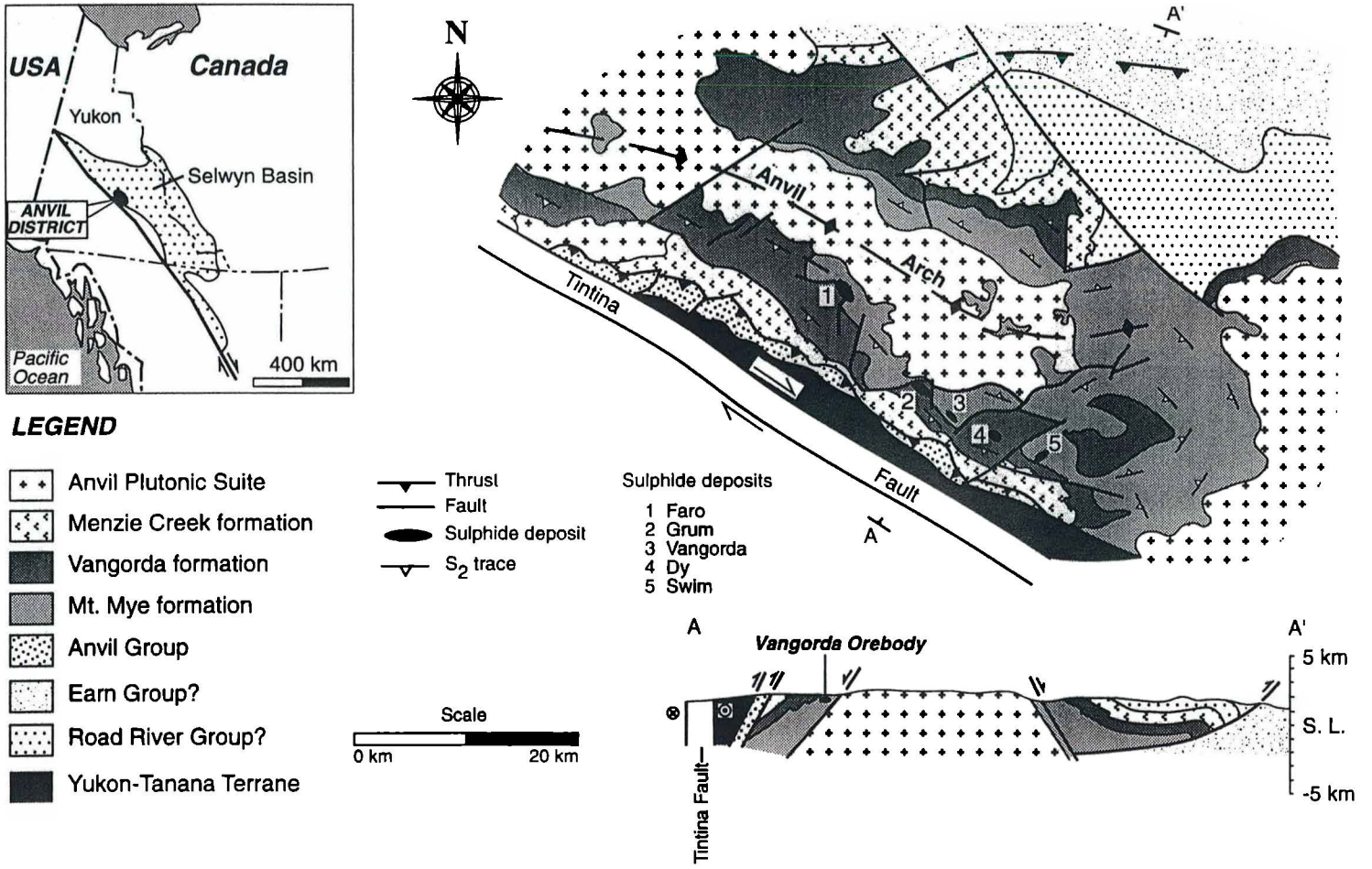

Figure 2.3. *Generalised geological map and cross section of the Anvil District. The massive sulphide deposits occur along a curvi-linear trend on the southwestern margin of the Anvil Batholith. Note the position of the Vangorda orebody in the cross section. (Redrafted from Jennings & Jilson 1986).*

upper part of this package in the Anvil District (Tempelman-Kluit 1977; Gordey 1981; Jennings & Jilson 1986; Abbott *et al.* 1986). The outcropping lithostratigraphy of the Anvil District (Figure 2.4) consists of up to 5 km of polydeformed, greenschist to amphibolite facies metasedimentary and metavolcanic rocks together with Cretaceous granites. Description and regional correlation of the rocks in the Anvil District are presented by Jennings & Jilson (1986) from which the following descriptions are taken.

The lowest unit exposed in the Anvil District is the Late Proterozoic to Lower Precambrian Mount Mye formation. (The stratigraphic nomenclature for the metasedimentary and metavolcanic rocks for the Anvil District are local and not official, therefore the 'f' in formation is lower case in accordance with procedure for stratigraphic nomemclature (c.f. Whittaker *et al.* 1991)) The Mount Mye formation consists predominantly of noncalcareous metapelites and minor interbanded carbonaceous meta-semipelite, metadolostone, and metabasite. The Mount Mye

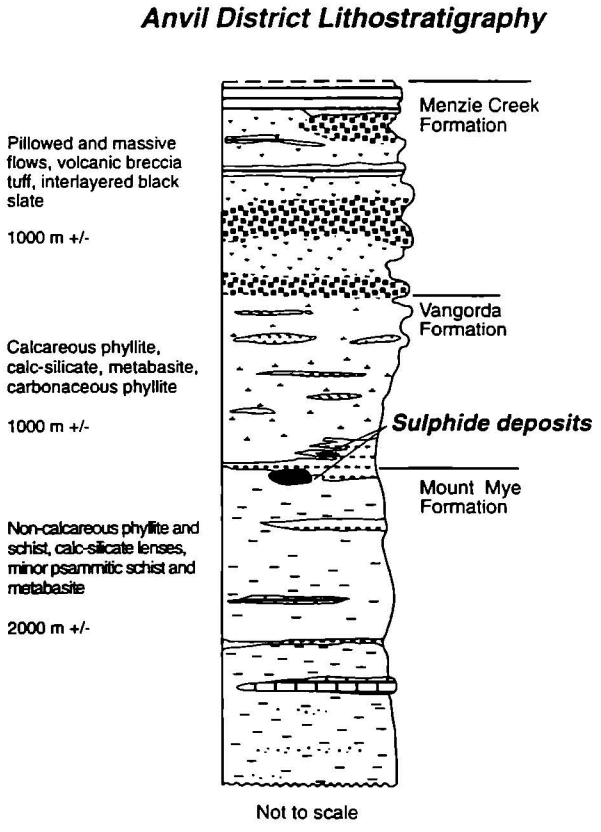

Figure 2.4. *Lithostratigraphic column of the Anvil District (after Jennings & Jilson 1986).*

formation has a structural thickness of up to 2 km but the base is not exposed. Based on lithological similarities elsewhere in Selwyn Basin, the Mount Mye formation is thought to be Cambrian to late Hadyrian although no positive correlation has been made (Jennings & Jilson 1986). Overlying the Mount Mye formation are Cambrian and Ordovician rocks of the Vangorda formation.

The Vangorda formation consists of calcareous metasediments and interbanded metavolcanics and its base is carbonaceous. It has a variable structural thickness ranging from 0.5 km to 1.5 km. The Vangorda formation is tentatively correlated with the Rabbitkettle Formation (Table 2.1) (Jennings & Jilson 1986).

The stratigraphically highest unit recognised in the Anvil District is the Ordovician to Silurian Menzie Creek formation. The Menzie Creek formation consists of metavolcanic and interbanded metasedimentary rocks and has a thickness of approximately 1.5 km. The Menzie Creek formation is correlated with the Road River Group (Table 2.1) (Jennings & Jilson 1986).

All the above lithostratigraphic sequence is intruded by Cretaceous granitoids of the Anvil Plutonic Suite. The Anvil Plutonic Suite is peraluminous to metaluminous, massive to foliated, medium to coarse grained, equigranular to serrate and alkali-feldspar megacrystic (Pigage & Anderson 1985). Rb -Sr whole rock and mineral analyses indicate cooling ages for the Anvil Plutonic Suite of 100 Ma. (Pigage & Anderson 1985). An Anvil suite granitic dyke cutting a syn-emplacement extensional fault has yielded a U-Pb zircon age of 98.6 $\pm$ 0.2 Ma. (Pigage pers. com.).

2.2.3.2 Structural geology

Five deformation events (D_1 to D_5) have been recognised in the Anvil District (Jennings

& Jilson 1986), the first two of which (D_1 and D_2) are regionally significant (Jennings & Jilson 1986). D_1 is interpreted to be related to the pre- to mid-Cretaceous docking of the allochthonous Yukon-Tanana terrane onto the continental margin (Tempelman-Kluit 1979) causing northeast-directed nappe emplacement, folding, thrusting and metamorphism of the continental margin sediments. D_1 deformation resulted in development of northeast-verging F_1 folds and a penetrative regional foliation (S_1) (Figure 2.5a) and regional metamorphism (M_1). D_2 deformation is related to emplacement, uplift and unroofing of the Anvil Batholith (Jennings & Jilson 1986). D_2 resulted in southwest-directed folding, development of a wavy, shallowly southwest-dipping, penetrative foliation (S_2), extensional faulting and greenschist to amphibolite facies metamorphism (M_2) (Jennings & Jilson 1986; Smith & Erdmer 1990). F_2 folds are nearly coaxial with F_1 and, where seen, the interference pattern is typically type 3 (Ramsay 1967) (Figure 2.5b). Brittle to ductile extensional faulting, related to unroofing of the Anvil Batholith, is late- to post-D_2 folding (Pigage & Jilson 1985; Brown & McClay 1992). Many post D_2 faults in the Anvil District have subhorizontally-plunging slickensides indicating late strike-slip faulting (Jennings & Jilson 1986; Brown & McClay 1992). The D_3 to D_5 deformation events produced minor folding and steeply dipping crenulation foliations that locally overprint the D_1 and D_2 structural elements.

2.2.3.3 Metamorphism

Metamorphism in the Anvil District occurred during both the regional D_1 and D_2 deformation events (Tempelman-Kluit 1972; Jennings & Jilson 1986). Within the district, D_2 and M_2 have penetratively overprinted D_1 and M_1 structures and mineral assemblages. However, mineral assemblages that may represent M_1 are found in D_2 lithons, between the S_2 foliation where they define the S_1 foliation (see Figure 6.1a). The common mineral assemblage that defines S_1 is muscovite + chlorite + quartz, the

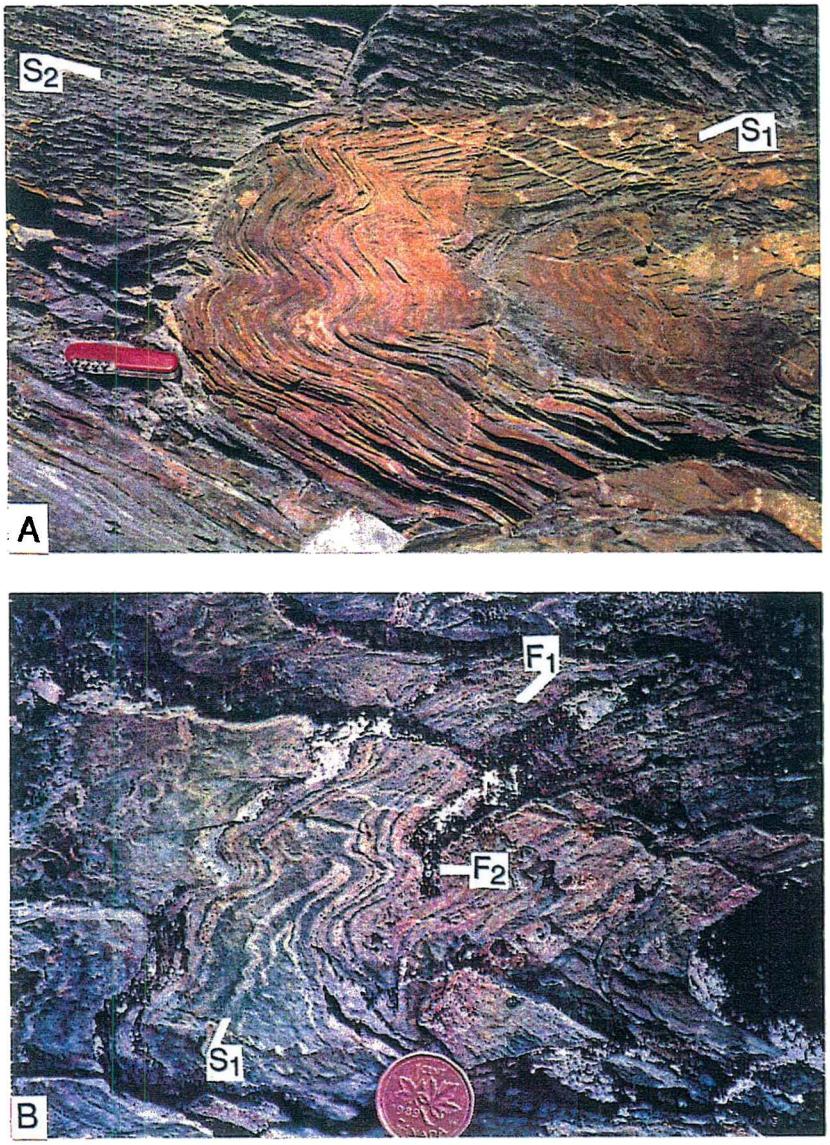

Figure 2.5. *Field photographs of F_2 folded phyllite near the Vangorda orebody. A) F_2 folded S_1 cleavage with well developed S_2 axial planar cleavage. B) Type 3 fold interference pattern. The photo is taken looking towards the northwest, down the axis of the F_2 fold. The overprinting relationship is S on Z suggesting the structural position is in the normal limb of a macroscopic F_2 fold. All F_1 folds in area, although rare, have Z - asymmetries suggesting the normal limb of a F_1 fold.*

same as that defining S_2, suggesting either comparable M_1 and M_2 conditions or recrystallisation of S_1 minerals during M_2.

The M_2 regional grade in the Anvil District decreases outward from the Anvil Batholith in a Buchan-type facies series in which the biotite, garnet, andalusite, staurolite, and sillimanite isograds in the metapelites are concentric to the batholith (Tempelman-Kluit 1972; Smith & Erdmer 1990) (Figure 2.6). An andalusite + staurolite + garnet + biotite + muscovite + quartz + plagioclase mineral assemblage is locally developed in the metapelites immediately adjacent to the batholith contact. Locally andalusite has altered to sillimanite and sillimanite is abundant in a roof pendant (Pigage & Andersen 1985; Smith & Erdmer 1990). The absence of kyanite in this assemblage indicates peak metamorphic pressure conditions during M_2 of less than 4 kb. Along the northeast margin of the Anvil Batholith, the isograds are closely spaced and cut straight across topography suggesting a steeply dipping contact. In the southwest, in the area

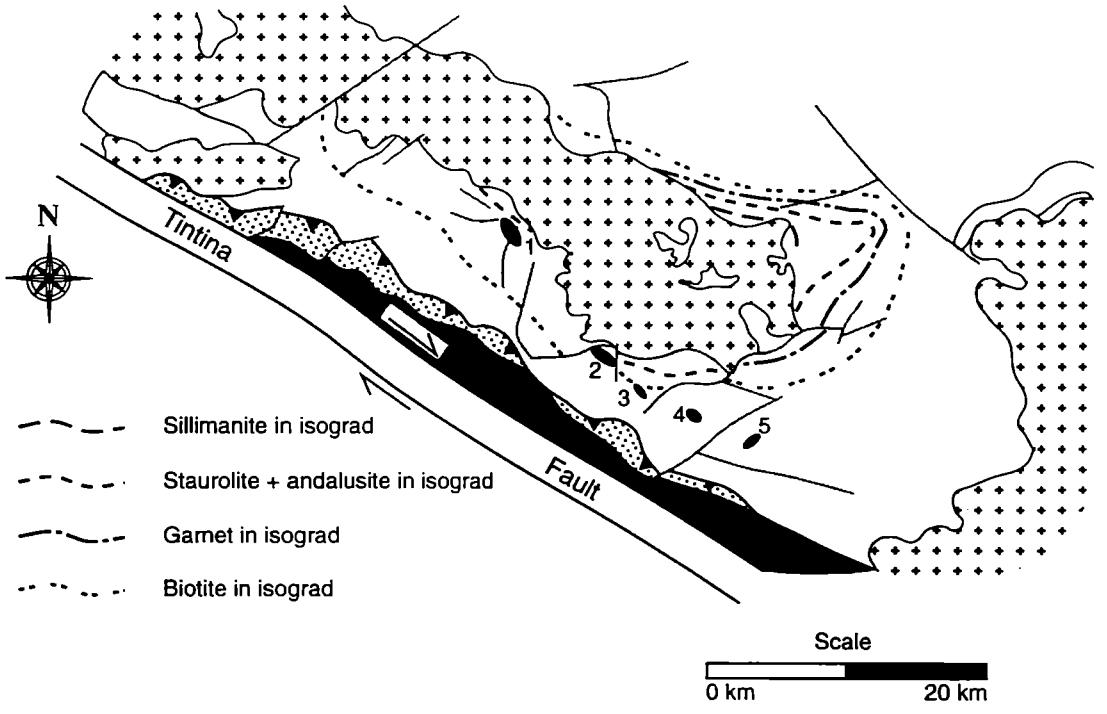

Figure 2.6. *Schematic map of the Anvil District showing the concentric distribution of the metamorphic isograds around the Anvil Batholith. The Vangorda orebody is located near the biotite 'in' isograd. Isograds are from Tempelman-Kluit (1972) and Smith & Erdmer (1990).*

encompassing the Vangorda deposit, the isograds are more openly spaced suggesting that the contact dips more shallowly.

Using petrogenetic relations Smith & Erdmer (1990) determined pressures and temperatures of M_2 to be 3 kb and 400 - 500 °C for the chlorite + biotite zone and 600 - 620 °C for the biotite + almandine + sillimanite zone. However, pressure - temperature estimates made using thermobarometry give spurious results, with pressure ranging from 2.8 - 10 kb and garnet + biotite temperatures ranging from 509 - 872 °C (Smith & Erdmer 1990). Limited sphalerite barometry by Kuo (1976) provided pressures of approximately 3 kb.

2.3 Massive sulphide mineralisation in Selwyn Basin

2.3.1 Mineralisation in Selwyn Basin

The northern Canadian Cordillera hosts one of the worlds largest concentrations of sediment-hosted, stratiform Pb - Zn deposits (Figure 2.2). These deposits occur in the third and fourth megasequences of Thompson *et al.* (1987) which were accompanied by three major episodes of stratiform Pb - Zn mineralisation in Selwyn Basin (Table 2.1). The first major mineralisation event was the deposition of the Late Proterozoic to early Ordovician Anvil District deposits that are hosted by rocks that are in part correlated with the Rabbitkettle Formation (Table 2.1) (Jennings & Jilson 1986). The second phase of stratiform mineralisation occurred during the early Silurian with the development of the Howards Pass deposits which are hosted by the Road River Group (Table 2.1) (Morganti 1979; Goodfellow & Jonasson 1984). The third phase of stratiform mineralisation occurred in the mid- to upper Devonian and resulted in the development of the Macmillan Pass, Gataga District, and Cirque deposits which are

hosted by the Earn Group (Table 2.1) (Carne 1979; McIntyre 1982, 1992; McClay & Bidwell 1987; Pigage 1987).

2.3.1.1 Sulphur isotopes

It is evident that Selwyn Basin formed as a fault-controlled epicratonic basin during rifting and subsidence of the continental margin of northwestern Canada (c.f. Tempelman-Kluit 1981; Goodfellow 1981) and that conditions favourable for stratiform massive sulphide mineralisation occurred at least three times during its history. Furthermore, it is has become apparent that during its rifting history Selwyn Basin was closed to open global oceanic circulation during these periods of massive sulphide

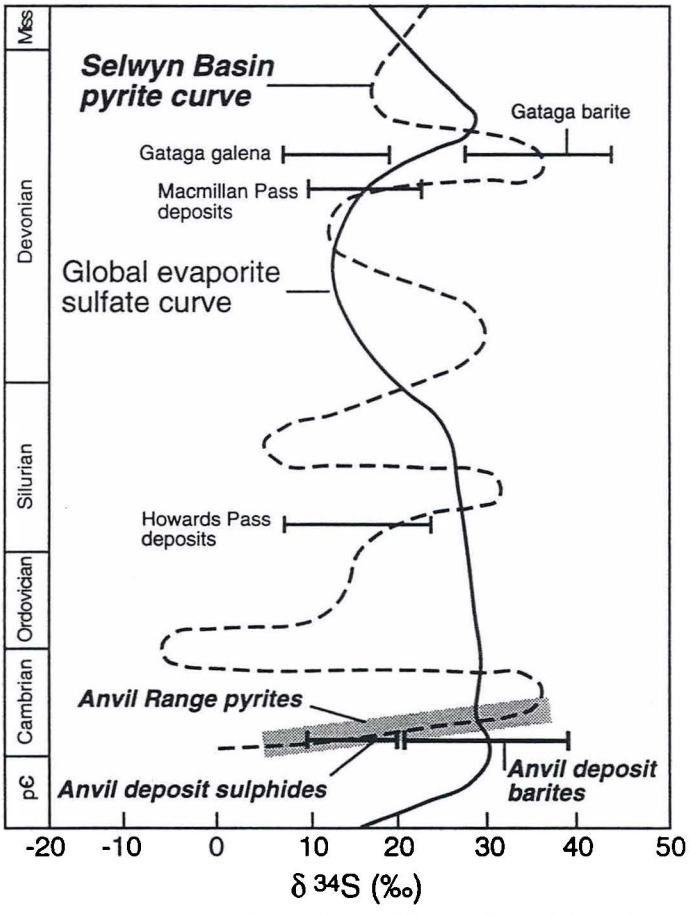

Figure 2.7. *Sulphur isotope age curves for pyrite and barite from Selwyn Basin. The curves show four early Palaeozoic stagnation events indicated by sedimentary $\delta^{34}S$ values approaching and exceeding the global seawater sulphate curve of Claypool et al. (1980). Isotope data is from Goodfellow & Jonasson (1984) and Shanks et al. (1987).*

mineralisation.

Closure of Selwyn Basin to open ocean circulation is reflected in the $\delta^{34}S$ values for pyrite which increase significantly over those of the mean ocean water evaporate curve (Claypool *et al.* 1980) during periods of stagnation (Figure 2.7). Goodfellow & Jonasson (1984), using sedimentary pyrite remote from sulphide deposits, have identified at least three cycles during the Ordovician to Mississippian when the water column in Selwyn Basin alternated from open circulation to closed and stratified (Figure 2.7). Shanks *et al.* (1987) have confirmed another, similar event in the Cambrian (Figure 2.7). However, the $\delta^{34}S$ barite curve defined by Goodfellow & Jonasson (1984) for Selwyn Basin is similar in shape to that of the mean ocean water evaporite curve but at higher $\delta^{34}S$ values, suggesting prolonged restriction of Selwyn Basin to open ocean circulation (Goodfellow & Jonasson 1984). These sulphur isotope data provide strong evidence that the stratabound massive sulphide deposits of Selwyn Basin formed during periods of stagnation in which the basin was restricted from open ocean circulation.

2.3.1.2 Lead isotopes

Godwin & Sinclair (1982) constructed an empirical three stage lead isotope growth curve for shale-hosted Pb - Zn deposits of the Canadian Cordillera that dates individual deposits (Figure 2.8). Godwin & Sinclair (1982) and Godwin *et al.* (1982) identified three major mineralisation events dating at about 520 Ma, 370 Ma and 90 Ma, corresponding to the Anvil District, Howards Pass and Macmillan Pass / Gataga District (Figure 2.8), which fall within the third and fourth rift-related megasequences of Thompson *et al.* (1987) and metamorphic remobilisation during the Cretaceous.

Lead isotopes also provide a useful indicator of the source of the lead in the ore fluids.

The lead isotopes values obtained by Godwin & Sinclair (1982) and Godwin *et al.* (1982) imply an isotopically restricted upper crustal lead source for the deposits, possibly the Proterozoic 'Grit unit' of the Windermere Supergroup, although local variations may represent contamination by other sources (Shanks *et al.* 1987).

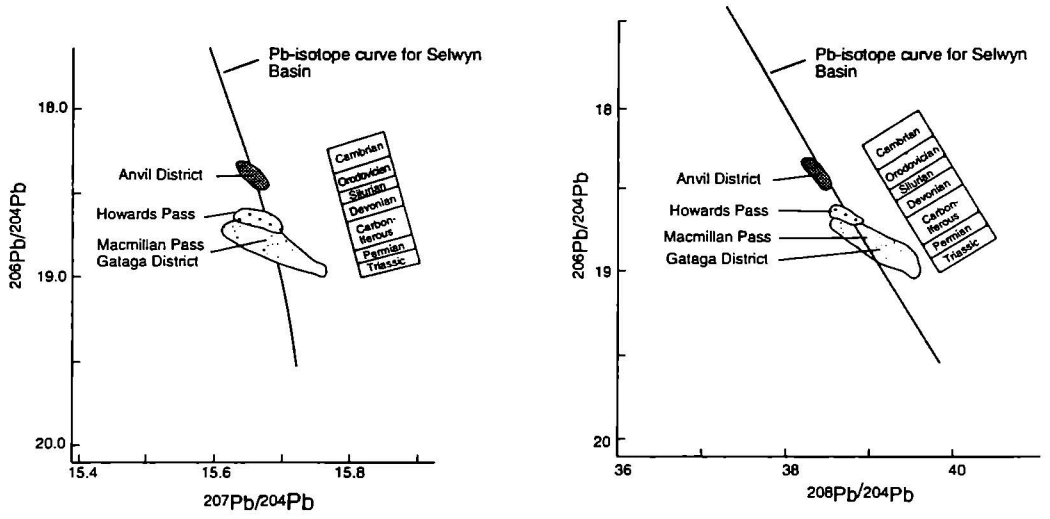

Figure 2.8. *Lead isotope growth curves for statiform massive sulphide deposits in the Canadian Cordillera (after Godwin & Sinclair 1982).*

2.3.2 A general SEDEX model for the Selwyn Basin Pb-Zn-(Ba) deposits

Lydon *et al.* (1985), Lydon (1986), Goodfellow (1985, 1987) and Russell (1986) have proposed a general fluid model for the formation of stratabound massive sulphide deposits in extensional rift basins (Figure 2.9). The model involves S - poor, Zn-, Pb -and Ba-rich brines that have passed through a source unit being exhaled along extensional faults into a rift basin restricted to open ocean circulation. With prolonged stagnation, the water column within the basin becomes anoxic and stratified and enriched in bacterially reduced sulphur. Expulsion of the Pb- Zn - rich brines into this water column results in precipitation of laminated and massive tabular sheets and lenses of barite, sphalerite, galena and pyrite (Figure 2.9).

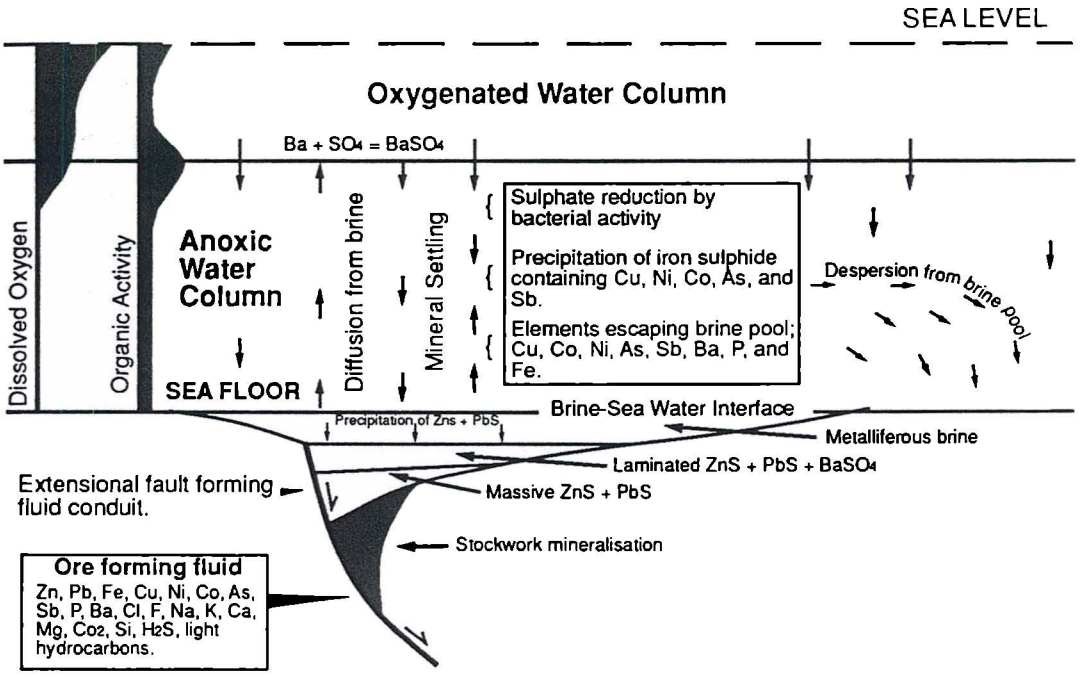

Figure 2.9. *Model for the formation of stratiform Pb-Zn deposits in Selwyn Basin (after Goodfellow 1985).*

This model is probably applicable to the Selwyn Basin deposits because of the existence of the rifting and basin formation events (Thompson *et al.* 1987), the occurrence of periods of restricted circulation (Goodfellow & Jonasson 1984; Shanks *et al.* 1987) and a source unit (Godwin & Sinclair 1982). The Macmillan Pass and Gataga deposits have been shown to have formed in restricted basins with an extensional architecture (McClay *et al.* 1989; McClay 1991; McIntyre 1992). All the stratiform Pb - Zn deposits of Selwyn Basin occur in laminated tabular, lensoidal, to wedge shapes with a basic mineralogy of pyrite, barite, sphalerite and galena (Table 2.2). The "Grit unit" of the Windermere Supergroup provides a source for the metals (see section 2.3.2.1) and the uppermost Proterozoic and Palaeozoic basinal sediments may have acted as act as cap rocks (Lydon *et al.* 1985).

Using the model of Lydon *et al.* (1985), Lydon (1986), Goodfellow (1985, 1987) and Russell (1986) and the geometry and form of the Selwyn Basin deposits (Table 2.2),

Table 2.2. Features of stratiform Pb-Zn deposits of the northern Canadian Cordillera.

Deposit	Form	Mineralisation	Mineralogy	Feeder zone	Size ($t \times 10^6$)
Anvil District	Tabular to lensoidal	Massive and semi-massive sulphides, sulphides and barite	Pyrite, barite, sphalerite, galena, pyrrhotite and magnetite	Not identified	120
Macmillan Pass (Tom)	Tabular to lensoidal	Massive sulphides, sulphides and barite, massive barite	Barite, sphalerite, galena and pyrite	Located at south end of Tom west	15
Howards Pass	Disc shaped sheet	Finely laminated sulphides in cherts and thin limestones	Sphalerite, galena and pyrite	Not identified	525
Gataga District (Cirque)	Wedge-shaped lens	Baritic, pyritic and laminated pyritic facies	Barite, pyrite, sphalerite and galena	Not identified	32.2
(Driftpile)	Tabular sheet	Baritic and laminated pyritic facies	Barite, pyrite, sphalerite and galena	Not identified	20

Modified from McClay (1991) with data from Jennings and Jilson (1986).

McClay (1991) outlined several geometric types of stratiform massive sulphide deposit based on the shape of the sulphide body and its proximity to the fluid conduit - vent system (Figure 2.10). These include; *vent proximal or supra-vent deposits* in which the

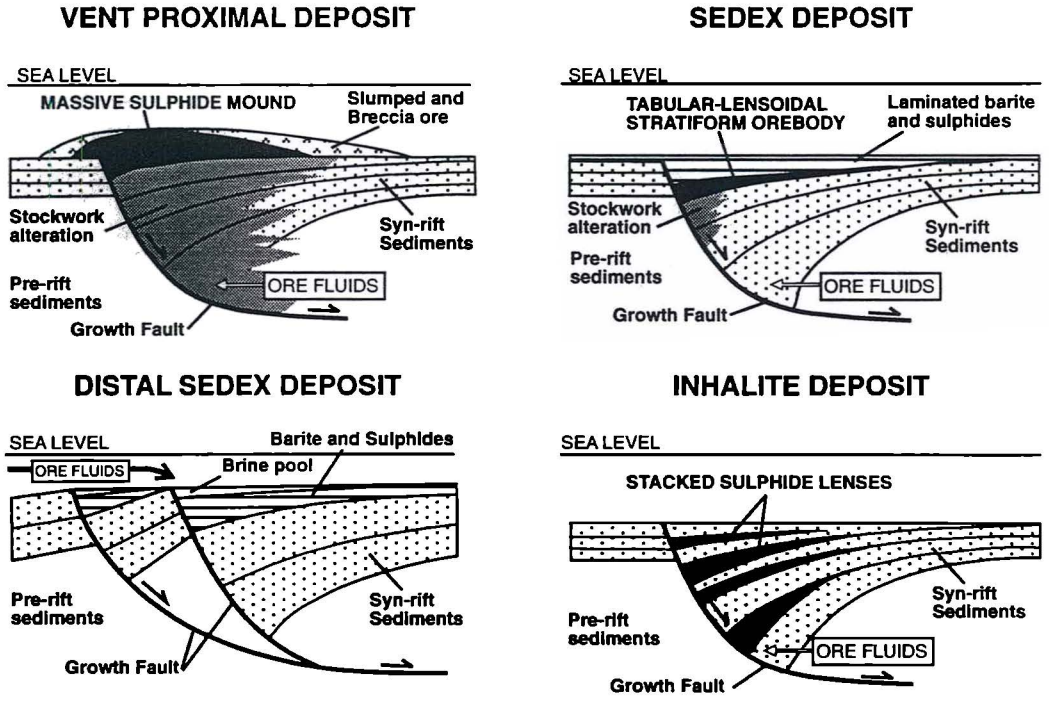

Figure 2.10. *Idealised geometric models for stratiform Pb-Zn (barite) deposits (after McClay 1991).*

sulphide mound is formed directly above or on top of the vent, *stratiform SEDEX style deposits* deposited in the basin adjacent to or on top of the vent, *vent distal SEDEX deposits* that form sheet-like, tabular bodies of large lateral extent but with no apparent relationship to the vent and *inhalite type deposits* that are deposited by infiltration of the sedimentary pile by the metaliferous brines.

2.3.3 Deformation and metamorphism of Selwyn Basin deposits

Very little quantitative pressure - temperature work has been done on the stratiform deposits of Selwyn Basin outside of the Anvil District (this thesis). Most deposits, with the exception of some Anvil District deposits (see section 2.3.4.1), are sub-greenschist to lower-greenschist facies. The pressure-temperature conditions of metamorphism of the major stratiform Pb - Zn deposits in the Selwyn Basin are shown in Figure 2.11.

In an indepth study of the deformation and metamorphism of several major stratiform deposits of the northern Canadian Cordillera, with the exception of the Anvil District, McClay (1991) found that these low metamorphic grade deposits are characterised by

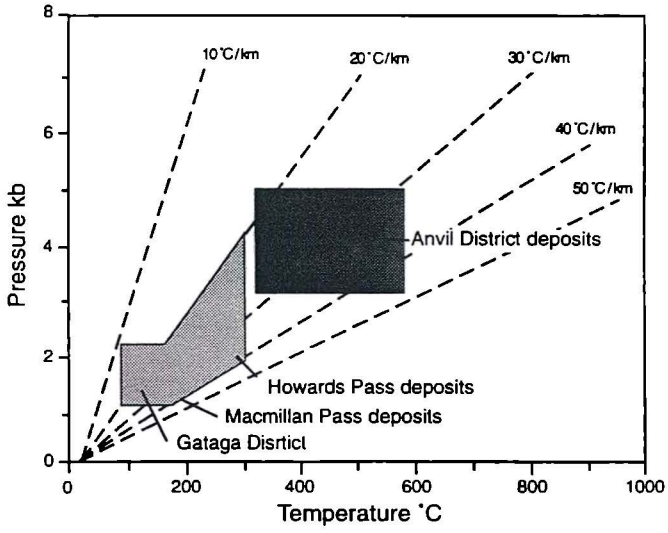

Figure 2.11. *Approximate pressure and temperature conditions of metamorphism for the statiform massive sulphide deposits (after McClay & Ellis 1983). Anvil District data is from Jennings & Jilson (1986) and this study.*

cataclastic flow and brecciation in the coarse-grained massive pyritic sulphides, and by folding, recrystallisation and cleavage development in the finer-grained, barite-rich sulphides. Deformation is in these deposits is characterised by pressure solution in barite and in fine-grained pyrite layers and sulphide-carbonate beds and local transposition accompanied by remobilisation of galena, barite and pyrite. However, relict primary depositional and diagenitic features can still be found in these deposits (McClay 1991, Lianxing & McClay 1992).

2.3.4 Anvil District mineral deposits

2.3.4.1 General deposit geology

The Anvil District is one of the largest Pb-Zn district in northern Canada (see Table 2.2) with estimated geological reserves before mining of 120 million tonnes with a combined Pb + Zn grade of 9.3% (Table 2.3) (Jennings & Jilson 1986). The district contains five Pb-Zn-Ag (barite) deposits of ecomonic significance (two of which have been mined) that lie along a curvilinear trend on the southwest flank of the Anvil Batholith (Figure 2.3). The deposits occur within 150 metres of the carbonaceous boundary between the Mt. Mye formation and the Vangorda formation.

The Anvil deposits have been interpreted to be SEDEX in origin (Carne & Cathro 1982) since they all display a prevalent and well developed compositional layering, an interlayering of sulphides and unmineralised sediments and all deposits in the district occur within a restricted stratigraphic position associated with graphitic or carbonaceous metapelites and thelower metamorphic grade deposits (i.e. Grum and Vangorda) have metamorphic overprinting of primary mineral textures (e.g. Brown & McClay 1993a). The deposits in the Anvil District display a distinct vertical and lateral arrangement of sulphide lithofacies that Jennings *et al.* (1980) and Jennings & Jilson (1986) termed

Table 2.3. Tonnage and ore grade figures of Anvil District deposits, June 1983.

	Tonnage x 10^6	Pb %	Zn %	Ag (g/t)	Cutoff (%Pb + Zn)
Faro	ceased operations, Sept. 1992				
Geological reserves before mining	57.6	3.4	4.7		5.0
Open pit reserves	—	—	—	—	—
Grum					
Geological reserves	30.8	3.1	4.9	49	4.0
Open pit reserves	16.9	3.0	4.9	47	4.0
Vangorda					
Geological reserves before mining	7.1	3.4	4.3	48	4.0
Open pit reserves	presently being mined				
Dy					
Geological reserves before mining	20.3	5.7	7.0	82	9.0
Swim					
Geological reserves before mining	4.3	3.8	4.7	42	6.0
Total					
Geological reserves before mining	120.1	3.7	5.6	—	—

- Data taken from Jennings and Jilson (1986)

the 'Anvil Cycle'. Reconstruction of the strongly deformed deposits indicates a general lensoidal shape (Figure 2.12). However, the exact primary geometry of the Anvil deposits is impossible to determine because of the strong structural and metamorphic overprint. The ore lithostratigraphy consists of a lower ribbon-banded, carbonaceous quartzite; a pyritic quartzite; a massive pyritic quartzite; and a baritic massive sulphide. These different sulphide lithofacies of the Vangorda orebody are discussed in detail in Chapter 3.

The only metamorphism of the Anvil District deposits that can be discerned with any confidence is associated with intrusion of the Anvil Plutonic Suite (i.e. M_2). The M_2 grade of the Anvil deposits is middle-greenschist to amphibolite facies, higher than that of other stratiform deposits in Selwyn Basin (Figure 2.11). The massive sulphide deposits are variably affected by the various deformation events affecting the Anvil District (see section 2.2.3), with D_1 and D_2 being dominant (Jennings & Jilson 1986). The large Faro deposit (Figure 2.13a) is deformed by D_1 through to D_4 and

The Anvil Cycle Lithostratigraphy

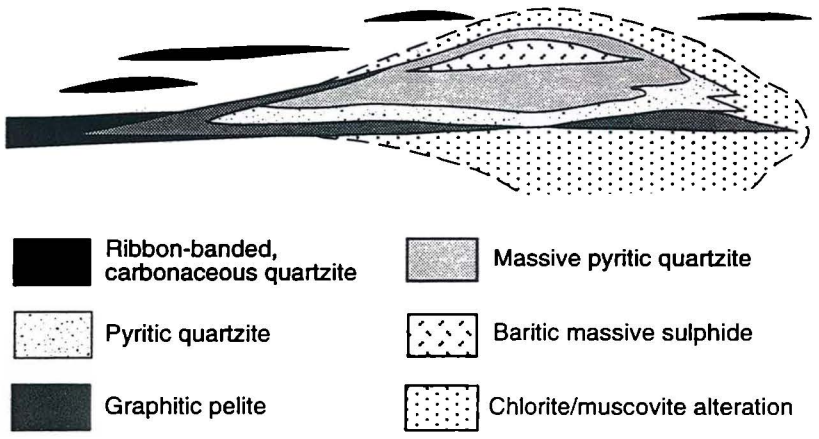

Figure 2.12. *The Anvil District massive sulphide lithostratigraphic sequence termed the Anvil Cycle by Jennings & Jilson (1986).*

metamorphosed to amphibolite facies. Grum (Figure 2.13b), Vangorda and Dy (Figure 2.13c) are mostly affected by D_1 and D_2 folds, with only minor F_3 folding and crenulation development, and reach greenschist facies metamorphism.

Tempelman-Kluit (1970) and McClay & Ellis (1983) noted a crude correlation between pyrite grain size and metamorphic grade in the Anvil deposits. The amphibolite facies Faro deposit has coarser grained pyrite than does the greenschist facies Grum and Vangorda deposits. The Swim deposit in the southeast (Figure 2.3), the lowest metamorphic grade deposit in the deposit, has the smallest pyrite grain size (Tempelman-Kluit 1970).

Deformation in these deposits is characterised by tight to isoclinal folding, cataclastic flow, shearing, extensive remobilisation of sulphides and barite and brittle extensional faulting (e.g Jennings & Jilson 1986; Brown & McClay 1992, 1993b). Grain-scale deformation processes in the Anvil deposits involve cataclasis, pressure solution, dislocation processes and annealing (Lianxing & McClay 1992; Brown & McClay

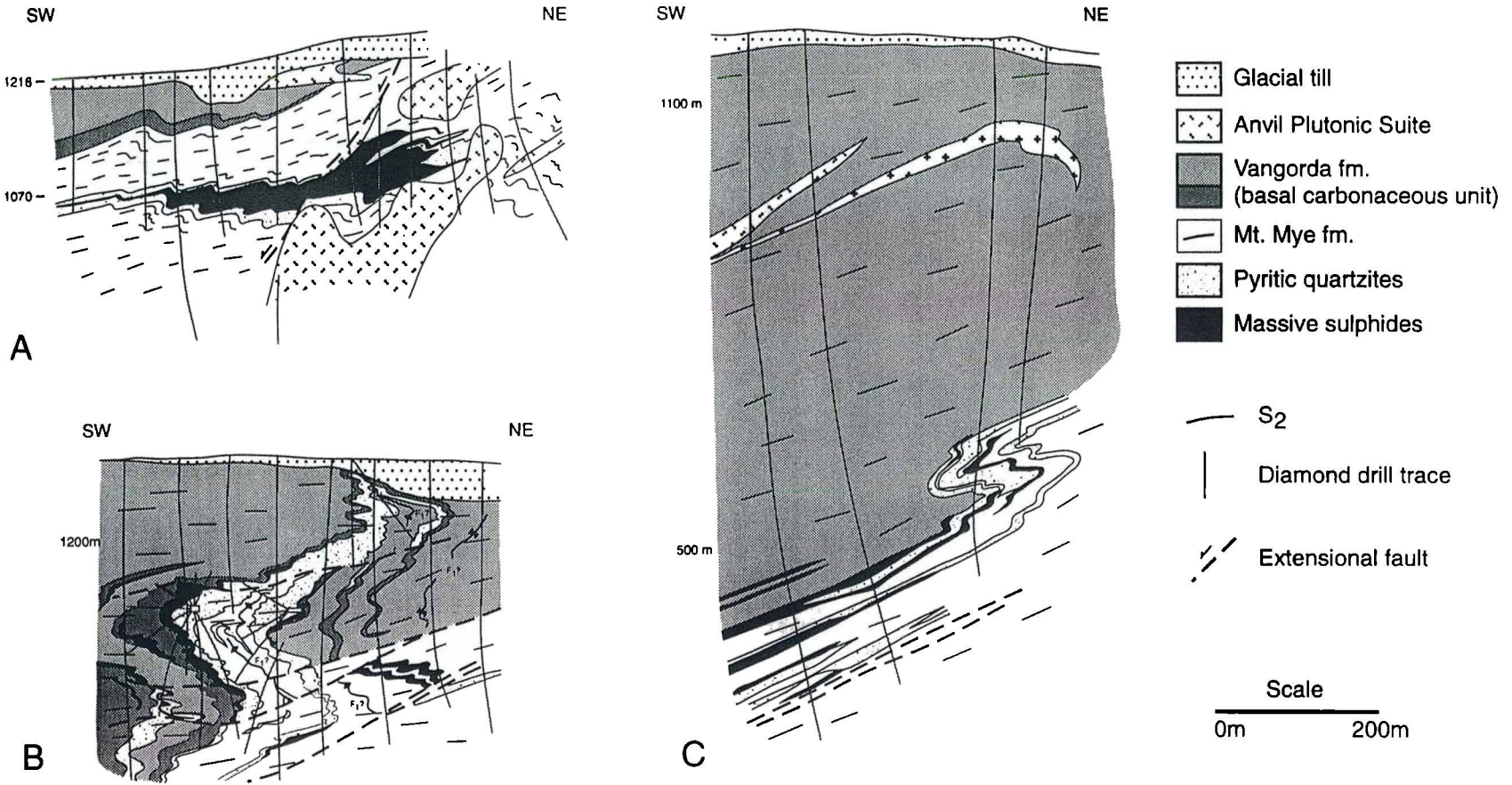

Figure 2.13. *Cross sections through three of the Anvil District deposits. A) Faro orebody. B) Grum deposit. C) Dye deposit. (After Jennings & Jilson 1986).*

1993). Further discussion of the deformation and metamorphism affecting the Anvil deposits, with the exception of Vangorda, is beyond the scope of this thesis and the reader is referred to Jennings & Jilson (1986) for an overview.

2.3.4.2 Sulphur and lead isotopes

Shanks *et al.* (1987), using sedimentary pyrite $\delta^{34}S$ data from the Anvil district (Table 2.4), have extended the Selwyn basin sulphate curve to include the Cambrian (Figure 2.9) where $\delta^{34}S$ values tend to be much lower than, to slightly higher than, the mean ocean water evaporite curve. Shanks *et al.* (1987) found that within the Anvil District barite $\delta^{34}S$ values closely approximate the mean ocean water evaporite curve (Figure 2.9), although there are significant variations between deposits in the district (Table 2.4). Shanks *et al.* (1987) also noted a systematic upwards increase in $\delta^{34}S$ values that they interpreted to be the result of bacterially induced sulphate reduction and stratification of the water column. Furthermore, the variations in $\delta^{34}S$ values between the Anvil deposits may indicate that they formed in separate 2nd to 3rd order basins with local sulphate mineralisation conditions (Shanks *et al.* 1987).

The Anvil District lead isotope data was used by Godwin & Sinclair (1982) to construct the Selwyn Basin lead isotope growth curve (Figure 2.10). The lead isotope values fall

Table 2.4. $\delta^{34}S$ isotope data for Anvil District deposits. [1]

	$\delta^{34}S$ (‰)					
	SpGaPo[2]	Pyrite	Sphalerite	Galena	Pyrrhotite	Barite
Faro	12.8 to 19.2	13.6 to 20	——	——	——	23.5 to 26.8
DY	11.3 to 22.4	12.6 to 22.4	——	——	12.4 to 17.3	21.3 to 48.5
Grum	——	7.3 to 21.9	10.8 to 19.2	9.4 to 18.7	——	28.0 to 35.2

[1]From Shanks *et al.* (1987).

[2]Sphalerite + Galena + Pyrrhotite

within the Cambrian - Ordovician part of the 200 Ma period defined by Godwin & Sinclair (1982) as the mineralisation interval of Selwyn Basin.

Table 2.5. Lead isotope data for Anvil District deposits. [1]

	$^{206}Pb/^{204}Pb$	$^{207}Pb/^{204}Pb$	$^{208}Pb/^{204}Pb$
Faro	18.316 to 18.414	15.625 to 15.674	38.205 to 38.364
DY	18.376 to 18.473	15.591 to 15.685	38.193 to 38.539
Grum	18.375 to 18.846	15.642 to 15.717	38.227 to 38.899

[1]From Shanks *et al.* (1987).

2.3.4.3 Model for formation of Anvil District deposits

Based on the $\delta^{34}S$ data, together with the stratigraphic position and form of the deposits Jennings & Jilson (1986) and Shanks *et al.* (1987) have interpreted the Anvil District massive sulphide deposits to have formed in anoxic, restricted 2nd to 3rd order extensional basins in larger epicratonic to intracratonic rift basins related to the third rifting event of Thompson *et al.* (1987), similar to younger deposits described elsewhere in Selwyn Basin by Lydon *et al.* (1985), McClay (1991) and McIntyre (1992). Furthermore, the lead isotope values and the $\delta^{34}S$ values point to the source of the metals in the Anvil deposits, like those in Howards Pass, the Gataga District and Macmillan Pass as being the Proterozoic "Grit unit" (Godwin & Sinclair 1982; Shanks *et al.* 1987). However, there is some variation in lead isotope values between deposits within the Anvil district (Table 2.5) which may reflect local isotopic contamination suggesting a lead source other than the "Grit unit" for some of the lead in the deposits. Mafic igneous rocks may be a possible source of this lead (Shanks *et al.* 1987). However, the variations in lead and sulphur isotopes may be a result of the differing amount of deformation and the metamorphic grade of the deposits (*op. crit.*).

The isotopic data, inferred basin development and similarity between the Anvil deposits

and other, less deformed and better studied massive sulphide deposits in the northern Canadian Cordillera, suggest that the model outlined for the formation of these latter stratiform Pb-Zn deposits can be applied to the deposits in the Anvil District. The Anvil District deposits are possibly of the SEDEX or INHALITE types of McClay (1991). However, important information about the development of the Anvil deposits is missing. For instance, direct evidence for a basin-bounding fault(s) is lacking, although the linear arrangement of the sulphide deposits may reflect such a fault. Also, to date, no feeder zone has been unequivocally defined for any of the Anvil deposits (Jennings & Jilson 1986).

CHAPTER 3

Geology and Lithostratigraphy of the Vangorda Orebody

3.1 Introduction

This chapter discusses the macroscale structural context in which the Vangorda orebody occurs and describes the host rock lithostratigraphy and the sulphide lithofacies. The major element distribution within the various sulphide lithofacies is discussed.

3.2 Geology of the Vangorda orebody

The Vangorda orebody is located in the greenschist facies fault block of the Anvil District (Jennings & Jilson, 1986), in the hangingwall of the Tie fault (Figure 3.1). The Tie fault is one of a group of extensional faults in the district related to unroofing of the Anvil Batholith (section 2.2.3). This fault places greenschist facies rocks in its hangingwall against amphibolite facies rocks in its footwall. The Vangorda orebody is truncated to the northwest by the Northwest fault and is located in its hangingwall (Figure 3.1). The large Grum orebody is located in a fault block approximately three kilometres to the northwest, also in the hangingwall of the Tie fault.

A moderate to well exposed stream section from the Anvil Batholith to the overlying Yukon-Tanana Terrane (see Figure 2.3) crosses the orebody, allowing a schematic S_1/S_2 cross section to be constructed (Figure 3.1). Based on this section and on regional mapping, together with diamond drill core analysis, the Vangorda orebody is interpreted to occur in the hinge zone of a southwest-verging, northwest-plunging, shallowly downward-facing to recumbent macroscopic F_2 antiform or synformal-antiform (Figure 3.1). The orebody plunges shallowly northwest parallel to this regional F_2 fold axes.

The orebody has been polydeformed and metamorphosed to lower-greenschist facies during the regional D_1/M_1 and D_2/M_2 deformation and metamorphic events discussed in Section 2.2.3 (Tempelman-Kluit 1972; Jennings & Jilson 1986; Brown & McClay 1992). The D_2 deformation event strongly affected the orebody, resulting in the formation of structures and penetrative fabrics (section 4.3) that, in many cases, make D_1 structures difficult to distinguish. However, the preservation of D_1 structural elements such as S_1 allow a detailed structural analysis to be carried out (see section 4.3). Definition of any primary features is ambiguous.

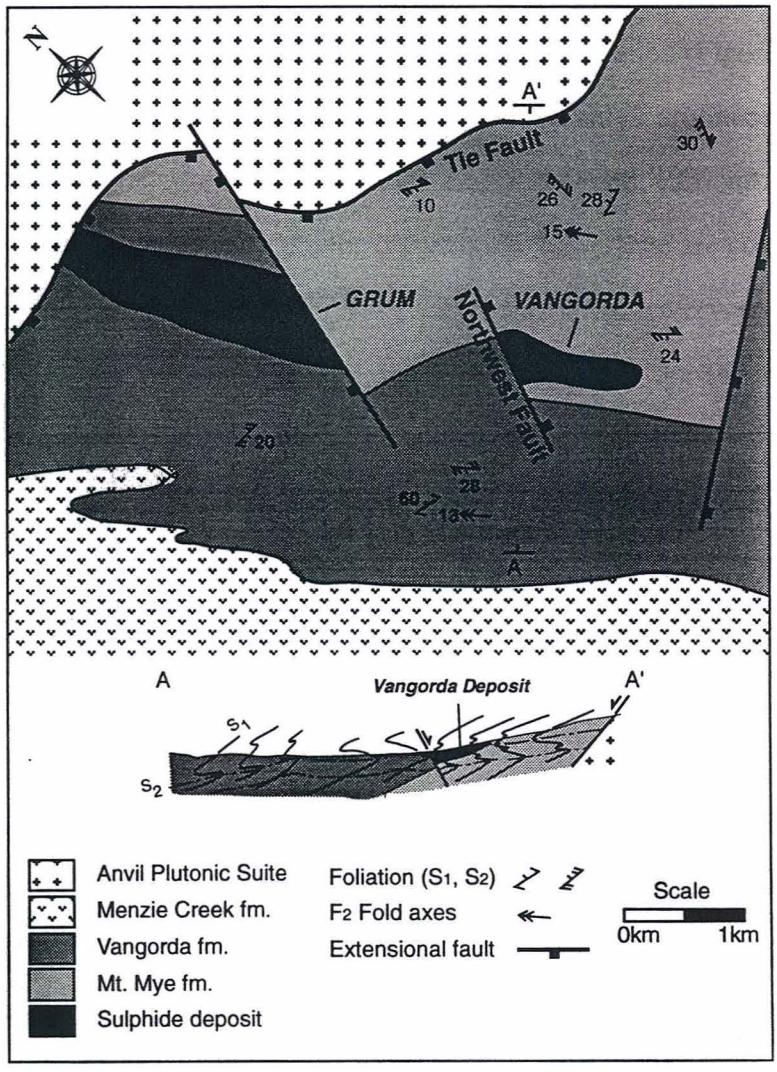

Figure 3.1. *Schematic geological map and cross section of the area around the Vangorda orebody.*

3.3 Lithostratigraphy

3.3.1 Host rock lithostratigraphy

The Mount Mye and Vangorda formations are the two non-sulphide lithostratigraphic units that outcrop in the Vangorda open pit. The Vangorda orebody occurs 50 to 100 metres below the basal carbonaceous unit of the Vangorda formation (Figure 2.5), entirely within the Mount Mye formation.

3.3.1.1 The Mount Mye formation

In the vicinity of the Vangorda orebody the Mount Mye formation (Figure 3.2) consists of light to medium grey noncalcareous, fine-grained, weakly carbonaceous, quartz + muscovite ± chlorite ± biotite phyllite with lesser, interlayered, carbonaceous phyllite, calcareous phyllite, and metabasic phyllite. Pyrrhotite and pyrite are common, though not abundant, sulphides in the phyllites. These rocks have a very well developed, penetrative cleavage and, locally, a well developed lithon texture (see Chapter 4 for discussion for these fabrics). Mount Mye formation phyllites are the host to the Vangorda orebody and are interbanded with the sulphide lithofacies rocks on a scale of centimetres to metres. Bands of massive sulphide up to one metre thick are also common within the phyllites. Locally, especially in the footwall of the deposit, Mount Mye phyllites are strongly altered to a quartz + muscovite assemblage. Formation of the alteration zone may be a primary feature related to ore forming fluids, or it may be a metamorphic feature (Jennings and Jilson 1986) or is a result of both processes. Further discussion of the alteration zone is beyond the scope of this thesis. Locally, minor amounts of fuchsite-bearing phyllites are found and these may represent extensively altered metabasic rocks.

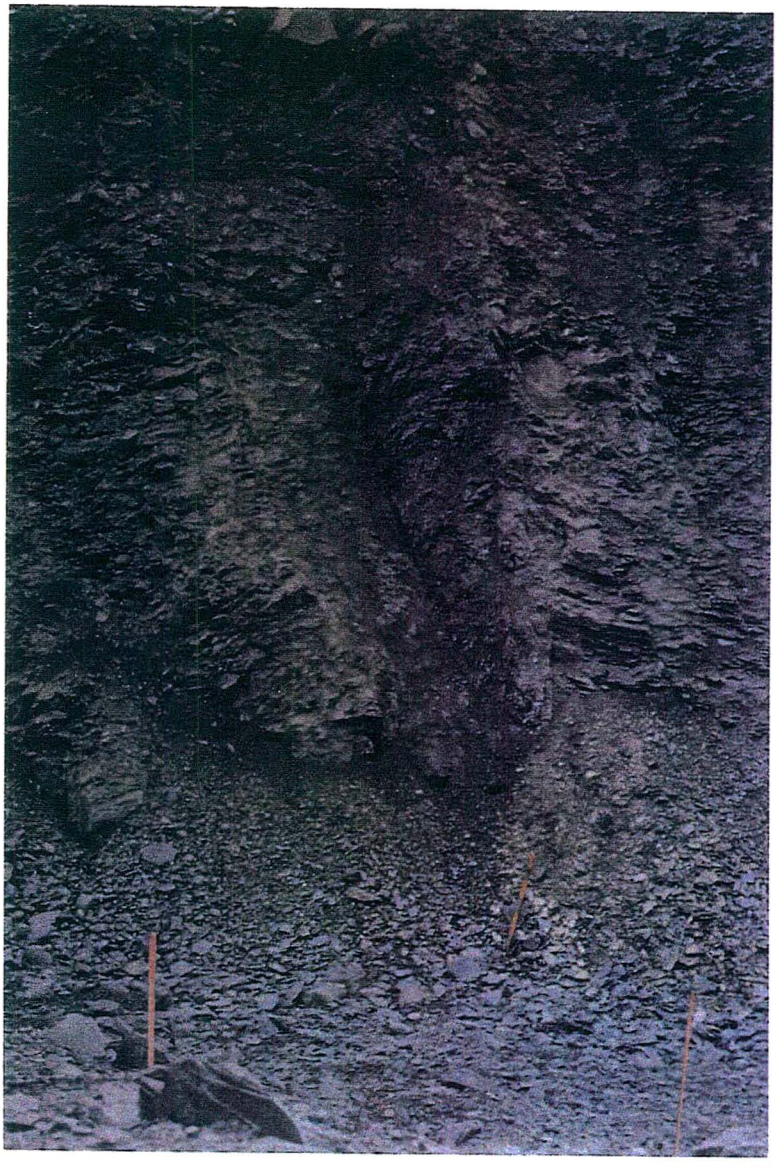

Figure 3.2. *Field photograph of the Mount Mye formation phyllite. The sub-horizontal fabric is S_2. The stake in the foreground is approximately one metre high.*

3.3.1.2 The Vangorda formation

The Vangorda formation consists of light to medium grey, fine-grained, calcareous, weakly carbonaceous muscovite-chlorite phyllite and light grey, quartz + calcite (± dolomite) phyllite with interbanded metabasite, carbonaceous phyllite, and phyllitic limestone (Figure 3.3). The Vangorda formation also has a well developed foliation and

a locally developed lithon texture. The Vangorda formation is only exposed along the northwestern wall of the open pit and is in fault contact with the sulphide lithofacies rocks (also see Figure 4.2).

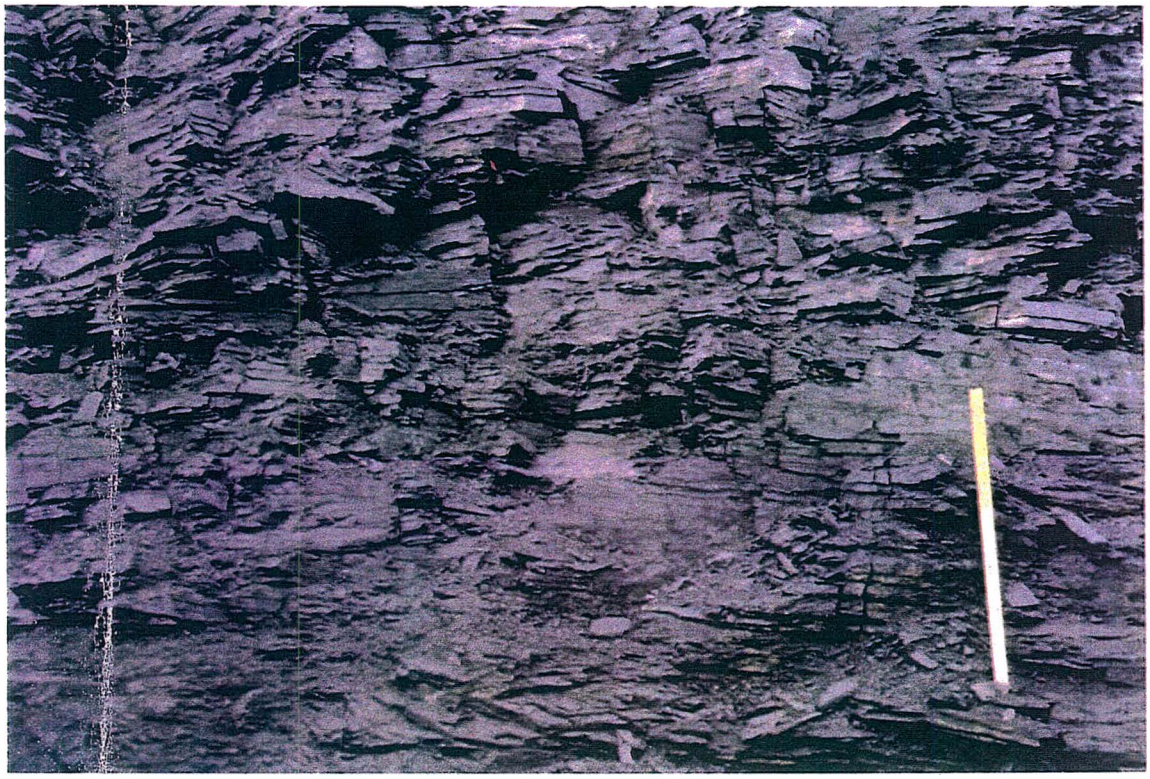

Figure 3.3. *Field photograph of the Vangorda formation phyllite. The sub-horizontal fabric is* S_2. *The stake is approximately one metre high.*

3.3.2 Ore Lithofacies

The Vangorda orebody consists of one to three major, stacked sulphide lenses of varying thickness and bulk sulphide composition. The typical sulphide mineralogy of the deposit is pyrite, sphalerite, galena and pyrrhotite with minor chalcopyrite, arsenopyrite and marcasite. End-member ore lithofacies include a ribbon-banded, carbonaceous quartzite, a pyritic quartzite, a pyritic massive sulphide, a baritic massive sulphide and a pyrrhotite, sphalerite, galena massive sulphide. These lithofacies are interbanded on a scale of centimetres to metres and display a complete gradation from one to another.

3.3.2.1 Ribboned-banded, carbonaceous, pyritic quartzite

These are well banded, fine grained, carbonaceous, phyllitic to siliceous quartzite and interbanded, sulphide-bearing (pyrite, sphalerite, and galena) coarsely crystalline quartzite (Figure 3.4). A differentiated layering is typically well-developed and ranges from 0.2 mm to 2.0 mm in thickness and contains 10% to 30% sulphides. Lithon textures are widespread. Pyrite in these rocks forms 0.2 mm to 1.0 mm subhedral to euhedral porphyroblasts. Sphalerite and galena form 0.05 mm to 0.1 mm porphyroblasts with coarser sphalerite reaching 1 mm in size. This lithofacies is locally economic.

The non-sulphide gangue minerals include 0.2 mm to 1.0 mm equant to subhedral quartz and minor carbonate. Minor chlorite and muscovite together with carbon (graphite?) occurs along both the S_1 and S_2 foliations.

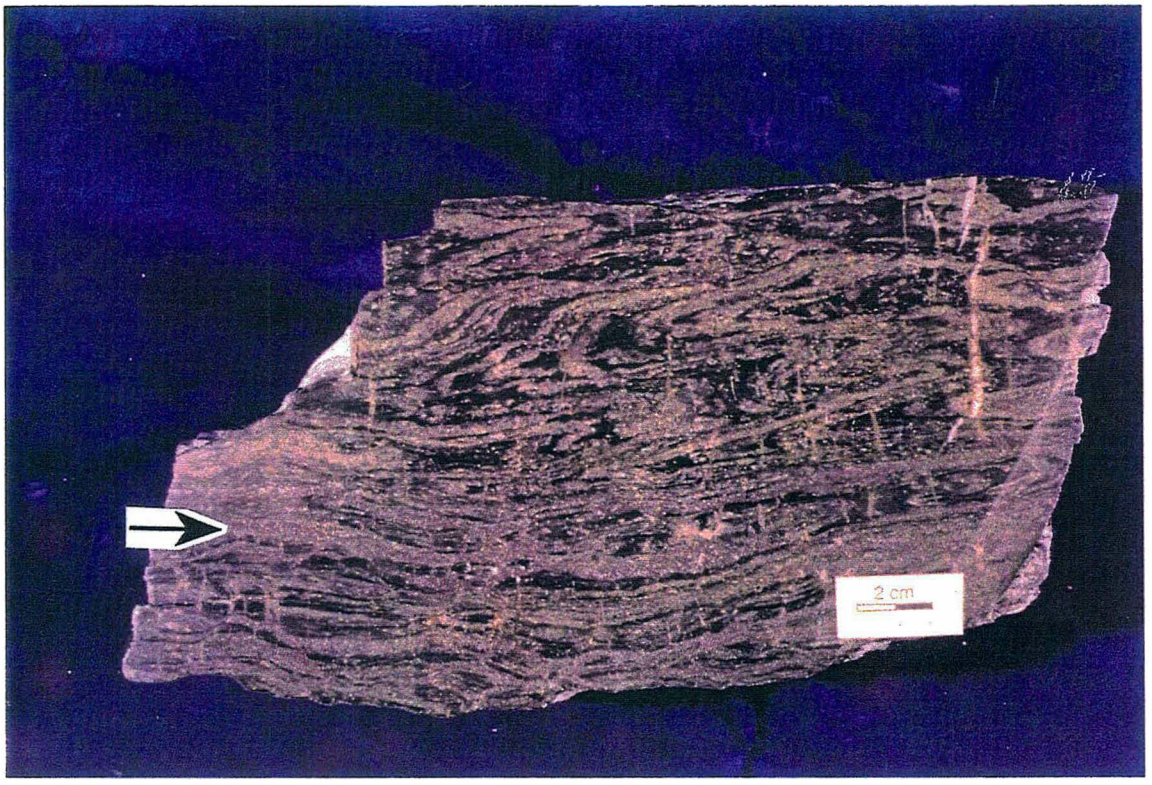

Figure 3.4. *Ribbon-banded, carbonaceous quartzite lithofacies. The dominant, sub-horizontal fabric is S_2. S_1 occurs as lithons between S_2.*

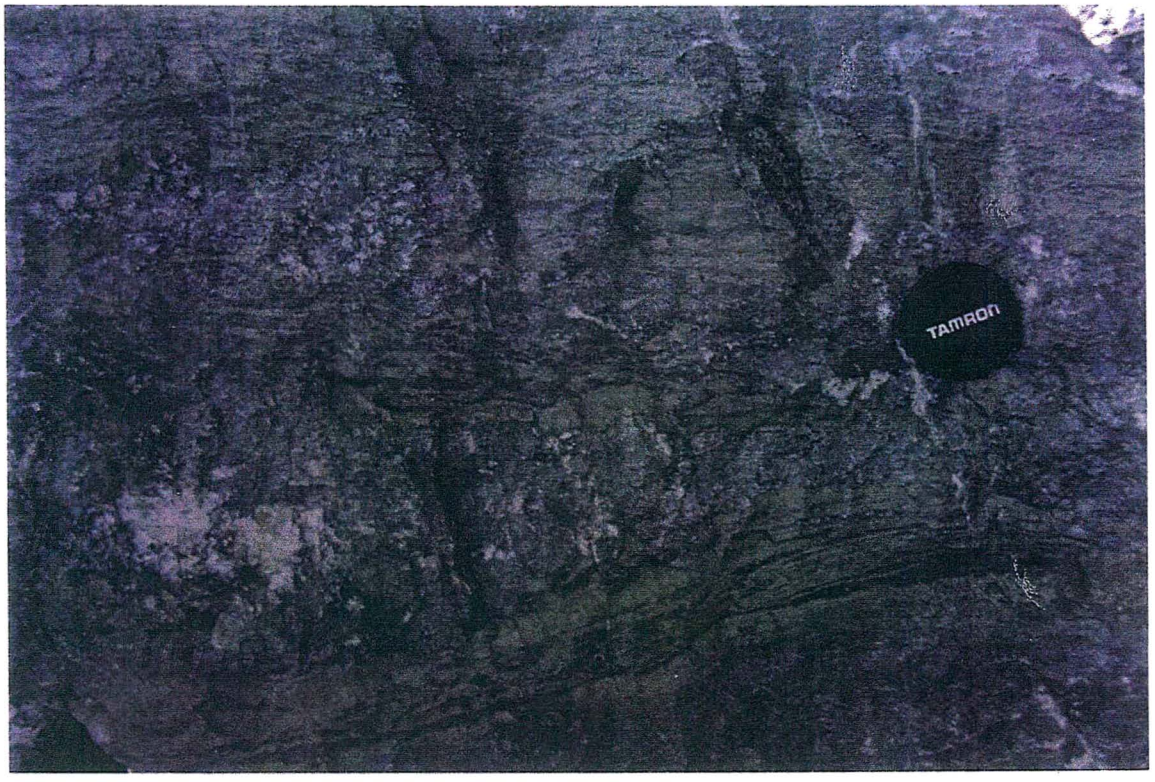

Figure 3.5. *Pyritic quartzite lithofacies with well-developed S_1 differentiated layering.*

3.3.2.2 Pyritic quartzite

This lithofacies consists predominantly of quartz with up to 40% pyrite with sphalerite, galena, and minor pyrrhotite and chalcopyrite (Figure 3.5). These rocks have a moderately to poorly developed differentiated layering with, locally, a well developed micaceous (muscovite ± chlorite) foliation. Pyrite occurs as subhedral to euhedral, 0.01mm - 0.5mm porphyroblasts that locally reach sizes of up to 1.5 mm. Sphalerite and galena are subhedral to euhedral, 0.05 to 0.2 mm porphyroblasts. Chalcopyrite ± pyrrhotite and minor marcasite commonly infill subvertical, post-F_2 fractures or occur as very fine grained matrix. The pyritic quartzites are generally non-economic, though they do contain mineable Pb-Zn grade locally.

The major non-sulphide gangue minerals include 0.2 mm to 1.0 mm, equant to subhedral quartz, carbonates (calcite and dolomite), minor barite and carbon (graphite?). Locally, chlorite and muscovite define a weak S_2 foliation.

3.3.2.3 Massive pyritic sulphides

This lithofacies consists of massive pyrite with lesser sphalerite, galena, pyrrhotite, and minor magnetite and chalcopyrite (Figure 3.6). Total sulphide content varies from between 60% to close to 100%. Quartz, barite, and carbonates are disseminated throughout or occur in aggregates. Differentiated layering is developed on a scale of centimetres to metres as alternating massive pyrite and pyritic quartzite, often grading from one to the other. A magnetite + pyrrhotite + quartz foliation is common. Pyrite forms anhedral to euhedral, 0.1 mm to 1 mm porphyroblasts, with local coarser grained patches. Sphalerite, galena and pyrrhotite occur has intergrowths of subhedral to euhedral 0.05 to 0.5 mm porphyroblasts interstitial to pyrite porphyroblasts. Minor chalcopyrite, pyrrhotite and marcasite infill fractures. The massive pyritic quartzite is

Figure 3.6. *Massive pyrite lithofacies with moderately developed S_1 differentiated layering.*

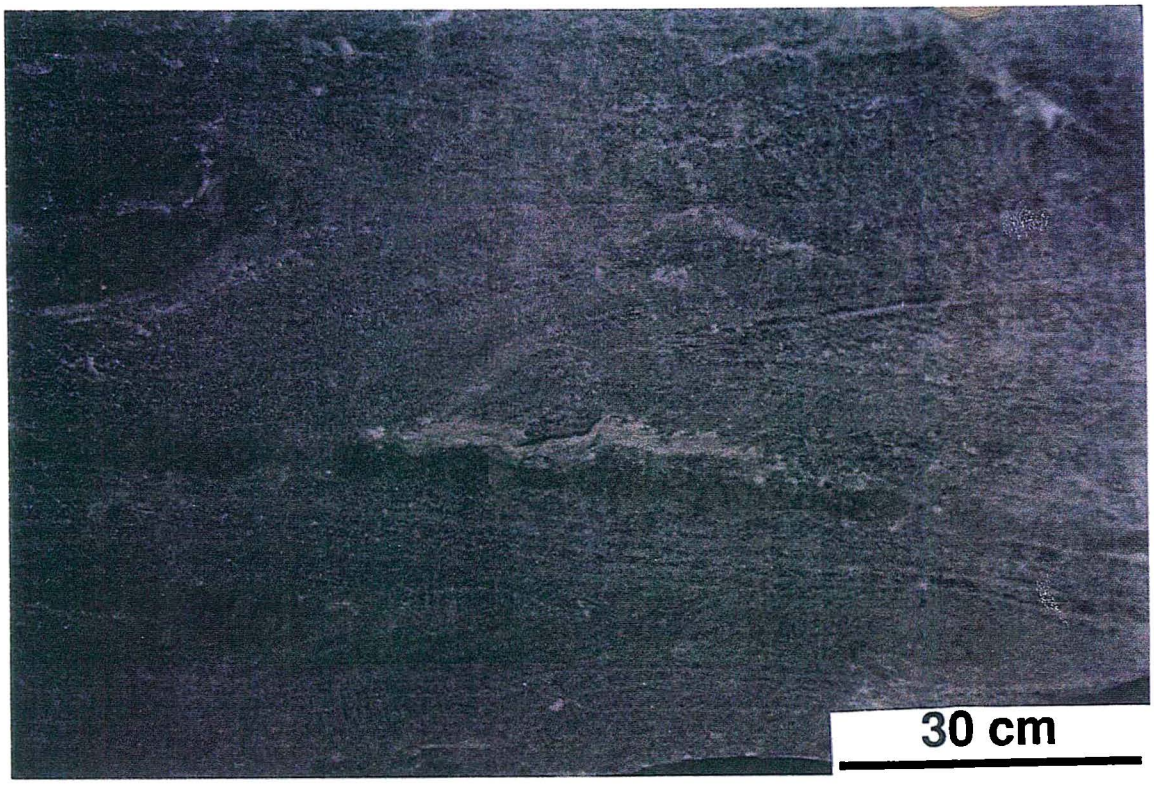

Figure 3.7. *Baritic massive sulphide lithofacies with well-developed S_1 differentiated layering*

gangue.

3.3.2.4 Baritic, massive pyritic sulphides:

This lithofacies consists predominantly of barite with pyrite, sphalerite, and galena, with minor pyrrhotite, magnetite, quartz and carbonate (Figure 3.7). Millimetre- to centimetre-scale differentiated layering of pyrite-rich and barite-rich layers is ubiquitous. Clasts of pyrite and phyllite are common. Total barite content varies but may be has high as 50 %. Massive barite does not occur. Barite occurs as equant, 0.25 mm to 0.75 mm grains. Pyrite forms anhedral to euhedral, 0.1 mm to 0.5 mm porphyroblasts. Sphalerite and galena form subhedral to euhedral, 0.02 to 0.1 mm porphyroblasts. Minor chalcopyrite and pyrrhotite infill fractures. There is complete gradation between the baritic massive sulphide ores and the massive pyritic ore. This lithofacies is the major ore rock in the deposit.

3.3.2.5 Pyrrhotite + sphalerite + galena massive sulphides

This lithofacies consists predominantly of pyrrhotite and sphalerite with lesser pyrite, magnetite, and galena (Figure 3.8). This lithofacies is highly strained with a well developed sulphide and micaceous foliation and often contains breccia clasts of other lithofacies around which the foliation anastomoses. Tailed porphyroblasts, winged inclusions, foliation boudins, and rolling structures are common (see Chapters 4 and 5). Pyrrhotite forms 0.05 to 0.2 mm euhedral to elongate porphyroblasts that have a well developed preserved grain shape orientation locally. Sphalerite occurs as 0.02 to 0.5 mm subhedral to euhedral porphyroblasts. Pyrite occurs as 0.1 to 1.5mm-sized equant to subhedral porphyroblasts, often replacing pyrrhotite. Locally, minor arsenopyrite occurs in an assemblage with pyrrhotite or as overgrowths on pyrite. This lithofacies is often economic.

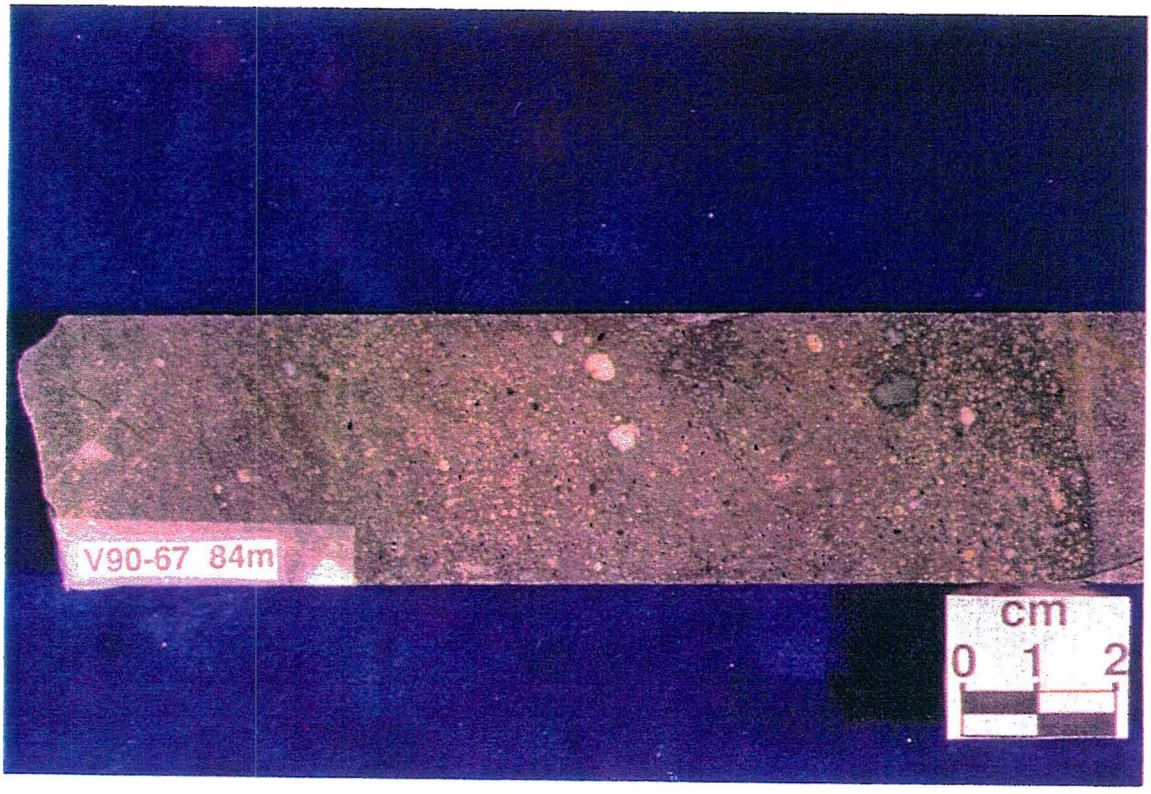

Figure 3.8. *Pyrrhotite + sphalerite + galena massive sulphide lithofacies. Note the rounded inclusions of quartz.*

3.4 Distribution of metals in the sulphide lithofacies

The main ore unit in the Vangorda orebody is the baritic massive sulphides which generally contains Pb + Zn grades of 8 to 16 % with much higher grades locally (Figure 3.9). The pyrrhotite + sphalerite + galena massive sulphides also contain high Pb + Zn grades locally (8 - 12 %) (Figure 3.9) but these are volumetrically a minor lithofacies. The other lithofacies generally have sub-economic Pb + Zn grades with economic concentrations occurring only locally (Figure 3.9). The pyritic quartzites, massive pyritic sulphides and pyrrhotite + sphalerite + galena massive sulphide all have a high concentration of iron

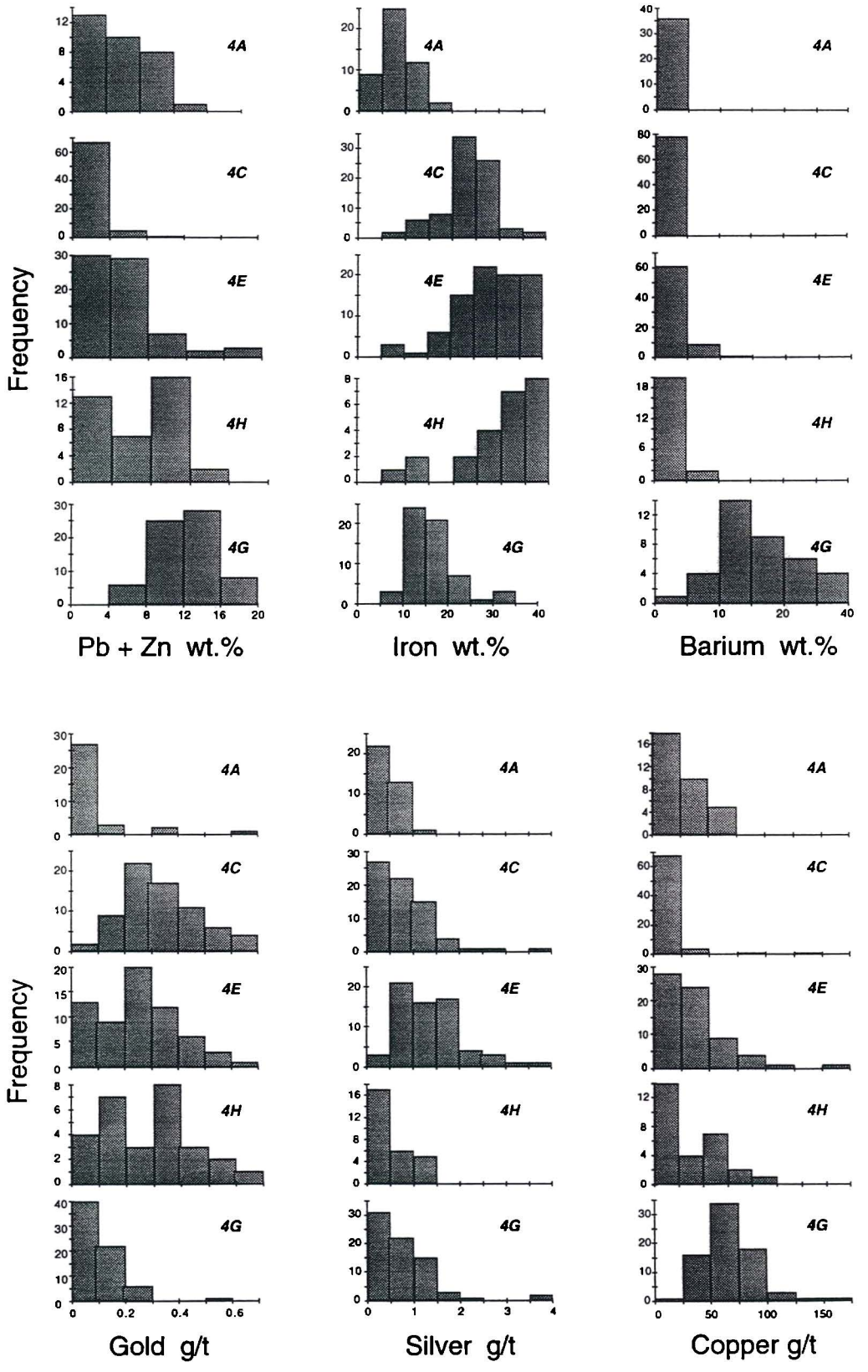

Figure 3.9. *Grade histograms for the various lithofacies in the Vangorda orebody. See text for discussion. 4A = Ribbon-banded, carbonaceous quartzite, 4C = pyritic quartzite lithofacies, 4E = massive pyrite lithofacies, 4H = pyrrhotite + sphalerite + galena lithofacies, 4G = Baritic massive sulphide lithofacies.*

(20- 40 wt.%) (Figure 3.9). High iron concentrations in the latter is likely due to the presence of a high modal abundance of pyrrhotite. The ribbon-banded, carbonaceous quartzite and baritic massive sulphides have much lower weight % iron (5 - 20 wt.%) (Figure 3.9). Barium is concentrated in the baritic massive sulphides with all other lithofacies having only minor barium (Figure 3.9).

Minor element distribution shows various trends (Figure 3.9) with gold occurring mainly in the pyritic quartzites, massive pyritic quartzites and pyrrhotite + sphalerite + galena massive sulphides. Silver occurs predominantly in the massive pyrite with significant lower grades in the pyritic quartzites and the baritic massive sulphide lithofacies (Figure 3.9). Copper occurs mainly in the baritic lithofacies with lower grades in massive pyrites (Figure 3.9).

Whole rock assay analyses indicate an extremely good correlation between wt% Pb and wt% Zn of approximately 0.75. This trend is similar to deposits formed in calcareous sediments (c.f. Lydon 1983; Sangster 1990). There is a strong correlation between Cu and Zn (Figure 3.10) with the highest copper grades occurring in the baritic massive sulphides. There is a weaker correlation between Au and Fe (Figure 3.10) but the gold is concentrated in the pyritic quartzite and massive pyrite lithofacies (Figure 3.9). The is no apparent correlation between Ag and Pb (Figure 3.10) and the highest Ag grades occur in the massive pyrite lithofacies and slightly lower grades in the pyritic quartzite and baritic massive sulphide lithofacies, respectively (Figure 3.9).

The correlations between Cu and Zn suggests that copper in the orebody is associated with sphalerite, either substituting for Zn or as inclusions. However, microprobe analysis indicate sphalerite has a very low Cu content (see Appendix 3) so the majority of Cu must be chalcopyrite inclusions in sphalerite grains or infilling fractures. Similarly the correlation between Au and Fe and the occurrence of the highest Au assays in pyritic

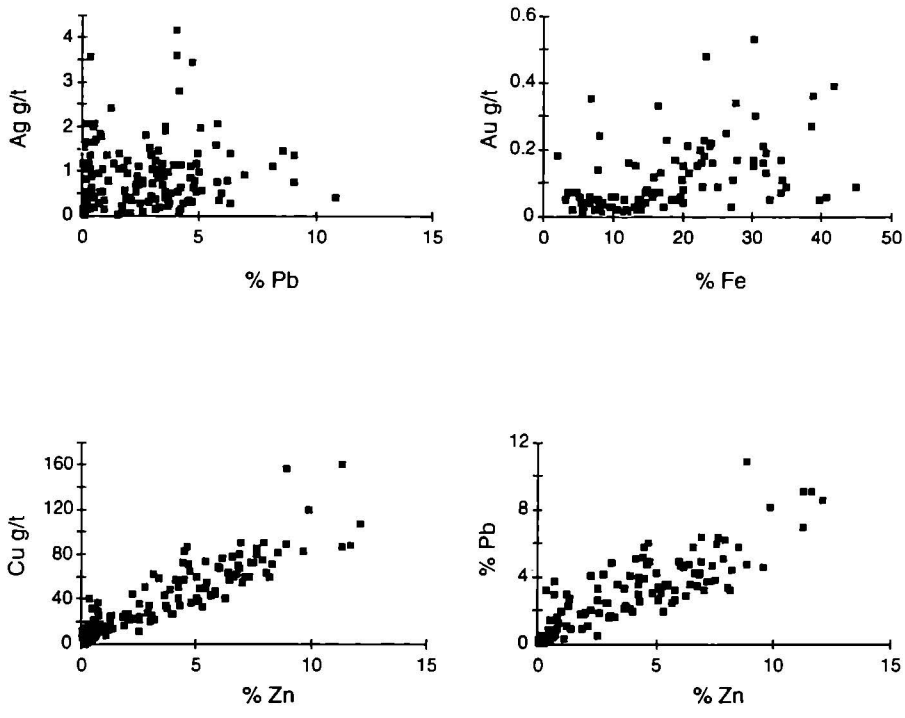

Figure 3.10. *Graphs showing correlation's between various elements in the Vangorda orebody. See text for discussion.*

quartzite and massive pyrite lithofacies suggests that gold is associated with pyrite. However, only one grain of gold was identified petrographically in association with pyrite and microprobe analysis indicates gold in pyrite occurs at the lower range of the detection limit. The lack of a correlation between Ag and Pb suggests that, contrary to expectation, the silver is not uniformly substituting for Pb in galena, nor has it been found to occur as fine-grained inclusion in the galena. However, microprobe analysis shows that galena is the only major silver-bearing mineral, though the poor correlation between Pb and Ag shown by the whole rock assay values is maintained. No silver bearing minerals were found petrographically.

CHAPTER 4

Structural element analysis of the Vangorda orebody

4.1 Introduction

Open pit mining operations began in the Vangorda orebody during July of 1990 and continued until October of 1992. During this time mapping of the open pit walls was carried out at a 1 : 200 scale and diamond drill core was re-examined in order to get a better understand of the structural elements found in the core using the information obtained from mapping. A 1:1000 scale map (Figure 1.2) and three 1:1000 scale diamond drill core cross sections (Figures 1.3, 1.4 and 1.5) are enclosed in the back pocket of this thesis. These form the base from which a number of the figures in this chapter are taken and a location map is provided along with the figures so the reader can readily identify the geological context in which these examples occur. With the exception of one regional cross section (discussed in section 4.2), mapping was confined to the mine.

This chapter discusses the geology of the Vangorda open pit mine, documenting the various geological features and structural elements and textures found in outcrop. These are then used to interpret the diamond drill core data.

4.2 The Vangorda orebody

As discussed in Chapter 3 the Vangorda orebody is located in the greenschist facies fault block of the Anvil District (Jennings & Jilson, 1986), in the hangingwall of the Tie fault (Figure 4.1) and is truncated to the northwest by the Northwest fault (Figure 4.2). The Vangorda orebody is interpreted to occur in the hinge zone of a southwest-verging, northwest-plunging, shallowly downward-facing to recumbent macroscopic F_2 antiform

or synformal-antiform (Figure 4.1) and plunges shallowly northwest, parallel to this regional F_2 fold axes. (The F_2 fold nomenclature is based on the fact that the axial planes generally dip shallowly towards the southwest and the folds verge towards the southwest, hence the antiforms are 'downward-facing' or synformal-antiforms. However, because of minor post-F_2 reorientation the axial surfaces are locally subhorizontal and the folds appear to be recumbent.)

The orebody has been subdivided into three major sulphide-bearing fault blocks and two phyllite fault blocks (Figure 4.2), each with different structural features but similar structural styles (see section 4.3). These fault blocks are bounded by, and internally

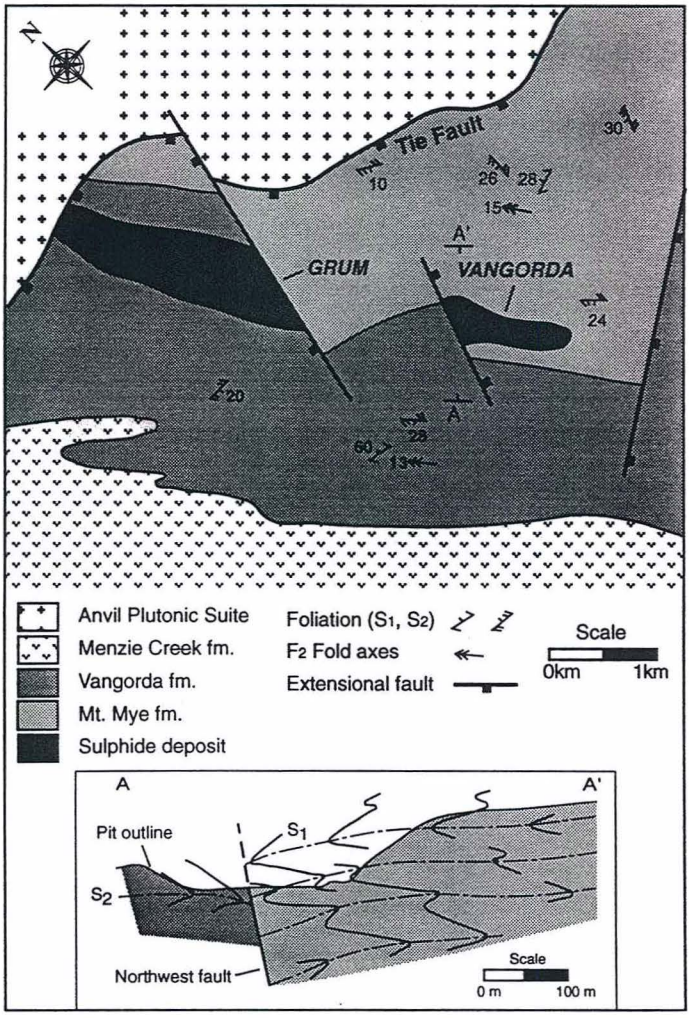

Figure 4.1. *Generalised geological map of the Vangorda area. The cross section in the inset shows the S_1/S_2 relationships and the nature of the F_2 folds that affect the orebody.*

deformed by, predominantly steeply northwest- to southeast-dipping extensional faults with a graben to half-graben style (Figure 4.3) (see also section 4.3.3.3). Minor strike-slip faults cut the extensional faults (Figure 4.2).

The most northwestern sulphide-bearing fault block (fault block 4) contained a thick sulphide package that made up the bulk of the mining reserves (Figure 4.3). This fault block is bound by the Northwest fault and the Cross fault and individual structural features and sulphide lithostratigraphic units cannot be traced into the other fault blocks to the southeast. Southeast of the Cross fault, fault blocks 2 and 3 contain a much thinner sulphide package (Figure 4.3). These are bound by the Sump fault and the Cross fault. The two phyllite fault blocks (fault blocks 5 and 1) are partially exposed in the open pit, in the footwall to the Northwest fault and in the hangingwall of the Sump fault (Figure 4.2).

4.3 Structural element analysis

The rocks of the Vangorda orebody contain structural elements (Table 1) that can be correlated with the regional D_1 and D_2 deformation events identified in the Anvil District

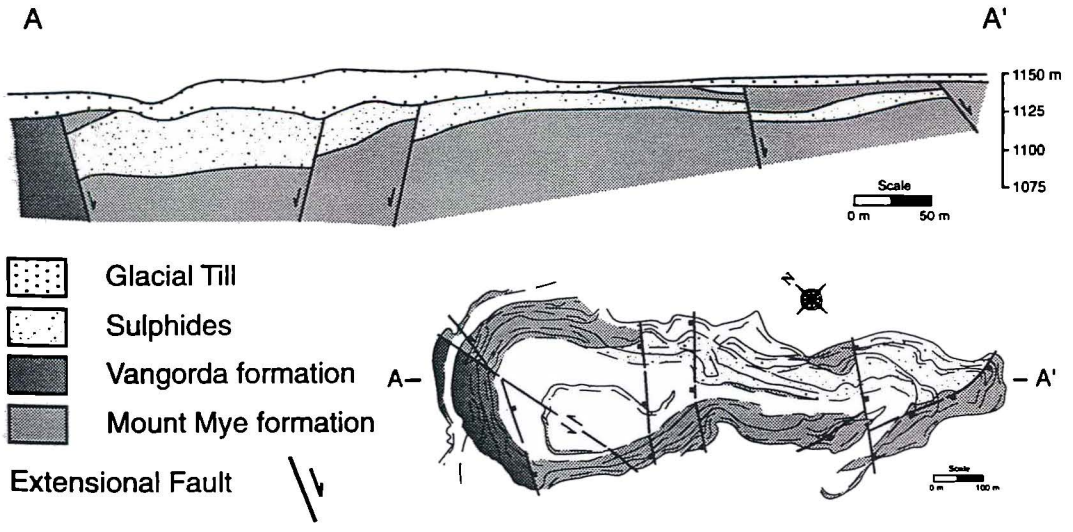

Figure 4.3. *Schematic long section through the Vangorda orebody.*

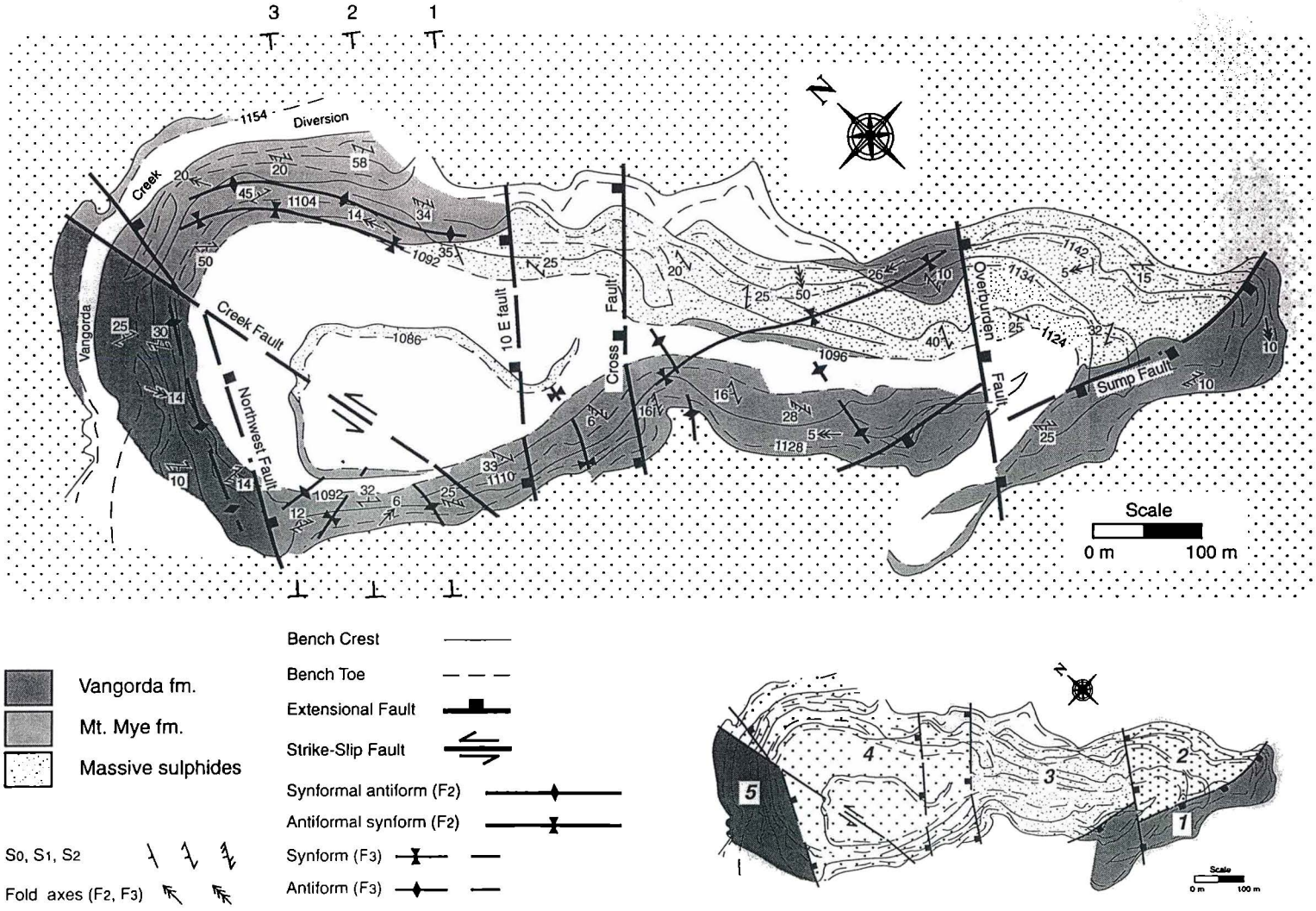

Figure 4.2. *Simplified geological map of the Vangorda open pit based on the 1 : 1000 - scale map (Figure 1.2). The inset shows the location of the various fault blocks discussed in the text.*

(Jennings & Jilson 1986). Structural orientation data are plotted for each fault block in Figure 4.4. S_1 data in Figure 4.4 is plotted only from those areas in which the structural position of the data point (i.e. normal or overturned limb of an F_2 fold) is unambiguously known from either mesoscopic fold asymmetries or from S_1/S_2 relationships. The structural position of all S_1 data points shown on maps such as Figure 1.2 and Figure 4.10 is not so rigorously controlled although the location of the data point is. Figure 4.4 shows that all structural element data within each fault block have an overall similar trend. Each generation of structural element is discussed separately in the following section.

4.3.1 Pre-D_1 features

The unambiguous existence of pre-D_1 features in the orebody have proved difficult to find. However, in two localities within the mine there is a marked angular relationship between banding in the sulphides (S_1) and the cleavage in the phyllites (S_2) (see section 4.3.2 and 4.3.3) and the unfaulted sulphide/phyllite hangingwall lithological contact (Figure 4.5). The unfaulted sulphide/phyllite contact likely represents a primary feature and is here interpreted to be bedding (S_0). The angular relationship between these three planar features (S_0, S_1 and S_2) suggests that all primary features have not been fully transposed into parallelism with subsequent deformation fabrics though it does indicate significant overprinting. However, it is likely that bedding features transposed into parallelism with later deformation fabrics does occur locally.

4.3.2. D_1 structural elements

4.3.2.1 S_1 cleavage

The earliest structural element that can be recognised in the mine is a muscovite-chlorite

Table 4.1. Summary of structural element data for the Vangorda deposit.

Event	Fabric element	Definition	Manifestation	Metamorphism
Pre-D_1	S_0	Bedding.	Possibly reflected in the contact between the phyllites and sulphides.	None
D_1	S_1	Cleavage developed during D_1.	Chlorite + muscovite cleavage within lithons. Differentiated layering in sulphides.	Probably greenschist facies, but lack of indicator mineral assemblages makes it difficult to define.
	F_1	Folds developed during D_1.	Not positively identified in the Vangorda deposit.	
	Faults	Faulting during D_1.	None identified.	
D_2	S_2	Cleavage developed during D_2.	A chlorite + muscovite + graphite crenulation cleavage axial planar to F_2 folds. Locally developed in sulphides.	Greenschist facies. T_{Max} = 363 °C and P_{Max} = 4 - 6 kb.
	F_2	Folds developed during D_2.	Shallowly NW-SE-plunging, SW-verging, tight to isoclinal. Folds S_1 in phyllites and differentiated layering in sulphides.	
	Faults	Faults developed during D_2.	None identified.	
Post-D_2	S_3	Cleavage developed post-D_2	Locally developed extensional cleavage cutting S_2.	Possible retrogression during cooling.
	F_3	Folds developed post-D_2.	Open, generally S-plunging folds in the hangingwalls of extensional faults. Folds the S_2 foliation.	
	Faults	Faults developed post-D_2.	Steeply NW-SE dipping brittle extensional faults that cut D_2 structures. Strike-slip faults that cut extensional faults. NW and SE directed thrusts.	

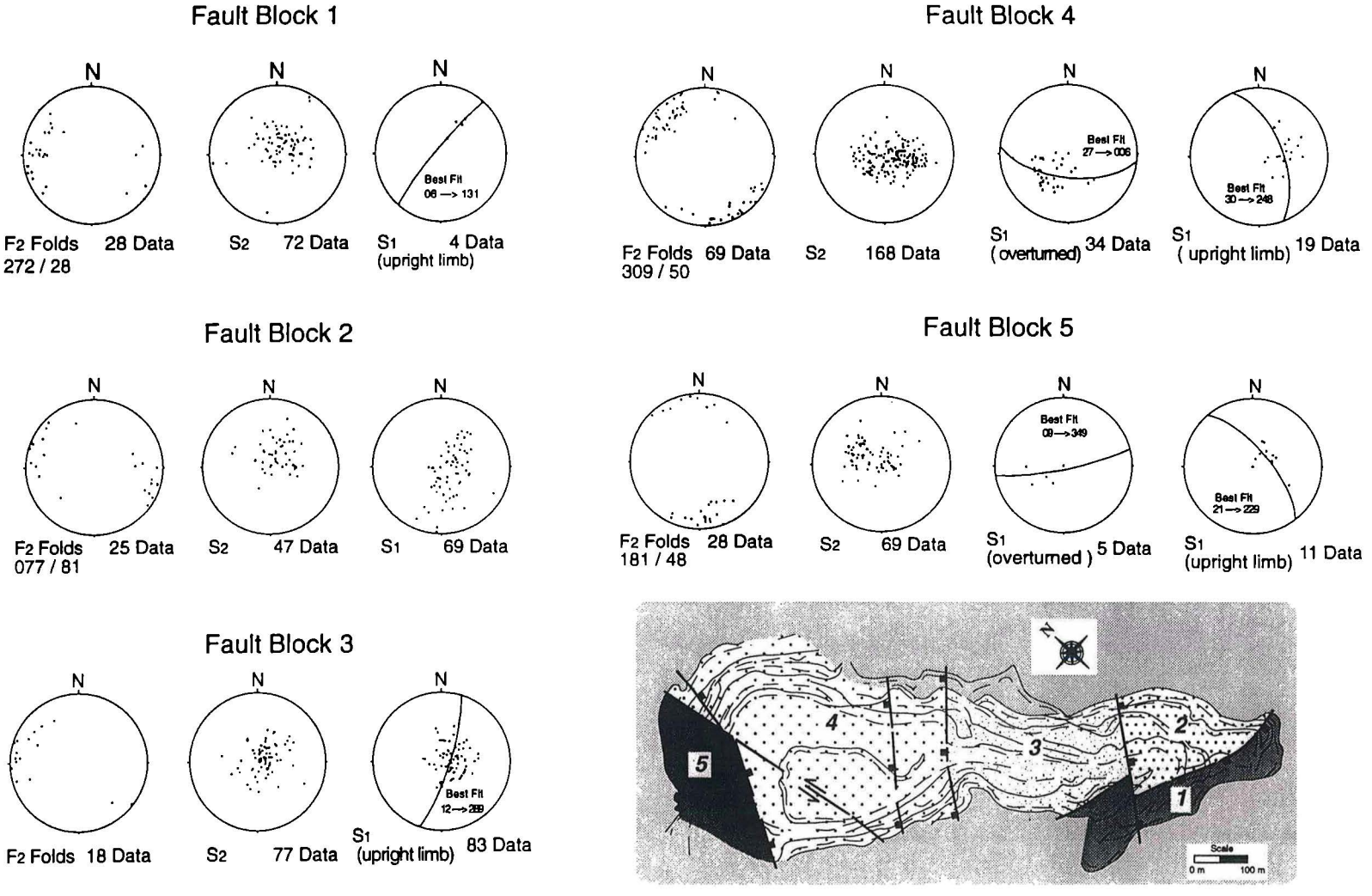

Figure 4.4. *Stereoplots of structural element data for the various fault blocks in the Vangorda orebody. Data from S_1 and S_2 are poles to planes.*

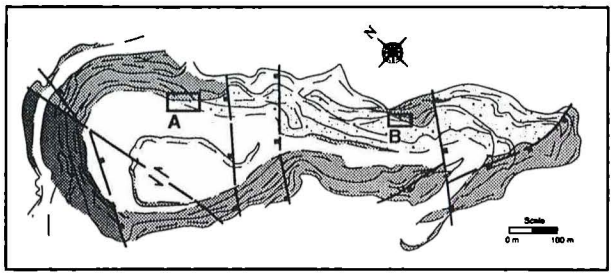

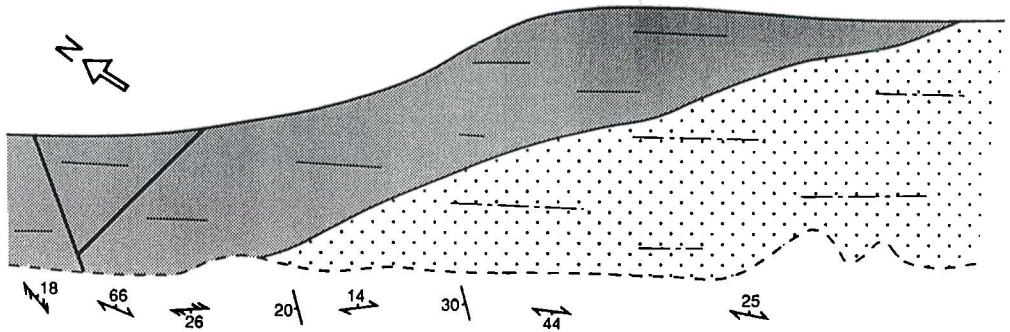

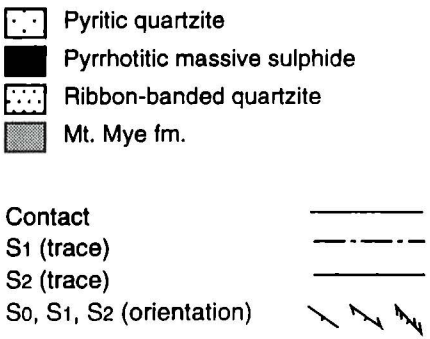

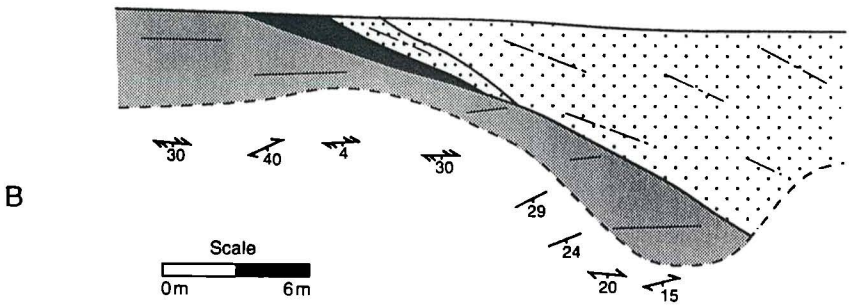

Figure 4.5. *Field sketches showing the relationship between the hangingwall sulphide/phyllite contact, S_1 and S_2. The locations of the sketches are shown in the inset.*

slaty cleavage preserved in D_2 lithons in the phyllites (Figure 4.6a). This cleavage is widespread in the phyllites and is interpreted to be the regional S_1 of Jennings & Jilson (1986). Throughout the orebody the sulphide lithofacies have a moderate to well-developed layering on a scale of millimetres to centimetres (Figure 4.6b). The angular relationships between S_0 and the layering discussed in Section 4.3.1 indicates that it is a differentiated layering related to deformation and metamorphism. The differentiated layering is pervasively folded by the same fold systems that resulted in the development of D_2 lithons and throughout the orebody it is overall parallel to S_1 in the phyllite, suggesting that both it and the within-lithon cleavage are D_1 structural elements (i.e. S_1).

The S_1 cleavage has two dominant trends depending on its position within the macroscopic fold structure (Figure 4.4). S_1 in the normal limbs of the recumbent F_2 folds dips predominantly towards the southwest to west, whereas in the overturned limbs it dips towards the north. Deviations from these trends, such as in fault block two (Figure 4.4), are caused by post-F_2 faulting (section 4.3.3.3).

4.3.2.2 F_1 folds

The widespread presence of S_1 in the ore lithofacies and surrounding phyllites and the evidence for F_1 folding in rocks in close proximity to the orebody (see Figure 2.5) indicate the relative importance of the D_1 deformation in the Anvil District and the possibility of large-scale F_1 folding in the mine area. The local angular relationship mapped between S_0, S_1 and S_2 (Figure 4.5) discussed in Section 4.3.1 indicates that large scale F_1 folds may exist within the orebody. However, any direct evidence that would positively identify the existence of large-scale F_1 folds in the mine has not been found.

Several isolated examples of refolded folds have been found in pit wall exposures and in

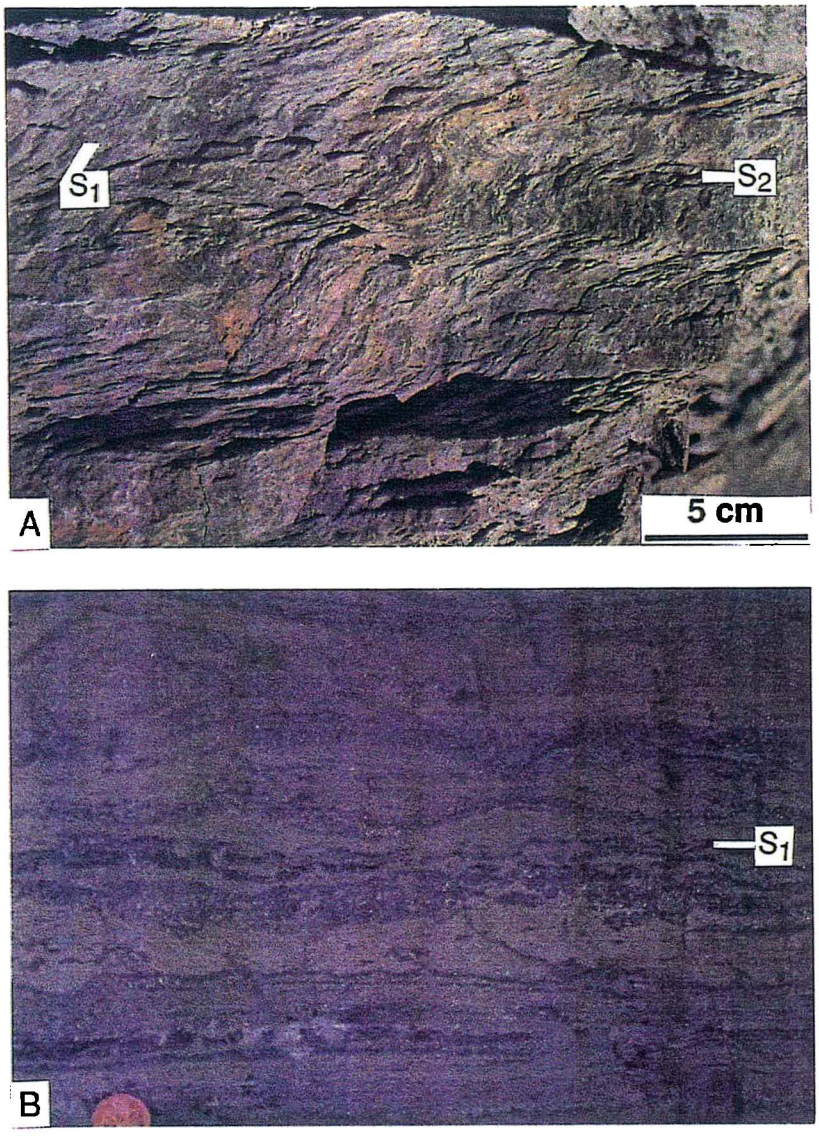

Figure 4.6. *A) S_1 cleavage in lithons between the S_2 crenulation cleavage. B) S_1 differentiated layering in the pyritic massive sulphides. S_1 in these rocks may partially reflect transposed primary layering.*

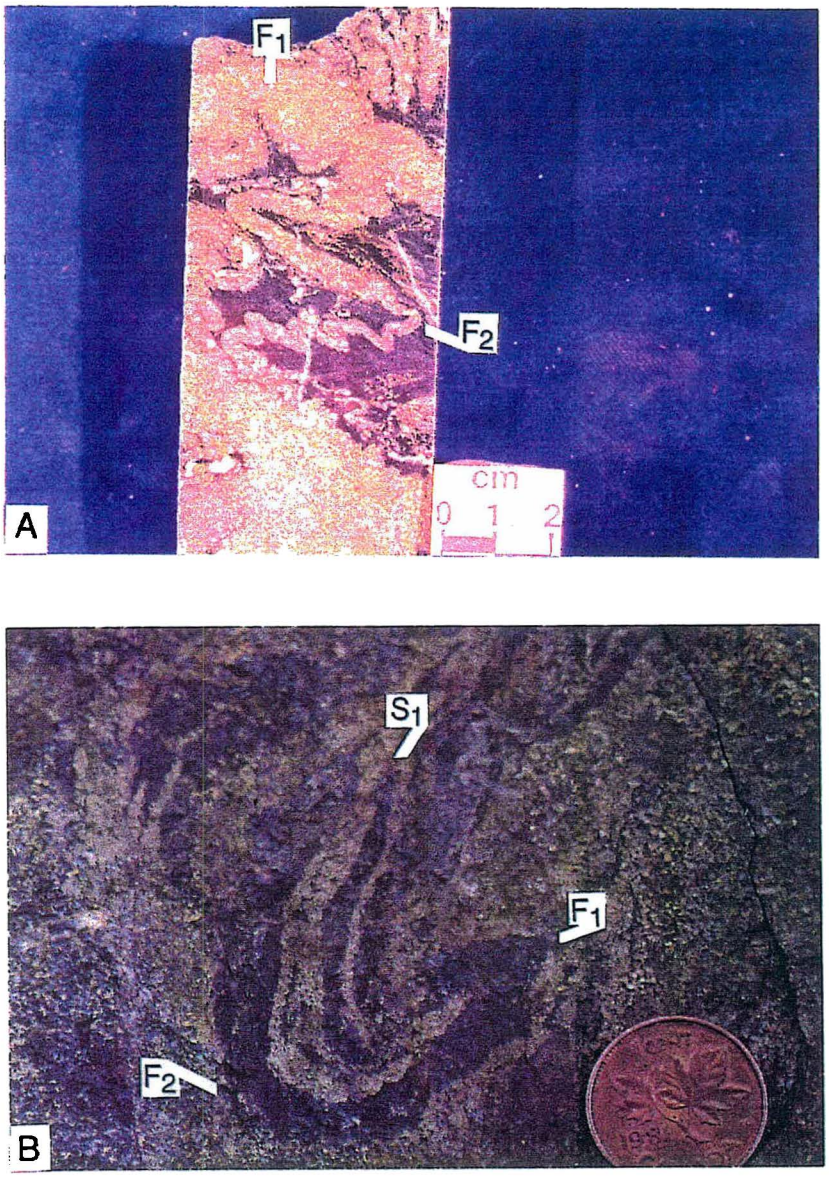

Figure 4.7. *Refolded folds. A) A quartz vein in the ribbon-banded, carbonaceous quartzite that has been folded by both F_1 anf F_2. This may be an example of F_2 overprinting F_1. B) Refolded pyrrhotite- and sphalerite-rich differentiated layering in the massive pyrite lithofacies. This differentiated layering is very similar to S_1 and the fold overprinting may be a result of continued folding during D_2.*

diamond drill core (Figure 4.7) but, because they are isolated, the fold evolution is not clear. The first-formed folds in these areas affect the S_1 cleavage suggesting they are F_2 folds that were subsequently refolded as a result of progressive folding during D_2 and not by F_1/F_2 overprinting.

4.3.3. D_2 structural elements

4.3.3.1 S_2 cleavage

Throughout the orebody, the host phyllites have a penetrative, millimetre- to centimetre-scale carbonaceous, muscovite-chlorite crenulation cleavage (Figure 4.8a) that is correlated with the regional S_2. In the quartz-rich phyllites this is manifested has a pressure solution cleavage. In most sulphide lithofacies S_2 is found only rarely, in high strain zones where shearing and pressure solution have resulted in the formation of a new, inhomogeneous S_2 pressure solution cleavage (e.g. Brown & McClay 1993) and a differentiated foliation. A differentiated foliation is particularly developed in the baritic massive sulphides and the pyrrhotite + sphalerite + galena + magnetite massive sulphides (see section 4.4.2). However, in the ribboned-banded, carbonaceous quartzite, a differentiated axial planar to pressure solution S_2 cleavage is well developed (Figure 4.8b).

The S_2 cleavage is axial planar to the F_2 folds and is shallowly-dipping and wavy, forming a scatter in the centre of the stereoplot in all fault blocks (Figure 4.4). The variations in the S_2 orientation shown in Figure 4.4 are due in part to the fact that it is overall subhorizontal. It has also been affected and reoriented by extensional and strike-slip faulting (see Section 4.3.3.3). Folding an irregularly shaped body such as the sulphide package, together with the marked competency contrasts between the orebody

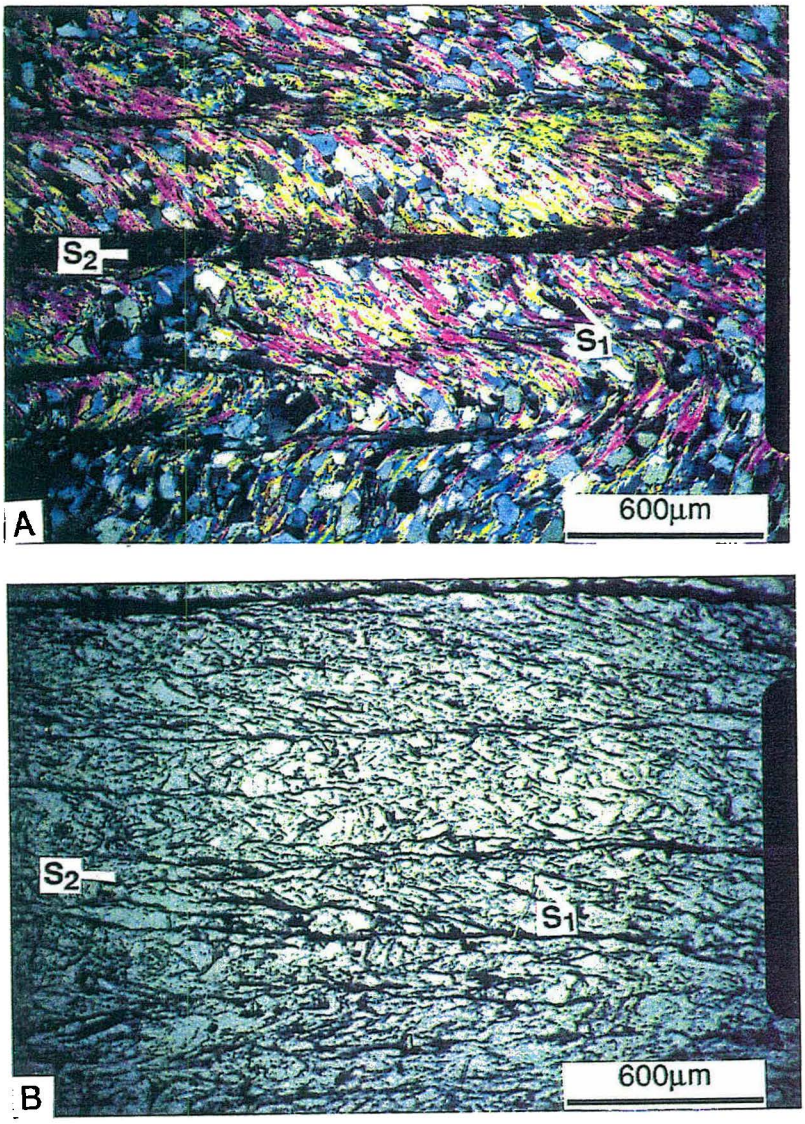

Figure 4.8. *A) S_2 crenulation and pressure solution cleavage in the Mount Mye formation phyllites. The pressure solution cleavage plane is outlined by graphite. The phyllosilicate phase is muscovite. Crossed polars. B) Crenulation cleavage in Mount Mye formation phyllite. The phyllosilicate phase is muscovite. Plane polarised light.*

and the phyllites may also account for some of the variation is the orientation of S_2 within the phyllites.

The previously inferred interpretation of a uniformly SW-dipping orientation for S_2 throughout the orebody assumed by previous workers (e.g. Jennings & Jilson 1986) and used as a reference fabric in diamond drill core section constructions for the orebodies in the Anvil District must clearly be approached with caution.

4.3.3.2 F_2 folds

The dominant fold phase identified in the Vangorda orebody clearly folds the S_1 cleavage and is therefore F_2. F_2 folds are often tight to isoclinal, similar folds (Figure 4. 9a/b). Within the different sulphide lithofacies the F_2 fold style is variable as a result of the different rheological properties but, in general, the similar fold style is maintained. Many mesoscale folds outcropping in the sulphides lithofacies show thickening in the hinge zone (Figure 4.9c) and in some cases there is evidence of material being mobilised into the low stress area at the fold closure (Figure 4.9/d).

The F_2 folds plunge shallowly northwest-southeast to east-west (Figure 4.4) and verge towards the southwest. The F_2 axial surfaces dip shallowly towards the southwest to west, although, as discussed in section 4.3.3.1, the axial surfaces are quite variable. The macroscopic F_2 folds are shallowly downward-facing and upward-facing to recumbent antiforms and synforms (see Figure 4.20).

In fault blocks 1, 2, and 3 the F_2 folds plunge shallowly northwest-southeast to east-west (Figure 4.4), whereas in fault block 4 they have a more north-northwest to south-southeast plunge (Figure 4.4). This more north-northwest to south-southeast orientation of the folds points to the possibility of rotation of fault block 4 during post-F_2 folding

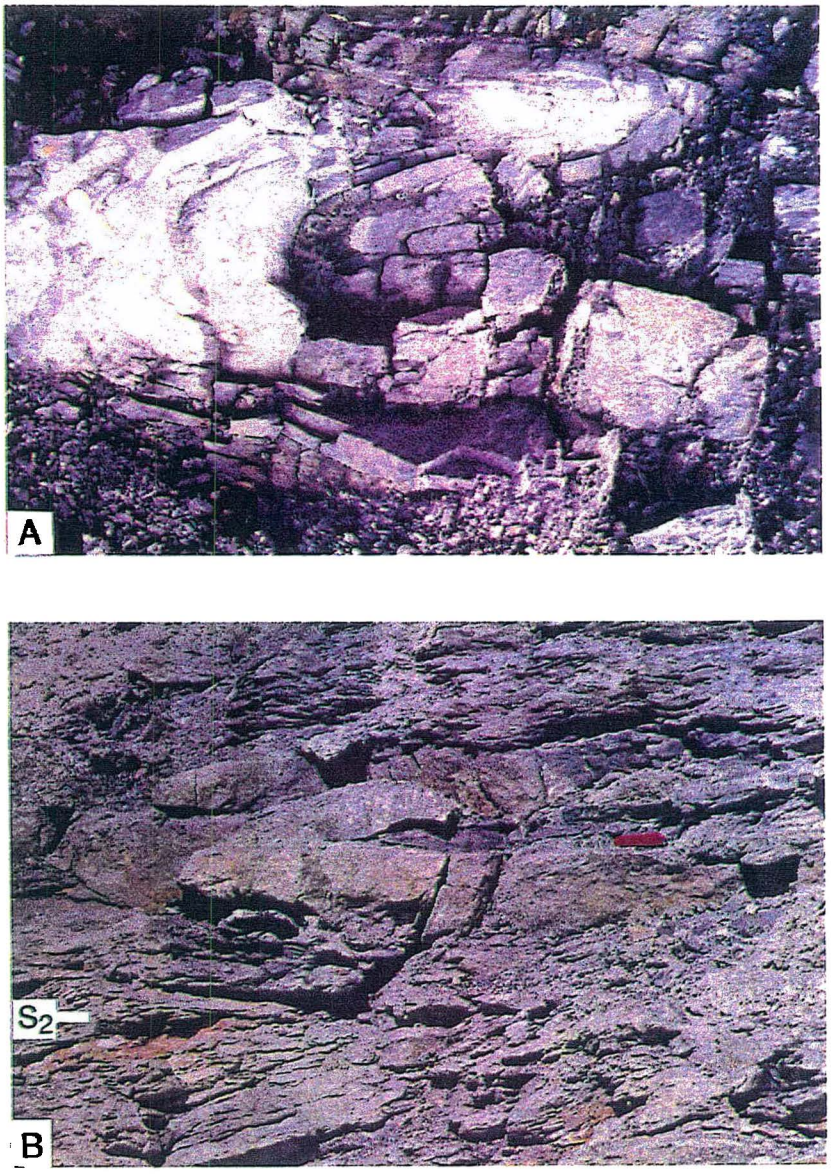

Figure 4.9. *F_2 folds in different lithofacies in the Vangorda orebody. A) Isoclinally folded quartz-rich layering in the Vangorda formation. B) Isoclinally folded massive pyrite band in the Mount Mye formation. Note the well-developed axial planar S_2 cleavage.*

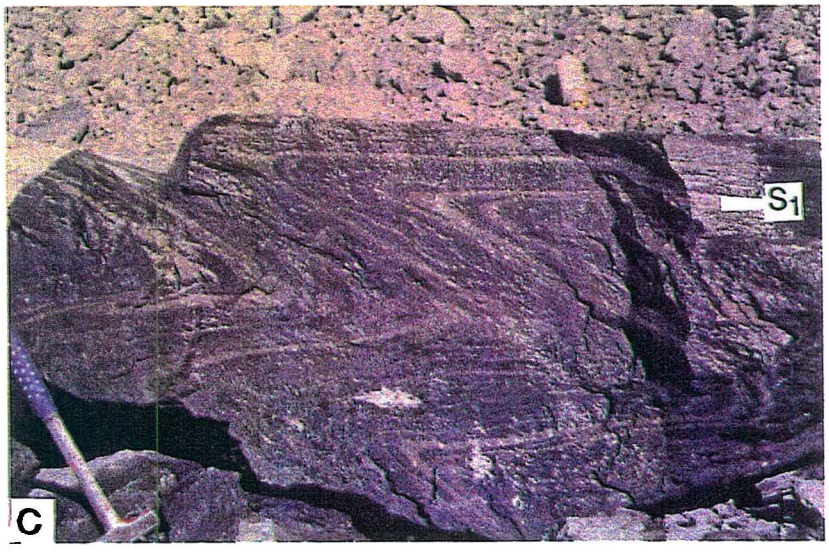

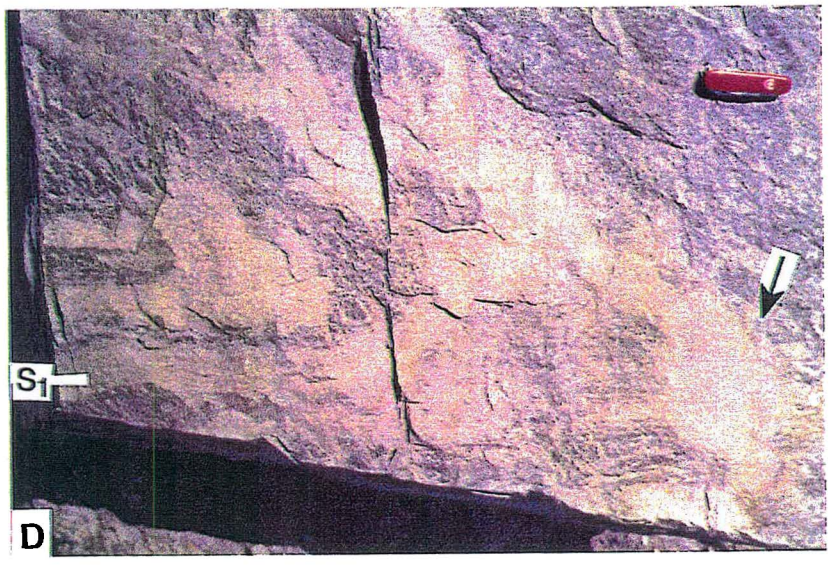

Figure 4.9. *(continued) C) Tightly folded ribbon-banded, carbonaceous quartzite. Note that the hinges of the folded pyritic layering have thickened slightly. D) Folded pyrite-rich layer in pyritic quartzite. Note that pyrite has been remobilised into an irregularly shaped patch in the hinge zone of the fold (arrow).*

extensional faulting. The north-northwest to south-southeast plunge of F_2 folds in fault block 5 (Figure 4.4) is more difficult to assess since this fault block is only exposed in the immediate footwall of the Northwest fault. All D_2 structural elements exposed in the footwall to the Northwest fault have been reoriented by deformation related to that fault (Figure 4.10), hence fault block rotation cannot be said, with certainty, to have occurred.

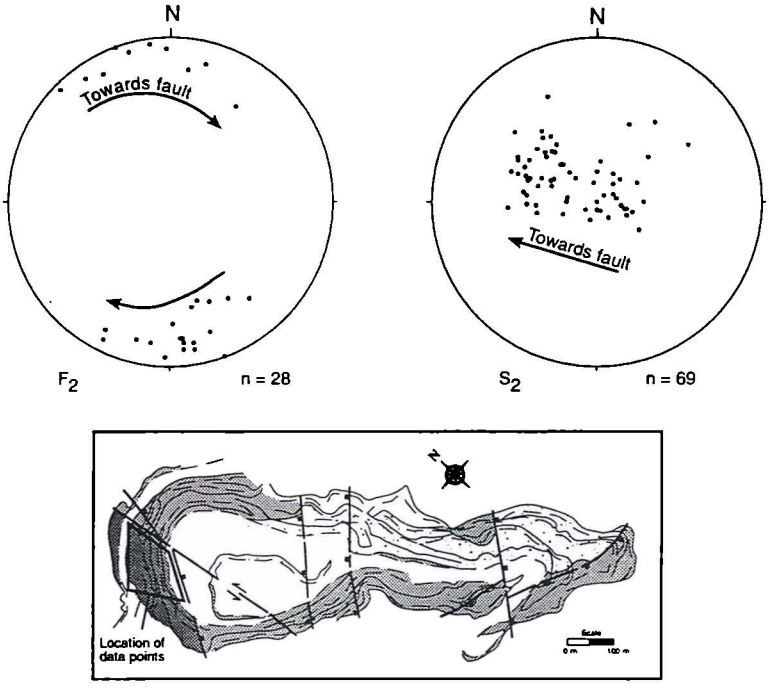

Figure 4.10. *Stereoplot data for F_2 fold axes and poles to S_2 in the footwall of the Northwest fault showing how they rotate as the fault is approached.*

4.3.3.3 Post-F_2 faulting

All faults examined in open pit exposures truncate the S_2 cleavage and F_2 folds and therefore clearly post-date or are late D_2. Faults generally dip towards the northwest to north or southeast (Figure 4.11) and form graben and half-graben systems (Figure 4.12). πThe orebody is cut by several major extensional faults which are shown on Figure 4.2 and by numerous minor ones which are shown on the 1:1000 scale map in the back pocket (Figure 1.2). The steeply southeast-dipping Northwest fault truncates the orebody in the northwest (Figure 4.2) putting older sulphide-bearing Mt. Mye formation

rocks in its hangingwall against younger Vangorda formation rocks in its footwall (Figure 4.13).

The thinning orebody is truncated in the southeast by the moderately to steeply south-dipping Sump fault (Figure 4.2). The Sump fault is cut by the southeast-dipping Overburden fault which juxtaposes two limbs of a F_2 fold (see section 4.3.3.6). The orebody is cut approximately in half by the steeply to moderately northwest-dipping Cross fault (Figure 4.2 and 4.3) which juxtaposes the northwest part of the orebody against the southeast part, dividing the orebody into two distinct structural units and bounding fault block 4. Fault block 4 is cut by the northwest-dipping 10E fault. A late strike-slip fault, the Creek fault, displaces the Northwest fault sinistrally approximately 30 to 40 metres (Figure 4.2). Other strike-slip faults are minor, with displacements of centimetres to a metre.

Displacement along most faults are difficult to determine because of the lack of marker horizons. However, dip-slip displacements of the phyllite sulphide contact, which is

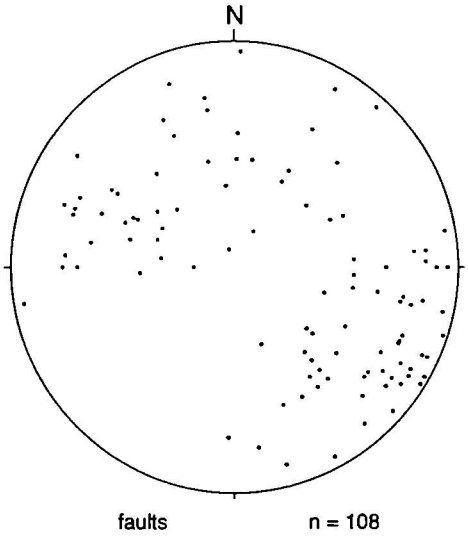

Figure 4.11. *Stereoplot of poles to extensional faults.*

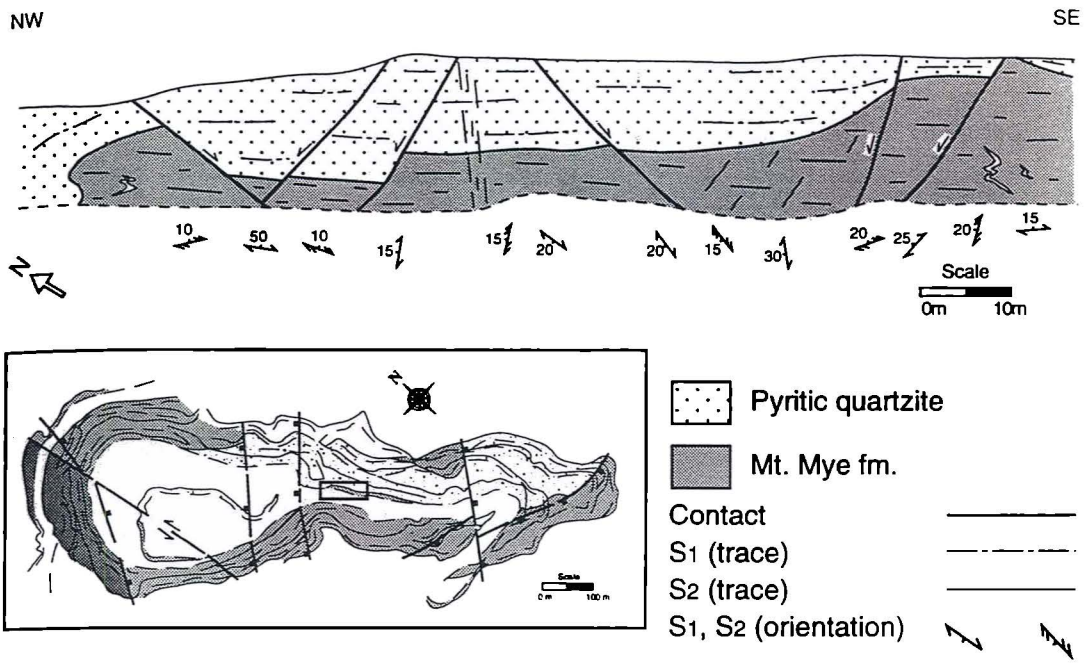

Figure 4.12. *Field sketch of a section of the open pit wall (the location is given in the inset) showing the graben style of the post-F_2 faulting.*

affected by many small-scale faults, are commonly on the order of centimetres to several metres (e.g. Figure 4.14a). The amount of dip-slip displacement on the major faults, such as the Northwest fault and Cross fault, are impossible to accurately determine. Based on the juxtaposition of Mount Mye formation and Vangorda formation the Northwest fault is thought to have a minimum dip-slip displacement of several hundred metres. Displacement across the Cross fault is difficult to estimate. However, since it juxtaposes to sulphide fault blocks, and if the sulphides are from the same lithostratigraphic package (i.e. 'Anvil Cycle') with a maximum of 60 metres thickness, then the dip-slip displacement is likely less than 60 metres. The amount of displacement across the Overburden fault is discussed in section 4.3.4. The amount of displacement across the Sump fault is impossible to determine.

Faults are commonly segmented and overlapping, forming fault zones rather than discrete fault surfaces (see Figure 1.2). Within the sulphide lithofacies rocks, faults form wide, steeply dipping zones of intense fracturing and cataclasis (Figure 4.14b). In phyllites

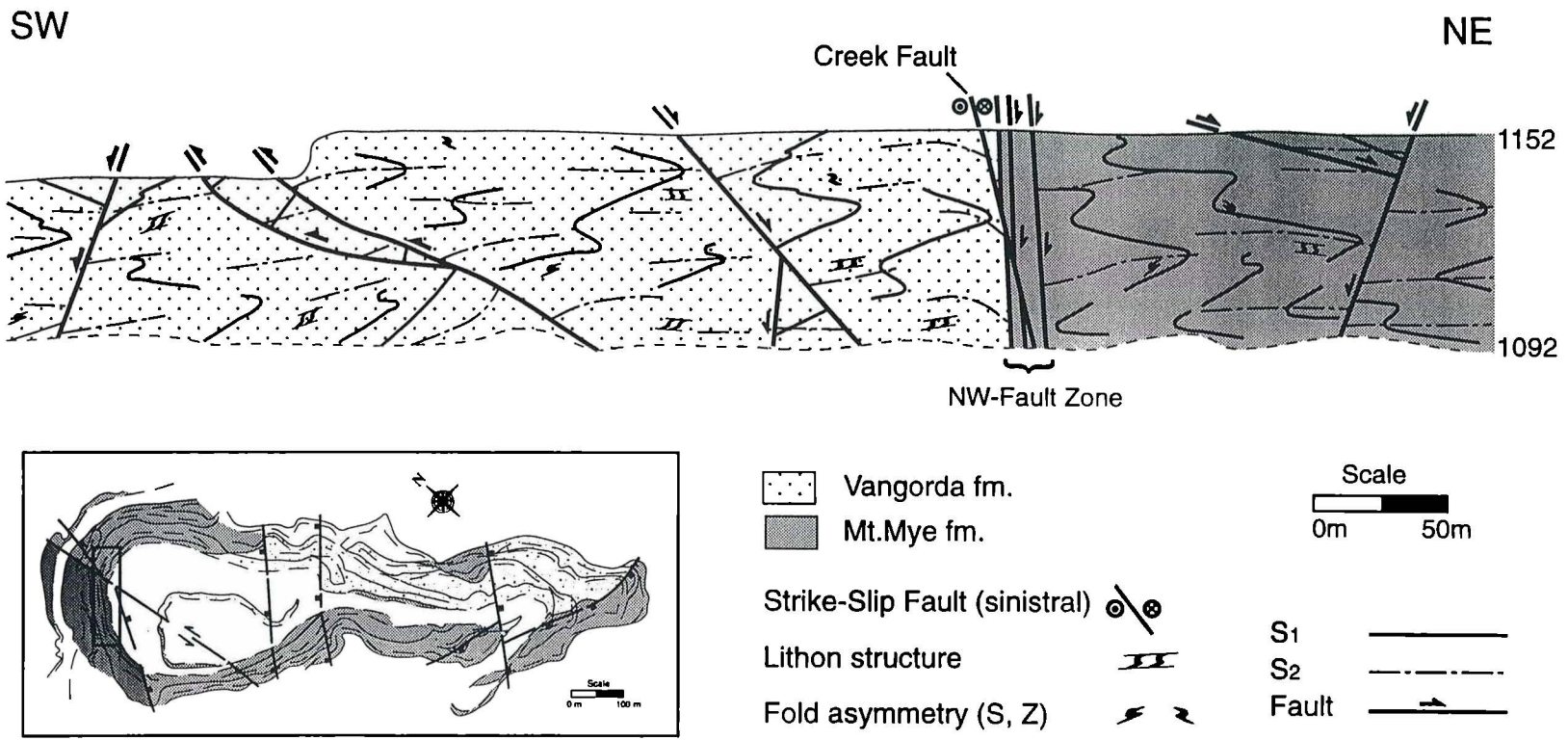

Figure 4.13. *Field sketch of the pit wall showing the Northwest fault with Mount Mye formation in its hangingwall and Vangorda formation in its footwall. The Creek fault cuts the Northwest fault, displacing it dextrally.*

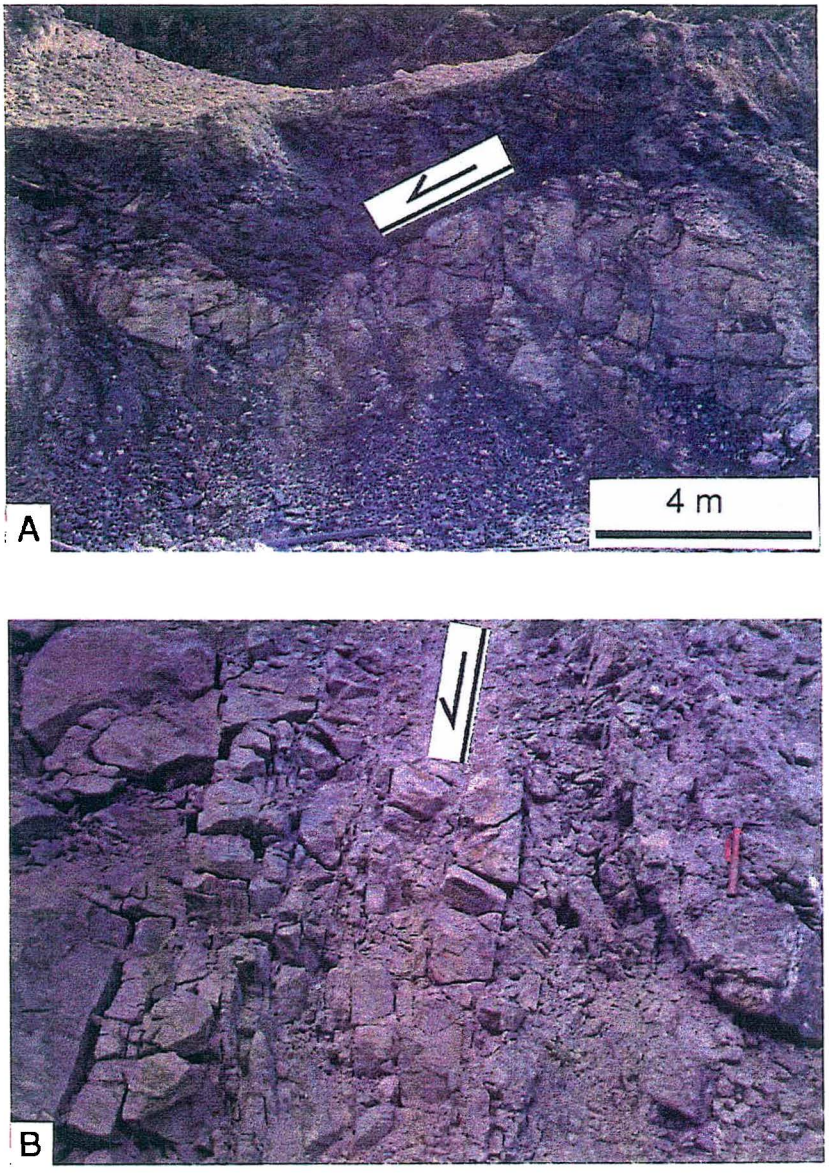

Figure 4.14. *Faults in the Vangorda orebody. A) Small extensional fault displacing the hangingwall sulphide-phyllite contact. B) A wide zone of intense, near vertical fracturing in massive sulphides marking the Cross Fault. Compare this the same fault in Figure 4.14c.*

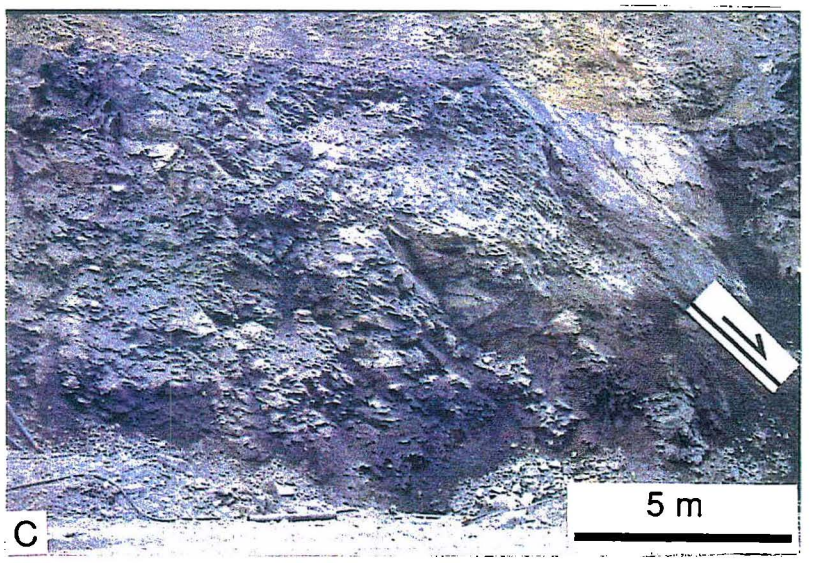

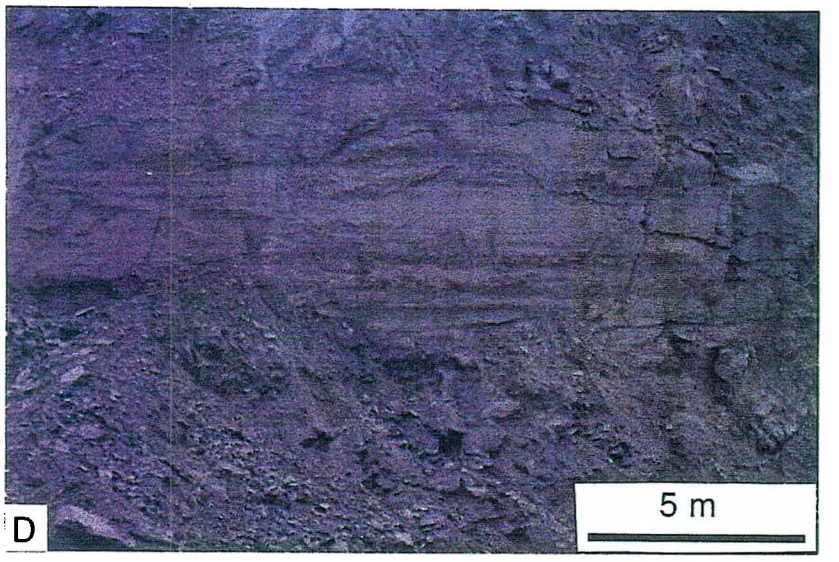

Figure 4.14. *(continued) C) A narrow, shallowly-dipping gouge zone in Mount Mye phyllite marking the Cross Fault. Unlike in the massive sulphides, the fault in the phyllites is large confined to the narrow gouge zone. Note, however, the development of small-scale faulting in the footwall of the gouge zone indicating footwall collapse. D) Sub-horizontal ridging along a fault plane denoting strike-slip displacement.*

they are shallower dipping and form discrete gouge zones (Figure 4.14c). Locally, faults are sealed by a matrix of phyllosilicates, quartz, and calcite and, in some instances, by pyrite.

Paucity of marker horizons also make it difficult to accurately determine the kinematics of most faults in the orebody. This is further complicated by poorly developed kinematic indicators. However, faults are generally accompanied by bending of the F_2 axes and S_2 cleavages in close proximity to faults (e.g. Figure 4.10) and, locally, an extensional cleavage is developed adjacent to fault surfaces. These can be used to indicate at least a final phase of relative extensional fault movement in most cases. Also, many fault surfaces have well-developed slickensides (Figure 4.14d) but these have a varying array of orientations, ranging from downdip to a high pitch angle in the fault plane, as in the case of the Northwest, Sump, and Cross faults, to subhorizontal, as in the case of the Creek fault. Individual faults also display sets of variably oriented slickensides ranging from down-dip to subhorizontal. The complete spectrum of slickenside orientations attest to a complicated fault kinematic history. Strike-slip reactivation of extensional faults, or vice versa, is possible.

4.3.3.4 Jointing

A conjugate set of joints is developed in all rock types in the orebody (Figure 4.15). These joints are steeply northwest-southeast dipping (Figure 4.16) {0kl} joints (c.f. Hobbs *et al.* 1976) related to the F_2 folding. These joints are distinctive in that they occur as a set with an acute angle of approximately 30° to 40°. In the pyritic quartzite lithofacies and to a lesser degree in other sulphide lithofacies, joints are accompanied by a set of centimetre-scale fractures that are infilled by chalcopyrite and pyrrhotite (see section 4.4.4).

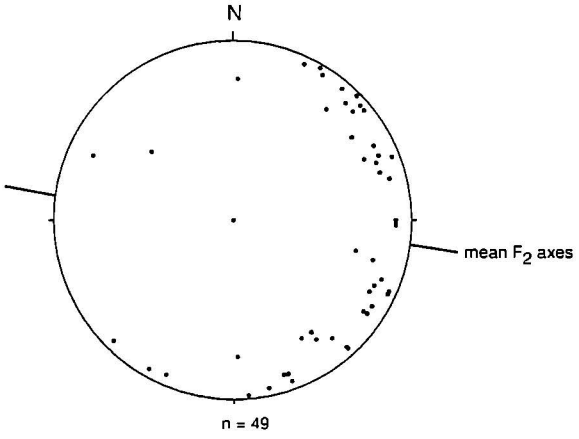

Figure 4.16. *Stereoplot of poles to joint surfaces.*

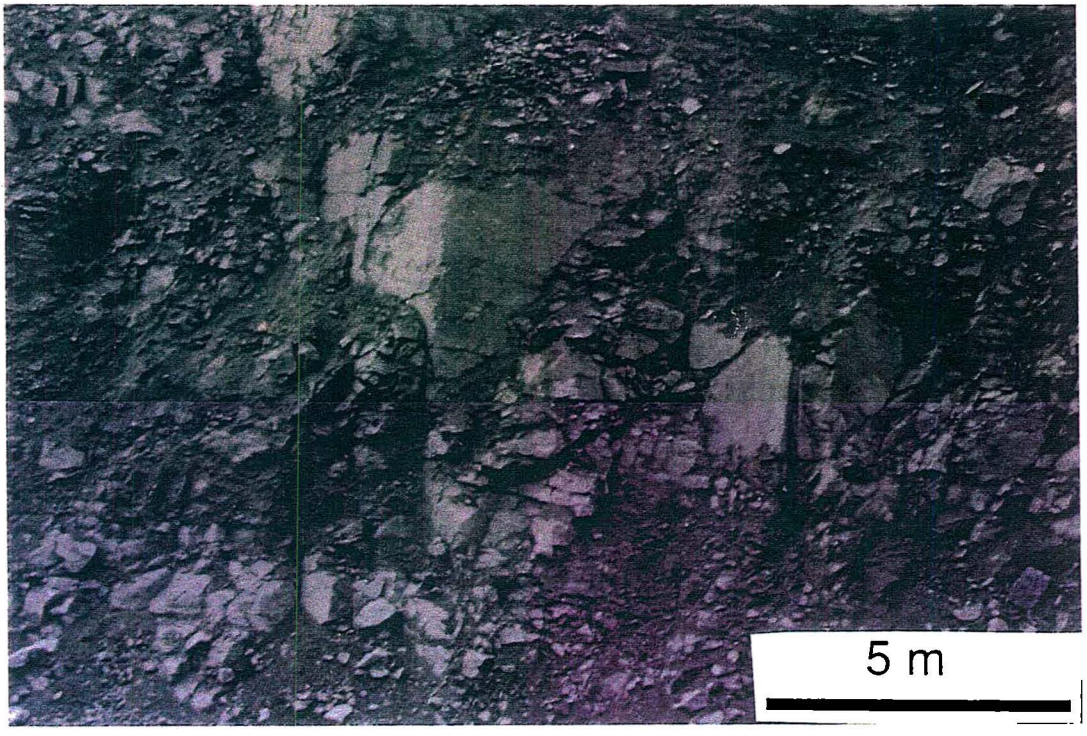

Figure 4.15. *Field photograph of joints sets in the sulphide lithofacies.*

4.3.3.5 Post-F_2 thrusting

Minor brittle thrusting occurs in fault blocks 1 and 5 (see Figure 1.2). In fault block 1

these dip 20° to 30° southwest and cut the S_2 cleavage (see Figure 4.19). Thrusting in fault block 1 has resulted in the development of a hangingwall antiform (Figure 4.17). Restoration of the S_2 in the antiform suggests a minimum displacement of 10 metres. Minor thrusts also occur in fault block 5 which dip 15° to 25° towards the north to northeast, cutting the S_2 cleavage (see Figure 4.13), but with only one to two metres of displacement.

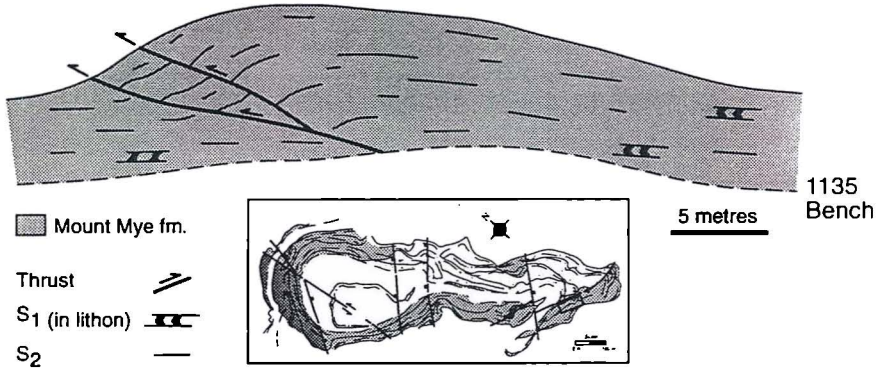

Figure 4.17. *Field sketch of thrust cutting the S_2 cleavage.*

4.3.4 Synthesis of structural element analysis

From the D_1 and D_2 structural elements and structural element orientations discussed above a S_1 and S_2 form surface map has been constructed (Figure 4.18a) from which the large scale fold structure affecting the orebody has been determined. Schematic cross sections have been constructed through each of the sulphide fault blocks (Figure 4.19) by projecting the fabric element along the plunge of the mean fold axis for that fault block (i.e. Figure 4.4) unto the plane of the section. The geometry of the S_2 cleavage was determined by constructing long section parallel to the fold axes (Figure 4.20). The structures elucidated by this method are shallowly southwest-dipping to recumbent F_2 folds with a wavelength of approximately 75 metres.

Warping of the S_2 form surface traces is prominently displayed on map scale (Figure

4.18b). In pit wall exposures, this is manifested as local broad warping of S_2 and is interpreted to be the result of south- to southwest-plunging, open F_3 folds. The proximity of the folded S_2 form surface traces, and the orientation of F_3 axes (Figure 4.4), with faults (Figure 4.20) in the orebody suggests F_3 may be related to post-S_2 faulting.

Fault blocks two and three contain a southwest-verging, shallowly downward-facing to recumbent antiformal F_2 fold and a northeast-verging, shallowly upward-facing to recumbent synformal F_2 fold, respectively (Figure 4.19; sections A-A' and B-B'). This antiform-synform pair are part of the same macroscopic fold that has been cut by the Overburden fault. Fault block two (Section A-A') contains the shallowly west- to northwest-dipping (Figure 4.4) overturned limb and part of the antiformal hinge. The hinge and part of the overturned limb have been openly warped by movement along the Sump fault. This warping accounts for the anomalous overturned limb orientation of S_1 shown in Figure 4.4. Fault block three (Section B-B') contains the synformal hinge and west-dipping upper limb of the fold pair. It is openly warped by movement along the Overburden fault and the Cross fault (Figure 4.18c).

The exact amount of displacement along the Overburden fault is difficult to calculate. However, based on a half wavelength of the fold cut by the fault being approximately 35 metres then the juxtaposition of the antiformal and synformal closures at the same elevation, taking into account a fold plunge of about 15° towards the northwest, indicates a of displacement approximately 20 - 30 metres.

The S_1/S_2 relationships in fault block four (Section C-C') defines a southwest-verging, shallowly downward-facing to recumbent antiform and northeast-verging, shallowly upward-facing to recumbent synform (Figure 4.19). The overturned limbs of these folds dip predominantly towards the north to northeast and the upper limbs dip southwest to

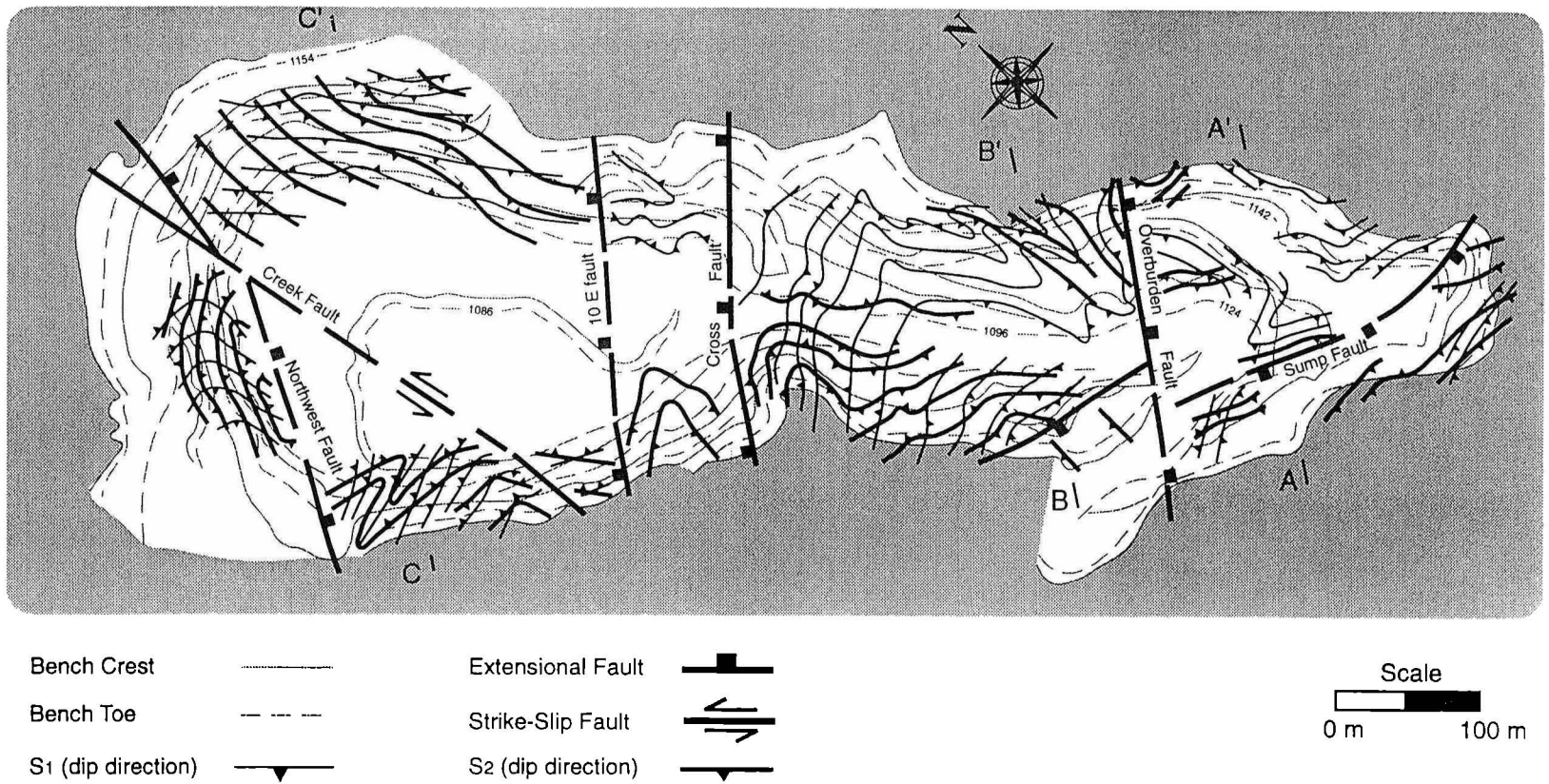

Figure 4.18. *S_1/S_2 form-surface traces in the Vangorda open pit. A) Combined S_1 and S_2 form-surface traces. The locations of cross sections A - A', B - B' and C - C' shown in Figure 4.19 are given.*

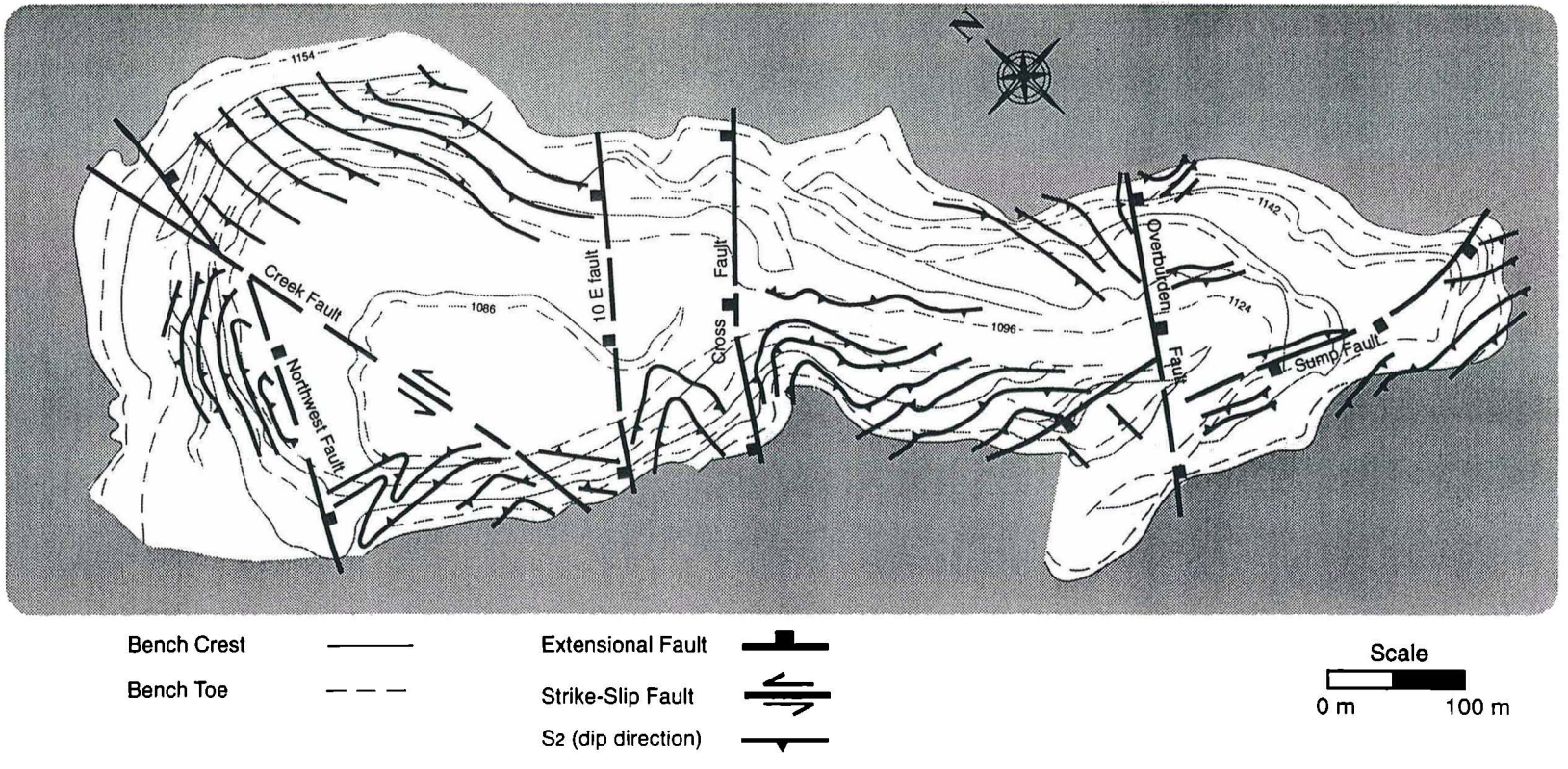

Figure 4.18. *(continued). B) S_2 form surface traces in the Vangorda open pit.*

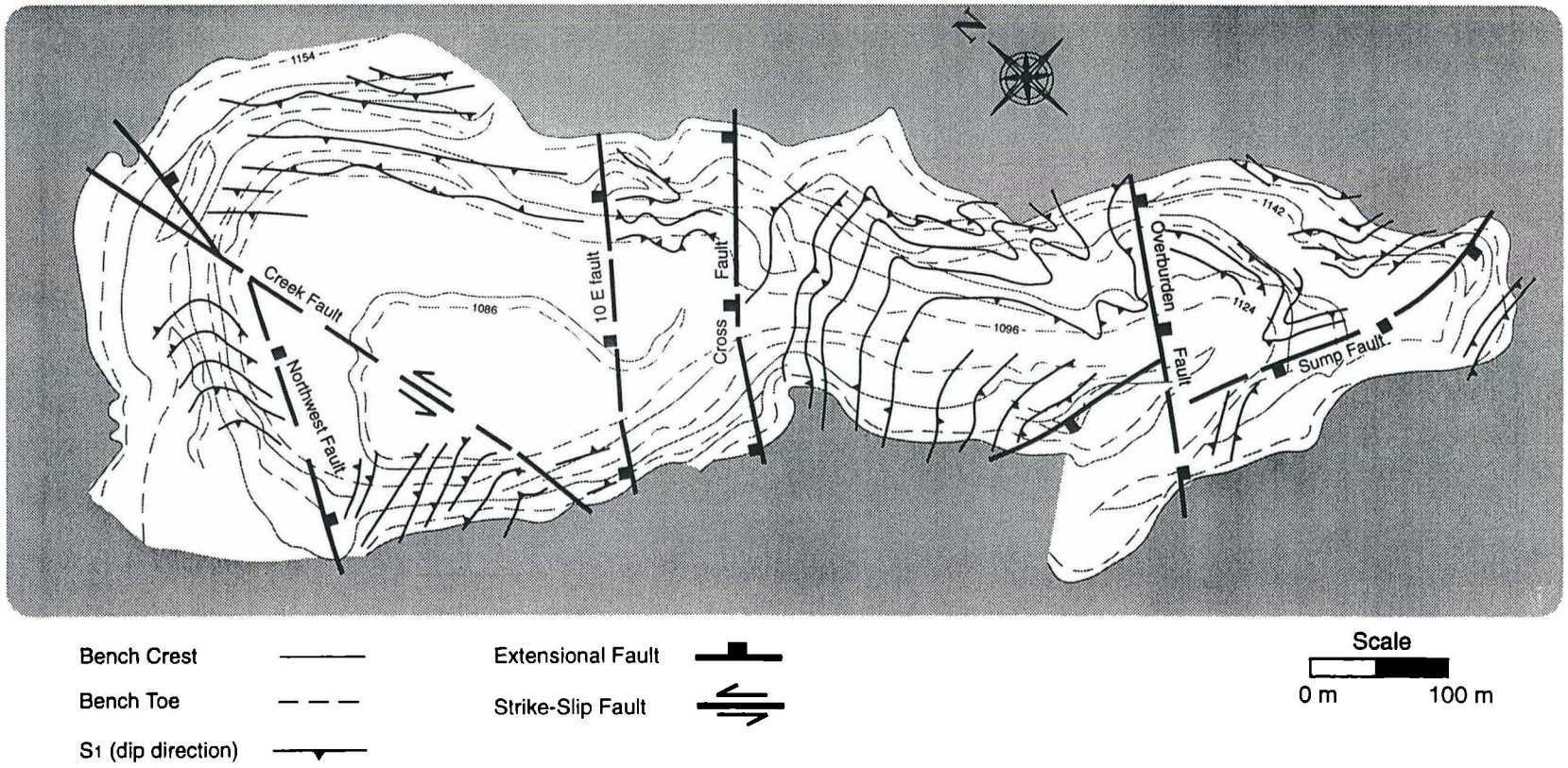

Figure 4.18. *(continued). C) S_1 form-surface traces in the Vangorda open pit.*

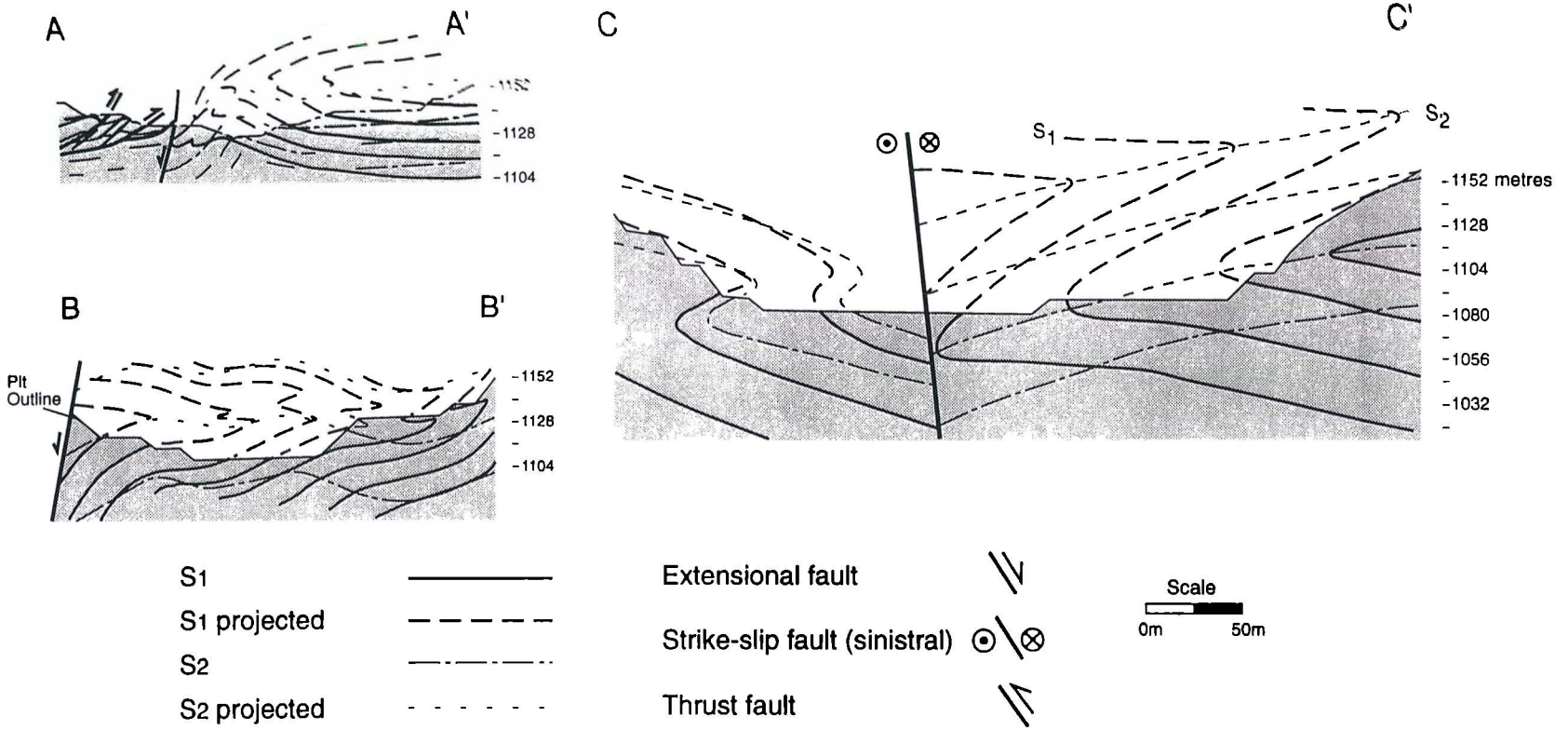

Figure 4.19. *S_1/S_2 cross section through the Vangorda open pit using the relationships shown in Figure 4.18. The location of the sections are shown in Figure 4.18a. See text for discussion.*

west. This fold pair is cut by the Northwest fault which juxtaposes it against a shallowly upward-facing synform in its footwall (Figure 4.13) and by the Creek fault. The S_1/S_2 relationship between the hangingwall of the Northwest fault and the Creek fault along the southwestern side of the mine is complicated by tight F_3 folding related to movement along these faults (Figure 4.18). However, the geometry is that of an overturned F_2 limb.

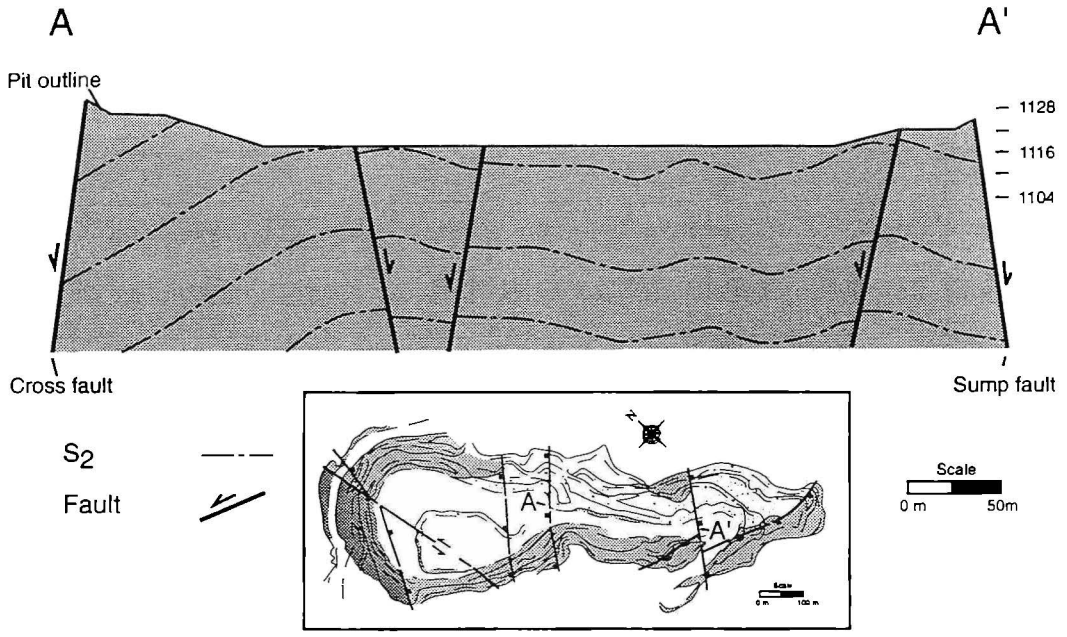

Figure 4.20. *Schematic long section showing folding of S_2. Location of the section is given in the inset.*

4.4 D_2 deformation textures

4.4.1 'Durchbewegung' textures

All sulphide lithofacies in the orebody have undergone varying degrees of 'durcbewegung-type' deformation (see Marshall & Gilligan 1989 for a definition of durchbewegung). Durchbewegung occurs in centimetre- to metre-thick zones,

generally along lithofacies contacts and in the overturned limbs of the macroscopic F_2 folds (see Figure 4.27). A common manifestation of durchbewegung in the sulphide rocks of the Vangorda orebody is the disruption of the S_1 differentiated layering and development of flaser-like structures (Figure 4.21a) accompanied by isoclinal, intrafolial and rootless folds of the differentiated layering. Evidence of extensional shearing (Figure 4.21a) of the layering is widespread. At very high strains, equant clasts of quartz, massive pyrite and siliceous phyllite occur in a matrix of pyrrhotite and sphalerite surrounded by strongly deformed massive pyrite (Figure 4.21b). Less common is the occurrence of similar clasts in a matrix of strongly deformed and foliated massive galena (Figure 4.21c).

Incipient durchbewegung is manifested as complexly folded, fractured and boudinaged differentiated layering (Figure 4.21d) in which the fold hinges and the fold limbs have undergone boudinage and fragments of massive pyrite have become detached and undergone shearing, forming asymmetric or symmetric, winged and naked inclusions (Figure 4.21d). The boundary of the pyrite-rich differentiated layering and the sheared clasts are extensively altered to pyrrhotite (Figure 4.21d) suggesting the breakdown of pyrite. Fractures within the differentiated layering and foliated inclusions form high angles to the flow plane and only rarely do fractures extent into the pyrrhotite-rich zone. Pyrrhotite and sphalerite piercement veins penetrate the differentiated layering in the hinges of the folds.

4.4.2 Shear textures

It must be noted that all samples discussed for shear textures were taken from unoriented diamond drill core or from material disaggregated by mining and therefore cannot be used to infer a shear sense *sensu strictu*. Furthermore, sulphides in the Vangorda orebody do not contain a tectonic lineation on a mesoscopic scale that can be

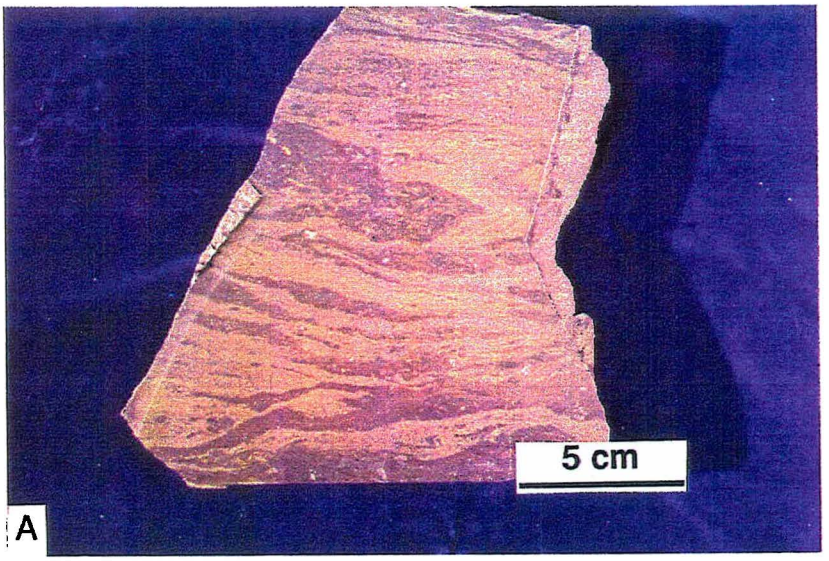

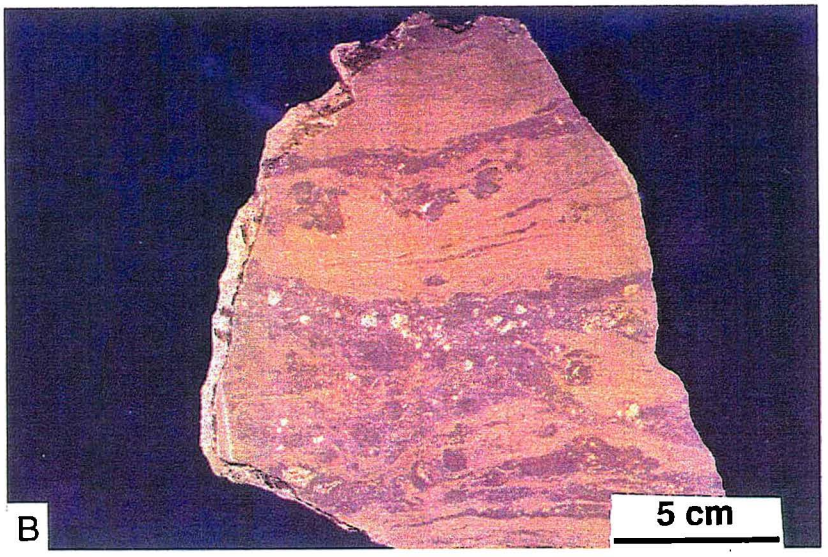

Figure 4.21. *A) Highly sheared massive sulphide with intrafolial folds and a well developed shear foliation. Note extension of the foliation in the bottom left corner. B) Durchbewegung textured massive massive pyritic sulphide. The central, dark area consists of pyrrhotite, sphalerite and galena with rounded inclusions quartz and magnetite-rich clasts.*

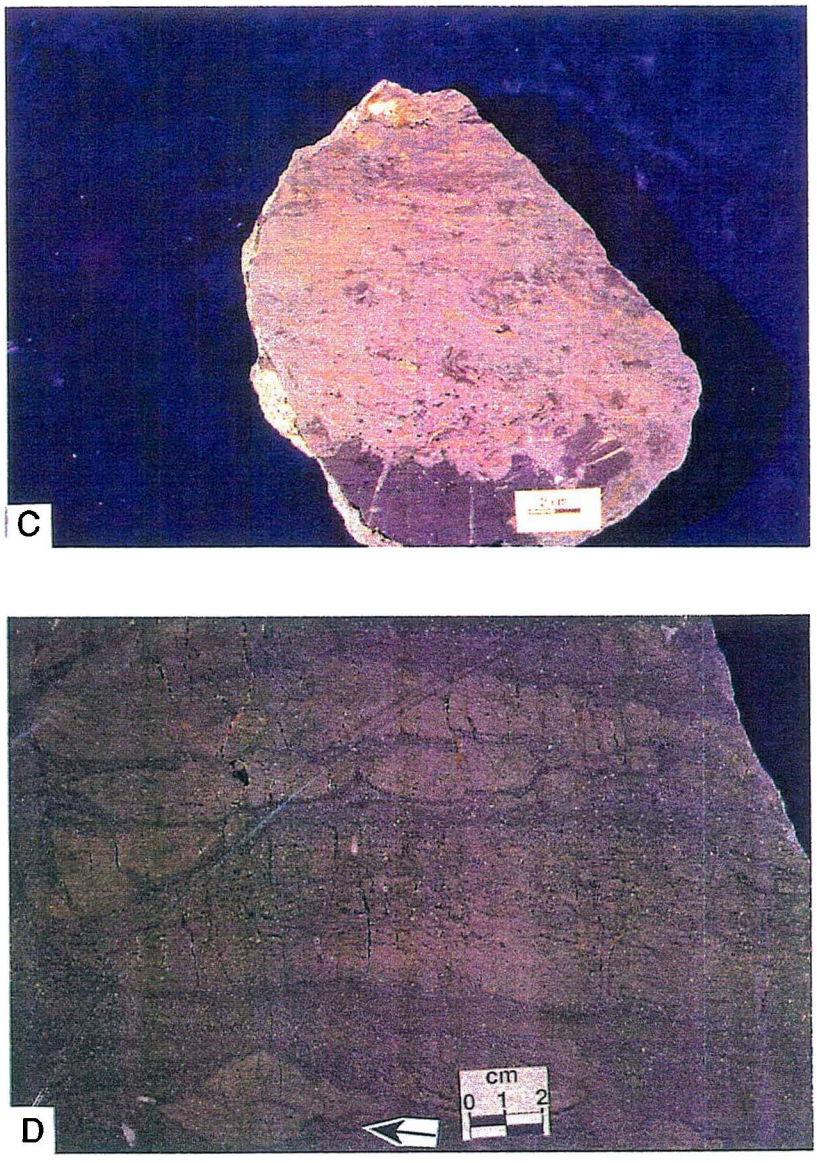

Figure 4.21. *(continued) C) Durchbewegung - textured massive galena with inclusions of quartz and phyllite. D) Incipent durchbewegung in which the massive pyrite is strongly sheared (note asymmetric clasts) and pyrite is altering to pyrrhotite. The massive pyrite is undergoing boudinage. Pyrrhotite defines the flow plane .*

used to estimate the position of the X-axis of the finite strain ellipsoid. For the discussion that follows samples were cut (or recorded in the field) perpendicular to the mylonitic foliation, which is taken to closely approximate the flow plane, and parallel to the X-Z plane of the finite strain ellipsoid (Figure 4.22).

Despite the intense deformation indicated by the widespread occurrence of durchbewegung there is also widespread deformation that can be directly attributed to shearing and shear-related processes. Shearing is accompanied by an increase in the modal abundance of pyrrhotite sphalerite. There is a lesser apparent relationship between shearing and modal abundance of sphalerite and galena, although both increase in areas of high shear strain. Magnetite content also increases slightly but grains are generally highly corroded and locally replaced by pyrrhotite or quartz. The increase in the modal abundance of pyrrhotite, sphalerite and galena generally occurs as discrete folia parallel to the shear plane (see below) and culminates in the pyrrhotite + sphalerite + galena lithofacies which is intensely sheared and often forms durchbewegung.

Zones of very intense shearing consisting predominantly of pyrrhotite, sphalerite and galena are generally fine-grained and brownish purple with numerous inclusions of quartz, carbonate, massive pyrite and phyllite and have a poor to, locally, well-developed mesoscopic pyrite porphyroblastic and phyllosilicate internal foliation that wraps the

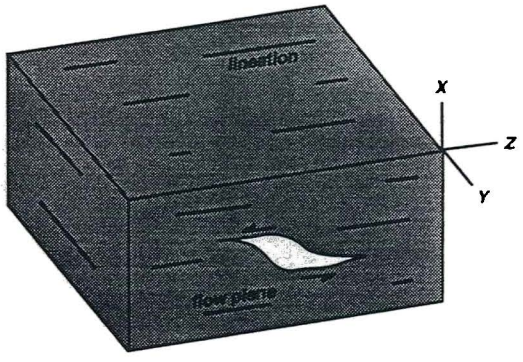

Figure 4.22. *Kinematic reference and orientation of samples discussed in text.*

inclusions (Figure 4.23). These zones range in thickness from a centimetre up to 2 metres. The internal foliation is weakly to strongly discordant to the external differentiated layering (S_1). In several examples S_1 curves sigmoidally into the shear zone.

Contacts between the shear zones and the host rocks range from sharp to gradational. Gradational contacts are developed over a distance of centimetres to decimetres as mesoscopic brecciation of the host rock and infilling of fractures by pyrrhotite, sphalerite and galena. At sharp contacts, the transition from unsheared host to shear zone is a centimetre or less in thickness. Microscopic brecciation is common at sharp contacts. In many areas, shear zone contacts have a marked increase in pyrite grain size. Towards the centre of the shear zone the quartz, carbonate, barite, massive pyrite, and phyllite clasts that have been mechanically degraded from the host rock are incorporated into the shear zones as inclusions and become rounded to elongate and often wrapped by the shear cleavage.

Pressure solution, though common in the ribbon-banded, carbonaceous quartzite and on a grain-scale in all sulphide lithofacies (Chapter 5), is rarely found on a mesoscale in the semi-massive and massive sulphide lithofacies. However, mesoscale pressure solution can be demonstrated locally and one instance has resulted in the development of a spectacular example of a lithon texture in massive sulphides (Figure 4.24a). Pressure solution is common in the ribbon-banded, carbonaceous quartzite and locally, shear banding is well developed (Figure 4.24b). In this lithofacies the pressure solution cleavage and, when present, the shear bands are generally enriched in pyrrhotite and sphalerite (Figure 4.24b).

Inclusions and porphyroblasts in the shear zones form equant to elongate, asymmetric and symmetric, winged and naked porphyroclasts and inclusions (terminology of

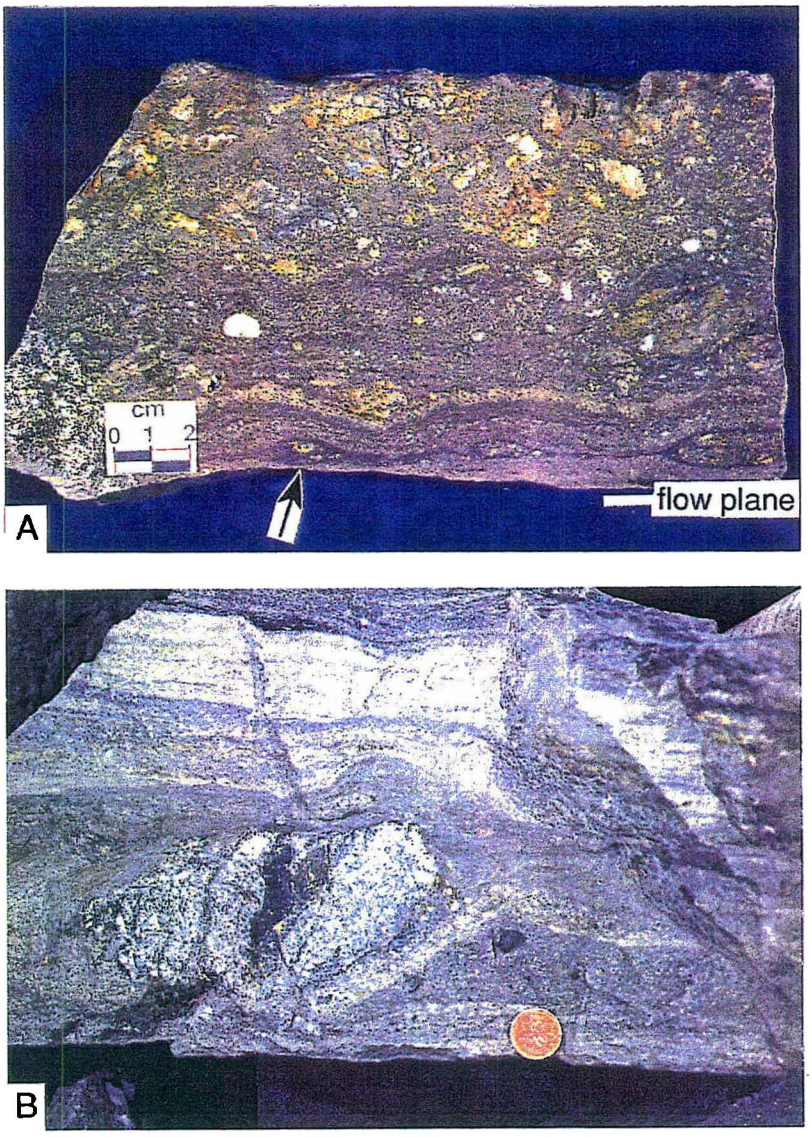

Figure 4.23. *A) Sheared massive sulphide with a strain gradient from top to bottom. Shearing is less intense at the top where inclusions are angular to rounded. Near the bottom inclusions are more asymmetric. At the base it is strongly sheared and boundinaged (arrow). Note that pyrrhotite and sphalerite defines the flow plane and that the pyrrhotite and sphalerite content increases in the higher strain area. B) Asymmetric clast of massive sulphide with the shear foliation wrapping around it. The flow plane is defined by pyrrhotite and sphalerite.*

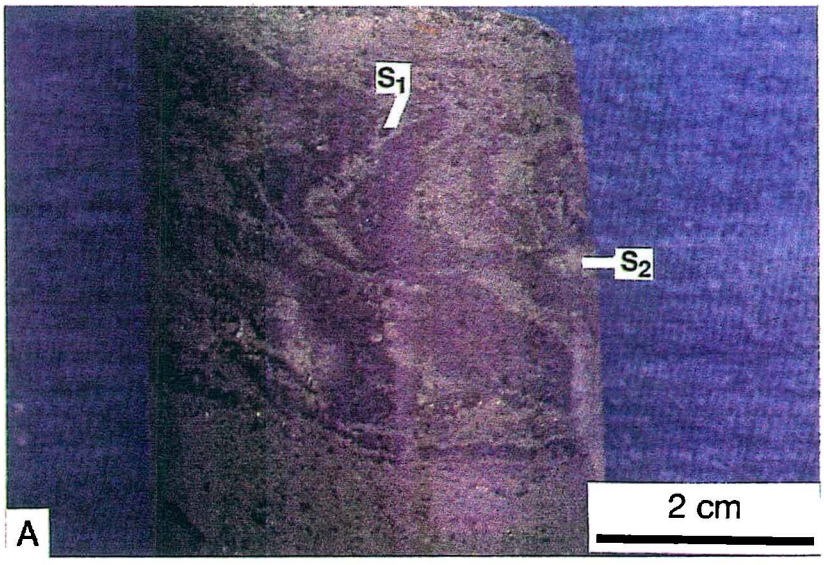

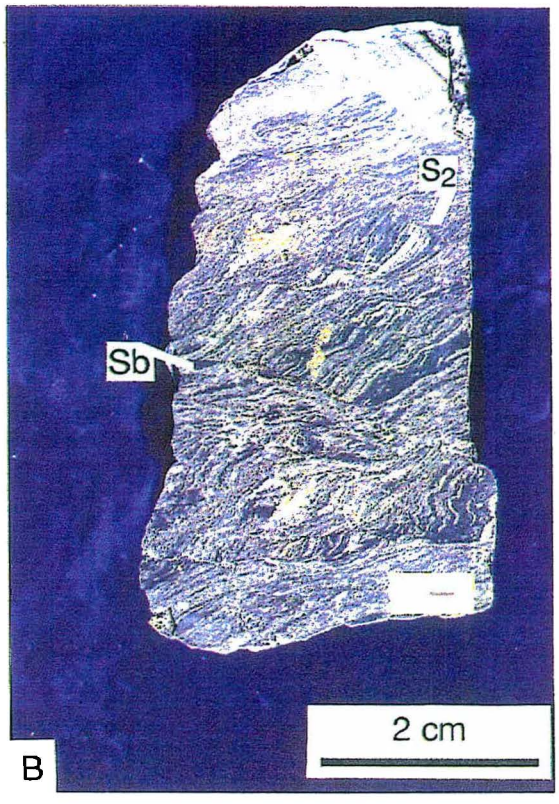

Figure 4.24. *A) Pressure solution cleavage in massive sulphide. The indicated cleavage plane is defined by quartz. B) Shear banded (Sb) ribbon-banded, carbonaceous quartzite.*

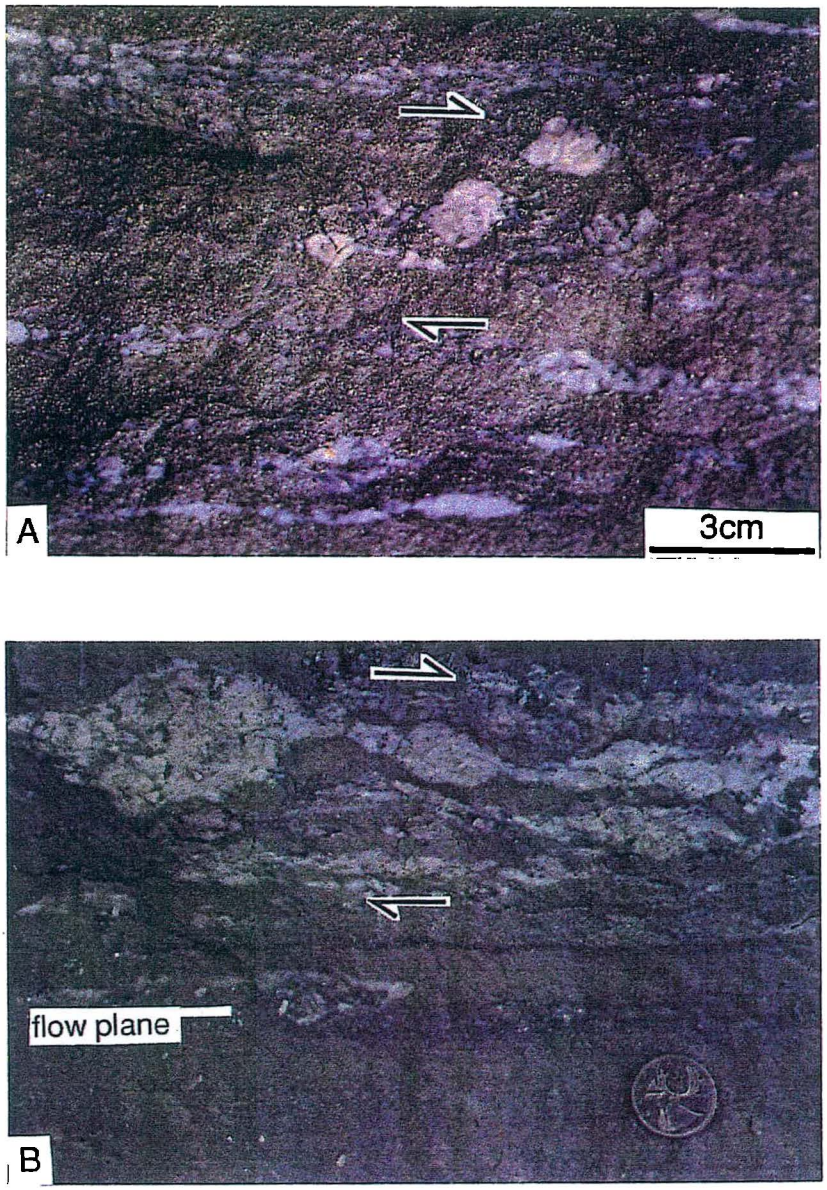

Figure 4.25. *A) Asymmetrically tailed σ quartz clasts in massive pyrite. The sense of shear is indicated. Note that the tails consist of recrystallised quartz derived from the clast. B) Asymmetrically tailed σ quartz inclusions in massive pyrite. Note that the tails joint several clasts. The flow plane is defined by pyrrhotite and sphalerite.*

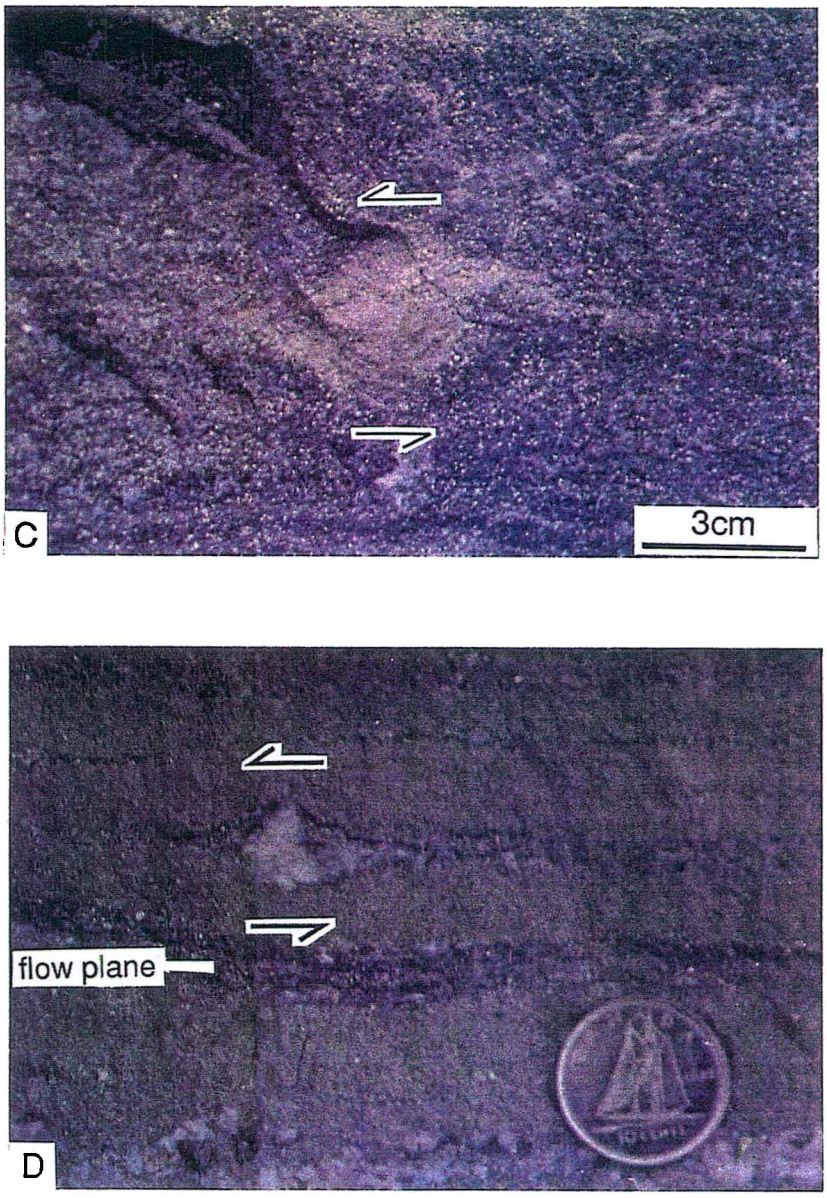

Figure 4.25. *(continued) C) δ clast of massive pyrite in baritic massive sulphides. The pyrite grains in the clast have completely recrystallised to form pyrite cubes. Note that the tails consist of pyrite derived from the clast. D) Symmetrically tailed quartz clast. The tails are pressure shadows consisting of quartz and sulphide. The flow plane is defined by pyrrhotite and sphalerite.*

Hanmer & Passchier 1991). The porphyroclasts and inclusions have the typical σ, δ in-plane and stair-step geometries noted in silicate rocks, though σ geometries predominate (Figure 4.25a). Wings also develop more complex geometries and may be folded or form thinned portions of layers that are materially continuous with the inclusion (Figure 4.25b). The latter may be continuous over a distance of a decimetre to a meter and join more than one inclusion. Pyrrhotite, sphalerite, galena and quartz form a very fine-grained band parallel to the flow plane (Figure 4.25b).

Wings consist of fine-grained polycrystalline material that is materially attached to, and have the same composition as, the porphyroclast or inclusion (Figure 4.25c), or are coarsely crystalline pyrrhotite, sphalerite, chalcopyrite, and galena, ± quartz, carbonate, and barite pressure shadows (Figure 4.25d). Again, note the pyrrhotite, sphalerite, galena and quartz folia parallelling the flow plane in Figure 4.25c and 4.25d. In the former, wings are either attenuated bands or are inclusion-derived recrystallised grains with some pressure shadow material. The latter consist of material deposited in the pressure shadow, with only minor inclusion-derived grains. Individual pyrite grains in massive pyrite inclusions and wings have recrystallised and undergone grain growth and now form euhedral porphyroblasts.

Inclusions often have a folded or sigmoidal internal foliation that is discordant to the external mylonitic foliation. Examples where the internal foliation in the inclusions or pyrite porphyroblasts unambiguously maintains continuity with the external foliation have not been found.

4.4.3 Cataclastic textures

Fracturing and cataclasis are widespread at a microscopic scale which will be discussed in Chapter 5. However, on a scale other than microscopic cataclasis is generally not

found except in areas that can be directly attributed to post-D_2 extensional faulting. Fracturing is found at shear zone boundaries and in several instances clasts incorporated into the shear zone appear to have do so via cataclasis.

4.4.4 Syn- to post-D_2 mobilisation features

Remobilisation in the sense of Marshall & Gilligan (1987) is an implicit feature of durchbewegung and shearing since these involve mechanical and chemical translocation resulting in modified concentration and distribution of the rock mass. It can therefore be said remobilisation occurred throughout the Vangorda deposit. Evidence for macroscale remobilisation are discussed in Section 4.5. Mobilisation in the sense of Marshall & Gilligan (1987), which involves translocation and modified concentration and distribution of preexisting semi-massive and massive sulphides has occurred on a microscopic (see Chapter 5) and mesoscopic scale in the Vangorda orebody.

The most common mobilisation feature found in the Vangorda orebody is associated with syn-D_2 fractures. These fractures are near vertical and parallel to the {0kl} joints (Figure 4.16) and occur throughout the orebody but are most common in the pyritic quartzite lithofacies. They are several millimetres to several centimetres high and several millimetres wide. These fractures are infilled by pyrrhotite, chalcopyrite, marcasite, sphalerite, magnetite, quartz, and carbonate and combinations of these (Figure 4.26a).

Another prominent mobilisation feature is concentration of massive galena, often associated with milky quartz (Figure 4.26b). This type of mobilisation is generally found in localised patches up to several tens of centimetres in size and in one location massive galena occurred over an area of several square metres. It has also been noted to occur in areas of intense fracturing related to extensional faulting. Unlike the well foliated, fine-grained galena in the durchbewegung (e.g. Figure 4.21c) galena in these mobilised areas is unfoliated and generally very coarse-grained (Figure 4.26b). In most

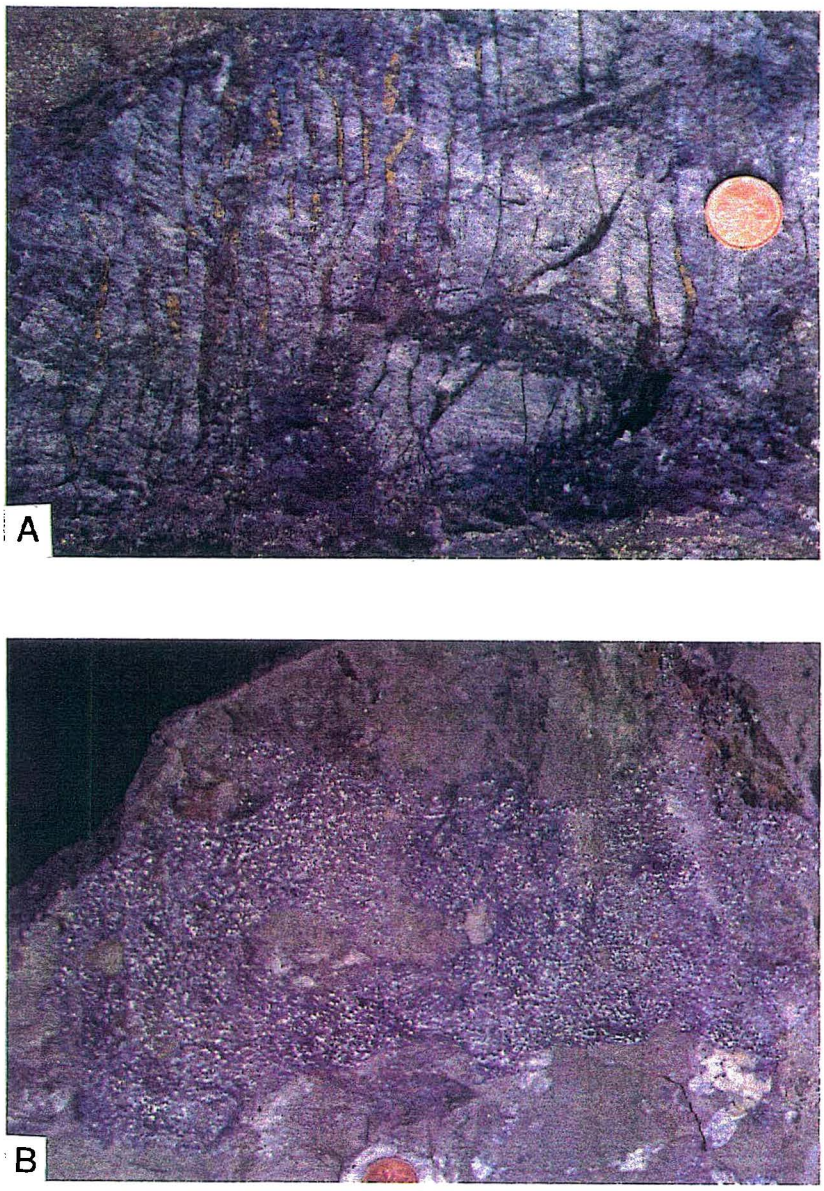

Figure 4.26. *A) Remobilised pyrrhotite and chalcopyrite in vertical fractures in pyritic quartzites. B) Post - D_1 and D_2 , coarse grained, remobilised galena. Note the coin for scale.*

instances the mobilised areas cut both the D_1 and D_2 structural elements.

4.5 Diamond drill core analysis

The complex structural characteristics of the orebody found in diamond drill core (Figure 4.27, see also Figures 1.3, 1.4 and 1.5) can be better understood by extrapolating the structural element analysis (Section 4.3) and the deformation textures (Section 4.4) to the drill core interpretation. Hence, the overall fold style and fold geometry and location is partially constrained by open pit mapping. The drill core structural element data upon which these interpretations are based is shown, in part, in Figure 4.28. From the diamond drill core it can be seen that the hangingwall and footwall phyllite and sulphide lithofacies contact is faulted locally, but is generally gradational, marked by an increase in chlorite/muscovite content in the phyllites and concomitant decrease in quartz and sulphide content (Figure 4.28).

The diamond drill core cross sections through fault block 4 (Figure 4.27) show a number of complexly folded lenses of massive and disseminated sulphides and baritic massive sulphides in host phyllites. The extreme fold complexity apparent in these sections is due in part to the lensoidal nature of the sulphide lithofacies involved, to minor faulting, to unconstrained orientation of the marker structural element (S_2) in drill core, and to errors in projecting drill traces onto the plane of the section. However, it is clear that the sulphide lithostratigraphic sequence and host phyllites are folded by southwest-verging, tight, symmetric to slightly asymmetric F_2 folds with a wavelength of 50 m to 75 m. The antiformal closure on section 6+00E (Figure 4.27) corresponds closely to the antiformal closure indicated by the S_1/S_2 cross section C - C' in Figure 4.19.

The folds are significantly thickened in their hinge zones and thinned along the limb. Hinge zone thickening is developed in the baritic lithofacies which has undergone

extensive cataclasis and shearing. Lenses of sulphide, concordant with the S_2 cleavage, have penetrated into the phyllites in the hinge zone (Figure 4.27, Section 4 + 00E).

Although durchbewegung and shearing are manifested to some degree throughout the orebody, intense plastic deformation is focused in high strain areas in the hinges and limbs of F_2 folds, along discrete shear zones (Figure 4.27 and 4.28). Only rarely do they continue into the surrounding phyllites.

Durchbewegung and shear zones appear to be developed on two scales; as centimetre to decimetre-scale thickness shears within lithofacies (Figure 4.28), commonly in hinge zones (Figure 4.27), and as decimetre to metre-scale thickness shears along fold limbs (Figure 4.27). Most are planar lenses that are continuous along strike for several tens of metres, pinching out as another is developed. One such major shear zone is developed along or near the contact with the lower pyritic quartzite unit and the above, folded lithofacies (Figure 4.27) partially detaching the upper, less competent, complexly folded sulphide package from the lower more competent quartzite package.

Pyritic massive sulphides within the baritic ores form lenses that have also undergone cataclasis, boudinage and shearing and may themselves be large tectonic inclusions or boudins incorporated into the deformed baritic rocks. In several locations the baritic massive sulphides have penetrated into the host phyllite along the S_2 cleavage. This phenomenon has been well documented in the blasthole maps used in the mine operations.

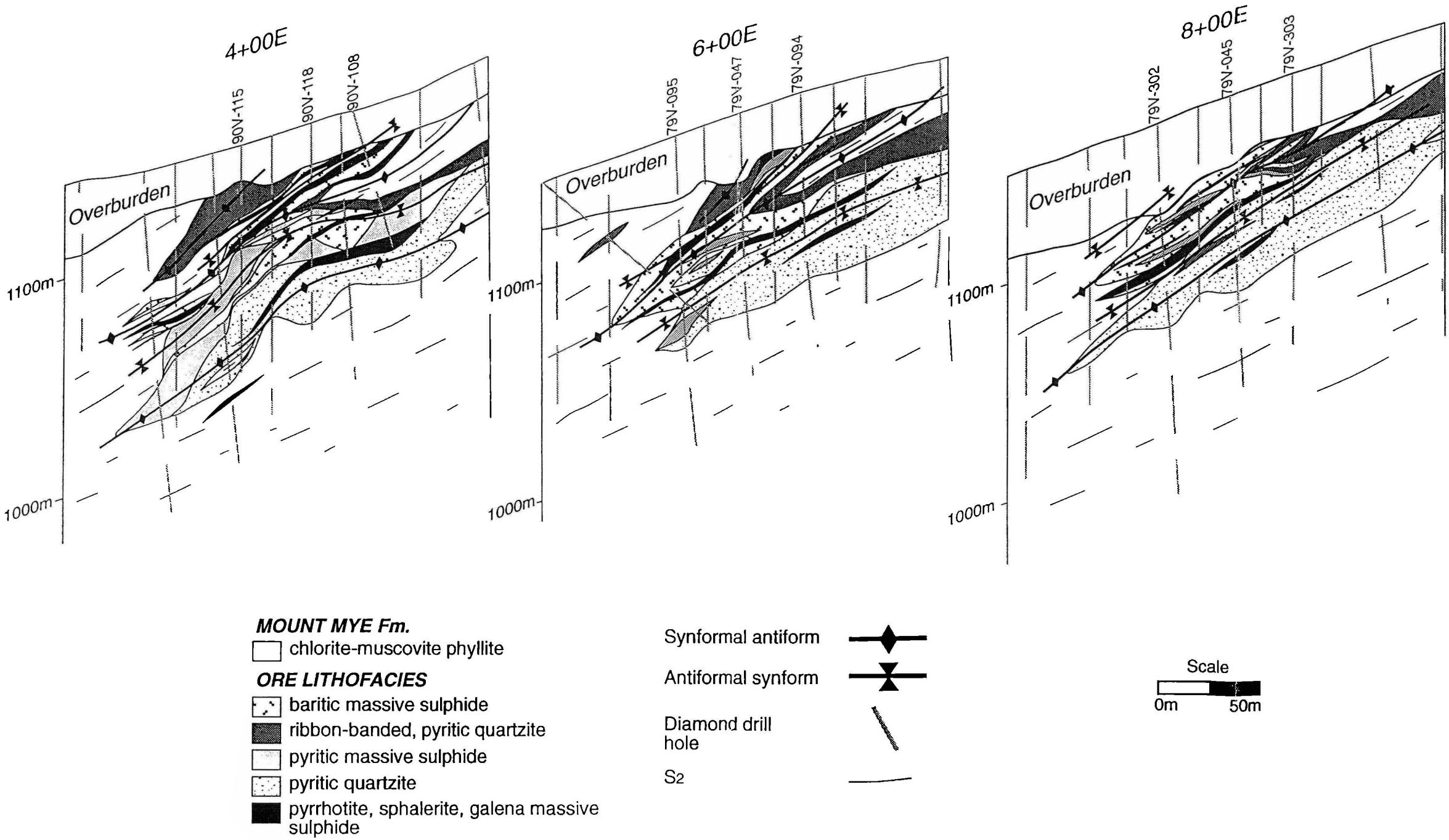

Figure 4.27. *Drill core cross sections through fault block 4 (the locations of the sections are shown in Figure 4.2). Fault block four makes up the bulk of the mineable reserves and also provides the best example of the F_2 fold style affecting the sulphides. Note the pyrrhotite + sphalerite + galena massive sulphides (shear zones) along the limbs of the F_2 folds, parallel to the axial surface. These shear zones pinch out laterally.*

Section 4+00E

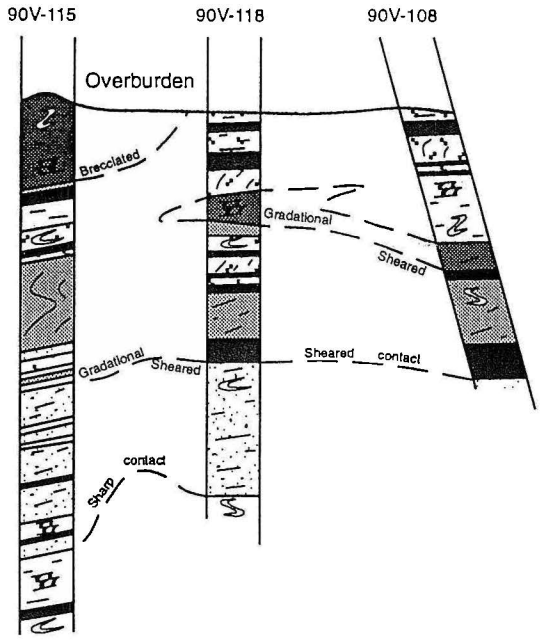

Weakly developed S1. Overall Z assymetry.

Interbanded sulphides and phyllites. Thin (5 - 10cm) pyrr breccias in phyllite. Minor folding, fold axes down dip in S2. Phrr + sph + mag shear zones in baritic sulphides.

Broken and leached over top 3m. Weak banding indicating fold hinge. Minor brecciation. Pyrite sand in bottom 4m (gouge?).

Poorly banded near top. Massive py banding developed towards bottom. Carbonaceous S2 foliation with increased muscovite content downwards. Fold hinge. Patchy, coarse ga.

Py bearing near top. Pyrr + mag shear zones developed. Overall M assymetry.

Well-developed py + mag foliation. Foliated pyrr + mag + ga shear zones with foliation wrapping clasts. Assymetry is M changing to S downwards. Carboanate-bearing.

Lithon-textured. Assymetry is M changing to Z.

Py + sph + mag banding parallel to S2. Py increases over last metre.

Strongly folded pyrr + sph + mag foliation. Porphyroblastic py growing across the foliation. Pyrr increases towards the bottom.

Weak foliation that is locally folded. Coarse sph rimming carbonate clasts.

Section 6+00E

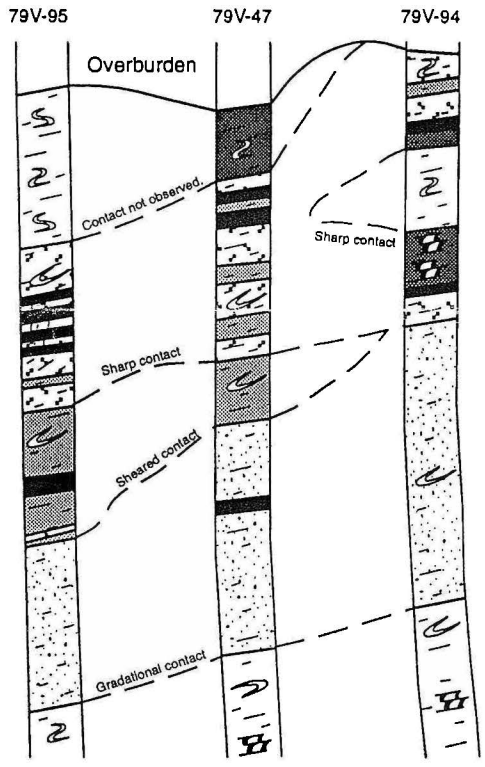

Well foliated phyllite with thin bands of baritic massive sulphide.

Tightly folded and boudinaged S1 py bands. M-asymmetry. Anastomosing pyrr + sph + mag shear zones containing tailed and rolled massive py breccia clasts.

Massive py with folded stringers (S1) of qtz and mag.

Folded S1 py banding. Locally developed, carbonaceous S2 foliation. Py porphyroblasts overgrow S2. Coarse-grained py, sph, mag and ga appear near lower contact.

Cm to m-scale banded massive py. Variable pyrr and mag content. Pyrr coronas on py.

Penetrative S2 foliation. Coarse (up to 2mm) patches of pyrr.

Lithon textured.

Tightly folded py bands. Disseminated 0.2mm to 1.5mm py porphyroblasts. Pyrr and mag are common. Pyrr coronas on py. Weak S2.

Isolated, intrafolial fold hinges with a chl S2 foliation. Py porphyroblasts aligned along S2.

Section 8+00E

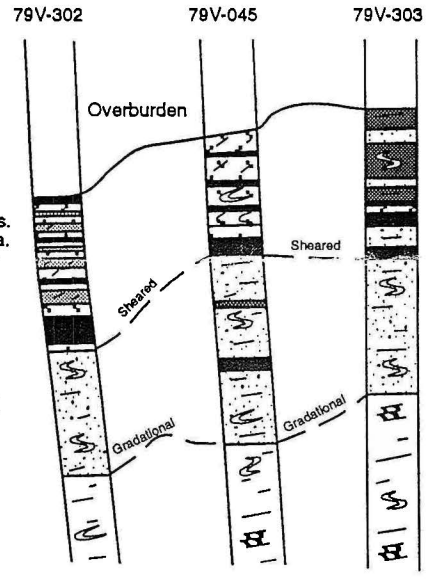

Thinnly interbanded massive pyrite and baritic sulphides. S1 foliation in massive pyrite defined by mag + qtz + ga. In baritic sulphide it is defined by qtz + ba + mag + ga + py and py + sph + qtz. Foliation wrapping clasts of sulphide, qtz, and phyllite. Foliation strongly folded. Widespread brecciation and shearing.

Local sph foliation. Foliation is folded. Mag is widespread but not common. Vertical fractures infilled by chalcopyrite and minor pyrr. Locally approching massive py.

Sulphide bearing. Chalcopyrite and pyrr infilling fractures. Lithons not well developed.

Well-developed lithons. Fold assymetry changes from S to Z downwards. Py porphyroblasts grow across the S2 foliation. Thin zones of brecciation.

Well-banded. Banding is defined by coarse, porphyroblastic py. Pyrr content in banding increases downward. Weak chl S2 foliation with py cross-cutting it locally. Vertical fractures infilled by chalcopyrite and pyrr.

Well-developed lithons. Minor py and pyrr along S1 and S2. Variably calcareous.

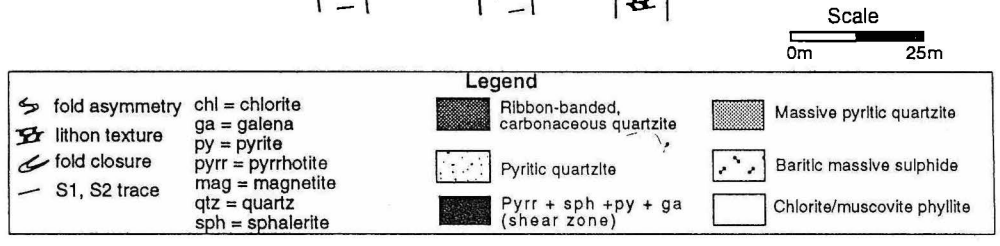

Figure 4.28. *Details of diamond drill core logs used in the construction of the cross sections in Figure 4.27.*

CHAPTER 5

Microtextural analysis of the sulphide lithofacies in the Vangorda orebody

5.1 Introduction

The active deformation mechanisms and resultant textures in pyrite, sphalerite, pyrrhotite and galena have been studied both experimentally and in natural occurrences and are known over a wide range of geological conditions (see Siemes & Hennig-Michaeli 1985; Cox 1987; Marshall & Gilligan 1987 for an overview). Rigorous textural analysis of the massive sulphide lithofacies and individual sulphide grains using etched and unetched polished sections and thin sections is fundamental for understanding the depositional and metamorphic evolution of the Vangorda orebody.

This chapter describes the mineralogy, equilibrium mineral assemblages and disequilibrium textures, paragenesis and grain textures of pyrite, sphalerite, pyrrhotite and galena as well as magnetite, quartz and barite found in the individual sulphide lithofacies of the Vangorda orebody. The individual grain textures and overall deformation textures observed on a microscopic scale are related to processes that occur in different structural positions of the fold structure discussed in Section 4.5. Selected polished sections were etched with warm HNO_3 or thiorea + HCL or coated with a magnetic colloid to study growth features (e.g. twins, grain boundaries and overgrowths), different mineral phases and inclusions and deformation textures (e.g. dislocation, diffusion and recrystallisation structures). Other polished sections were studied without being etched. Thin sections from each lithofacies were examined for textures in non-opaque grains.

5.2 Petrography of the sulphide lithofacies

5.2.1 *Massive pyritic sulphides*

The massive pyritic sulphides consist predominantly of matrix-supported cubes of porphyroblastic pyrite (Figure 5.1a) or subhedral grains in which matrix material is interstitial along pyrite grain boundaries and at triple junctions (Figure 5.1b). Matrix development is not continuous, varying from supporting the pyrite grains to occurring at pyrite triple junctions over distances of several centimetres .

Porphyroblastic pyrite constitutes 60 -90% of the lithofacies (Table 5.1). The matrix consists of fine-grained quartz, carbonate, and barite, with minor fine-to medium-grained sphalerite, pyrrhotite, galena, magnetite, and chalcopyrite. Quartz, calcite and/or dolomite and barite are disseminated throughout or occur in patches. Late fractures that post-date pyrite growth are infilled with coarse-grained subhedral to euhedral chalcopyrite, pyrrhotite, quartz, carbonate and, rarely, marcasite.

Disequilibrium textures in which all matrix mineral phases appear to be overgrowing all adjacent grains and contain inclusions of all other phases, except pyrite, are widespread (Figure 5.1c). Pyrite porphyroblasts overgrow and contain inclusions of all other grains and grow across all matrix assemblages. Equilibrium textures and thus

Table 5.1. Relative abundance of sulphide minerals and magnetite

Lithofacies	Relative abundance of sulphides minerals						
	pyrite	sphalerite	galena	pyrrhotite	chalcopyrite	arsenopyrite	magnetite
Massive pyritic sulphides	60 - 90	1 - 5	1 - 5	1 - 5	< 2	< 1	1 - 2
Pyrrhotite + sphalerite + galena massive sulphides	10 - 20	20 - 25	10 - 20	40 - 60	< 2	< 1	1 - 5
Pyritic quartzites	20 - 40	1 - 5	1 - 5	5 - 15	2 - 5	< 1	5 < 15
Baritic massive sulphides	10 - 30	5 - 20	5 - 10	5 - 10	< 2	< 1	1 - 2
Ribbon-banded, carbonaceous quarzite	10 - 20	1 - 5	1 - 5	1 - 5	< 2	< 1	< 1

assemblages of matrix sulphides are difficult to determine. Matrix sulphides with equant to subhedral, 0.02 mm to 0.1 mm grains with straight to gently lobate and 120° dihedral angles suggest the common matrix sulphide assemblage is sphalerite + galena (Figure 5.1d) (Table 5.2). Similar textures are rare in the pyritic massive sulphides but intergrowths of sulphide phases with interpenetrating grain boundaries suggest other assemblages occur locally (Table 5.2).

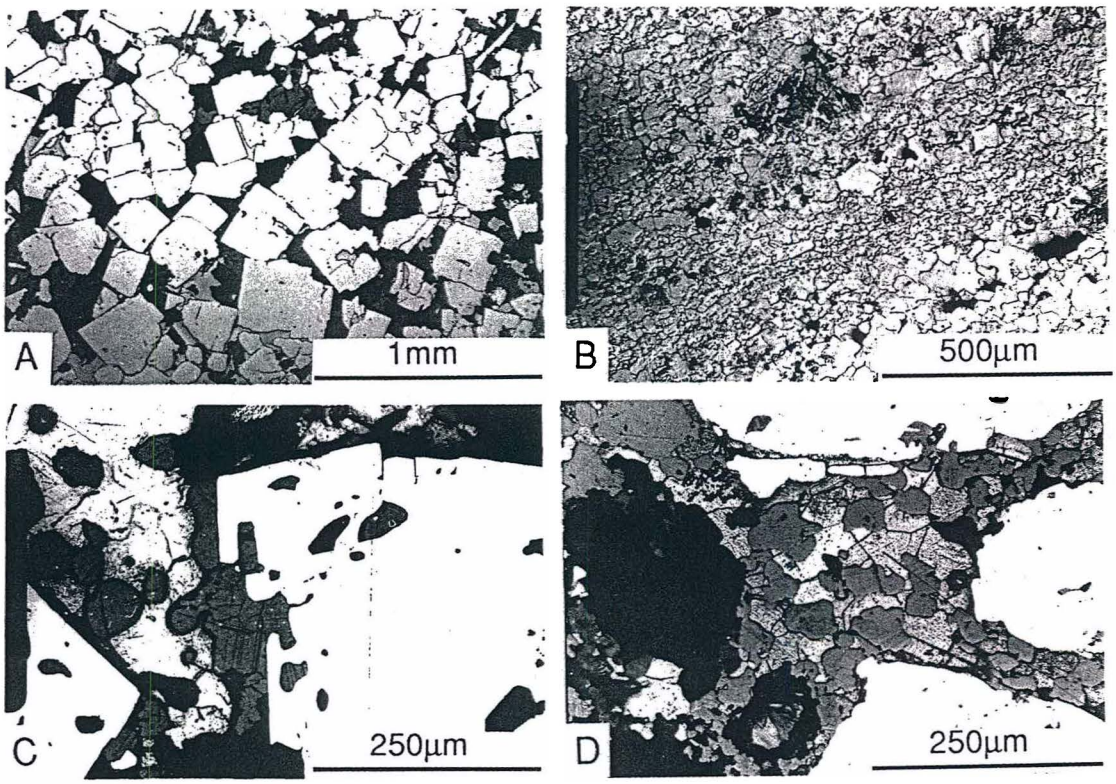

Figure 5.1. *Photomicrographs of textures in the massive pyrite lithofacies. A) Euhedral pyrite porphyroblasts (light grey) in a matrix of quartz (black) and sphalerite (medium grey). Sample 90-126 PPL.. B) Fine-grained, subhedral pyrite. Sample 90-46. Normanski interference C) Large pyrite porphyroblast (light grey) overgrowing sphalerite (dark grey) and quartz (black). Galena (medium grey) is also a matrix phase. Sample 91-43. PPL. D) Equilibrium matrix assemblage of sphalerite (dark grey) + galena (medium grey) interstitial to pyrite porphyroblasts (light grey). The large clast is quartz (black) Sample 91-32. PPL.*

Table 5.2. Sulphide mineral assemblages in the sulphide lithofacies.

Lithofacies	Mineral assemblages
Massive pyritic sulphides	sphalerite + galena sphalerite + pyrrhotite pyrrhotite + pyrite
Pyrrhotite + sphalerite + galena massive sulphides	sphalerite + galena sphalerite + pyrrhotite pyrrhotite + pyrite pyrrhotite + arsenopyrite arsenopyrite + pyrite
Pyritic quartzite	sphalerite + galena sphalerite + pyrrhotite pyrrhotite + pyrite
Baritic massive sulphides	sphalerite + galena sphalerite + pyrrhotite pyrrhotite + pyrite pyrrhotite + arsenopyrite arsenopyrite + pyrite
Ribbon-banded, carbonaceous quartzite	sphalerite + galena

5.2.2 Pyrrhotite + sphalerite + galena massive sulphides

This lithofacies consists predominately of fine-grained pyrrhotite, sphalerite, and galena with equant porphyroclasts of inclusion-rich pyrite (Figure 5.2a). Either pyrrhotite or sphalerite, but only rarely galena, may be the dominant sulphide phase present, locally constituting up to 60% of the rock (Table 5.1). Magnetite is a common phase and quartz and barite occur in polycrystalline clasts. Minor arsenopyrite also occurs. Late fractures affect all mineral phases and are infilled by chalcopyrite, pyrrhotite, quartz, carbonate and, rarely, marcasite.

Etched sections show that sulphide equilibrium assemblages, although not widespread, are preserved in this lithofacies (Table 5.2). The common assemblages are sphalerite + galena and sphalerite + pyrrhotite (Figure 5.2b). A pyrrhotite + pyrite assemblage,

although not common, is found locally (Figure 5.2c). However, disequilibrium textures, typified by grain growth textures (Figure 5.2d) and by most phases occurring as inclusions in other grains, are widespread. Single pyrite grains often contain all other phases

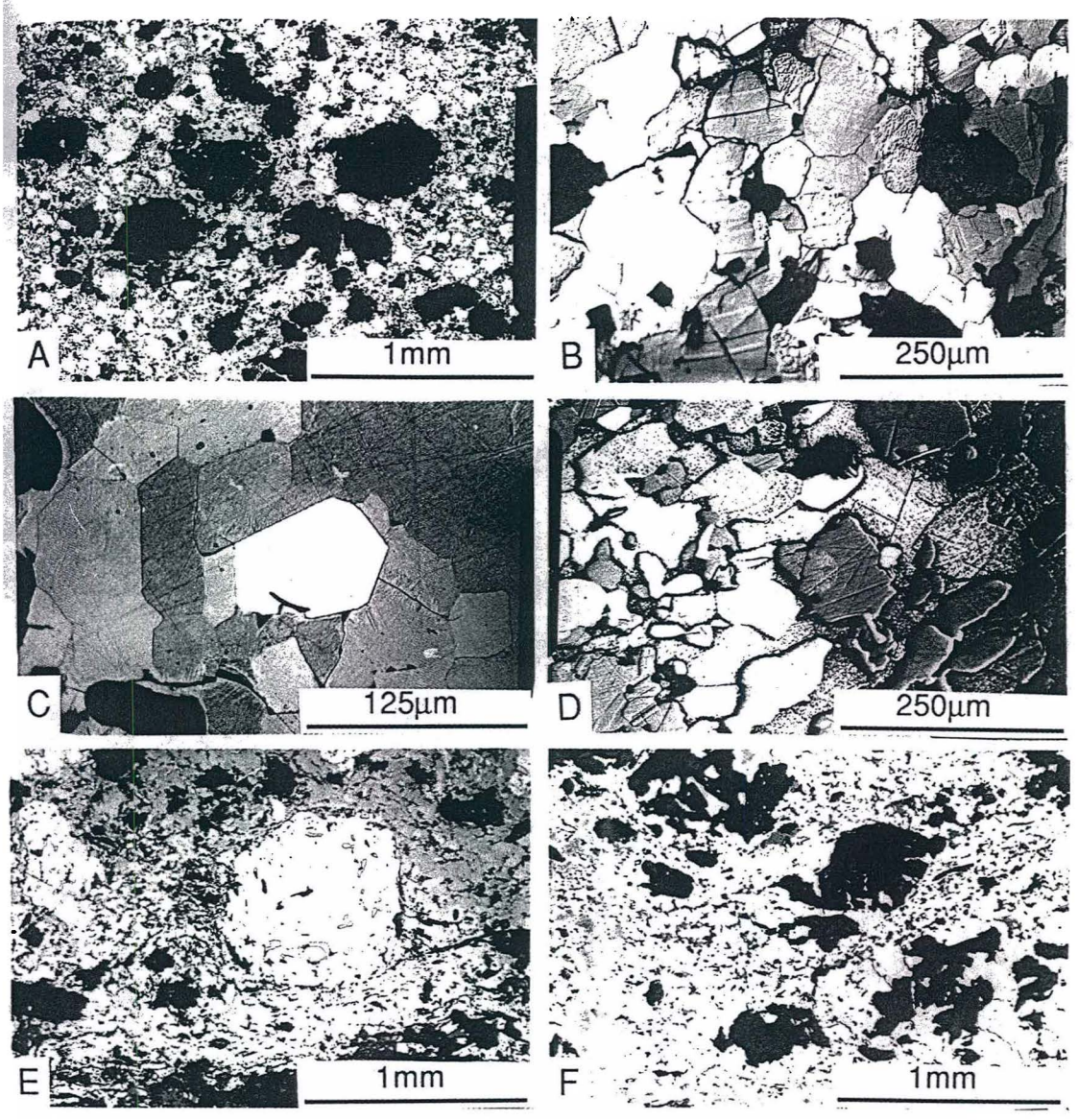

Figure 5.2. *Photomicrographs of textures and assemblages in the pyrrhotite + sphalerite + galena lithofacies. A) Fine-grained, equant pyrite porphyroclasts (light grey) in a matrix of pyrrhotite + sphalerite + galena (medium grey). The large black clasts are quartz and barite. Sample 91-130. PPL. B) Common equilibrium assemblage of sub-edral sphalerite (medium grey) and galena (light grey). Sample 91-39. PPL. C) Equilibrium assemblage of pyrrhotite (dark grey) and pyrite (light grey). Sample 91-133. PPL. D) Grain growth textures of pyrrhotite (light grey) and sphalerite (dark grey) overgrowing galena (light grey). Sample 91-13. Normanski interference. E) Pyrite porphyroblast (light grey) in foliated massive pyrrhotite. Note the helicitic inclusion pattern in the pyrite. Sample 90-132. PPL F) σ-clast of quartz (black) in massive pyrrhotite. Sample 91-01. PPL.*

These rocks are strongly sheared and generally have a well developed foliation and microscopically the foliation can be seen to wrap clasts and porphyroclasts (Figure 5.2e). This foliation is often discordant to S_1 in the surrounding rock. In many cases the porphyroclasts and inclusions have symmetric and asymmetric wings and pressure shadows (Figure 5.2f).

5.2.3 Pyritic quartzite

The pyritic quartzite consists of quartz and pyrite (Table 5.1) and grades into the massive pyritic sulphides at between 40% and 60% pyrite content. The predominant sulphide is porphyroblastic pyrite and the matrix sulphides consist of sphalerite, galena, pyrrhotite, chalcopyrite and minor marcasite and arsenopyrite (Figure 5.3a). Anhedral to subhedral magnetite (Figure 5.3b) is a common phase. Muscovite, although widespread, is a minor phases. Minor chlorite and biotite also occur. Subhedral to euhedral calcite and/or dolomite occurs in coarse polycrystalline patches.

Equilibrium textures are not widely preserved in the matrix of the pyritic quartzites. However, mildly sutured and interpenetrating grain boundaries together with relatively minor grain growth textures indicate a common relic equilibrium assemblage of sphalerite + galena (Figure 5.3c). Other, minor assemblages occur locally (Table 5.2). In general disequilibrium textures in which all phases overgrow and contain inclusions of other phases and coarse-grained pyrite porphyroblasts overgrow all other grains and assemblages are dominant.

The pyritic quartzites are generally strongly fractured and brecciated with the fractures infilled by chalcopyrite, pyrrhotite, locally marcasite, quartz, carbonate and barite. It is common that both marcasite and pyrrhotite in the fractures are altering to

pyite

5.2.4 Baritic massive sulphides

The baritic massive sulphides consist predominantly of barite, quartz and porphyroblastic pyrite (Figure 5.4a) with lesser sphalerite, galena, pyrrhotite, quartz and magnetite and minor chalcopyrite and arsenopyrite (Table 5.1). Calcite and dolomite form patches of subhedral to euhedral grains. Muscovite and chlorite are

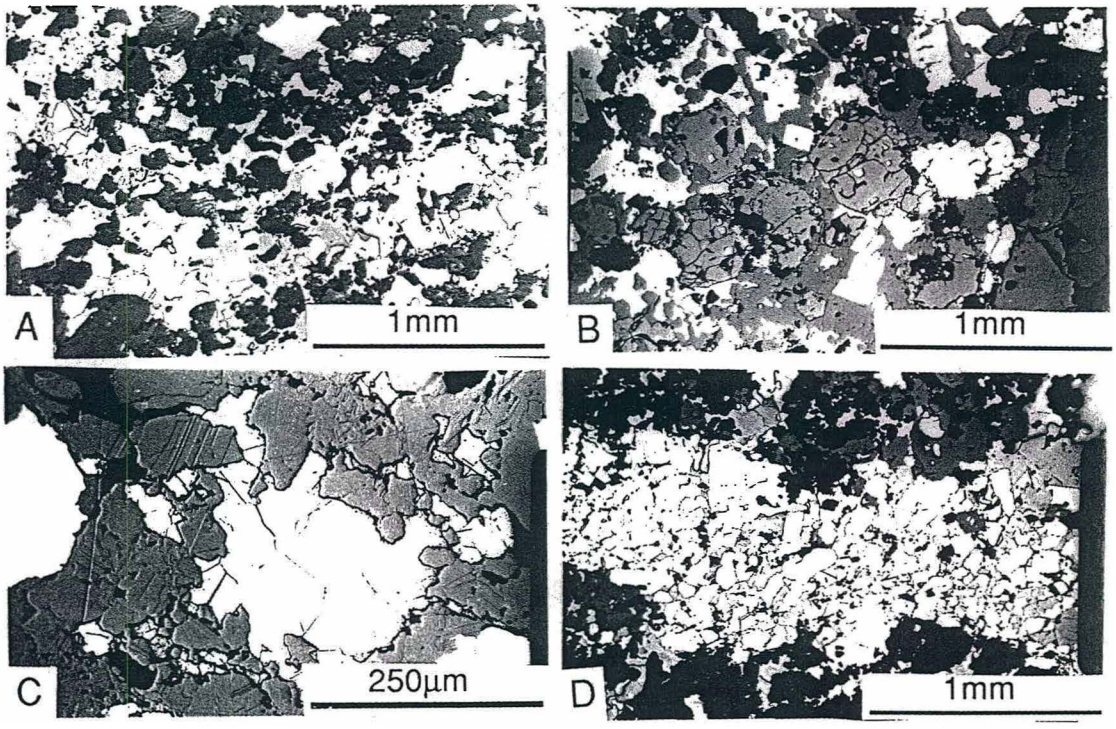

Figure 5.3. *Photomicrographs of textures and assemblages in the pyritic quartzite lithofacies. A) Common textures of pyrite (light grey), sphalerite (medium grey) and quartz (black). 91-130. PPL. B) Subhedral magnetite porphyroblast (medium grey), euhedral pyrite (light grey) and sphalerite dark grey. Sample 91-89. PPL. C) Relic (equilibrium assemblage?) of sphalerite (dark grey)+ galena (light grey). Sample 91-123. PPL. D) Pyrite (light grey) forming from pyrrhotite (medium grey) infilling fracture. Sample 91-94. PPL.*

Equilibrium assemblages are not widespread in the baritic lithofacies. However, locally preserved relic textures indicate two common assemblages of pyrite + pyrrhotite (Figure 5.4b) and sphalerite + galena (Figure 5.4c). Other, minor assemblages also occur (Table 5.2). Disequilibrium textures are widespread and the

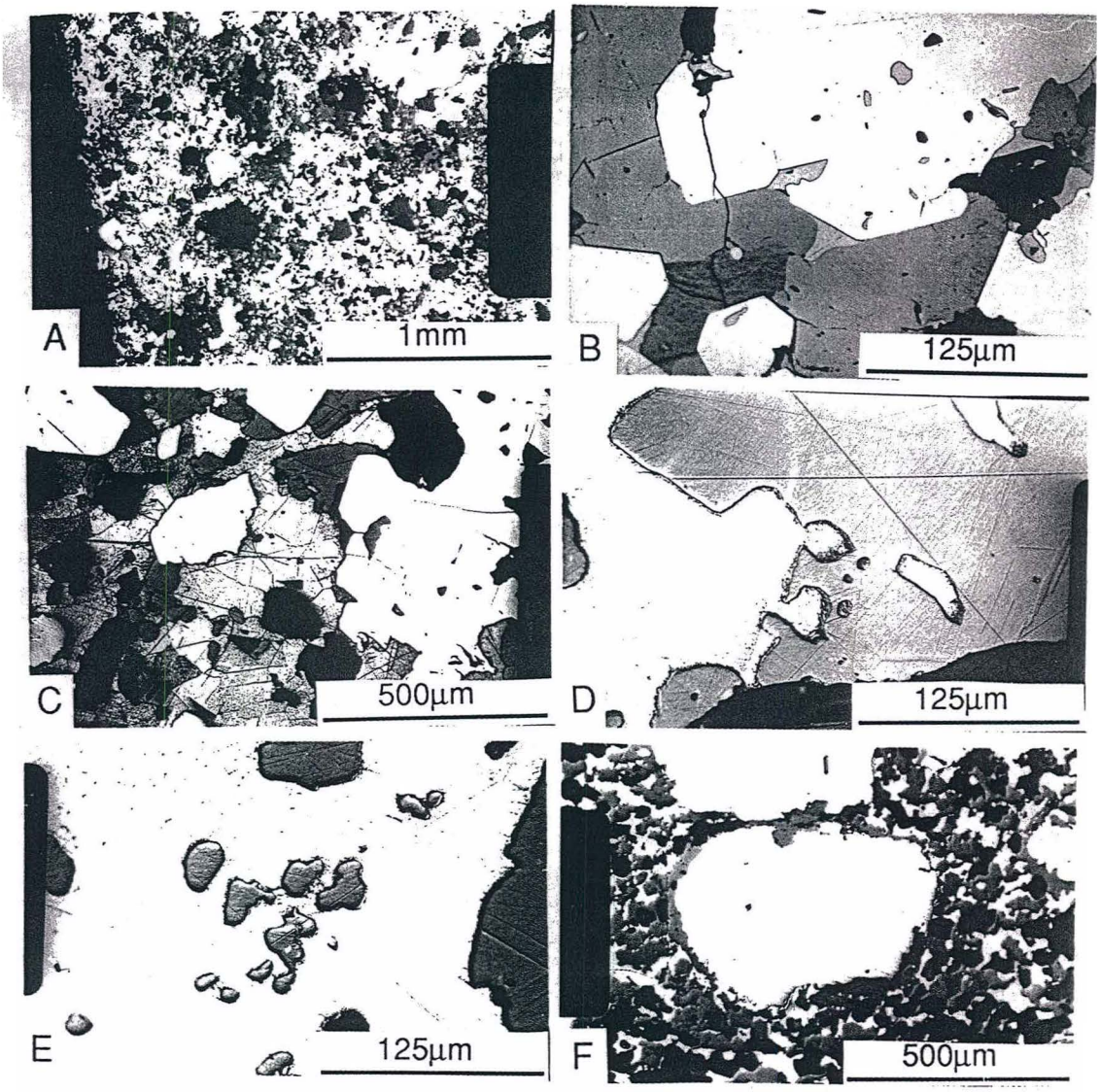

Figure 5.4. *Photomicrographs of textures and assemblages in the baritic massive sulphide lithofacies. A) Common texture with late pyrite porphyroblasts (light grey), sphalerite (medium grey) and galena (light grey). Barite and quartz are black. Sample 91-88. PPL. B) Equilibrium assemblage of pyrite (light grey) + pyrrhotite (medium grey). Sample 90-147. PPL. C) Equilibrium assemblage of sphalerite (dark grey) and galena (medium grey) being overgrown by pyrite (light grey). Sample 90-76. PPL. D) Sphalerite (medium grey) overgrowing and including galena (light grey). Sample 90-76. PPL. E) Galena (light grey) overgrowing and including sphalerite (medium grey). Sample 90-76. PPL. F) Sphalerite corona (medium grey) on pyrite porphyroblast (light grey) in sheared baritic lithofacies. Sample 90-32. PPL.*

petrogenetic relationships are complex and difficult to determine since most phases overgrown and include others. For instance, in the same sample sphalerite clearly overgrows and includes galena (Figure 5.4d) and galena clearly overgrows sphalerite (Figure 5.4e). In highly sheared areas sphalerite coronas developed on pyrite are common (Figure 5.4f) which clearly points to sphalerite postdating the pyrite porphyroclast growth.

The baritic massive sulphides are very strongly deformed and display mesoscale brittle and plastic deformation textures (see for example Figure 4.25c). On a microscale these textures display a well developed shear foliation that wraps inclusions and defines the flow plane.

5.2.5 Ribbon-banded, carbonaceous quartzite

The ribbon-banded, carbonaceous quartzite consist predominantly of quartz and pyrite with minor sphalerite, galena and pyrrhotite (Table 5.1). Carbon (graphite?), muscovite and chlorite define the S_1 and S_2 cleavages (Figure 5.5a). Sulphide grains and polycrystalline patches also occur along S_1. Where these grains and patches abut S_2 they have commonly undergone dissolution and subsequent precipitation along S_2 (Figure 5.5a/b). Locally, elongate polycrystalline patches of remobilised sulphides occur along the S_2 foliation (Figure 5.5c). Euhedral pyrite porphyroblasts grow across S_2 and/or display indentation and dissolution seams parallel to S_2 (Figure 5.5d).

Sulphides, and therefore any sulphide mineral assemblage, in the ribbon-banded, carbonaceous quartzite occurs in the coarsely crystalline ribbons (see Section 3.3.2). This lithofacies has only one readily identifiable assemblage is sphalerite + galena (Table 5.3).

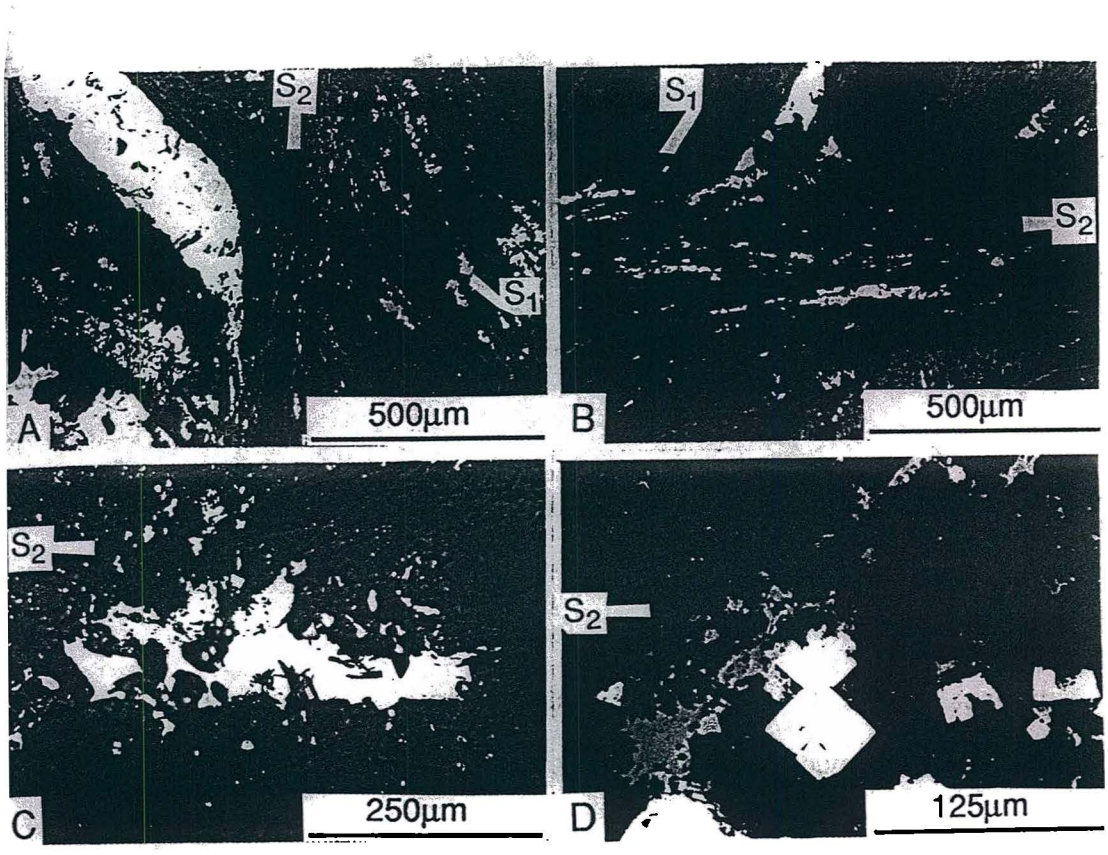

Figure 5.5. *Photomicrographs of textures in the ribbon-banded, carbonaceous quartzite. A) Elongate patch of polycrystalline pyrrhotite (light grey) aligned along S_1 being transposed into S_2. Sample 90-9. PPL. B) Pyrrhotite defining both S_1 and S_2. Sample 90-9. PPL. C) Galena (light grey) and pyrrhotite (medium grey) remobilised along S_2. Sample 90-86. PPL. D) Euhedral pyrite grains (light grey) with dissolution seam parallel to S_2. Sample 90-130. PPL.*

5.3 Deformation textures in sulphides

5.3.1 Pyrite textures

5.3.1.1 Primary textures in pyrite

Pyrite is the only sulphide mineral in the Vangorda orebody in which any primary feature is preserved. Relict, primary colloform pyrite grains and relict spheroids and framboids, although not widespread, can still be found (Figure 5.6a). The colloform

and zoned grains are 0.1 mm to 0.25 mm sized, equant to xenoblastic and occur alone or, more commonly, as cores in metamorphic porphyroblasts.

5.3.1.2 Brittle deformation textures in pyrite

Deformation of single pyrite grains (Table 5.3) and massive pyrite in all lithofacies occurred mainly by fracturing and cataclasis, resulting in an overall reduction in grain-size. Where pyrite grains impinge upon each other, indentation and dissolution, axial cracking and microfracturing occur (Figure 5.6b). Intense brittle shearing (Figure 5.6c) of single grains or cataclastic flow in polycrystalline pyrite forming aggregates of finely crushed, angular grains is common . These zones are commonly sealed by quartz, carbonate, and mica. Locally, pyrite displays internal microfracturing, suggesting inelastic strain accommodation in the core of the grains. Grain boundary sliding, which is geometrically necessary to accommodate diffusional deformation, is indicated by microfracturing along and parallel to grain boundaries where two grains impinge upon each other (Figure 5.6d).

Table 5.3. Deformation mechanisms and textures in sulphides in the Vangorda orebody.

Mineral	Deformation mechanisms and textures
Pyrite	Cracking and cataclasis. Grain boundary sliding. Dislocaton glide and climb resulting in subgrain formation. Slip planes developed locally. Pressure solution causing preferred grain shape orientation. Annealing and grain growth indicated by 120° dihedral angles and grain boundary bulging.
Sphalerite	Rare deformation twinning. Broad, parallel-sided growth and annealing twinning. Annealing and grain growth indicated by 120° dihedral angles and grain boundary bulging.
Pyrrhotite	Growth and annealing feather twinning predominate. Dislocation glide causing crystallographic preferred orientation. Pressure solution causing preferred grain shape orientation. Annealing indicated by 120° dihedral angles and local grain boundary bulging. Monoclinic overgrowths on hexagonal cores.
Galena	Annealing indicated by 120° dihedral angles.

5.3.1.3 Plastic deformation textures in pyrite

Readily identifiable ductile deformation textures in pyrite in the Vangorda orebody are not widespread but are found locally (Table 5.3). The lack of ductile deformation features is most likely a result of strong post-deformation annealing that produced grain growth and an overall increase in grain-size.

Dislocation microstructures in pyrite occur mainly in the massive pyritic sulphides. The dislocation microstructures are characterised by straight to slightly curved, stepped, or branching dislocation etch pits that outline dislocation tangles and walls forming parallel to <100> and <110> (cf. Cox *et al.* 1981; Graf *et al.* 1981) (Figure 5.6e). Movement of dislocations through the crystal, possibly along the {100} <001> slip plane, is evidenced by slip lines. Etch pits commonly intersect to form grid-like arrays that mark subgrain boundaries and the onset of polygonisation (Figure 5.6e). The subgrains are 1 μm to 10 μm in size.

Dynamically recrystallised grains are widespread in the massive pyritic sulphides and the pyritic quartzite and are found to a lesser degree in the baritic massive sulphides. Subgrain formation commonly occurs along the boundaries of parent grains (Figure 5.6f) and in extreme cases results in the formation of a core mantle texture. Recrystallised grains are typically 5μm - 50μm, equant grains with straight to slightly curved grain boundaries. Post-recrystallisation grain growth has likely resulted in an increase in pyrite grain-size.

Preferred grain shape orientation in pyrite occurs only in the massive pyritic sulphides, in areas of high bulk strain in which thin, discontinuous, often anastomosing zones of elongate pyrite define a crude S_2 foliation. Grains in these locations have straight to slightly curved, mildly sutured, and lightly indented grain boundaries (Figure 5.6g).

Figure 5.6. *Pyrite textures in the Vangorda orebody. All samples etched in warm HNO_3. A) Relict premary colloform grain forming core in metamorphic porphyroblast. Normanski interference. Sample 90-52. B) Indentation and axial cracking of subhedral pyrite porphyroblasts. PPL. Sample 90-37. C) Cataclastic flow in pyrite porphyroblast. PPL. Sample 91-83. D) Microfracturing parallel to grain boundaries indicating grain boundary sliding. Normanski interference. Sample 90-121. E) Arrays of etch pits that form subgrain walls indicating the onset of polygonisation. PPL. Sample 90-39. F) Dynamically recrystallised grains forming at the boundary of older grains. PPL. Sample 90-46. G) Preferred grain shape orientation in pyrite. PPL. Sample 90-39. H) Annealed grains showing lobate grain boundaries and 120° dihedral angles. Normanski interference. Sample 90-46.*

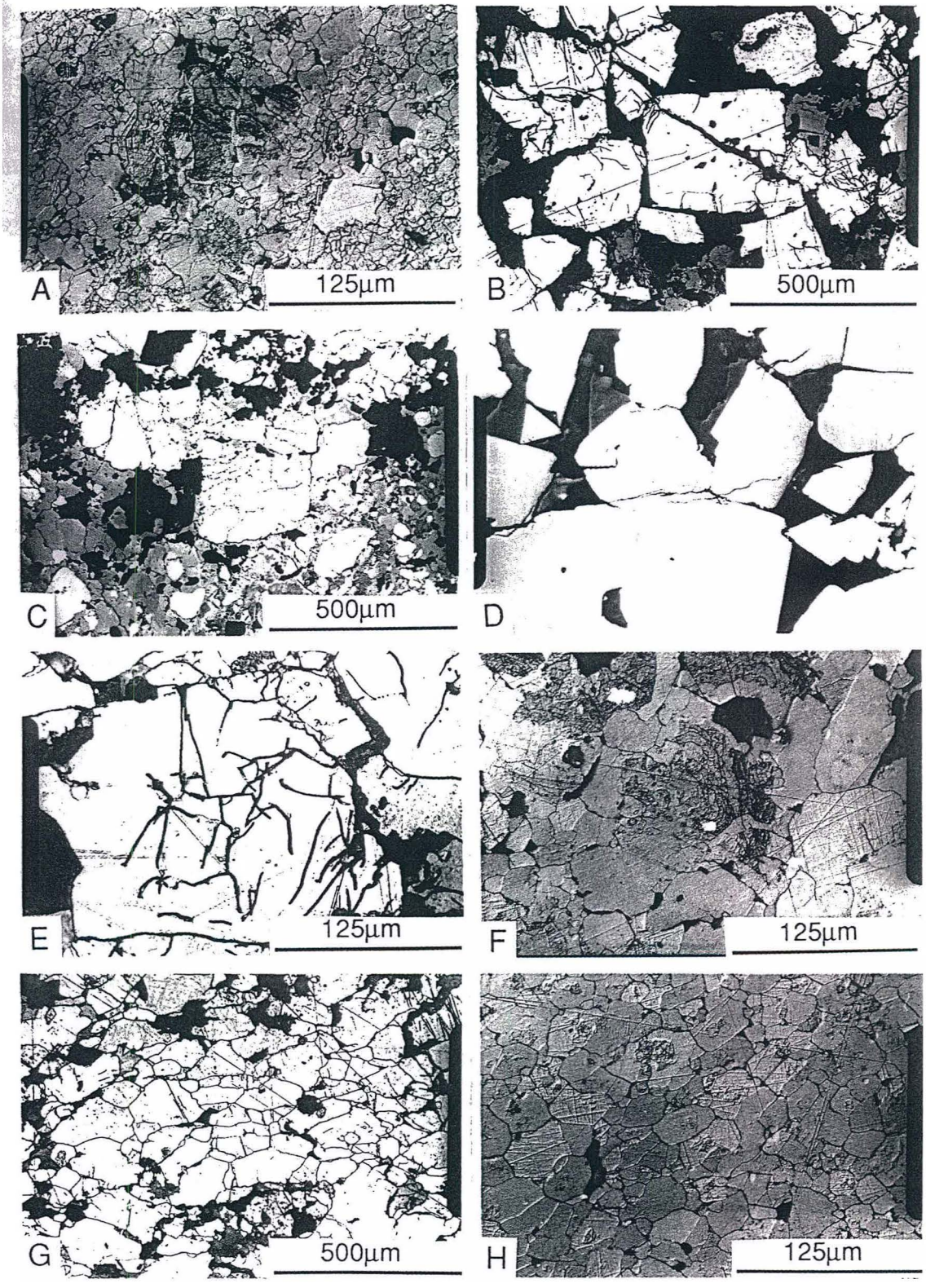
A
125µm
B
500µm
C
500µm
D
E
125µm
F
125µm
G
500µm
H
125µm

Within individual grains there is little or no evidence of brittle deformation, and dislocation textures are rare. Preferred grain shape orientation is likely the result of pressure solution which is particularly well displayed in aggregates of small grains which have relict spheroidal and framboidal cores. However, overgrowths are not apparent on all elongate grains. These features suggest grain-scale dissolution and mobilisation have occurred.

Pyrite grains in the baritic massive sulphides and in the pyrrhotite + sphalerite + galena massive sulphides are commonly rounded to asymmetric with deeply embayed grain boundaries and are inclusion-rich, locally with concentric and helicitic inclusion patterns (e.g. Figure 5.2e). Many grains have coronas of sphalerite (Figure 5.4f). Rounding and development of asymmetric grains is possibly due to rolling of the pyrite in the more ductile pyrrhotite, galena, sphalerite and barite matrix (c.f Vokes 1969), to alteration of the grain to pyrrhotite (or sphalerite?) and to shear related grain boundary processes such as recrystallisation. Concentric matrix inclusion patterns in pyrite grains suggest multiple phases of grain growth in which inclusions were trapped along preexisting grain boundaries. Rare, helicitic inclusions patterns indicate either porphyroblast rotation (Graig *et al.* 1991) or multistage porphyroblast growth overgrowing successive foliations (cf. Bell 1985).

5.3.1.4 Annealing and grain growth textures in pyrite

As well as deformation textures, pyrite shows a number of annealing and grain growth textures due to metamorphism (Table 5.3). In the massive pyritic lithofacies, grains are commonly 0.2mm to 1.5mm in size, equant with straight to mildly sutured grain boundaries that meet at 120° dihedral angles (Figure 5.6h). When completely surrounded by matrix, pyrite grains are generally euhedral cubes. Strongly lobate grain boundaries, which are indicative of grain growth during annealing, are widespread.

5.3.2 *Pyrrhotite textures*

5.3.2.1 *Brittle deformation textures in pyrrhotite*

Pyrrhotite is not widely affected by brittle deformation. However, it has been affected by the post-F_2 fracturing (see Figure 5.7b and 5.7d).

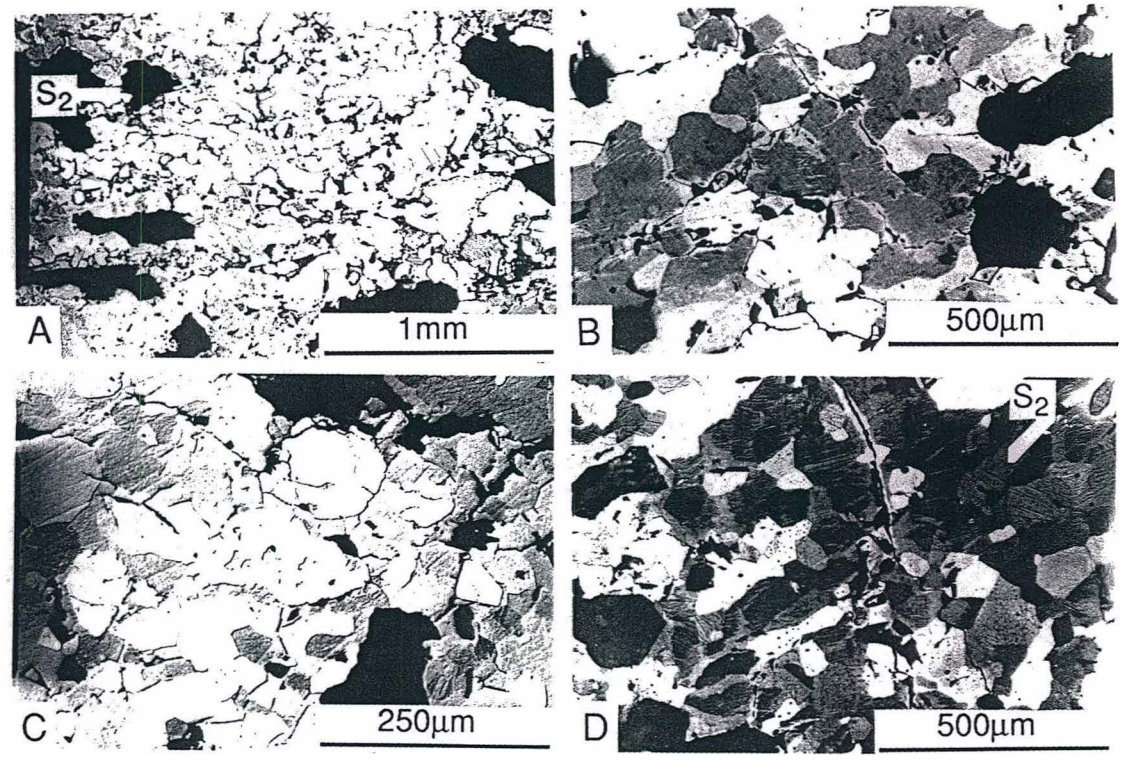

Figure 5.7. *Textures in pyrrhotite. A) Elongate pyrrhotite defining S_2. Sample 91-13. PPL. B) Subhedral hexagonal pyrrhotite cores with monoclinic pyrrhotite overgrowths. Note the feather growth twinning in the hexagonal cores. Sample 91-4. PPL. C) Euhedral, annealed hexagonal pyrrhotite (medium grey) with pyrite porphyroblasts (light grey) overgrowing it. Sample 91-4. PPL. D) Slightly elongate hexagonal, feather twinned pyrrhotite defining S_2.*

5.3.2.2 Plastic deformation textures in pyrrhotite

Plastic deformation textures in pyrrhotite are rare in the Vangorda ores (Table 5.3). However, in several localities in the pyrrhotite + sphalerite + galena massive sulphides there is a differentiated sulphide foliation in which pyrrhotite 'ribbons' are separated by zones of coarser grained, subhedral to euhedral sphalerite ± galena. In some instances there are two oblique sulphide foliations defined by elongate pyrrhotite and/or pyrrhotite 'ribbons' (Figure 5.7a). Pyrrhotite grains in these localities are elongate parallel to the foliation or form euhedral grains, often with uniform extinction, that make up the 'ribbons'. Both the elongate grains and euhedral grains with uniform extinction indicate plastic deformation processes such as pressure solution and dislocation glide, respectively, were active.

5.3.2.3 Annealing and grain growth textures

Pyrrhotite porphyroblasts in all lithofacies have widespread development of tapered growth twinning in their cores with, commonly, untwined pyrrhotite overgrowths (Figure 5.7b and 5.7d). A magnetic colloid applied to these pyrrhotite grains adheres to the cores but not to the rims suggesting the cores are hexagonal and the rims monoclinic (c.f. Scott 1974). Pyrrhotite grains are euhedral with straight to lobate grain boundaries and near 120° dihedral angles (Figure 5.7c and 5.7d). Pyrrhotite grain boundary bulging into all other sulphide phases (though only rarely into pyrite) is widespread. Pyrrhotite rarely contains inclusions but when it does magnetite and pyrite are the most common.

5.3.3 Sphalerite textures

5.3.3.1 Brittle deformation textures in sphalerite.

Brittle deformation in sphalerite is restricted to post-F_2 fracturing (e.g Figure 5.8b).

5.3.3.2 Plastic deformation textures in sphalerite

Plastic deformation textures in sphalerite (Table 5.3) are restricted to one occurrence in which a porphyroclast has thin, tapered deformation twins (Figure 5.8a). These are

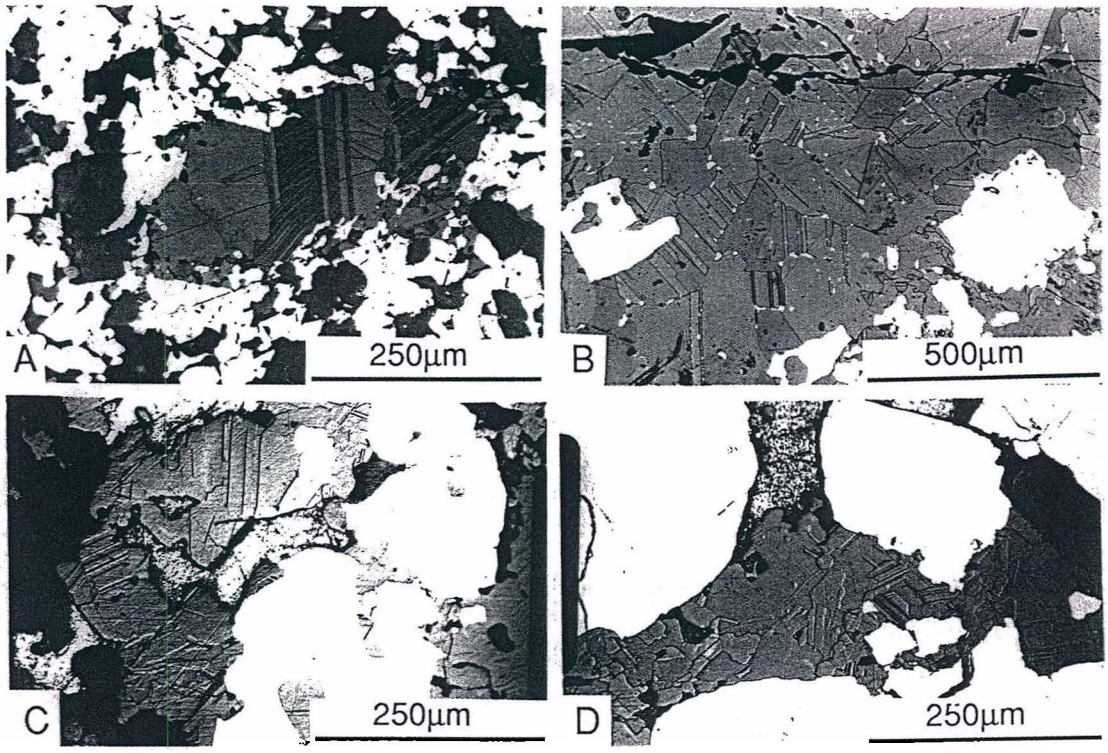

Figure 5.8. *Textures in sphalerite. A) Tapered deformation twins (inclined) in a sphalerite porphyroblast overprinted by growth twins (vertical). Sample 91-27. PPL. B) Euhedral, annealed sphalerite (medium grey) with well-developed broad, parallel-sided growth twins. Sample 91-27. PPL. C). Annealed, euhedral sphalerite (medium grey) with well-developed growth twins being overgrown by pyrite (light grey). Sample 90-138. PPL. D) Annealed sphalerite (medium grey) with well developed growth twins interstitial to pyrite (light grey). Sample 90-95. PPL.*

overprinted by annealing twins that are nearly perpendicular to the deformation twin boundaries. However, this occurrence does indicate that sphalerite has undergone ductile deformation.

5.3.3.3 Annealing and growth textures in sphalerite.

Sphalerite is anhedral to euhedral and displays widespread development of broad, parallel-sided growth or annealing twins (Figure 5.8b/c/d) that, in several instances, are openly bent. However, kinking has not been found. Twins are randomly oriented from grain to grain. In areas of monomineralic sphalerite grains have straight to serrate boundaries and near 120° dihedral angles (Figure 5.8b). Grain boundary bulging is widespread in sphalerite and it overgrows both pyrrhotite and galena (Figure 5.8c). Euhedral, twinned sphalerite is a common, fine-grained phase that occurs interstitial to pyrite which overgrows it (Figure 5.8d). Locally, sphalerite grains contain inclusion of chalcopyrite (Figure 5.8b). In several instances these chalcopyrite inclusions cut growth twins in the sphalerite.

5.3.4 Galena textures

5.3.4.1 Brittle deformation textures in galena

Galena displays only minor brittle deformation related to post-F_2 fracturing.

5.3.4.2 Plastic deformation textures in galena

Plastic deformation textures were not found in galena.

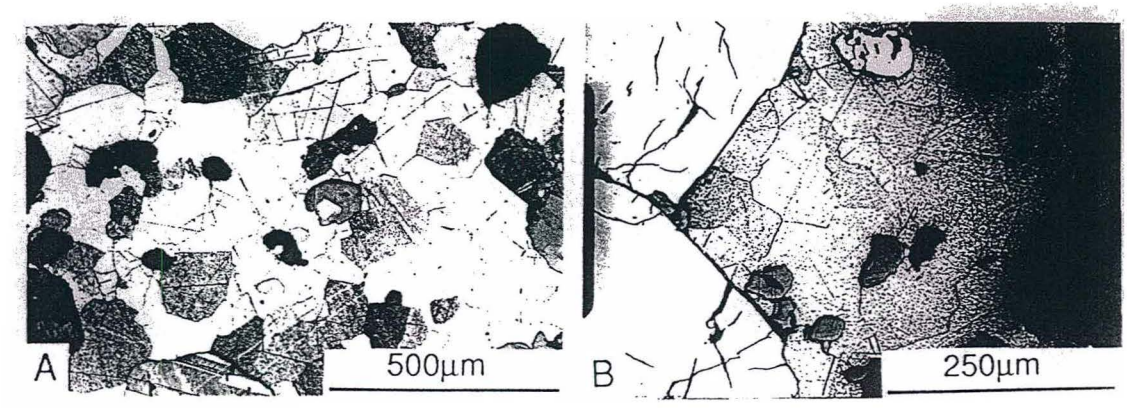

Figure 5.9. *Textures in galena. A) Euhedral, annealed galena with 120° dihedral angles. Sample 91-76. PPL. B) Euhedral, annealed galena (medium grey) adjacent euhedral pyrite (light grey). Sample 91-76. PPL.*

5.3.4.3 Annealing and growth textures in galena

Throughout the orebody galena occurs either as well annealed grains (Table 5.3) or as anhedral grains being overgrown by another phase. Galena forms subhedral to euhedral grains and, in monomineralic areas, galena generally has straight grain boundaries with approximately 120° dihedral angles (Figure 5.9a/b). Galena displays only minor grain boundary bulging, generally into other galena porphyroblasts although it does overgrow sphalerite locally (e.g. Figure 5.4e).

5.4. Deformation textures in magnetite, quartz and barite

5.4.1 *Magnetite*

Magnetite is a common phase in all lithofacies except the ribbon-banded, pyritic quartzite. It is a major phase in the pyritic quartzite (Table 5.2). Magnetite, in all lithofacies in which it is found, occurs as anhedral grains with highly corroded, deeply embayed grain boundaries (Figure 5.10a). Magnetite is commonly association with quartz which extensively replaces it along cleavage planes and along

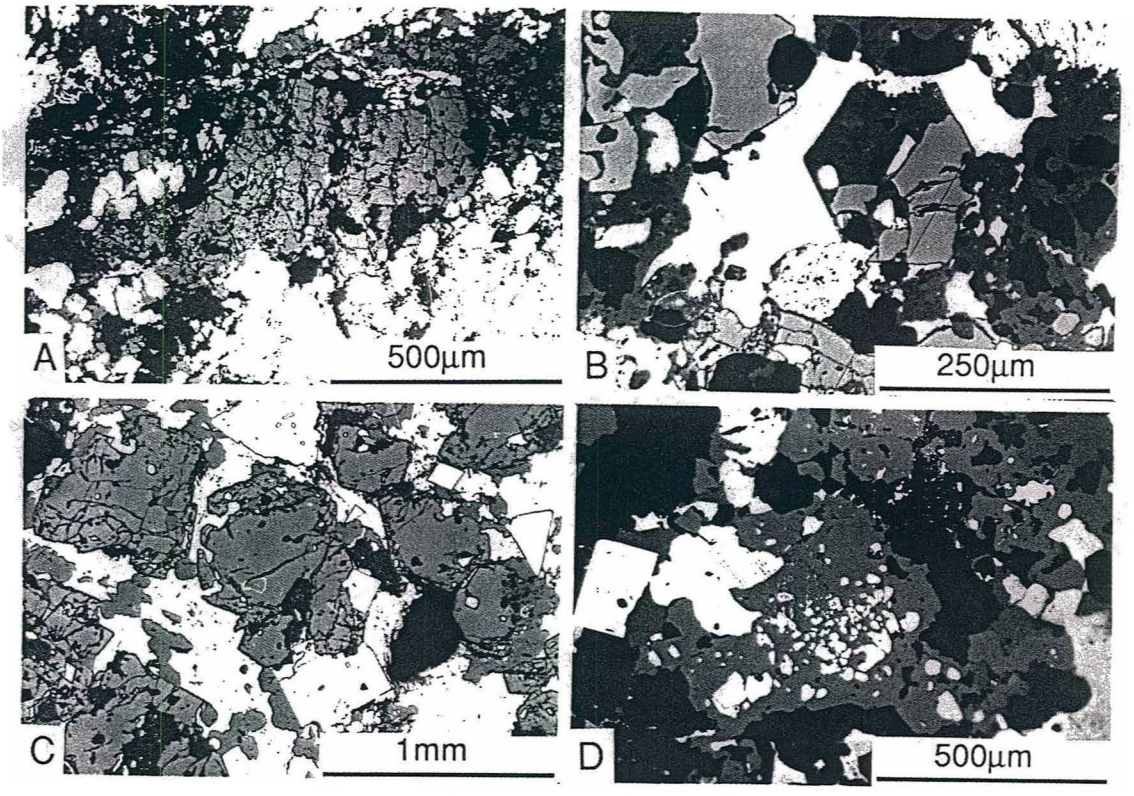

Figure 5.10. *Textures in magnetite. A) Highly corroded magnetite (dark grey) porphyroclast being replaced by quartz (black). Sample ps1507. PPL B) Quartz (black) psuedomorphing euhedral magnetite (medium grey). Sample 91-88. PPL. C) Euhedral magnetite overgrowths on corroded magnetite cores. Note that magnetite (dark grey) is overgrowing pyrrhotite (medium grey) and pyrite (light grey) is overgrowing magnetite. Sample 91-89. PPL. D) Pyrite (light grey) and pyrrhotite (medium grey) inclusions in a magnetite porphyroblast. Sample 90-146. PPL.*

the corroded and embayed grain boundaries (Figure 5.10a). Fine-grained euhedral magnetite also occurs. Locally, these euhedral grains are partially psuedomorphed by quartz (Figure 5.10b) or they have euhedral overgrowths on equant cores (Figure 5.10c). Magnetite commonly overgrows and includes pyrite and pyrrhotite (Figure 5.10d).

5.4.2 Quartz

Thin sections were examined to determine the textures in quartz. Quartz in all lithofacies generally forms equant to slightly elongate grains with undulose extinction (Figure 5.11a). In the pyrrhotite + sphalerite + galena massive sulphides and the baritic massive sulphides quartz more often occurs as equant grains in anhedral to rounded to asymmetric polycrystalline quartz clasts. In several areas in the ribbon-banded, carbonaceous quartzite and the pyritic quartzite quartz has a preferred grain shape orientation parallel to the S_2 foliation (Figure 5.11b). Pressure solution, although not widespread, does occur in narrow, anastomosing zones in these two lithofacies. In these areas of high strain, fine-grained euhedral strain-free quartz grains occur along the grain boundaries of deformed quartz grains suggesting grain boundary recrystallisation.

5.4.3 Barite

Barite occurs predominately in the baritic lithofacies but is also found in the pyritic quartzite and the pyrrhotite + sphalerite + galena massive sulphides. In the latter it almost always occurs as anhedral grains in equant to elongate to asymmetric polycrystalline clasts. In the baritic massive sulphides and the pyritic quartzites barite forms equant to anhedral to slightly elongate grains with undulose extinction (Figure 5.12a). Locally, fine-grained, equant, strain-free barite grains occur along the

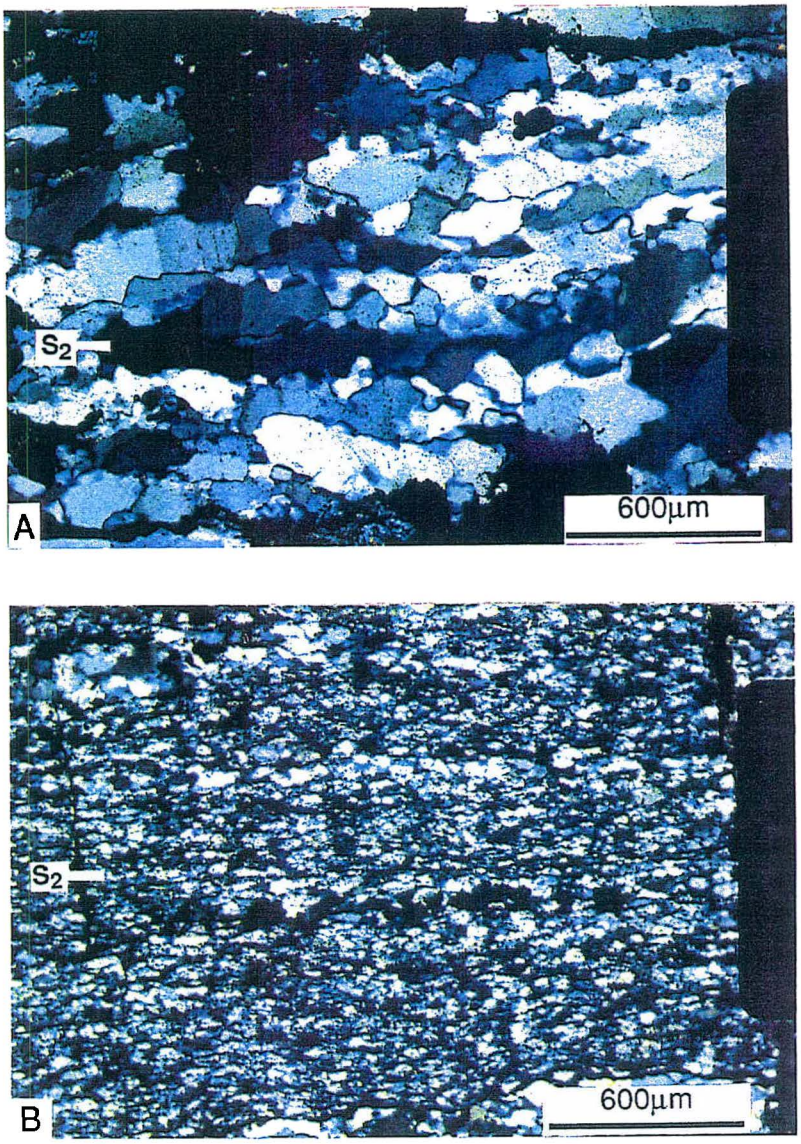

Figure 5.11. *Photomicrographs of deformation textures in quartz. A) Preferred grain shape orienatation in quartz grains defining the S_2 cleavage. B) Fine grained, recrystallised quartz in well foliated phyllite.*

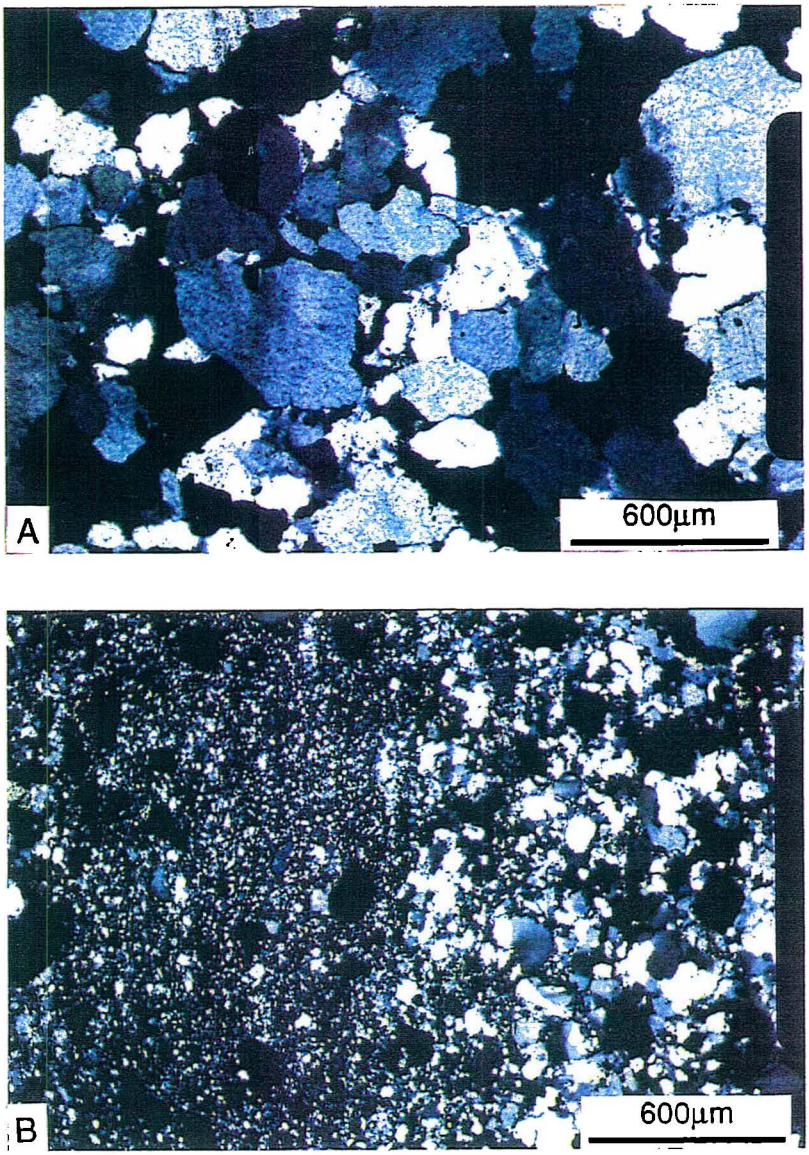

Figure 5.12. *Photomicrographs of deformation textures in barite. A) Weakly deformed, equant barite grains with undulose extinction. B) Strain gradient in baritic massive sulphides with equant to rounded barite grains.*

boundaries of strongly deformed grains as a result of grain boundary recrystallisation. Rarely, barite has a weakly developed preferred grain shape orientation suggesting pressure solution may have been active (Figure 5.12b).

5.5 Distribution of microtextures in the orebody

As discussed in Chapter 4, the Vangorda orebody is tightly folded with high strain zones developed along the limbs of the folds, in the fold cores, parallel to the axial surface and near the upper contact with the thick pyritic quartzite unit in the footwall (see Section 4.5). The location and type of structures developed in the Vangorda orebody indicate a high degree of strain partitioning into areas of high stress. This section describes the microscale deformation textures found in different structural positions within the Vangorda orebody.

The shear zones developed along the limbs of folds are marked by an increase in the abundance of pyrrhotite and sphalerite and extreme grain size reduction (Figure 5.13, 5.14, 5.15 and 5.16). Pyrite porphyroclasts, quartz, barite, carbonate and phyllite clasts are equant to asymmetric and often elongate (Figure 5.13a/f; 5.15e). Clasts, inclusions and porphyroclasts have moderately to well-developed tails and pressure shadows of pyrrhotite, sphalerite, galena of chalcopyrite are developed (Figure 5.13f). Massive pyrite in the shear zone generally has a moderately developed grain-shape preferred orientation (Figure 5.14a). A foliation defined by elongate pyrrhotite, quartz and barite clasts is common. Along the edges of the shear zones fracturing is strongly developed and the fractures are infilled by pyrrhotite, sphalerite, galena and chalcopyrite and locally marcasite (Figure 5.14b).

Baritic massive sulphides in the limbs of the folds is often highly sheared (Figure 5.14e/f; 5.15a). It is marked by extreme grain size reduction, development of

asymmetric, symmetric and elongate clasts with tails and pressure shadows and commonly a well-developed shear foliation, often over a distance of a few centimetres (Figure 5.16). This is generally accompanied by an increase in the abundance of pyrrhotite.

The upper contact of the pyritic quartzite in the footwall of the orebody is and the sulphides structurally above is strongly fractured and sheared (Figure 5.13h; 5.15b/e). Fractures are infilled by pyrrhotite, sphalerite, galena and chalcopyrite. Shearing along the contact is manifested by the development of the pyrrhotite +

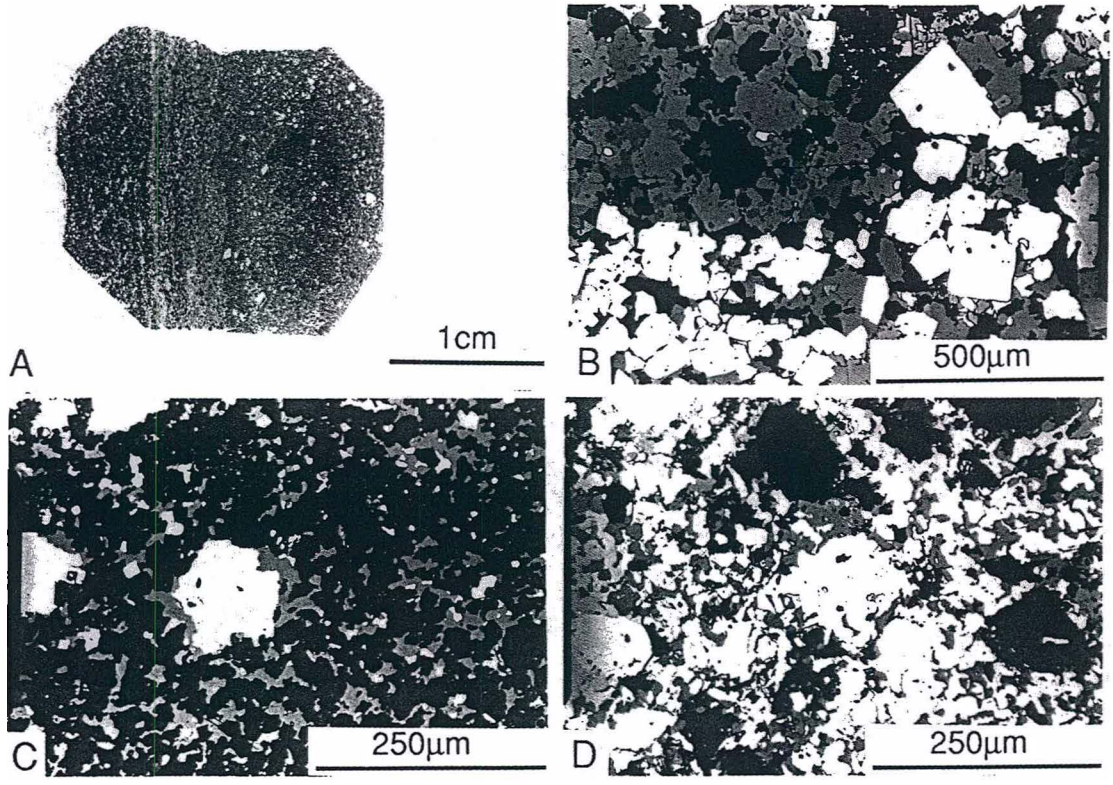

Figure 5.16. *Strain gradient in sheared baritic massive sulphide lithofacies. A) Photograph of the polished block. Note the sharp boundaries and rounded clasts. Sample 91-130. B) Coarse grained, euhedral pyrite (light grey) with few inclusions, sphalerite (medium grey) and barite + quartz (black). This is relatively unsheared. PPL. C) With an increase in strain the grain size has been significantly reduced and pressure shadows of sphalerite are forming on rounded pyrite. Pyrrhotite (medium grey) content is increased. PPL. D) With a further increase in strain the grain size has been reduced even more, pyrrhotite (medium grey) has become a major phase and pyrite is rounded and inclusion-rich. PPL.*

sphalerite + galena massive sulphides. As in the limb and core position of the folds this shear zones have well-developed asymmetric, symmetric and elongate porphyroclasts and inclusions with tails and pressure shadows (Figure 5.15e). The fracturing and shearing is widespread in footwall pyritic quartzite (Figure 5.13d/h; 5.14g/h). Mesoscale fracturing is ubiquitous (see Figure 4.26a). The S_1 and S_2 cleavages are moderately to well-developed (Figure 5.15f).

The hinge zones of the folds are typified by medium to coarse grained, subhedral to euhedral porphyroblasts of pyrite (Figure 5.13b). Pressure solution, although not common, is also developed. Fracturing increases in intensity from the hinge zone to the limb position culminating in the highly fractured areas adjacent to the shear zones. Fractures in all positions are infilled by pyrrhotite, sphalerite, galena and chalcopyrite and locally marcasite.

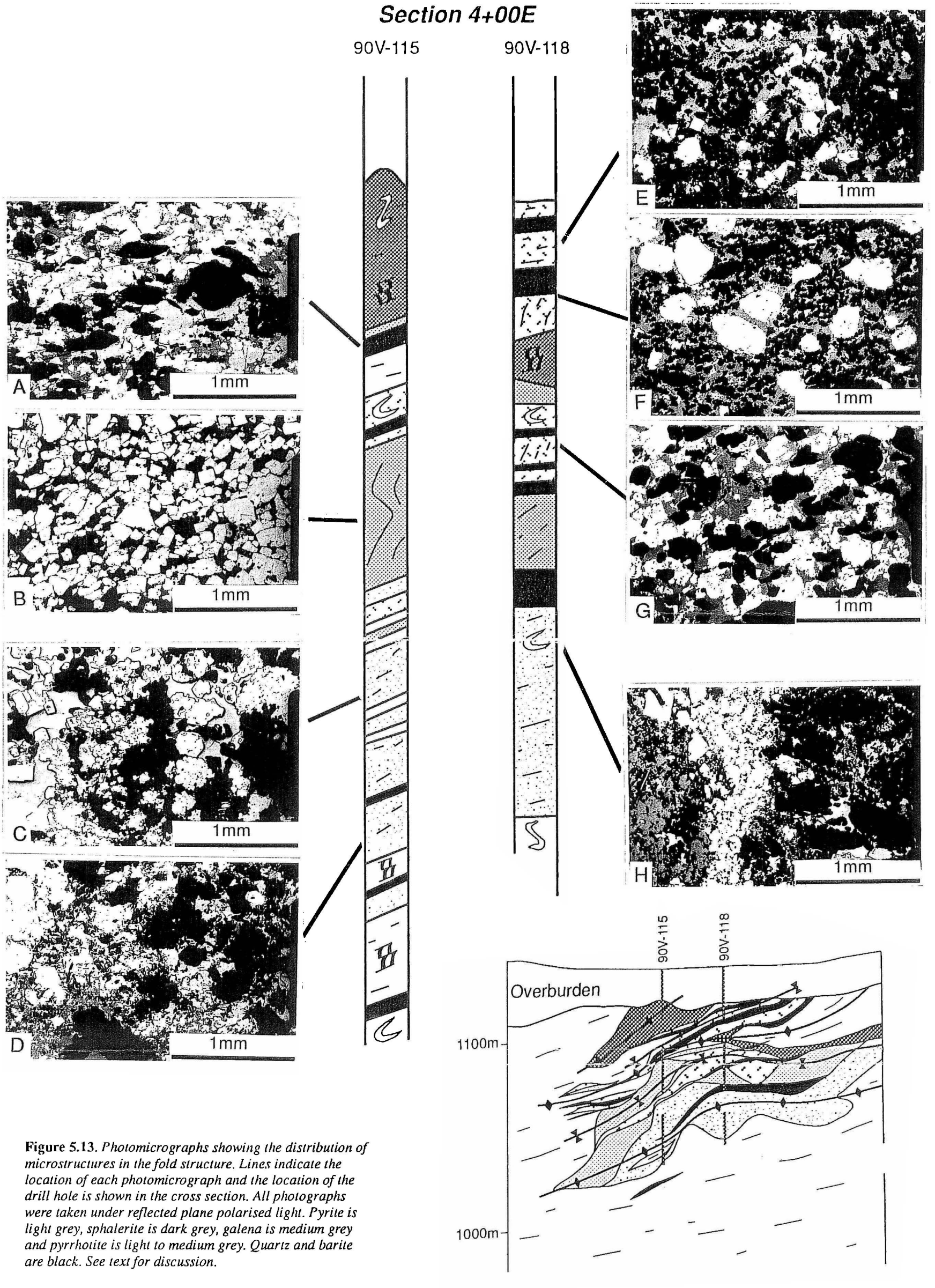

Figure 5.13. *Photomicrographs showing the distribution of microstructures in the fold structure. Lines indicate the location of each photomicrograph and the location of the drill hole is shown in the cross section. All photographs were taken under reflected plane polarised light. Pyrite is light grey, sphalerite is dark grey, galena is medium grey and pyrrhotite is light to medium grey. Quartz and barite are black. See text for discussion.*

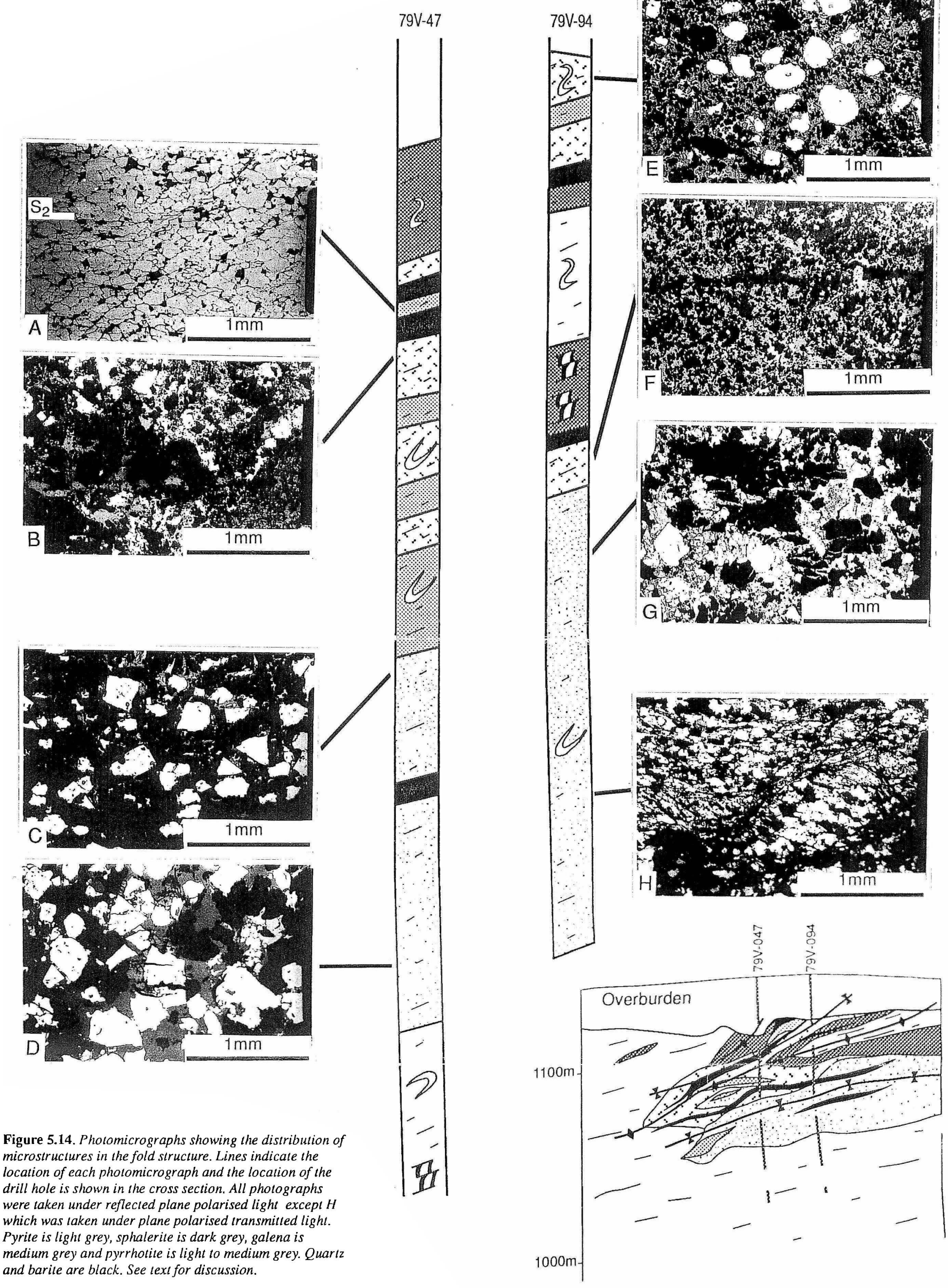

Figure 5.14. *Photomicrographs showing the distribution of microstructures in the fold structure. Lines indicate the location of each photomicrograph and the location of the drill hole is shown in the cross section. All photographs were taken under reflected plane polarised light except H which was taken under plane polarised transmitted light. Pyrite is light grey, sphalerite is dark grey, galena is medium grey and pyrrhotite is light to medium grey. Quartz and barite are black. See text for discussion.*

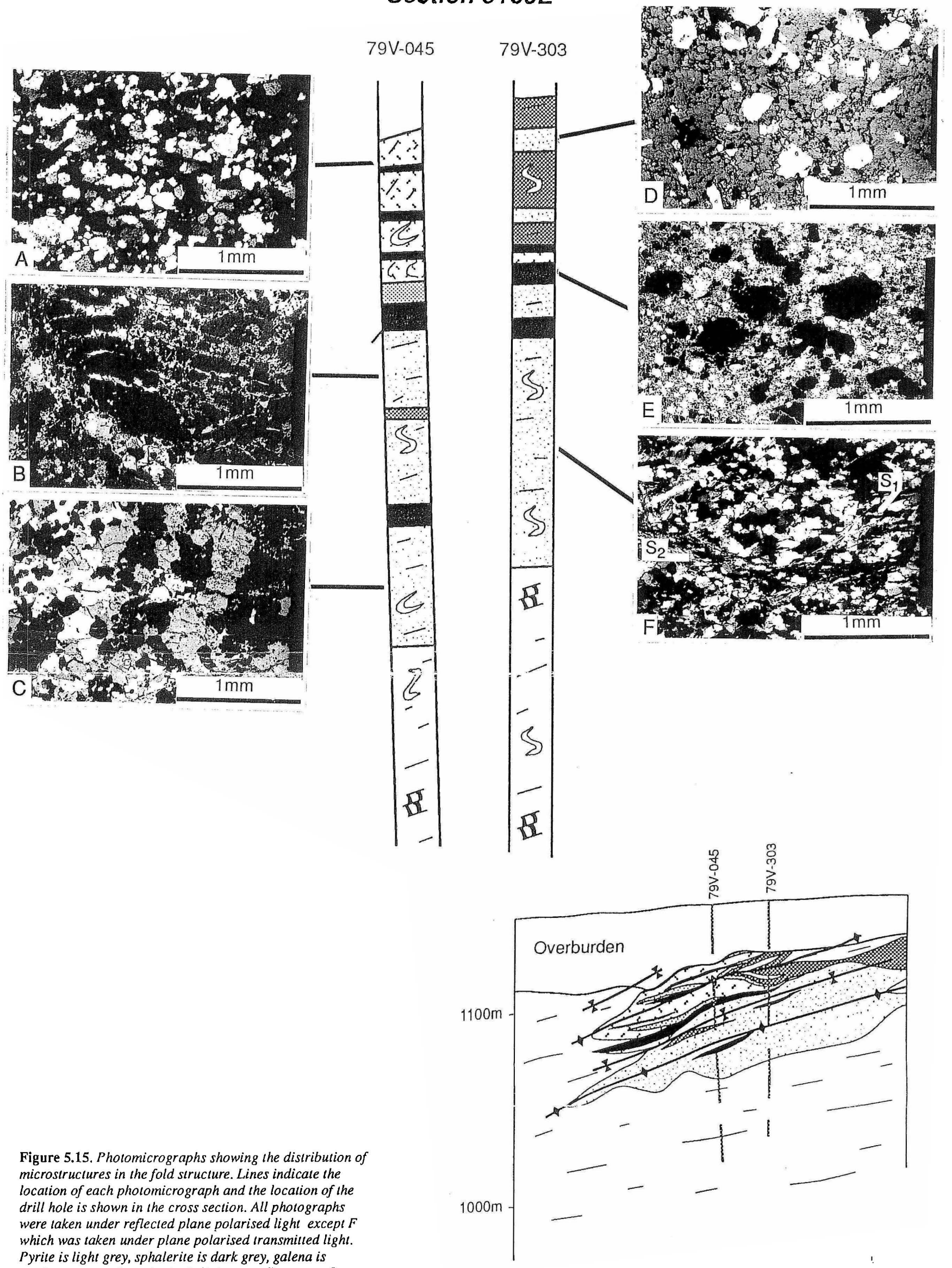

Figure 5.15. *Photomicrographs showing the distribution of microstructures in the fold structure. Lines indicate the location of each photomicrograph and the location of the drill hole is shown in the cross section. All photographs were taken under reflected plane polarised light except F which was taken under plane polarised transmitted light. Pyrite is light grey, sphalerite is dark grey, galena is medium grey and pyrrhotite is light to medium grey. Quartz and barite are black. See text for discussion.*

CHAPTER 6

Thermobarometry of Vangorda orebody sulphides and phyllites

6.1 Introduction

The Vangorda orebody has been metamorphosed by the regional M_1 and M_2 discussed in section 2.2.3.3. Based on the M_2 indicator mineral assemblage of muscovite + chlorite + quartz the in the phyllites hosting the orebody the metamorphic grade has been interpreted to be lower greenschist facies (Tempelman-Kluit 1972). Quantitative analysis of the temperature and pressure conditions of metamorphism of the Anvil District orebodies has been confined to limited sphalerite barometry which indicates pressures on the order of 3 kb. (e.g. Kuo 1976). This thesis is the first comprehensive quantitative investigation of the temperature and pressure conditions of metamorphism of the Vangorda orebody.

The absence of appropriate mineral assemblages for thermobarometry in the phyllites hosting the Vangorda orebody has made quantitative temperature and pressure estimates difficult to carry out. However, calibrations of site occupancy in chlorite as a function of temperature (Cathelineau & Nieva 1985; Cathelineau 1988) has partially alleviated that problem. These authors have calculated chlorite site occupancy in hydrothermal systems and have suggested that their calculations (Appendix 2) can be extrapolated to low temperature and low pressure metamorphic environments.

In recent years there have been several calibrations of the pressure-temperature response of sulphide ores in hydrothermal systems and metamorphic terranes (see Appendix 2). These have incorporated both an empirical approach (e.g. Hutchison & Scott 1981) and a more rigorous thermodynamic approach (e.g. Bryndzia *et al.* 1988,

1990). Both these approaches have stemmed from a significant amount of research into the Fe - Zn - Cu - As - S systems (e.g. Toulmin & Barton 1964; Barton & Toulmin 1966; Barton 1969; Scott & Barnes 1971; Craig & Scott 1974; Rau 1976; Kretchmar & Scott 1976, Hutchison & Scott 1981; Scott 1983; Sharp *et al.* 1985; Bryndzia *et al.* 1988). However, sulphides, because of their highly nonrefractive nature, remain an elusive indicator of hydrothermal and metamorphic pressure and temperature conditions, requiring careful petrographic analysis and cautious application of quantitative analysis to thermobarometric applications.

This chapter examines the metamorphic conditions that have affected the orebody using chlorite thermometry and sulphide thermobarometry. All microprobe data are summarised in this chapter but are given in full in Appendix 3. Sample numbers are given and sample locations are provided in Appendix 1. Temperatures and pressures, are calculated using several calibrations to cross-check and compare the calculations. The results of the calculations are summarised in this chapter but all the individual results are provided in Appendix 4. The equations used and their source are given in Appendix 2.

6.2 Thermobarometry

6.2.1 Microprobe Operating conditions

All data were acquired by wave-length dispersive analysis using a Cameca SX50 automated electron microprobe at the University of Oviedo, Spain. Chlorite analysis were carried out using a natural standard, a beam current of 15nA, an accelerating voltage of 20 kV and a count time of 15 s. Sulphide analysis were carried out using synthetic pyrite, sphalerite, pyrrhotite, and arsenopyrite standards, a beam current of 30 nA, an accelerating voltage of 20 kV and a count time of 15 s. Data was corrected using ZAF corrections.

6.2.2 Chlorite thermometry

Chlorite thermometry was carried out on phyllite from the Mount Mye formation. hosting the Vangorda orebody in an attempt to determine if a temperature difference could be found between M_1 and M_2. For this purpose samples were probed in which there was within-lithon, generally blocky, 0.25 to 1.0 mm S_1 chlorite and acicular to prismatic, 0.2 to 0.75 mm chlorite lying along the S_2 crenulation cleavage (Figure 6.1a). Temperature estimates were calculated using the empirical equation derived by Cathelineau (1988).

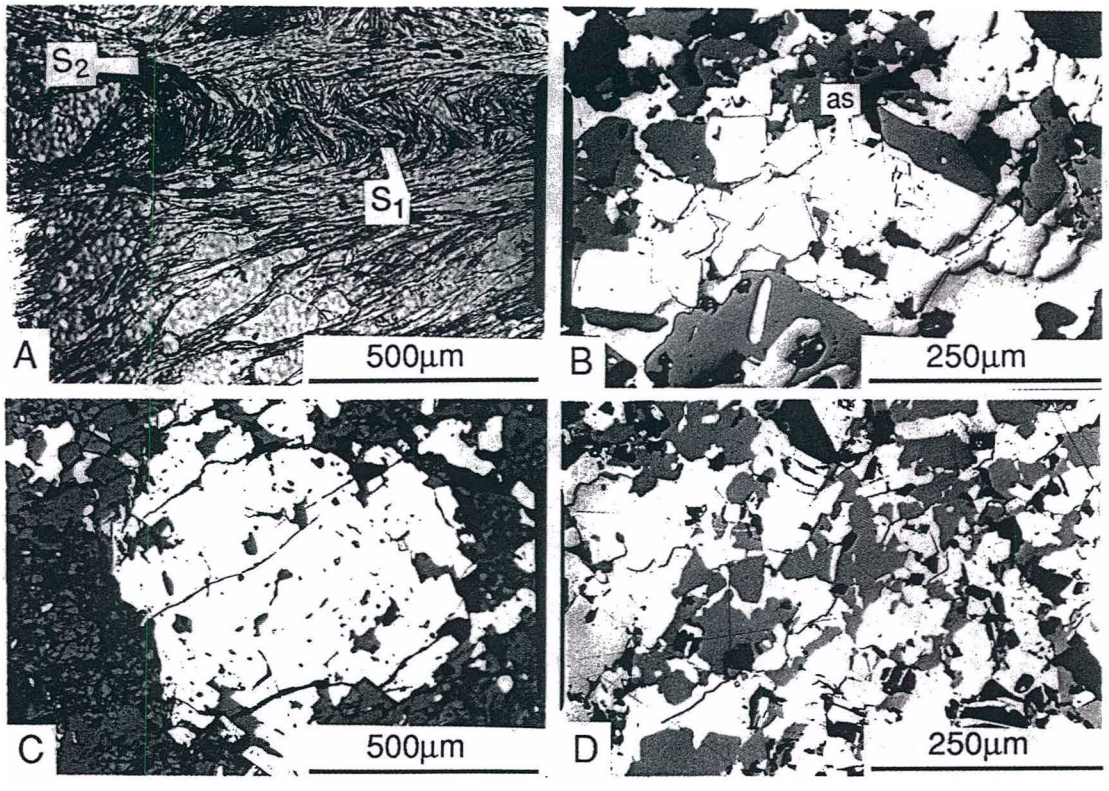

Figure 6.1. *A) Photomicrograph of chlorite defining the S_1 and S_2 cleavages. Plane polarised light. B) Photomicrograph of arsenopyrite porphyroblasts coexisting with pyrite and pyrrhotite. C) Photomicrograph of sphalerite inclusions in a M_2 pyrite porphyroblast. D) Photomicrograph of coexisting M_2 sphalerite and hexagonal pyrrhotite.*

All chlorite analysed plot within the relatively Al-poor chlorite field (Figure 6.2). Chlorite in lithons (i.e. defining S_1) have a mean tetrahedral site $Al_{(IV)}$ occupancy of 1.29 ($2\sigma = \pm 0.08$), corresponding to a mean temperature of 355 °C ($2\sigma = \pm 27$ °C) (Table 6.1). Chlorite defining the S_2 cleavage have a mean tetrahedral site $Al_{(IV)}$ occupancy of 1.34 ($2\sigma = \pm 0.06$), corresponding to a mean temperature of 372 °C ($2\sigma = \pm 18$°C) (Table 6.1).

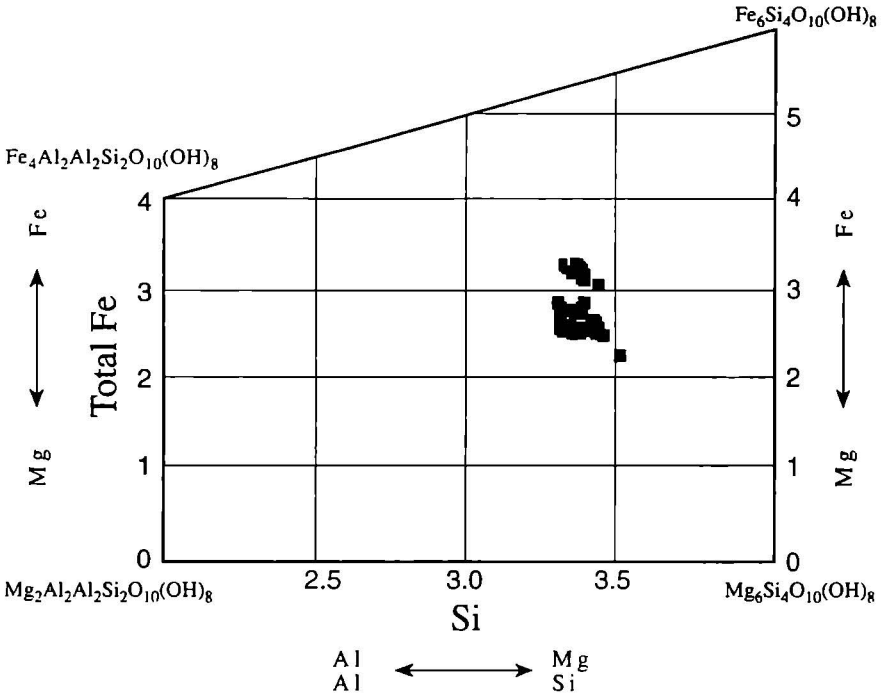

Figure 6.2. *Vangorda chlorite plotted in chlorite composition space.*

6.2.3 Arsenopyrite thermometry

Arsenopyrite is a minor phase in the Vangorda ores where it forms subhedral to euhedral, 0.01 to 0.1 mm grains in grain-grain contact with pyrite and/or pyrrhotite (Figure 6.1b) which provides an effective assemblage to buffer S_2 (Barton 1969). In several instances arsenopyrite forms overgrowths on pyrite. In these instances, however, there is no increase in the As content in pyrite adjacent to the overgrowth. All the arsenopyrite analysed for this study have a consistent mean composition (Figure 6.3) of 30.56 ($2\sigma = \pm 0.31$) atomic % As (Table 6.2). Core - rim analysis

Table 6.1. Representative chlorite analyses and compositions.

	90-28 b1-a1	90-28 b1-c1	90-28 b1-f1	90-110 a1-a2	90-128 b2-d2	90-28 b2-d1	90-128 c1-a1	90-128 c1-f1
wt. %	S_1	S_1	S_1	S_1	S_2	S_2	S_2	S_2
SiO_2	23.73	24.50	23.72	23.73	24.17	24.11	23.97	23.92
Al_2O_3	19.84	19.53	20.59	21.70	19.48	19.90	22.00	21.55
TiO_2	0.07	0.05	0.00	0.05	0.03	0.00	0.02	0.06
FeO	35.65	34.82	35.14	30.91	35.27	34.81	29.04	29.19
MnO	1.86	1.67	2.02	0.59	1.69	1.55	0.27	0.27
MgO	7.32	7.79	7.12	11.09	7.61	7.76	12.33	12.47
CaO	0.02	0.10	0.00	0.04	0.01	0.00	0.05	0.00
Na_2O	0.00	0.01	0.01	0.03	0.01	0.00	0.02	0.00
K_2O	0.04	0.02	0.03	0.00	0.02	0.00	0.04	0.00
Sum	88.53	88.49	88.63	88.14	88.29	88.13	87.78	86.38
Si_{IV}	2.66	2.73	2.64	2.58	2.70	2.69	2.58	2.59
Al_{IV}	1.34	1.27	1.36	1.42	1.30	1.31	1.42	1.41
T - site	4.00	4.00	4.00	4.00	4.00	4.00	4.00	4.00
Al_{VI}	1.28	1.28	1.35	1.36	1.27	1.31	1.38	1.34
Ti	0.01	0.00	0.00	0.00	0.00	0.00	0.00	0.01
Fe	3.34	3.24	3.28	2.81	3.30	3.25	2.62	2.64
Mn	0.18	0.16	0.19	0.05	0.16	0.15	0.03	0.02
Mg	1.22	1.29	1.18	1.80	1.27	1.29	1.98	2.01
Ca	0.00	0.01	0.00	0.00	0.00	0.00	0.01	0.00
Na	0.00	0.00	0.00	0.00	0.00	0.00	0.00	0.00
K	0.01	0.00	0.00	0.01	0.00	0.00	0.01	0.00
O - site	6.03	5.99	6.01	6.03	6.01	6.00	6.02	6.03
O	9.94	9.94	9.95	9.93	9.92	9.91	9.91	9.88
OH	8.06	8.06	8.05	8.07	8.08	8.09	8.09	8.12

General formula $(Fe_{2.83}Mg_{1.71}Al_{1.34}Mn_{0.07}Ti_{0.01})[(Al_{1.31}Si_{2.68})O_{9.95}](OH_{8.04})$

S_1 Tet. Al_{IV}	1.29 (2σ = +/- 0.08)	n = 27
S_2 Tet. Al_{IV}	1.34 (2σ = +/- 0.06)	n = 29
S_1 T (°C)	355 (2σ = +/- 27)	
S_2 T (°C)	372 (2σ = +/- 18)	
Mean T (°C)	363 (2σ = +/- 24)	n = 56

and grain traverses show no appreciable variation in composition across grains that results in large temperature differences (Table 6.2). Minor element concentration is at the minimum detection limit of the microprobe.

Table 6.2. Representative arsenopyrite analyses.

At. %	90-125 a1-as1 core	90-125 a1-as2 rim	90-125 a1-as3 core	90-125 a1-as4 rim	90-131 b1-as1 core	90-131 b1-as2 rim	90-131 b1-as3 core	90-131 b1-as4 rim	90-131 b1-as10 core	90-131 b1-as11 rim
As	31.17	31.03	30.28	30.50	29.11	30.77	30.09	30.60	30.21	30.50
Fe	34.06	33.72	34.08	33.96	34.45	34.35	34.13	33.92	33.99	34.06
S	34.72	35.14	35.47	35.47	36.40	34.74	35.68	35.41	35.60	35.32
Sum	99.95	99.89	99.83	99.93	99.96	99.86	99.80	99.93	99.80	99.88

At. % As	30.60 (2σ = +/- 0.0.30)	n = 46
log f S_2	-8.99 (2σ + +/- -0.55)	
Mean T (°C)	336 (2σ = +/- 20)	

Arsenopyrite temperatures calculated using the po - asp + py buffering curve (Kretschmar & Scott 1976) are consistent with $Al_{(IV)}$ temperatures in chlorite, with a mean of 336 °C ($2\sigma = \pm$ 20 °C) (Figure 6.4a) and show no differences related to the buffering assemblage or phase. Mean log fS_2 values of -8.99 ($2\sigma = \pm$ -0.55) (Table 6.2) are obtained using the po - asp + py sulfidation curve of Barton (1969) at 336 °C. However, the fS_2 calculated using the pyrrhotite-indicator method of Toulmin & Barton (1964) for pyrrhotite of composition $Fe_{0.93}S$ co-existing with arsenopyrite, by both their equation and that of Rau (1976) gives a mean log fS_2 values of -7.54

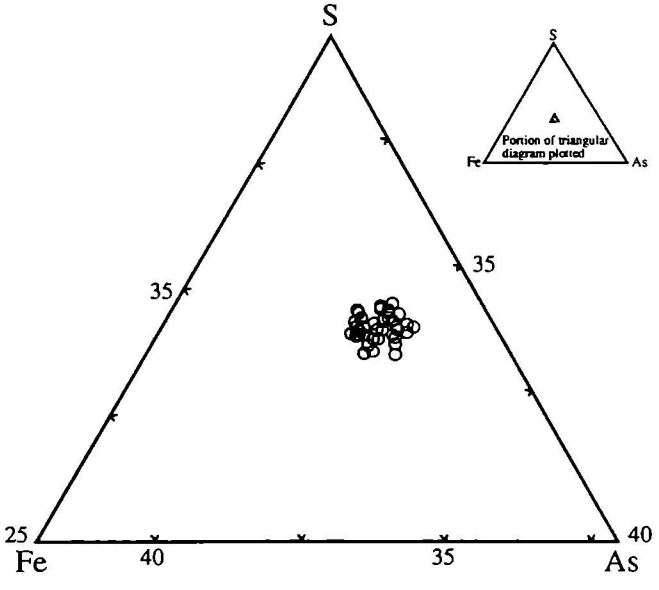

Figure 6.3. *Ternary Fe-As-S diagram showing the composition of Vangorda arsenopyrite.*

($2\sigma = \pm$ -0.84) and -7.34 ($2\sigma = \pm$ -0.78), respectively. These latter fugacities are more than one log unit less than that estimated for arsenopyrite and outside the stability range of arsenopyrite in the Fe-As-S system (Figure 6.4b).

Kretschmar & Scott (1976) point out that proper application of arsenopyrite thermometry requires an estimate of $a\ S_2$. Activity of S_2 at 336 °C (the mean arsenopyrite temperature) was calculated using the equation of Rau (1976) to have a mean log $a\ S_2$ -3.67 ($2\sigma = \pm$ -0.41); again outside the stability field of arsenopyrite (Figure 6.4b).

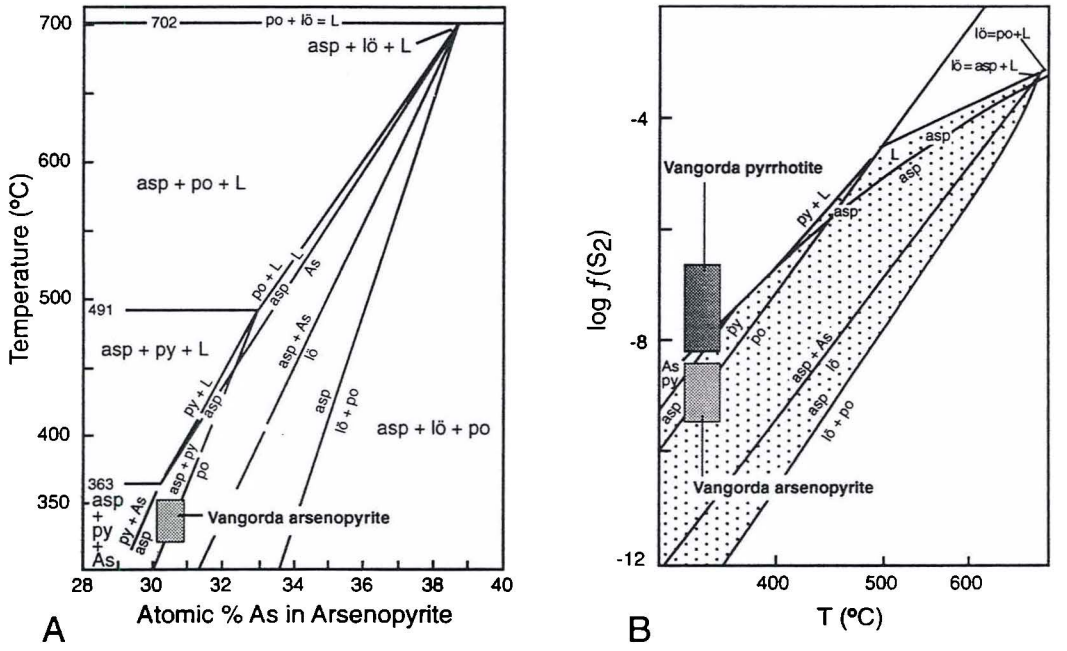

Figure 6.4. *A) Position of the Vangorda arsenopyrite on a T-X diagram. Buffering curves are from Kretschmar & Scott (1976). The edges of the grey box represent 2σ for both X_{as} and T. B) Position of the Vangorda arsenopyrite and coexisting hexagonal pyrrhotite on the sulfidation curves in the Fe-As-S system (after Barton 1969). The stability field of arsenopyrite is shaded. Log fS_2 in pyrrhotite was calculated using a mean temperature of 336 °C at 1 bar. Edges of the box represent 2σ.*

6.2.4 Sphalerite, hexagonal pyrrhotite (+ pyrite) barometry

Sphalerite was analysed in two different textural relationships; as inclusions in pyrite using the sphalerite + hexagonal pyrrhotite + pyrite barometer (Hutchison and Scott

Table 6.3. Representative analyses of sphalerite inclusions in pyrite.

At %	90-132 a1sp8 1	90-132 a2sp2 2	90-132 a2sp1 3	90-132 a2sp6 4	90-129 b2as2 5	90-129 b2as3 6	90-129 b2as4 7	90-129 b2bs1 8	90-129 b2bs2 9	90-129 b2cs1 10
Fe	9.22	10.06	9.27	8.60	8.91	6.01	5.66	7.85	5.40	9.21
Zn	40.74	39.51	41.75	42.23	42.19	44.69	44.69	42.82	45.06	41.05
S	50.01	50.41	48.90	49.09	48.90	49.22	49.62	49.24	49.47	49.73
Sum	99.97	99.98	99.93	99.92	100.00	99.92	99.97	99.91	99.93	99.99

Mol% FeS 15.62 (2σ = +/- 2.78) n = 24

P (kb) 3.98 (2σ = +/- 2.68)[1]

[1] Equation of Hutchison and Scott (1981)

1981) and coexisting with hexagonal pyrrhotite using the sphalerite + hexagonal pyrrhotite barometer (Bryndzia *et al.* 1988, 1990). The only locations in which the correct mineral assemblages were found was D_2 sulphide shear zones along the limbs of F_2 folds (see Figure 4.27). The minor element composition of all sphalerite analysed, including copper, is negligible (Appendix 3).

Sphalerite inclusions in pyrite are generally 0.01 mm to 0.03 mm sized grains totally encapsulated by subhedral to euhedral pyrite (Figure 6.1c). Pyrrhotite inclusions accompanying sphalerite were not found. However, sphalerite inclusions were selected in which pyrrhotite was in contact with the pyrite porphyroblast and in which pyrrhotite formed a significant proportion of the sample. These sphalerite grains have a mean mol% FeS of 15.62 ($2\sigma = \pm 2.87$) (Table 6.3) corresponding to a mean pressure of 3.98 kb ($2\sigma = \pm 2.7$) (Table 6.3).

Sphalerite + hexagonal pyrrhotite occur together in shear zones within the massive sulphide body as 0.02 to 0.1 mm subhedral to euhedral grains (Figure 6.1d) commonly accompanied by galena. Locally, rare, fine-grained, retrograde equant to euhedral pyrite occurs but was avoided in these analyses. Chalcopyrite is rare in these

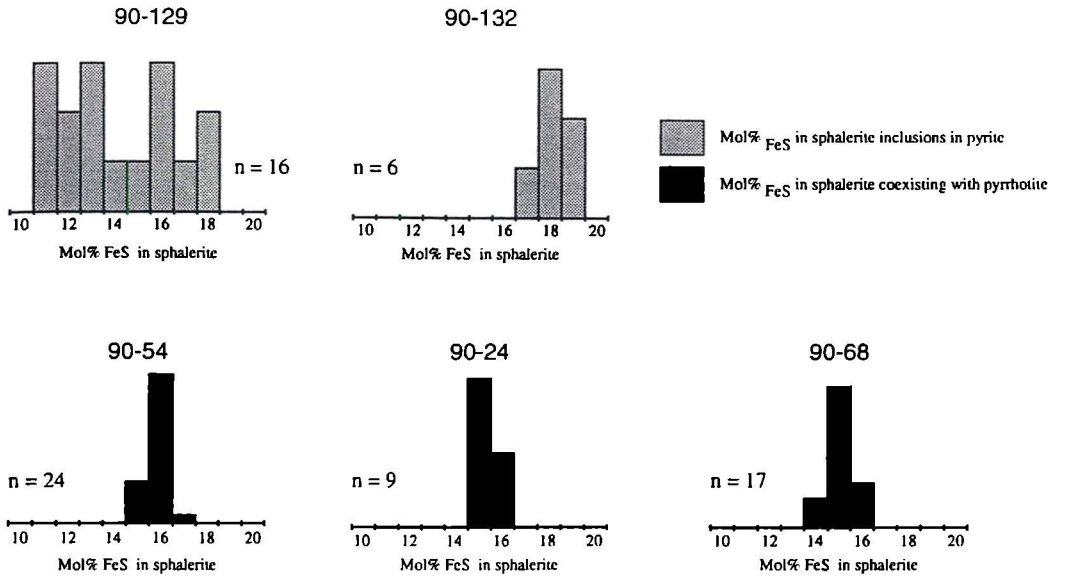

Figure 6.5. *Mole% FeS in sphalerite as inclusions in pyrite and sphalerite coexisting with hexagonal pyrrhotite.*

shear zones and in general does not form an exsolved phase in sphalerite and so is easily avoided. Etched pyrrhotite grains locally have thin overgrowths to which a magnetitic colloid does not readily adhere suggesting they may be non-magnetic monoclinic pyrrhotite (c.f. Scott 1974). To avoid any possibility of the monoclinic phase only pyrrhotite cores were analysed.

Pyrrhotite grains in the D_2 shear zones have a mean composition of $Fe_{0.94}S$ (Table 6.4) and coexist with sphalerite with a mean mole % FeS of 15.75 ($2\sigma = \pm 0.63$) (Figure 6.6). The activity of FeS was calculated at 363 °C to be 0.53 ($2\sigma = \pm 0.07$) and 0.57 ($2\sigma = \pm 0.06$) using the equations of Toulmin and Barton (1964) and Rau (1976), respectively (Table 6.4). The composition of pyrrhotite and the low a_{FeS} indicate that pyrrhotite deviates from stochiometric FeS and it lies on or near the pyrite + pyrrhotite solvus, although within the pyrite + pyrrhotite field at 5 kb (Figure 6.7). The composition of pyrrhotite and the a_{FeS} in the Vangorda orebody D_2 shear zones are at the lower limit of the values used in the experiments of Bryndzia et al. (1988). However, the absence of pyrite suggests that the assemblage is applicable to the

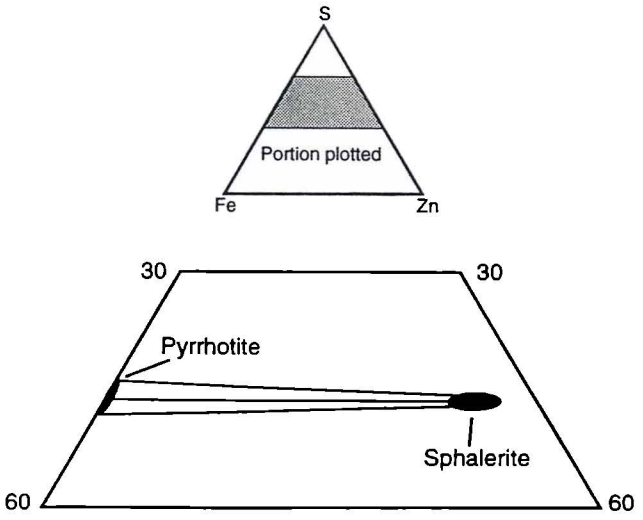

Figure 6.6. *Ternary Fe-Zn-S diagram showing the compositional field of coexisting sphalerite and coexisting hexagonal pyrrhotite in the Vangorda orebody.*

Table 6.4. Representative analyses for co-existing pyrrhotite and sphalerite pairs.

	Pyrrhotite									
At. %	90-24 b1po5	90-24 b2po18	90-24 b2po20	90-54 a1po6	90-54 a1po13	90-54 a1po19	90-54 a2po8	90-68 a2po3	90-68 a2po4	90-68 a2po16
Fe	46.92	46.95	46.98	46.96	46.83	46.85	46.94	47.12	46.77	46.97
S	52.98	53.01	52.81	52.81	52.94	53.05	52.82	52.49	53.15	52.94
Sum	99.99	99.96	99.79	99.77	99.77	99.90	99.76	99.61	99.92	99.91
	Sphalerite									
At. %	90-24 b1s1	90-24 b2s18	90-54 a1s6	90-54 a1s6	90-54 a1s12	90-54 a1s20	90-54 a2s7	90-68 a2s7	90-68 a2s23	90-68 a2s15
Fe	8.07	7.59	7.78	7.44	8.15	7.61	7.95	8.39	8.41	8.50
Zn	41.67	43.02	42.88	42.96	42.21	42.82	42.85	39.52	39.67	39.36
S	50.23	49.39	49.31	49.55	49.62	49.48	49.16	52.11	51.90	51.99
Sum	99.97	100.00	99.97	99.95	99.98	99.91	99.96	100.02	99.98	99.95

a FeS	0.53 (2σ = +/- 0.07)[1]	0.57 (2σ = +/- 0.06)[2]	n = 49
$Mol\%_{FeS}$	15.75 (2σ = +/- 0.63)		
N_{FeS}	0.94 (2σ = +/- 0.03)[1]		
γ	3.38 (2σ = +/- 0.44)[1]		
$P_{(kb)}$	6.11 (2σ = +/- 1.58)[3]		

[1] Equation of Toulmin and Barton (1964)

[2] Equation of Rau (1976)

[3] Equation of Bryndzia et al. (1988, 1990)

sphalerite + hexagonal pyrrhotite barometer.

Following Bryndzia et al. (1988, 1990) only the a_{FeS} of Toulmin and Barton (1964) was used in determining the activity coefficients. The mean activity coefficient (γ) in the sphalerite + hexagonal pyrrhotite assemblage is 3.38 ($2\sigma = + 0.443$) corresponding to a mean pressure of 6.1 kb ($2\sigma = \pm 1.58$ kb) (Table 6.4).

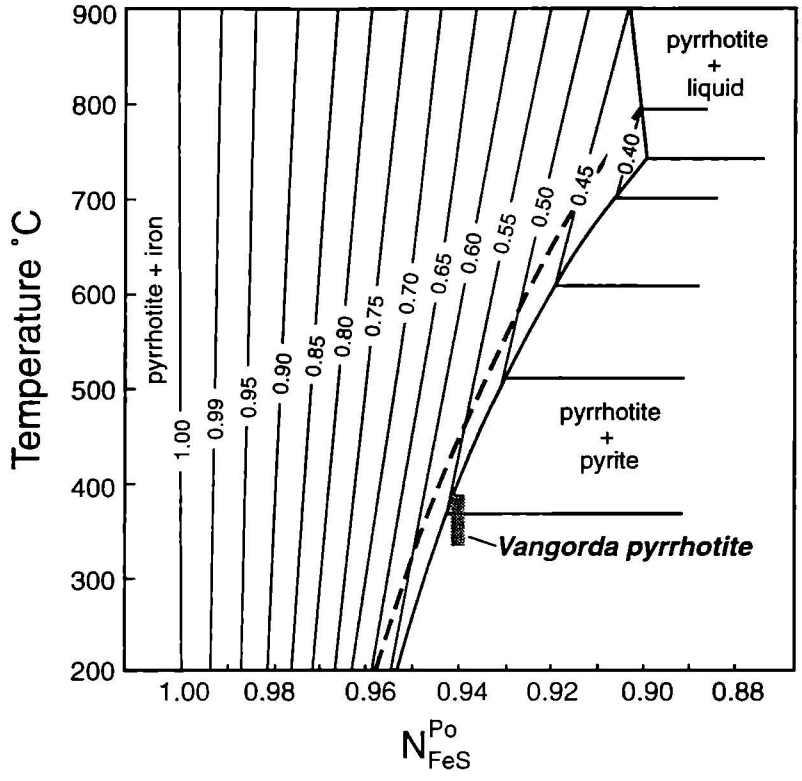

Figure 6.7. *Activity of FeS in pyrrhotite as a function of temperature and N_{FeS} and the location of the pyrite - pyrrhotite solvus at 1 bar. The thick dashed line is the pyrite - pyrrhotite solvus at 5 kb. The a $_{FeS}$ of hexagonal pyrrhotite in the D_2 shear zones in the Vangorda orebody plot within the pyrite + pyrrhotite field at 5 kb and touch the pyrite - pyrrhotite solvus at 1 bar. The edges of the grey box represent 2σ.*

CHAPTER 7

Discussion

7.1 Deformation and metamorphism of the Vangorda orebody: implications for the Anvil District

The D_2 and post-F_2 structures provide the main structural control on the geometry of the orebody and the M_2 metamorphic cycle has significantly modified any earlier textures in the sulphide minerals. The orebody is complexly folded and elongate in a northwest-southeast orientation and is cut by several major extensional faults with displacements of 10's to perhaps hundreds of metres (Figure 7.1).

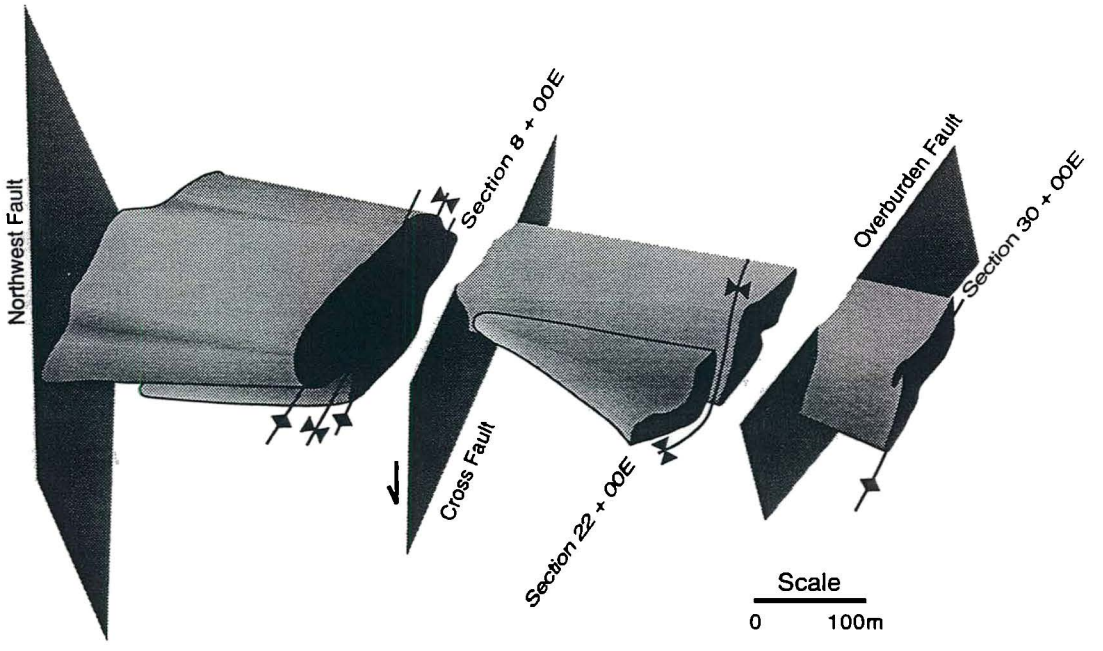

Figure 7.1. *Schematic block diagram of the Vangorda orebody showing the folded massive sulphides and their relationship with the major extensional faults.*

7.1.1 The effects of D_1 and M_1 on the orebody

This thesis has shown that the Vangorda orebody has been deformed and metamorphosed during two major deformation (D_1 and D_2) and metamorphic (M_1 and M_2) events. The peak M_1 and M_2 mineral assemblages define both the S_1 and S_2 cleavages (Section 4.3) indicating that peak metamorphism and deformation coincided during both events.

Because of the penetrative overprinting of D_1 and M_1 features the effect of these events on the Vangorda orebody could not be fully determined. However, the angular relationships between the phyllite/sulphide contact (S_0), S_1 and S_2 suggests the presence of a macroscopic D_1 structure, possibly a F_1 fold. It is not possible to further elucidate the nature or effects of D_1 other than that it resulted in the development of a penetrative S_1 cleavage in the Mount Mye and Vangorda formation phyllites and a differentiated layering in the sulphide lithofacies. S_1 in the phyllites is defined by peak M_1 mineral assemblages of quartz + muscovite $\pm$ chlorite, similar to the assemblage defining the S_2 cleavage and was possibly developed under mid-greenschist facies conditions.

7.1.2 The geometry and effects of D_2 on the orebody

7.1.2.1 Geometry of Vangorda orebody

The Vangorda orebody occurs in the hinge of a southwest-verging, northwest-plunging, macroscopic F_2 fold (Figure 4.1). The mesoscale F_2 folds that affect the orebody are shallowly downward-facing to recumbent, tight, similar folds with a wavelength of approximately 75 metres. An S_2 differentiated layering is developed only locally in the massive sulphides, along the limbs of F_2 folds and in the baritic massive sulphides in

fold hinges. However, a penetrative, F_2 axial planar S_2 crenulation cleavage and pressure solution cleavage is widespread in the host phyllites and in the ribbon-banded, carbonaceous quartzite.

Faults in the Vangorda orebody clearly displace F_2 folds and the S_2 cleavage and therefore post-date or are late D_2. Major faults (i.e. Northwest fault, Cross fault, and Sump fault) dip steeply towards the northwest or southeast and have moderate to steeply-plunging slickensides. Slickensides indicate a final oblique- to dip-slip component of movement. The lack of marker horizons make it difficult to impossible to determine the exact amount of displacement on many faults or to determine their kinematic history. The extensional faults have similar orientations and characteristics to those described elsewhere in the Anvil District as being related to unroofing of the Anvil Batholith (Jennings & Jilson 1986; Pigage 1990) and are also interpreted to be related to the unroofing event.

A post-extensional phase of strike-slip faulting strikes NE-SW and N-S. The Creek fault displaces the Northwest fault sinistrally approximately 50 metres. It is not clear if strike-slip faults are reactivated extensional faults. The strike-slip faults may also be related to unroofing of the batholith. An alternative explanation is that they are related to movement along the Tintina Fault, 25 km to the west. However, neither of these explanations can be proved because of the lack of regional exposure.

7.1.2.2 Remobilisation in the Vangorda orebody

Remobilisation is a common feature in deformed and metamorphosed massive sulphide deposits (Gilligan & Marshall 1987; Marshall & Gilligan 1993). Remobilisation in massive sulphides involves a wide range of mechanical and chemical processes acting either alone or together (Table 7.1). The processes whereby remobilisation takes places

Table 7.1 Mechanisms of mobilisation/remobilisation[1]

Solid-state "mechanical" transfer	
Cataclastic flow	
Dislocation flow	(a) Dislocation glide (b) Dislocation creep
Diffusive mass transfer	(a) Grain-boundary diffusion (b) Lattice diffusion
Grain-boundary sliding	
Liquid-state "chemical" transfer	
Solution transfer	(a) Fluid-assisted diffusion (b) Advective transfer
Magmatic transfer	
Mixed-state transfer	
Concurrent "chemical" and "mechanical" processes	

[1] Redrafted from Marshall & Gilligan (1993)

in the Vangorda orebody appears to be focused along durchbewegung zones and shear zones whose locations are controlled by the sulphide lithofacies is reflected in an array of textures (Gilligan & Marshall 1987).

The Vangorda orebody has textures such as tailed and winged clasts and inclusions (Figure 4.25), pressure solution fabrics, rootless folds, durchbewegung, and limb thinning and hinge zone thickening of folds that reflect extensive shearing and mechanical and chemical remobilisation of the orebody. The diamond drill core sections (Figure 4.27) show that hinge zone thickening has occurred in the Vangorda orebody, especially in the baritic massive sulphides. Similarly, mesoscale folds have thickened hinges and in some cases have increased sulphide concentrations in the hinge zone region (Figure 4.9d). Lenses of sulphides concordant with S_2 have penetrated into the phyllites in the hinge area (Figure 4.27, Section 4 + OOE). Remobilisation of sulphides into areas of low relative stress such as fold closures, fractures, and boudin necks has been widely documented (e.g. Pederson 1980; Maiden *et al.* 1986; Skinner & Johnson

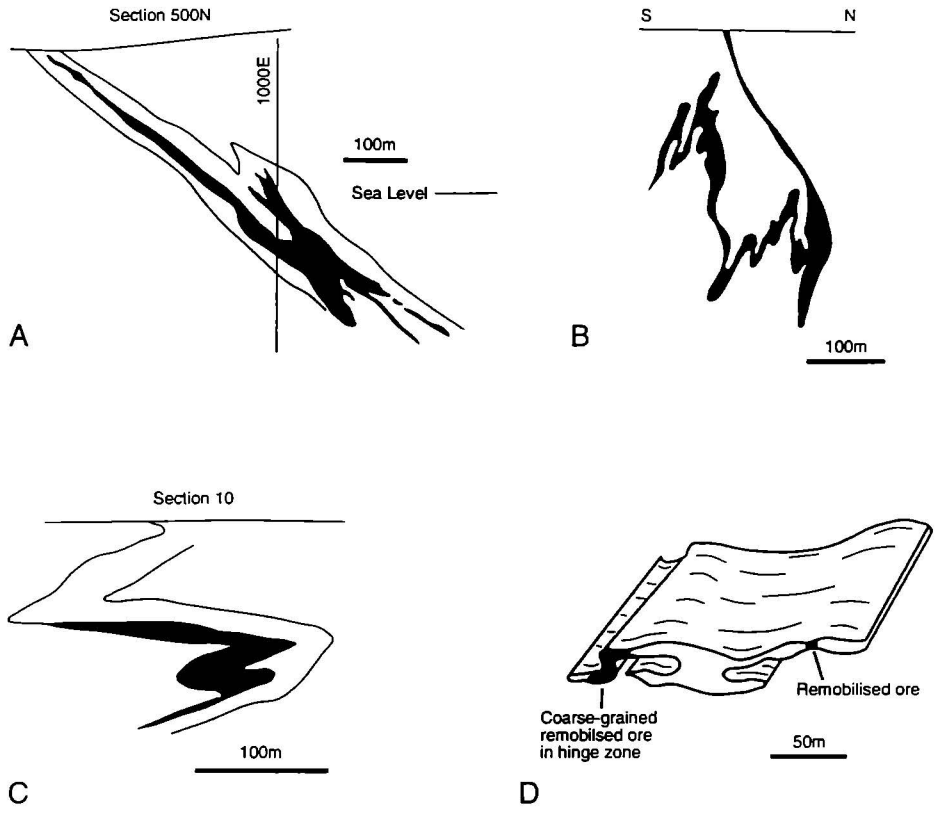

Figure 7.2. *Remobilisation in folded massive sulphide orebodies resulting in limb thinning and hinge zone thickening and boudinage along the limbs. A) Rosebery mine, Australia (after Green et al. 1981). B) Heath Steele mines, Canada (after de Roo et al. 1991). C) Stekenjokk mine, Sweden (Juve 1974). D) Black Angel mine, Greenland (after Pedersen 1980).*

1987; de Roo *et al.* 1991) in other deformed and metamorphosed massive sulphide deposits (Figure 7.2).rheologies (i.e. the upper contact with the footwall pyritic quartzite) and by the strain localisation along the limbs of the large-scale F_2 fold structure and within the baritic massive sulphides (Figure 4.26). These zones of high strain are generally marked by the pyrrhotite + sphalerite + galena massive sulphides. The contacts between the pyrrhotite + sphalerite + galena massive sulphides are sharp to gradational but almost always the wall rock to the shear zone is extensively fractured and the fractures are infilled by remobilised pyrrhotite, sphalerite and galena. Within the shear zones and durchbewegung the grain size of pyrrhotite, sphalerite and galena are significantly reduced and pyrite porphyroclasts are rounded to asymmetric (Figure

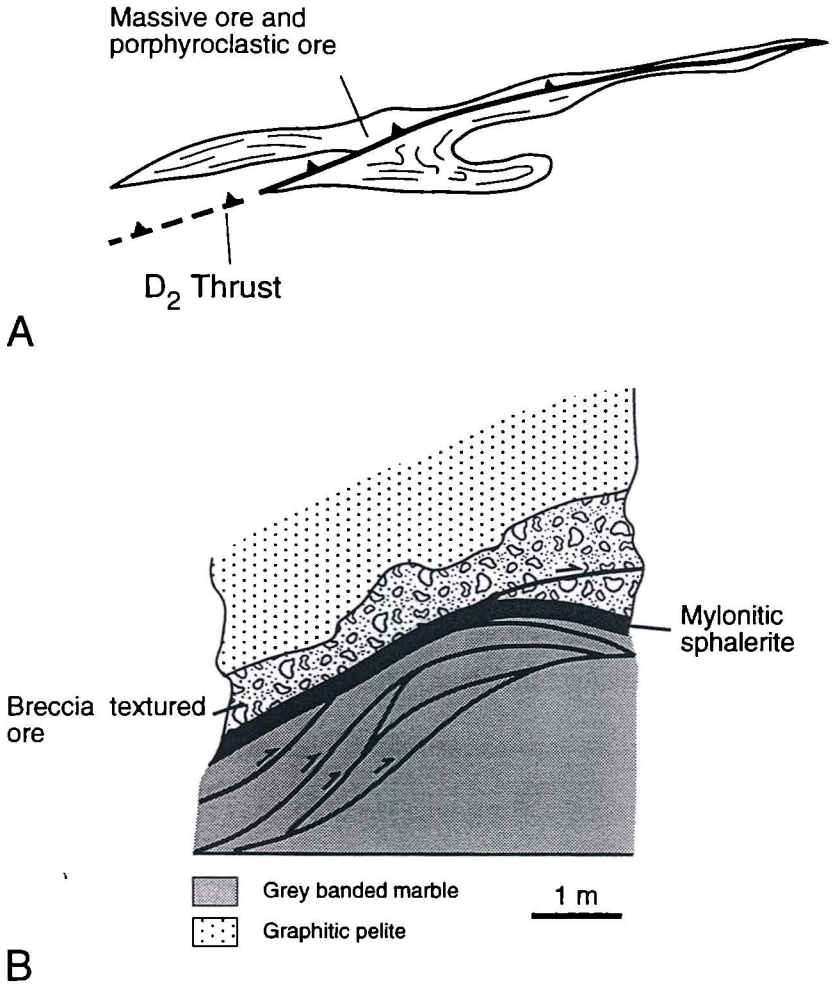

Figure 7.3. *A) Thrusting in the Black Angel mine of Greenland (after Pedersen 1980). B) Detail of mylonite formation in massive sulphides in the Black Angel mine related to thrusting. The contact between the brecciated ore and the grey banded marbles is mylonitic sphalerite (after Carmichael 1988). This relationship between brecciated ore, mylonites and lithofacies contacts is similar to occurrences of mylonititc massive sulphides in the Vangorda orebody, especially along the upper contact with the footwall pyritic quartzite.*

5.16).

Pedersen (1981) and Carmichael (1988) described D_2 thrusts in the sulphides of the Black Angel mine in Greenland (Figure 7.3) that display rounded and sheared breccia clasts in a matrix of fine grained plastically deformed and recrystallised sphalerite and galena. At very high strains sphalerite $\pm$ galena mylonites are developed (Figure 7.3). Pyrrhotite is not a significant phase in the Black Angel shear zones but a similar

relationship between the increased strain and pyrrhotite content discussed here for the Vangorda orebody has been noted in the Ducktown massive sulphide mine in Tennessee by Brooker *et al.* (1987). The process of fracturing, infiltration of fractures by pyrrhotite, sphalerite and galena and finally incorporation of breccia fragments into a plastically deforming sulphide matrix has been noted in several other massive sulphide deposits (i.e. Maiden *et al.* 1986).

The pyrrhotite + sphalerite + galena shear zones and durchbewegung in the Vangorda orebody are thought to enhance the mechanical and chemical remobilisation of the sulphides by solution and strain-induced plastic deformation processes. The change in the relative abundance of mineral phases between the shear zone and the lithofacies being sheared is reflected in the increase in pyrrhotite, sphalerite and galena content in the shear zone, suggesting chemical remobilisation was an important processes during shearing. Furthermore, this type of shear folding in which shearing occurs along the fold limb is a common mechanism for producing similar folds. The shear zones provide a mechanically weakened zone that enhances mechanical movement of material within the deforming sulphide package

The major effect of the D_2 deformation in the Vangorda orebody on the distribution of the metals is the remobilisation of the baritic massive sulphides, the major ore lithofacies, into the hinge zones of the folds (Figure 4.27), concentrating it in a thick, continuous package parallel to the F_2 fold axes. The high, but variable concentrations of Pb+Zn, Fe and gold and to a lesser degree copper in the pyrrhotite + sphalerite + galena massive sulphides (Figure 3.9) indicate remobilisation of these elements into this lithofacies. However, this is a minor lithofacies and not of particular ecomonic importance. Copper occurs mainly in the baritic massive sulphides where it is positively correlated with Zn (Figure 3.10) and therefore likely associated with sphalerite and in the pyritic quartzite where it has been remobilised in to fractures (Figure 4.26a). Again

this is a minor feature and of little economic importance.

7.1.2.3 Microtextures

Equilibrium textures such as 120° dihedral angles and straight grain-grain boundaries in sulphide mineral assemblages in the Vangorda orebody are rare. By far the most common textures are grain boundary bulging, partially reacted grain boundaries and replacement of one grain by another suggesting that disequilibrium is more widespread (Section 5.2). The widespread occurrence of disequilibrium textures together with the localised nature of equilibrium suggests that equilibrium may have been metastable in the Vangorda orebody if it occurred at all and that both processes may have been active simultaneous.

Grain growth in all sulphide phases is post-shearing throughout the orebody. However, it is difficult to determine a paragenetic sequence for growth since within any single sample all phases, with the exception of pyrite, can be seen to overgrow and contain inclusions of all other phases. Pyrite is generally the last phase to have undergone grain growth.

The microtextures described in Chapter 5 show that, with the exception of pyrite, the annealed sulphide minerals in the Vangorda orebody (Table 5.3) display few of the plastic deformation textures found in sulphides (Table 7.2) but that all are affected by brittle deformation. The scarcity of ductile deformation textures in the sulphides is due to post-deformation annealing and grain growth. Pyrite has primary depositional textures such as colloform and growth banded grains, relic spheroidal and framboidal aggregates.

Table 7.2. Deformation mechanisms active in common sulphides.[1]

Deformation mechanism	References
Pyrite	
Cracking and cataclasis dominant up to approximately 450°C. Pressure solution and grain boundary sliding may be important in this temperature range. Dislocation glide begins at slightly less than 450°C and dislocation flow and subgrain formation between 450° and 550°C. Synkinematic recrystallisation is important above 550°C. Annealing and grain growth are important at 550°C	Cox (1987) Cox *et al.* (1981) McClay & Ellis (1983, 1984)
Sphalerite	
Dislocation glide and twinning are important up to approximately 400° C and synkinematic recrystallisation above 450° C. Annealing initiates at temperatures slightly below 100° C and may be complete at 300° C. Deformation twinning is dominated by grain growth and annealing twinning between 200° and 450° C.	Stanton & Gorman (1968) Stanton & Willey (1971) Clark & Kelly (1973) Siemes & Borges (1979) McClay (1983)
Pyrrhotite	
Cataclasis decreases rapidly and glide and kinking are important to 225° to 275° C and intense kinking and twinning above 275° C. Twinning becomes important after the monoclinic-hexagonal transformation occurs. Recovery and recrystallisation is unimportant up to 450° C at geological strain rates.	Clark & Kelly (1973) Atkinson (1974) McClay (1983)
Galena	
Decreasing cataclasis, dislocation glide and kink-band formation upto 150° to 275° C; glide and kinking are common up to 300° C. Coble creep could be important at temerpatures as low as 200° C. Synkinematic recrystallisation is important above 300° C. Recovery is important above 200° C. Annealing begins at 200° to 300° C.	Stanton & Gorman (1968) Salmon *et al.* (1974) Atkinson (1974, 1977) Siemes (1976) McClay (1978)

[1] Redrawn from Marshall & Gilligan (1987)

Deformation, recrystallisation and grain growth textures predominate in all sulphide phases. Pyrite deformation textures identified in this study include brecciation in cataclastic shear zones, grain fracturing, grain boundary sliding, preferred pyrite grain shape orientations, pressure solution, dislocation structures (slip lines and dislocation walls), subgrain formation and dynamic recrystallisation (Figure 5.6). Elongate pyrrhotite and, locally, uniform extinction. Only in one instance does sphalerite display any plastic deformation texture (Figure 5.8a), deformation twinning. These textures indicate that pyrite, pyrrhotite and likely sphalerite in the Vangorda orebody deformed by both brittle and plastic mechanisms including pressure solution, dislocation creep, glide and climb and deformation twinning. The deformation processes, in general, have led to an overall reduction in grain-size, especially in pyrite. Post-deformation annealing, however, has resulted in an increase in relative grain-size, formation of equant grains and development of porphyroblasts.

Grain fragmentation and axial cracking indicate that brittle deformation of pyrite grains and of the massive pyrite has occurred throughout the deposit. However, textures indicating strong plastic deformation of pyrite (bands of dynamically recrystallised grains and preferred grain-shape textures) are restricted to areas of high strain along fold limbs (Section 5.5) indicating deformation mechanism partitioning and the simultaneous action of brittle and plastic deformation mechanisms during a single deformation event (D_2).

The plastic deformation textures in pyrite found in this study (slip lines, kink bands, subgrains, dynamically recrystallised grains and preferred grain shape orientations) also indicate that, at geological strain rates, plastic deformation of pyrite occurs well below the threshold of 450°C a at 300 MPa confining pressure determined experimentally in the laboratory (Cox *et al.* 1981). In addition relict deformed spheroidal and framboidal textures together with overgrowth features indicate that pressure solution played an important role in the deformation of pyrite in the Vangorda orebody.

Post deformational thermal annealing in the Vangorda orebody, as in the other Anvil District deposits (e.g. Faro - McClay & Ellis, 1983), resulted in the formation of foam textures with 120° triple junctions together with grain boundary migration, grain growth and porphyroblast formation. The annealing event and subsequent grain growth has largely obscured and destroyed the earlier depositional, diagenitic, overgrowth and deformation textures and has led to an overall increase the grain size.

7.1.3 Pressure and temperature conditions of metamorphism

The calibrations used to determine the temperature and pressure of metamorphism of the Vangorda orebody provide consistent values. The M_2 temperatures of 336 °C to 363 °C at pressures of 4 - 6 kb (Table 7.3) are in good agreement with those derived from

petrogenetic relationships by Smith and Erdmer (1990). They provide quantitative evidence that the D_2 deformation and M_2 metamorphism occurred at low temperature and low pressure. Analyses of S_1 chlorite and of inclusions in pyrite yield temperatures and pressures similar to those that are unambiguously M_2 and suggest that the pressure and temperature conditions during M_1 may have been similar to those during M_2 and the two cannot be distinguished. Alternatively, M_1 assemblages may have re-equlibrated during M_2 and reflect only M_2 temperature and pressure.

Chlorite temperatures determined from both S_1 and S_2 are similar and it is thought that compositions of chlorite grains in lithons (S_1) represent M_2 conditions. The average formula for the Vangorda chlorites is

$$(Fe_{2.83}Mg_{1.71}Al_{1.34}Mn_{0.07}Ti_{0.01})[(Al_{1.31}Si_{2.68})O_{9.95}](OH_{8.04})$$

and the average temperature given by the total chlorite population is 363 °C ($2\sigma = \pm 24$ °C). The S_2 foliation in the phyllite is defined by the chlorite and there is no evidence to suggest that it is a retrograde phases after biotite. The S_2 chlorite is therefore interpreted to represent a peak M_2 silicate mineral phase in the Vangorda orebody and 363 °C to be the peak M_2 temperature.

Temperatures of 336 °C estimated for arsenopyrite buffered by pyrite and/or pyrrhotite are consistent with those calculated for chlorite (Table 7.3). The textural relationships of the arsenopyrite coexisting with pyrite (i.e. as overgrowths) indicate that it grew late

Table 7.3. Summary of pressure and temperatures conditions of M_2 metamorphism.

Temperature	Chlorite 363 °C (2σ = 24 °C)	
	Arsenopyrite 336 °C (2σ = 20 °C)	
Pressure (at 363 °C)	Sphalerite inclusions in pyrite	3.98 kb (2σ = 2.7 kb)
	Sphalerite + hexagonal pyrrhotite	6.11 kb (2σ = 1.6 kb)

in the metamorphic cycle, possibly during waning of the metamorphism and 336 °C is therefore interpreted to be a cooling temperature. The fS_2 and $a\ S_2$ calculated for pyrrhotite coexisting with arsenopyrite falls outside of the stability fields for these phases. This may be the result of re-equilibration of the pyrite + pyrrhotite assemblage and the decomposition and decrease in sulphur content of pyrrhotite during cooling (c.f. Craig and Vokes 1993).

Sphalerite inclusions in pyrite have a wide ranging mol% FeS composition that provide a widely varying pressure value (Table 7.3). The variation in mol% FeS is likely due to the absence of the buffering assemblage of pyrite + hexagonal pyrrhotite or to departure from equilibrium during cooling. Since there is no bimodal distribution of mol% FeS it is not thought that these values represent different metamorphic events (i.e. M_1 and M_2). Nor is there any consistent change in sphalerite composition from core to rim of the enveloping pyrite grains to suggest changing pressure conditions during M_2. The pressure of 4.0 kb calculated from this method is in good agreement with the pressure determined from petrogenetic relationships (Smith and Erdmer 1990).

Sphalerite + hexagonal pyrrhotite pairs in the D_2 shear zones also appear to be a reliable assemblage for determining metamorphic pressures in the Vangorda orebody. Despite the fact that pyrrhotite lies approximately on the pyrite + pyrrhotite solvus or in the pyrite + pyrrhotite field (Figure 6.7) the assemblage provides a tightly bracketed mol% FeS in sphalerite (Table 6.4) that yields a geologically reasonable pressure of 6.1 kb (Table 7.3). However, 6.1 kb is a somewhat higher pressure than expected for the Anvil District (Figure 7.4). The absence of kyanite in silicate assemblages adjacent to the contact with the Anvil Batholith and the fact that near the contact andalusite alters to sillimanite (Pigage and Anderson 1985, Smith and Erdmer 1990) suggests that M_2 took place at pressures of less than 4 kb. These higher pressures indicate that regional uplift in the district may exceed the 10 km suggested by the lower pressure mineral

assemblages. Note that with the exception of the presence of kyanite the sequence of metamorphic reactions that have taken place in the aureole would be similar at 4 to 6 kb as a 3 kb (Figure 7.4).

The low a_{FeS} in pyrrhotite may be a retrograde effect in which it is on the verge of altering to pyrite during waning of the metamorphic conditions (c.f. Graig and Vokes 1993). This is possibly reflected in the position of pyrrhotite on or near the pyrite + pyrrhotite solvus (Figure 6.7) and in the occurrence of rare, retrograde pyrite overgrowing the sphalerite + pyrrhotite assemblage.

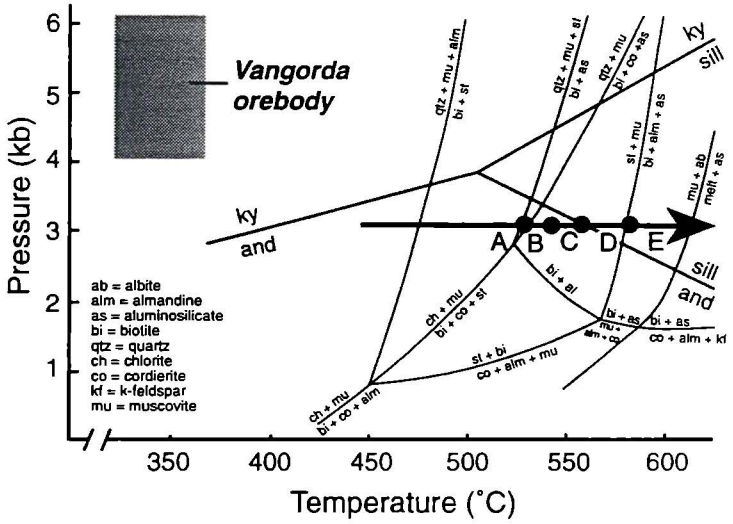

Figure 7.4. *Petrogenetic grid showing the metamorphic reactions interpreted to have taken place in the contact aureole around the Anvil Batholith (arrow indicates the sequence of reactions towards the batholith). A = chlorite - biotite zone, B = biotite - andalusite zone, C = biotite - andalusite - staurolite zone, D = biotite - sillimanite - staurolite zone, E = biotite - almandine - sillimanite zone and the black dots indicate the position of the zone boundaries (after Smith & Erdmer 1990). The Vangorda orebody records lower temperatures and higher pressures than those determined petrogenetically.*

7.2 Implications for deformation and metamorphism of massive sulphide deposits in the Anvil District

The deformation style, mesoscale and microscale structures and textures and metamorphic pressure and temperature conditions presented in this thesis for the

Vangorda orebody have a number of important implications for the massive sulphide deposits in the Anvil District. This research shows that any primary features, with the exception of rare colloform and framboidal pyrite (and possibly the lithostratigraphic sequence), have been completely overprinted by subsequent deformation and metamorphism. The D_2 and M_2 events have been shown as providing the dominant structural control and metamorphic imprint on the Vangorda orebody. This is important in the structural interpretation of the Grum and Dye deposits, both in greenschist facies and in the same regional structural position as the Vangorda orebody, which can be expected to display similar features as the Vangorda orebody. That is, tight to isoclinal, southwest-verging, recumbent F_2 folding with remobilisation and shearing focused along the limbs of the F_2 folds and extensive M_2 recrystallisation of sulphides.

The recognition of the differentiated layering as S_1 provides a key marker structural element that can be used to reference the relative ages of other structural features and to determine the D_2 structural style and geometry in other greenschist facies deposits in the district. Similarly, the Faro orebody sulphides have a penetrative differentiated layering that likely corresponds to S_1 and can be used as a marker structural element.

A significant point that arises from this thesis is that the Vangorda orebody has no texture or feature, besides rare relic pyrite textures, that points unequivocally towards its being a syngenetic SEDEX-type deposit other than the lack of evidence for its being epigenetic. The strongly developed F_2 folding in the orebody can be related to regional F_2 folding resulting from emplacement and unroofing of the Anvil Batholith clearly indicating that the orebody is not due to D_2/M_2 replacement associated with intrusion of the batholith. The penetrative D_2/M_2 overprint of D_1/M_1 features makes any statement about it being an epigenetic replacement deposit related to these earlier events impossible. The intense and penetrative nature of the deformation and metamorphism of the orebody also casts doubt on the significance of any isotope values (i.e. Shanks *et al.*

1987) since these would most likely be partially or entirely reset during the various events.

Despite the lack of evidence in the Vangorda orebody that conclusively points to it being SEDEX, the Anvil District has regional scale evidence (Jennings & Jilson 1986) that suggests that the Anvil District deposits are, in fact, synsedimentary, stratiform SEDEX-type deposits. This evidence includes;

1. The well developed sulphide lithostratigraphic sequence throughout the district (Figure 2.12).
2. The interlayering of sulphides and unmineralised metasediments and possibly metavolcanic rocks.
3. The occurrence of all deposits in the district within a restricted stratigraphic interval (Figure 2.4).
4. The curvilinear arrangement of the deposits along the southwestern flank of the Anvil Batholith (Figure 2.3) and their association with a graphitic or carbonaceous pelite facies changes possibly indicating a reduced basinal margin.
5. The deformation and metamorphic overprint of relic primary mineral textures (Figure 5.6).
6. The bulk rock Cu:Pb:Zn ratios plot in the field of stratiform deposits (Figure 7.5).

Based on the regional evidence for the Anvil District deposits being SEDEX a model for the evolution of the Vangorda orebody, and hence the Anvil District deposits, can be constructed (Figure 7.6). The Vangorda (and possibly Grum) orebody may have been deposited in a 2nd or 3rd order basin in a terraced extensional fault system in which the Mount Mye and Vangorda formation sediments were also being deposited. The ore-bearing fluids were being expulsed into the basin along the extensional fault system (Figure 7.6). During the early Mesozoic the basin was inverted and thrust towards the northeast and overthrust by the Yukon-Tanana terrane. The Vangorda orebody was

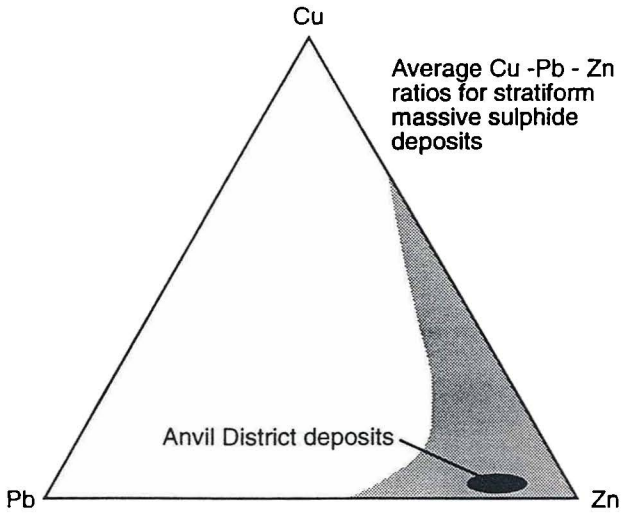

Figure 7.5. *Pb-Zn-Cu ternary plot showing the average ratios of these elements in stratiform massive sulphide deposits and the location of the Anvil District ores within this field.*

folded and metamorphosed by this event (D_1), developing a penetrative differentiated layering in the sulphides. During the early to mid Cretaceous the Anvil Batholith was emplaced resulting in uplift and extensional unroofing and development of southwest-verging F_2 folds, development of a penetrative S_2 cleavage and metamorphism to mid greenschist facies (D_2 and M_2). Unroofing of the batholith continued along extensional faults after cessation of folding and cleavage development. The final phase of deformation is strike-slip faulting which may be related to the unroofing event or to displacement along the Tintina Fault.

7.3 Shear textures and processes: implications for deformation of massive sulphides

7.3.1 Significance of shear textures

Studies of deformation structures and processes in massive sulphides have largely focused on folding (e.g. McClay 1983a, Hamilton *et al.* 1982; De Roo *et al.* 1991),

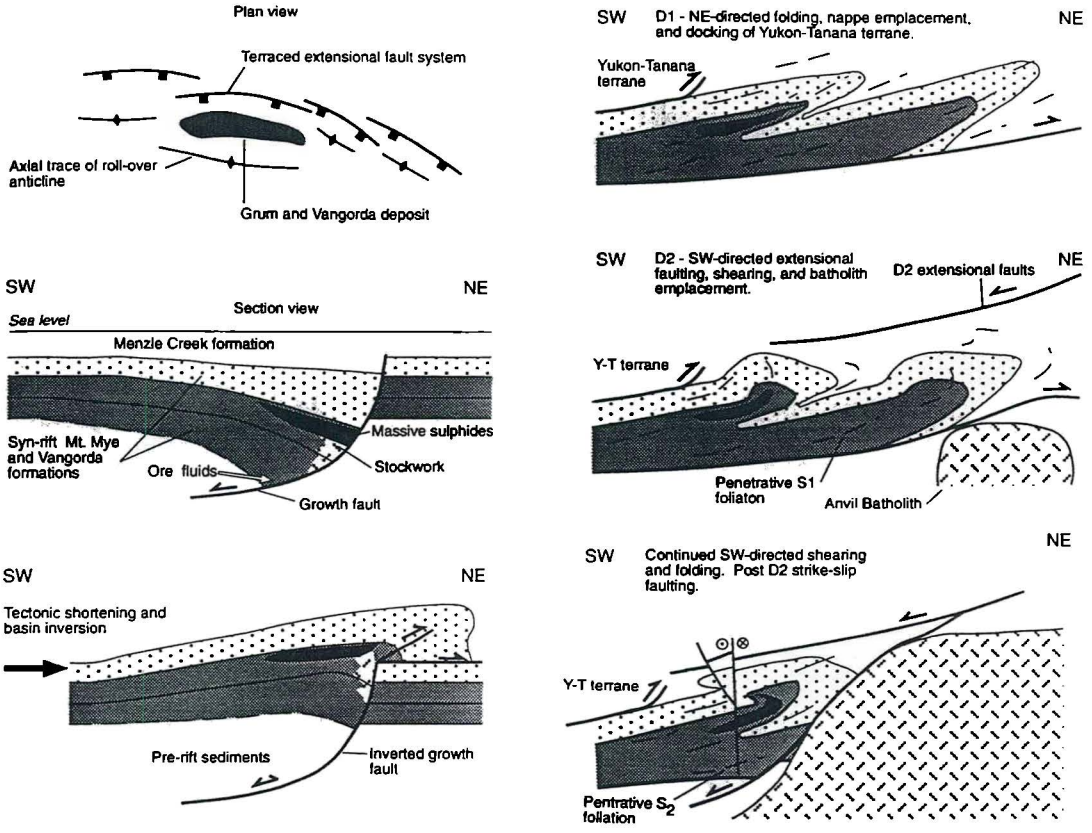

Figure 7.6. *Schematic model illustrating the geological evolution of the Vangorda and Grum deposits from their formation as SEDEX deposits through basin inversion and northeast telescoping followed by deformation and metamorphism associated with intrusion of the Anvil Batholith.*

those that point to remobilisation (see Gilligan & Marshall 1987, 1993 for and overview of these features), high strain chaotic flow or durchbewegung (Vokes 1969, 1973, Marshall & Gilligan 1989), and grain scale deformation processes (e.g. Atkinson 1975, Graf *et al.* 1980, Cox *et al.* 1981, McClay & Ellis 1983, Cox & Etheridge 1984, Cox 1987, Brown & McClay 1993a). Deformation structures such as tailed clasts and inclusion and shear bands, and the inferred processes from which they formed, often noted in highly deformed silicate rocks, have been described in relatively few massive sulphide deposits (e.g. Pesquera & Velasco 1993, 1989). This is because the high ductility of sulphide rocks and minerals (Siemes *et al.* 1991 Marshall & Gilligan 1993), even at moderate pressures and temperatures, often results in the destruction of many shear indicators.

In recent years, significant advances have been made in the understanding of deformation processes and the kinematic significance of the resultant shear structures found in plastically and cataclastically deformed silicate rocks (e.g. Behrmann & Mainprice 1987, Gapais *et al.* 1987, Passchier 1987, van den Driessche & Brun 1987, Gapais 1989). The most common structures used to determine kinematics and shear sense in plastically deformed rocks are C-S planes, winged porphyroblast/porphyroclast and inclusion systems, shear bands, sigmoidal fabrics, and linear fabrics (e.g. Berthé *et al.* 1979, Simpson & Schmid 1983, Lister & Snoke 1984, Passchier & Simpson 1986, Choukroune *et al.* 1987, Takagi & Ito 1988, Hanmer & Passchier 1991). Common cataclastic features include fractures, veining, gouge, and the development of slickensides. These structures have been interpreted to be the result of coaxial and noncoaxial flow (pure and simple shear, respectively) or an intermediate, general flow (see Hanmer & Passchier 1991 for a thorough review of shear processes and resultant structures) taking place in the brittle and plastic deformation fields or at the brittle-plastic transition zone.

The Vangorda massive sulphide orebody has undergone intense deformation during the low pressure and temperature D_2 and M_2 events. Intensity of deformation increases along discrete centimetre to metre-scale areas in high strain positions along the limbs of F_2 folds. These areas are typified by the occurrence of widespread cataclastic and shear textures and durchbewegung, a well-developed pyrrhotitic foliation and significantly reduced sulphide grain size, all of which provide strong evidence for their interpretation as shear zones.

The shear related structures and textures discussed in this thesis (Section 4.4.2) have many similarities with features found in mylonitised silicate rocks suggesting that processes such as simple shear or a general shear (both non-coaxial flow) are active in massive sulphides during shearing. The winged and pressure-shadowed inclusions,

porphyroclasts and porphyroblasts found in the shear zones in the Vangorda orebody have both stair-step and in-plane geometries and can be interpreted to have formed under conditions of bulk general noncoaxial shear or simple shear (c.f. Passchier 1987; Hanmer & Passchier 1991). Similarly, the naked inclusions and porphyroblast/clasts wrapped by the shear foliation can be interpreted to have developed in the same way. Inclusion-derived wings are materially continuous with the inclusion and have formed by processes involving shear induced recrystallisation along the inclusion boundary (e.g. Passchier 1987; Van Den Driessche & Brun 1987). Wings formed by pressure solution contain only minor amounts of material derived from inclusion boundary recrystallisation, most material is deposited in the low stress area adjacent to the inclusion by element movement along a chemical potential gradient (c.f. Takagi & Ito 1988).

These processes were active, and preserved, in the Vangorda massive sulphides at pressure (ca. 4 to 6 kb) and temperature (ca.~363 °C) conditions similar to those at which many upper crustal silicate mylonites form. However, grain-scale deformation textures in the sulphide minerals in the Vangorda orebody that would be indicative of shearing have been overprinted by dynamic recovery, annealing and grain growth following deformation. Other than pyrite, the low relative strengths of the most common sulphide minerals (Figure 7.7) will result in destruction of most grain-scale plastic deformation textures at low pressure - temperature conditions regardless of the mesoscopic state of strain. An important point here is that microtextural analysis alone is not enough to determine the deformation processes and amount of strain that have affected sulphide rocks, even at relative low metamorphic conditions. Microtextural studies must be carefully cross checked with macroscale and mesoscale studies. However, the similarities between the mesoscale shear textures and the inferred processes found in the Vangorda sulphides and those in mylonitised silicate rocks point to the fact that, if found *in situ* (which is not the case for the Vangorda orebody) these

textures and structures may be effectively used as shear and shear sense indicators in massive sulphides.

Shearing and shear sense studies in many sulphide orebodies are often impeded by the lack of appropriate textures. This is because sulphide rocks undergo large strains at low to moderate metamorphic conditions that often result in the formation of chaotic structures such as durchbewegung. Still, deformation textures similar to those described for the Vangorda orebody have been identified in other metamorphosed massive sulphide deposits. For instance, Pesquera & Velasco (1993, 1989) describe spectacular examples of inclusions with tails and pressure shadows and S-C planes from the Arditurri orebody in the Pyrennes. Craig *et al.*(1991) described an example of a helicitic inclusion pattern in pyrite from the Ducktown orebody that they interpreted to have resulted from rotation of the porphyroblast during growth. Hayward (1992) provided an alternative interpretation of the Ducktown pyrite that involved successive foliation development during as many as five foliation forming events. Importantly, the

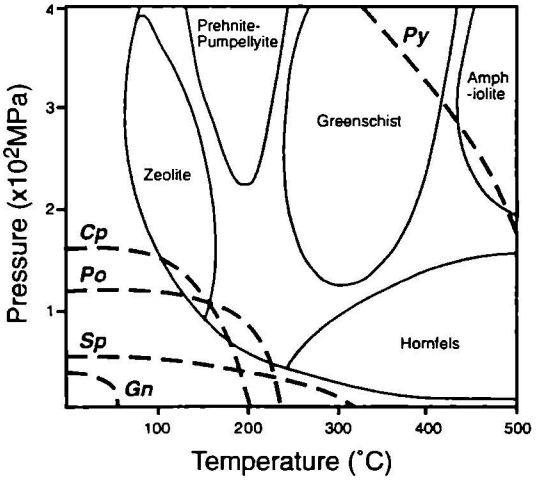

Figure 7.7. *Brittle-ductile transition of galena (Gn), sphalerite (Sp), pyrrhotite (Po), chalcopyrite (Cp) and pyrite (Py) at 5% ductile strain at strain rates in the order of 7.2 x 10^{x-5} (after Marshall & Gilligan 1987). Note that only pyrite behaves in a brittle fashion at the pressure and temperature conditions of metamorphism of the Vangorda orebody.*

deformation processes that resulted in the formation of the various deformation textures noted by these authors may be interpreted to have involved a non-coaxial shear and a component of shear-induced vorticity and/or spin during part of the deformation history. These textures, therefore, record at least part of the deformation history affecting these orebodies and can be used as shear and shear sense indicators.

7.3.2 Model for the development of shear zones and durchbewegung in sulphides

Figure 7.8 provides a qualitative and schematic model for development of shear zones in the Vangorda massive sulphide. With an increase in temperature and an increase in strain along the limbs of the folds there is a concomitant increase in pore fluid pressure in these areas resulting in fracturing and cataclasis. Deformation and metamorphism results in an increase in $a\,S_2$ and fS_2 in these areas and a phase change from pyrite to pyrrhotite (c.f. Craig & Vokes 1993). Although it has not been unequivocally proven in this thesis it can be seen that the fS_2 in the pyrrhotite + sphalerite + galena massive sulphides (shear zones) (Figure 6.7) is higher than that in less strained rocks (Figure 6.4). The increased pore fluid pressure and fluid flux in these areas also results in higher mobility of Zn and Pb which forms sphalerite and galena, the former overgrowing pyrite.

The increased modal abundance of these more ductile minerals, together with the disaggregation and clast-size reduction of the host rock, results in a switch in the deformation mechanism from cataclastic to plastic. This switch in deformation mechanism is caused, at least partially, by reaction-enhanced ductility (c.f. Brodie & Rutter 1985) as pyrite goes to pyrrhotite. Shearing proceeded under general non-coaxial flow or simple shear and inclusions and porphyroblasts/clasts develop wings and pressure shadows.

With a waning in the deformation and metamorphism the $a\ S_2$ and fS_2 decreases and pyrite porphyroblasts grow incorporating shear-related minerals as inclusions and overgrowing shear-related textures. With further cooling monoclinic pyrrhotite overgrowths form on hexagonal pyrrhotite.

The occurrence of highly corroded magnetite, locally altering to pyrrhotite, and late fine-grained euhedral magnetite with, locally, inclusions of pyrrhotite suggest a complex interaction between the $a\ O_2$ and fO_2 and $a\ S_2$ and fS_2 during deformation. These textural relationships suggest a relative increase in $a\ S_2$ and fS_2 early in the deformation history and breakdown of magnetite to form pyrrhotite and with a relative decrease late in the history, magnetite forms at the expense of pyrrhotite (c.f. Large 1977; Lianxing & McClay 1992).

The tight to isoclinal, similar, fold style and complex internal deformation indicates that the Vangorda orebody has undergone significantly high strains. Strain partitioning has produced breccia zones and shear zones in part controlled by the sulphide and matrix rheologies. Shear zones in particular are localised in the baritic massive sulphide facies. Shear zones have long been known to act as conduits for fluids during deformation (e.g. Carter et al., 1990, and references therein), and fluids are well known to affect the mechanical response of rocks during deformation (e.g. Hubbert and Rubey, 1959; Handin et al., 1963; Atkinson, 1984). To date, a full appreciation of the role of a fluid in the deforming Vangorda orebody has not been assessed. However, sealing of cataclastic zones and fractures by quartz, carbonate, and often pyrite, together with the occurrence of overgrowths on grains indicates that fluid infiltration and mobilisation did occur, and likely played an important role in the mechanical response of the sulphide rocks.

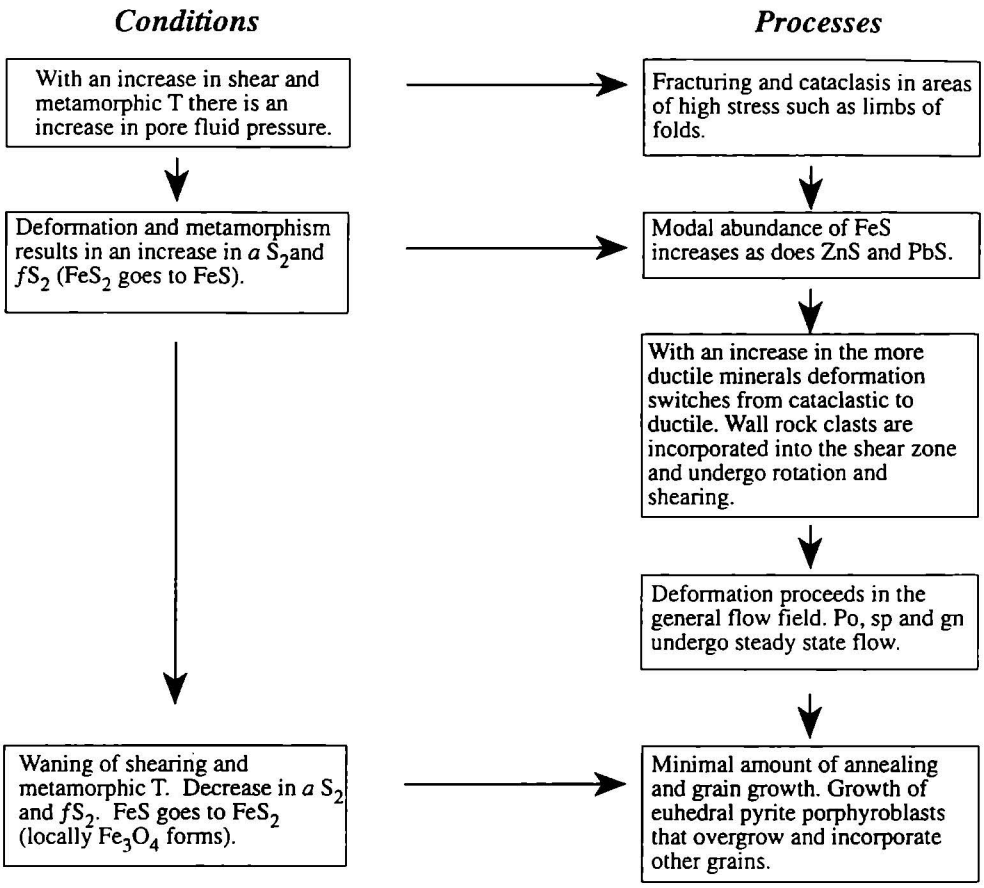

Figure 7.8. *Model for the formation of shear zones and, at high strains, durchbewegung. See text for discussion.*

The precise effects of pore fluids on the ductile deformation of sulphide minerals is largely unknown, and is beyond the scope of this paper. With the exception of pyrite little can be said about the effects of enhanced pore fluid pressure on the plastic deformation of sulphide minerals in the shear zones in the Vangorda orebody. Textural evidence, however, indicates that pressure solution is an important deformation mechanism in naturally deformed pyrite (McClay and Ellis, 1983; McClay, 1991). It may be expected that the focussing of a fluid phase along shear zones may significantly reduce the flow stress required to induce crystal plastic deformation in pyrite, in much the same way it affects the mechanical response of quartz and olivine (Blacic, 1972; Kirby, 1984; Kirby and Kronenberg, 1987). The effects of fluid chemistry on rock and mineral deformation are not well understood, although Hobbs (1981, 1984) suggests

that deformation and metamorphic reactions are closely tied. The deformation of pyrite in deposits such as Vangorda may be expected to have not only dramatically changed the textural characteristics of the ore but may also be expected to have affected the chemical and isotopic signatures.

Chapter 8
Conclusions

1. The Vangorda orebody consists of five complexly folded and faulted semi-massive and massive sulphide lithofacies in the core of an F_2 fold.

2. The dominant structural and metamorphic features in the orebody are D_2 and M_2 which are related to emplacement, uplift and unroofing of the Anvil Batholith. D_2 resulted in southwest-verging, northwest-southeast-plunging, tight to isoclinal, shallowly downward-facing to recumbent folding of the Vangorda orebody in the hinge zone of a macroscopic F_2 fold and M_2 resulted in syn-D_2 metamorphism to mid-greenschist facies.

3. The effects of the D_1 and M_1 metamorphic events on the Vangorda orebody are impossible to determine because of the penetrative overprint of D_2 and M_2.

4. F_2 folding resulted in remobilisation of sulphides into the hinge zones of the folds causing them to be thickened relative to the limbs. The F_2 fold limbs have undergone extensive shearing and development of pyrrhotite + sphalerite + galena shear zones.

5. Temperature and pressure conditions during M_2 are mid-greenschist facies. Chlorite thermometry records a peak M_2 temperature of 363°C and arsenopyrite coexisting with pyrite and/or pyrrhotite records a cooling temperature of 336°C. Pressure estimates using sphalerite inclusions in pyrite give reasonable although widespread results. Sphalerite coexisting with hexagonal pyrrhotite give consistent pressure estimates of approximately 6 kb which is slightly higher than expected based on the

mineral assemblages in the pelites.

6. With the exception of pyrite, sulphide minerals are strongly annealed and display few plastic deformation textures. Only pyrite displays any relic primary texture. Pyrrhotite locally forms elongate grains and has uniform extinction. One sphalerite grain was found with deformation twinning. Pyrite displays an both brittle and plastic textures including axial cracking, indentation and dissolution, grain boundary sliding, dislocation walls and tangles, subgrain formation and grain boundary recrystallisation and pressure solution. All sulphide minerals have undergone annealing and grain growth.

7. Microtextures indicate that brittle and plastic deformation processes were active simultaneously in the deposit indicating deformation mechanism partitioning in the orebody. Plastic deformation was active along high strain areas situated in the limbs of the folds. Brittle processes were active in the hinge to limb zones.

8. Sulphide equilibrium assemblages are rare in the Vangorda orebody, occurring in localised areas. Disequilibrium textures are by far the most common.

9. Despite the fact that the Vangorda orebody has undergone only low pressure - low temperature conditions during deformation and metamorphism there are no primary features remaining other than rare colloform and framboid cores in pyrite porphyroblasts that argue for its genesis as a SEDEX deposit. Only on the grounds of the regional setting, morphology and chemistry can this be argued. However, the strong D_2 and M_2 overprint of the orebody and the similarity in structural style between the orebody and the rest of the district argues strongly against Vangorda being a replacement orebody related to intrusion of the Anvil Batholith.

10. Shear zones and durchbewegung zones in the Vangorda orebody are located long the limbs of folds, in the baritic massive sulphides and at lithofacies contacts (in particular the upper contact of the footwall pyritic quartzite). The peripheries of these zones are generally fractured rock that is infiltrated by pyrrhotite, sphalerite and galena. These shear zones contain structures such as asymmetric and symmetric tailed and naked inclusions and porphyroclasts and inclusions and porphyroclasts with asymmetric and symmetric pressure shadows that are similar to those found in silicate mylonites. If found *in situ* (which is not the case for Vangorda) these structures can be used as shear and shear sense indicators.

11. A generalised model has been proposed for the development of shear zones and durchbewegung in which increased P and T conditions and strain partitioning into limbs of folds results in high pore fluid pressures in these areas, fracturing and infiltration of pyrrhotite, sphalerite and galena. Which an increase in the abundance of the less competent sulphide minerals the dominant deformation mechanism switches from brittle to plastic and breccia clasts are incorporated into the shear zone and sheared and rotated to form the tailed and naked inclusions. Deformation occurs in the general flow field which is reflected in the asymmetric wings of clasts and inclusions. With increased shear the flow becomes chaotic and durchbewegung forms.

12. This research has shown that shear textures in sulphides reflect similar processes as those active in silicate rocks. This implies that shear indicators such as winged clasts and inclusions and pressure shadows can be used as shear sense indicators in sulphides. It also suggests that durchbewegung is a highly strained end-member of plastic deformation in the general flow field.

13. Future research into the response of sulphides to deformation and metamorphism

must incorporate the mesoscale structures and textures such as tailed clasts and inclusions to determine shear sense and active the shear processes. It is also important to determine the paragenesis of the constituent sulphide phases and to work out metamorphic reactions and equilibrium/disequilibrium textures. This latter point is of paramount importance in applying thermobarometry to sulphide deposits. Thermobarometry needs to be more widely applied in research into deformed and metamorphosed sulphide deposits in order to more accurately constrain the P - T conditions under which deformation processes and metamorphic reactions are active in natural situations.

References

Abbott, J.G. (1982) Structure and stratigraphy of the Macmillan Fold Belt: evidence for Devonian faulting. *In.* Yukon Geology and Exploration 1981. Dept. of Indian and Northern Development (Canada), Northern Affairs Program. Expl. and Geol. Serv. Div., Whitehorse, Yukon. 22-23.

Abbott, J.G., & Turner, R.J. (1990) Character and Paleo-tectonic setting of Devonian Stratiform Sediment-hosted Zn, Pb, Ba deposits, Macmillan Fold Belt, Yukon. *In.* Proc. IAGOD Meeting, Ottawa 1990.

Abbott, J.G., Gordey, S.P., & Tempelman-Kluit, D.J. (1986) Setting of stratiform, sediment-hosted lead-zinc deposits in Yukon and northeastern British Columbia. *In* Mineral Deposits of Northern Cordillera (J.A. Morin, ed.). Can. Ins. of Mining and Metallurgy, Special Paper 37: 1-18.

Atkinson, B.K. (1975) Experimental deformation of polycrystalline pyrite: effects of temperature, confining pressure, strain rate and porosity. Econ. Geol. **70**. 473-87.

Atkinson, B.K. (1984) Subcritical crack growth in geological materials. J. Geophysical. Res. **89**. 4077-4114.

Atkinson, B.K. (1977) The kinetics of ore deformation. Its illustration and analysis by means of deformation mechanisms maps. Geol. Foren. Stockholm Forh. **99**, 186-197.

Barker, W.W., & Parks, T.C. (1986) The thermodynamic properties of pyrrhotite and pyrite: A re-evaluation. Geochim. Cosmochim. Acta. **50**, 2185-2194.

Barton, P.B. (1969) Thermochemical study of the system Fe - As - S. Geochim. Cosmochim. Acta. **33**. 841-857.

Barton, P.B., & Toulmin, P. III (1966) Phase relations involving sphalerite in the Fe - Zn - S system. Econ. Geol. **61**, 815-849.

Bell, T.H. (1985) Deformation partitioning and porphyroblast rotation in metamorphic rocks: a radical reinterpretation. J. Metamorphic Geol. **3**. 109-18.

Behrmann, J.H. & Mainprice, D. (1987) Deformation mechanisms in a high-temperature quartz-feldspar mylonite: evidence for superplastic flow in the lower crust. Tectonophysics. **140**. 297-305.

Berthé, D., Choukroune, P., & Jegouzo, P. 1979. Orthogneiss, mylonite, and non-coaxial deformation of granites: the example of the South Armorican Shear zone. J. Struct. Geol. **1**, 31-42.

Blacic, J.D. (1972) Effect of water on the experimental deformation of olivine. Am. Geophysical Union Mono. **16**. 109-15.

Brodie, K.H., & Rutter, E.H. (1985) On the relationship between deformation and metamorphism with special reference to the behaviour of basic rocks. *In* Advances in physical geochemistry 4. A.B. Thompson & D.C. Rubie (eds), 138-179. Berlin: Springer.

Brooker, D.D., Craig, J.R., & Rimstidt, J.D. (1987) Ore metamorphism and pyrite porphyroblast development at the Cherokee mine, Ducktown, Tennessee. Econ. Geol. **82**. 72-86

Brown, D., & McClay, K. (1992) Structure of the Vangorda Pb-Zn-Ag deposit, Anvil Range, Yukon Territory. *In* Current Research, Part A; Geol. Surv. of Can., Paper 92-1A: 121-128

Brown, D., & McClay, K. (1993a). Deformation textures in pyrite from the Vangorda Pb - Zn - Ag

deposit, Yukon, Canada. Min. Mag. **57**. 55-66.

Brown, D., & McClay, K. (1993b) The Vangorda deposit. Yukon Exploration and Geology, 1992. Exploration and Geological Services Division, Yukon, Indian and Northern Affairs Canada. 25-32.

Bryndzia, L.T., Scott, S.D., & Spry, P.G. (1988) Sphalerite and hexagonal pyrrhotite geobarometer: experimental calibration and application to the metamorphosed sulphide ores of Broken Hill, Australia. Econ. Geol. **83**. 1193-1204.

Bryndzia, L.T., Scott, S.D., & Spry, P.G. (1990) Sphalerite and hexagonal pyrrhotite geobarometer: correction in calibration and application. Econ. Geol. **85**. 408-411.

Carmichael, A.J. (1988). The tectonics and mineralisation of the Black Angel Pb-Zn deposits, central west Greenland. Unpublished Ph.D. thesis, University of London.

Carne, R.C. (1979) Geological setting and stratiform lead-zinc-barite mineralization, Tom Claims, Macmillan Pass, Yukon Territory. Can. Dept. Indian and Northern Affairs Report 1979-4. 30p.

Carne, R.C., & Cathro, R.J. (1982) Sedimentary exhalative (SEDEX) zinc-lead-silver deposits, northern Canadian Cordillera. Canadian Institute Mining and Metallurgy Bull., **75**. 66-78.

Carter, N.L., Kronenberg, A.K., Ross, J.V., & Wiltschko, D.V. (1990) Control of fluids on deformation of rocks. In *Deformation Mechanisms, Rheology and Tectonics* (R.J. Knipe and E.H. Rutter eds.). Geol. Soc. Special Pub. **54**. 1-13.

Cathelineau, M. (1988) Cation site occupancy in chlorites and illites as a function of temperature. Clay Minerals. **23**. 471-485.

Cathelineau, M., & Nieva, D. (1985) A chlorite solid solution geothermometer, the Los Azufres (Mexico) geothermal system. Contrib. Mineral. Petrol. **91**. 235-244.

Cecile, M.P. (1982) The Lower Paleozoic Misty Creek Embayment, Selwyn Basin, Yukon and Northwest Territories. Geol. Surv. Can. Bull. 335.

Choukroune, P., Gapais, D. & Merle, O. (1987) Shear criteria and structural symmetry. J. Struct. Geol. **9**, 525-530.

Clark, B.R., & Kelly, W.C. (1978) Experimental deformation of common sulphide minerals. In. *Physics and Chemisrty of Minerals and Rocks* (R.G.J. Strens eds.). Wiley, New York, N.K., p. 51-59.

Claypool, C.E., Holser, W.T., Saki, I.R., & Zak, I. (1980) The ages curves for sulfur and oxygen isotopes in marine sulfate and their mutual interpretation. Chem. Geol. **28**. 199-260.

Coney, P.J. (1989) Structural aspects of suspect terranes and accretionary tectonics in western North America. J. Struct. Geol. **11**. 107-125.

Coney, P.J., Jones, D.L., & Monger, J.W.H. (1980) Cordilleran suspect terranes. Nature. **288**. 329-333

Cox, S.F. (1987). Flow mechanisms in sulphide minerals. Ore Geol. Rev. **2**. 133-171.

Cox S.F. & Etheridge M. (1984). Deformation microfabric development in chalcopyrite in fault zones, Mt. Lyell, Tasmania. J. Struct. Geol. **6**. 167-182.

Cox, S.F.& Etheridge, M.A., & Hobbs, B.E. (1981) The experimental ductile deformation of polycrystalline and single crystal pyrite. Econ. Geol. **76**. 2105-18.

Gapais, D., Bale, P., Choukroune, P. Cobbold, P.R., Mahjoub, Y., Marquer, D. (1987). Bulk

kinematics from shear zone patterns: some field examples. J. Struct. Geol. **9**. 635-646.

Craig, J.R., & Vokes, F.M. (1993) The metamorphism of pyrite and pyritic ores: an overview. Min. Mag. **57**. 3-18.

Craig, J.R., Vokes, F.M., & Simpson, C. (1991) Rotational fabrics in pyrite from Ducktown, Tennessee. Econ. Geol. **86**. 1737-1746.

Craig, J.R., & Scott, S.D. (1974) Sulphide phase equilibria. *In:* Ribbe, P.H. (ed.) Sulphide Mineralogy. Mineral. Soc. Amer. Short Course Notes, Vol. 1.

De Roo, J.A., Williams, & P.F., Moreton, C. (1991) Structure and evolution of the Heath Steele base metal sulphide orebodies, Bathurst Camp, New Brunswick, Canada. Econ. Geol. **86**. 927-943.

Eisbacher, G.H. (1981) Sedimentary tectonics and glacial record in he Windermere Supergroup, Mackenzie Mountains, northwestern Canada. Geol. Surv. Can., Paper 80-27.

Froese, E., & Gunter, A.E. (1976) A note on the pyrrhotite-sulphur vapour equilibrium. Econ. Geol. Bull. Soc. Econ. Geol. **71**. 1589-1594.

Gabrielse, H. (1985) Major dextral transcurrent displacements along the Northern Rocky Mountain Trench and related lineaments in north-central British Columbia. Geol. Soc. Am. Bull. **96**. 1-14.

Gabrielse, H. (1967) Tectonic evolution of the northern Canadian Cordillera. Can. J. Earth Sci.. **4**. 271-298.

Gabrielse, H., & Yorath,C.J. (1989) DNAG #4. The Cordilleran Orogen in Canada. Geosci. Can. **16**. 67-83.

Gilligan, L.B. & Marshall, B. (1987) Textural evidence for remobilisation in metamorphic environments.I Mechanical and chemical (Re)mobilisation of Metaliferous Mineralization (B. Marshall & L.B. Gilligan eds.). Ore Geol. Rev. **2**. 205-230.

Godwin, C.I., & Sinclair, A.J. (1982) Average lead isotope growth curves for shale-hosted zinc-lead deposits, Canadian Cordillera. Econ. Geol. **77**. 675-690.

Godwin, C.I., & Sinclair, A.J., & Ryan, B.D. (1982) Lead isotope models for the genesis of carbonate-hosted Zn-Pb, shale-hosted Ba-Zn-Pb, and silver-rich deposits in the northern Canadian Cordillera. Econ. Geol. **77**. 82-94.

Goodfellow, W.D. (1987) Anoxic stratified oceans as a source of sulphur in sediment-hosted stratiform Zn-Pb deposits (Selwyn Basin, Yukon, Canada). Chem. Geol. (Isot. Geosci. Sect.). **65**. 359-382.

Goodfellow, W.D. (1985) Geochemistry unveils 'blind' deposits. GEOS. **14**. 17-20.

Goodfellow, W.D. (1981) Geochemistry of shales and cherts hosting stratabound Zn-Pb deposits, Selwyn Basin, Yukon Territory. Geol. Soc. Am. Abs. with Programs. **12**. 461

Goodfellow, W.D., & Jonasson, I.R. (1984) Ocean stagnation and ventilation defined by $\delta^{34}S$ secular trends in pyrite and barite, Selwyn Basin, Yukon. Geology. **12**. 583-586.

Gordey, S.P. (1981) Stratigraphy, structure and tectonic evolution of the southern Pelly Mountains in the Indigo Lake area, Yukon Territory. Geol. Surv. Can., Bull. 318.

Gordey, S.P., & Irwin, S.E.B. (1987) Geology, Sheldon Lake and Tay River map areas, Yukon Territory. Geol. Surv. Can, Map 19-1987.

Gordey, S.P., Abbott, J.G., & Orchard M.J. (1982) Devono-Mississippian (Earn Group) and younger

strata in east-central Yukon. *In*. Current Research, Part B; Geol. Surv. Can., Paper 82-1B. 93-100.

Graf, J.L., & Skinner, B.J. (1970) Strength and deformation of pyrite and pyrrhotite. Econ. Geol. **65**. 206-15

Green, D.R., Solomon, M., & Walshe, J.L. (1981) The formation of the volcanic-hosted massive sulphide ore deposits at Rosebery, Tasmania. Econ. Geol. **76**, 304-338.

Graf, J.L., Bras, J., Fagot, M., Levade, C., & Couderc, J.-J. (1981) Transmission electron microscope observation of plastic deformation in experimentally deformed pyrite. Econ. Geol. **76**. 738-44.

Hamilton, J.M., Bishop, D.T., Morris, H.C., Owens, O.E. (1982). Geology of the Sullivan orebody, Kimberly, B.C. Canada. Geol. Ass. Can. Special Paper 25, 567-665.

Hanmer, S. 1989. Initiation of cataclastic flow in a mylonite zone. J. Struct. Geol. **11**, 751-762.

Hanmer, S; & Passchier, C. (1991) Shear sense indicators: a review. Geol. Surv. of Can. Paper 90-17, 72 p

Handin, J., Hager, R.V., Jr., Friedman, M., & Feather, J.N. (1963) Experimental deformation of sedimentary rocks under confining pressure: pore pressure tests. A.A.P.G. Bull. **46**, 717-55.

Hayward, N. (1992). Rotational fabrics in pyrite from Ducktown , Tennessee - a discussion. Econ. Geol. **87**. 1688-1690.

Hobbs, B.E. (1981) The influence of metamorphic environment upon the deformation of minerals. Tectonophysics. **78**. 335-83.

Hobbs, B.E. (1984) Point defect chemistry of minerals under a hydrothermal environment. J. Geophysical Res. **89**. 4026-38.

Hobbs, B.E., Means, W.D., & Williams, P.F. (1976) *An Outline of Structural Geology*. John Wiley and Sons, INC. New York. 571 p.

Hubbert, M.K., and Rubey, W.W. (1959) Role of pore fluid pressure in mechanics of overthrust faulting. Geol. Soc. Amer. Bull. **70**. 115-66.

Hutchison, M.N., & Scott, S.D. (1981) Sphalerite geobarometry in the Cu-Fe-Zn-S system. Econ. Geol. **76**.143-153.

Jennings, D.S., & Jilson, G.A. (1986) Geology and sulphide deposits of the Anvil Range, Yukon. *In* Mineral Deposits of Northern Cordillera (J.A. Morin, ed.). Can. Ins. of Mining and Metallurgy, Special Paper 37: 319-361

Jennings, D.S., Jilson, G.A., & Pigage, L.C. (1980) Anvil Range stratigraphy, south-central Yukon Territory (abstract). Geol. Ass. of Can., Cordilleran Section, Programme and Abstracts, 16-17

Johnston, J.D. (1985) Interpretation of refolding and asymmetric folds using vergence concepts in drill core. J. Struct. Geol., **7**, 317-326.

Juve, G., (1974) Ore mineralogy and ore types of the Stekenjokk deposit, central Scandinavian Caledonides, Sweden. Sver. Geol. Unders. **68**, 1-154.

Kirby, S.H. (1984) Introduction and digest to the special issue on chemical effects of water on the deformation and strengths of rocks. J. Geophysical Res. **89**. 3991-95.

Kirby, S.H., & Kronenberg, A.K. (1987) Rheology of the lithosphere: Selected topics. Reviews in Geophysics. **25**. 1219-44.

Kretschmar, U., & Scott, S.D. (1976) Phase relations involving arsenopyrite in the system Fe - As - S and their application. Can. Min. **14**. 364-386.

Kuo, S.L. (1976) Geology and geochemistry of stratabound ore deposits in south central Yukon Territory and southwestern District of Mackenzie, Northwest Territories. Unpubl. Ph.D. thesis, University of Alberta, Edmonton, Canada.

Laing, W.P. (1977) Structural interpretation of drill core. Econ. Geol. **72**, 671-685.

Large, D.E. (1980) Geological parameters associated with sediment-hosted submarine exhalative Pb-Zn deposits: and empirical model for mineral exploration. Geol. Jahrb. **40**. 59-129.

Lianxing, G., & McClay, K.R. (1992) Pyrite deformation in stratiform lead-zinc deposits of the Canadian Cordillera. Min. Deposita. **27**. 169-181.

Lister, G.S. & Snoke, A.W. 1984. S-C mylonites. J. Struct. Geol. **6**, 617-638.

Lydon, J.W. (1986) Models for the generation of metaliferous hydrothermal systems within sedimentary rocks and their applicability to the Irish Carboniferous Zn-Pb deposits. *In*. Geology and Genesis of Mineral Deposits in Ireland (C.J. Andrews ed.) Irish Ass.for Econ. Geol, Dublin. 555-577

Lydon, J.W. (1983) Chemical parameters controlling the origin and deposition of sediment-hosted stratiform lead-zinc deposits. *In:* Mineralogical Association of Canada Short Course Handbook, v.8, Sediment-hosted stratiform lead-zinc deposits (D.F. Sangster, ed.). 175-250.

Lydon, J.W., Goodfellow, W.D., & Jonasson, I.R. (1985) A genetic model for stratiform baritic deposits of the Selwyn Basin, Yukon Territory and District of Mackenzie. *In*. Current Research, Part A, Geol. Surv. Can., Paper 85-1A. 651-660.

MacIntyre, D.G. (1992) Geological setting and genesis of sedimentary exhalative barite and barite-sulphide deposits, Gataga District, Northeastern British Columbia. Explor. Mining Geol. **1**. 1-20

MacIntyre, D.G. (1982) Geological setting of recently discovered stratiform barite-sulphide deposits in northeast British Columbia. Can. Inst. Mining and Metallurgy Trans. **75**. 99-113.

MacIntyre, D.G. (1979) Geological Fieldwork 1979. British Columbia Ministry of Energy Mines and Petroleum Res. 56-67.

Maiden, K.J., Chimimba, L.R., & Smalley, T.J. (1986) Cuspate ore-wall rock interfaces, piercement structures, and the localisation of some sulphide ores in deformed sulphide deposits. Econ. Geol. **81**. 1464-1472.

Marshall, B. & Gilligan, L.B. (1993 Remobilization, syn-tectonic processes and massive sulphide deposits. Ore Geol. Rev. **8**. 39-64.

Marshall, B. & Gilligan, L.B. (1989) Durchbewegung structure, piercement cusps, and piercement veins in massive sulphide deposits: formation and interpretation. Econ. Geol. **84**, .2311-2319.

McClay, K.R. (1991) Deformation of stratiform Zn-Pb (-barite) deposits in the northern Canadian Cordillera. Ore Geol. Reviews. **6**. 435-462

McClay, K.R. (1983a) Structural evolution of the Sullivan Fe-Pb-Zn-Ag orebody, Kimberley, British Columbia, Canada. Econ. Geol. **7**. 1398-1424.

McClay, K.R. (1983b) Deformation of stratiform lead-zinc deposits. *In* Sediment-hosted Stratiform Lead-Zinc Deposits. Short Course Notes. Mineral. Assoc. Can. 283-307.

McClay, K.R. (1977) Pressure solution and cobble creep in rocks and minerals: a review. J. Geol. Soc. London. **134**, 57-70.

McClay, K.R., & Bidwell, G.E. (1987) Geology of the Tom Deposit, Macmillan Pass, Yukon Territory. *In:* Mineral Deposits of the Northern Canadian Cordillera. (J.A. Morin ed.). Can. Inst. Min. Metall., Spec. Vol. 37. 100-114.

McClay, K.R., Insley, M.W., & Anderton, R. (1989) Inversion of the Kechika Trough, northeastern British Columbia, Canada. *In.* Inversion Tectonics (M.A. Cooper & G.D. Williams eds.). Spec. Publ. Geol.Soc. London, **44**. 235-258.

McClay, K.R., & Ellis, P.G. (1983) Deformation and recrystallisation of pyrite. Mineral. Mag. **47**. 527-38

McClay, K.R., & Ellis, P.G. (1984) Deformation of pyrite. Econ. Geol. **79**. 400-403.

Monger, J.W.H., & Price, R.A. (1979) Geodynamic evolution of the Canadian Cordillera - Progress and problems. Can. J. Earth Sciences. **16**. 770-791.

Monger, J.W.H., Price, R.A., & Tempelman-Kluit, D.J. (1982) Tectonic accretion and the origin of the two major metamorphic and plutonic belts in the Canadian Cordillera. Geology. **10**. 70-75

Mookherjee, A. (1971) Deformation of pyrite. Econ. Geol. **66**. 200.

Mookherjee, A. (1976) Ores and metamorphism: Temporal and genetic relationships. *In* Handbook of Stratabound and Stratiform Ore Deposits (K.H. Wolf ed.) Elsevier, Amsterdam. **4**, 203-60.

Morganti, J.M. (1979) The geology and ore deposits of the Howards Pass area, Yukon and Northwest Territories: The origin of basinal sedimentary stratiform sulphide deposits {Ph.D. thesis}: University of British Columbia, Vancouver, 317p.

Parrish, R., Carr, S.D., & Parkinson, D.L. (1988) Extensional tectonics of the southern Omineca belt, British Columbia and Washington. Tectonics. **7**. 181-212.

Passchier, C.W. 1987. Stable positions of rigid objects in non-coaxial flow - a study in vorticity analysis. J. Struct. Geol. **9**, 679-690.

Passchier, C.W. & Simpson, C. 1986. Porphyroblast systems as kinematic indicators. J. Struct. Geol. **8**, 831-844.

Pedersen, F.D. (1981) Polyphase deformation of the massive sulphide ore of the Black Angel mine, central west Greenland. Mineral. Deposita. **16**. 157-176.

Pedersen, F.D. (1980) Remobilisation of the massive sulphide ore of the Black Angel Mine, central west Greenland. Econ. Geol. **75**. 1022-1041.

Pesquera, A. & Velasco, F. (1993) Ore metamorphism in sulphide mineralisations from the Cinco Villas Massif (western Pyrenees, Spain). Econ. Geol. **88**. 266-282.

Pesquera, A. & Velasco, F. (1989) The Arditurri Pb-Zn-F-Ba deposit (Cinco Villas massif, Basque Pyrenees): A deformed and metamorphosed stratiform deposit. Mineral. Deposita. **24**. 199-209.

Pigage, L.C. (1990) Field Guide Anvil Pb-Zn-Ag District, Yukon Territory, Canada. *In* Mineral Deposits of the Northern Canadian Cordillera, Yukon-Northeastern British Columbia (J.G. Abbott & R.J.W. Turner, eds.), Geol. Surv. of Can., Open File 2169: 283-308

Pigage, L.C. (1987) Geology of the Cirque barite-zinc-lead-silver deposit, northeastern British Columbia. *In.* Mineral Deposits of the Northern Canadian Cordillera. (J.A. Morin ed.). Can. Inst. Min. Metall., Spec. Vol. 37. 100-114.

Pigage, L.C., & Jilson, G.A. (1985) Major extensional faults, Anvil Pb-Zn district, Yukon (abstract). Geological Society of America, Cordilleran Section Annual Meeting, Abstracts with Programmes. **17**. 400

Pigage, L.C., & Anderson, R.G. (1985) The Anvil Plutonic suite, Faro, Yukon Territory. Can. J. of Earth Sci. **22**. 1204-1216

Price, R.A. (1981) The Cordilleran foreland thrust and fold belt in he southern Canadian Rocky Mountains. *In:* Thrust and Nappe Tectonics. (N.J. Price & K.R. McClay eds.). Spec. Pub. Geol. Soc. London. **9**. 427-48.

Ramdohr, P. (1969) *The Ore Minerals and Their Intergrowths*. Pergammon Press, Oxford. 1174 pp.

Ramsay, J.G. (1967) *Folding and Fracturing of Rocks*. New York, McGraw-Hill, 568p.

Rau, H. (1976) Energetics of defect formations and interaction in pyrrhotite $Fe_{1-x}S$ and its homogeneity range. J. Phys. Chem. Solids. **37**. 425-429.

Russell, M.J. (1986) Extension and convection: A genetic model for the Irish Carboniferous base-metal and barite deposits. *In*. Geology and Genesis of Mineral Deposits in Ireland (C.J. Andrews ed.) Irish Ass.for Econ. Geol, Dublin. 545-554.

Salmon, B.C., Clark, B.R., & Kelly, W.C. (1974) Sulphide deformation studies: II. Experimental deformation of galena to 2000 bars and 400 °C. Econ. Geol. **69**, 1-16.

Sangster, D.F. (1990) Mississippi Valley-type and sedex lead-zinc deposits: a comparative examination. Trans. Instn. Min. Metall. **99**. B21-B42.

Scott, S.D. (1983) Chemical behaviour of sphalerite and arsenopyrite in hydrothermal and metamorphic environments. Min. Mag. **47**. 427-435.

Scott, S.D. (1974) Experimental methods in sulphide synthesis. Rev. Mineralogy. **1**. 1-38.

Scott, S.D., & Barnes, H.L. (1971) Sphalerite geothermometry and geobarometry. Econ. Geol. **66**. 653-669.

Shanks W.C., Woodruff, L.G., Jilson, G.A., Jennings, D.S., Modene, J.S., & Ryan, B.D.(1987) Sulphur and lead isotope studies of stratiform Zn-Pb-Ag deposits, Anvil Range, Yukon: Basinal brine exhalation and anoxic bottom-water mixing. Econ. Geol. **82**. 600-634.

Sharp, Z.D., Essene, E.J., & Kelly, W.C. (1985) A re-examination of the arsenopyrite geothermometer: pressure considerations and applications to natural assemblages. Canadian Min. **23**. 517-534.

Siemes, H. (1976) Recovery and recrystallization of experimentally deformed galena. Econ. Geol. **71**, 763-771.

Siemes, H. & Hennig-Michaeli, C. (1985) Ore Minerals. *In:* Preferred Orientation in Deformed Metals and Rocks: An Introduction to Modern Texture Analysis. (H.-R Wenk, ed.). Academic Press, Orlando Fla., 335-360.

Siemes, H., Hennig-Michaeli, C., Martens, L. (1991) The importance of deformation experiments on minerals for the interpretation of metamorphic ore textures. Ore Geol. Rev. **6**. 475-483.

Skinner, B.J., & Johnson, C.A. (1987) Evidence for movement of ore materials during high-grade metamorphism. Ore Geology Reviews. **2**. 191-204.

Simpson, C. & Schmid, S.M. 1983. An evaluation of criteria to deduce the sense of movement in sheared rocks. Geol. Soc. Am. Bull. **94**, 1281-1288.

Smith, J.M., & Erdmer, P (1990) The Anvil aureole, an atypical mid-Cretaceous culmination in the northern Canadian Cordillera. Can. J. of Earth Sciences. **27**. 344-356

Stacey, J.S., & Kramers, J.D. (1975) Approximation of terrestrial lead isotope evolution by a two stage model. Earth Planet. Sci. Letters. **26**. 207-221.

Stanton, R.L. & Willey, H.G. (1971) Recrystallization softening and hardening in sphalerite and galena. Econ. Geol. **66**, 1232-1238.

Stanton, R.L. & Gorman, H. (1968) A phenomenological study of grain boundary migration in some common sulphides. Econ. Geol. **63**, 907-923.

Takagi, H. & Ito, M. 1988. The use of asymmetric pressure shadows in mylonites to determine the sense of shear. J. Struct. Geol. **10**, 347-360.

Tempelman-Kluit, D.J. (1981) Geology and mineral deposits of southern Yukon. *In*. Yukon geology and exploration 1979-1980. Ottawa, Can. Dept. of Indian Affairs and Northern Development. 1-31.

Tempelman-Kluit, D.J. (1979) Transported cataclasite, ophiolite and granodiorite in Yukon Territory. Geol. Surv. Can., paper 79-14: 27 p.

Tempelman-Kluit, D.J. (1977) Stratigraphy and structural relations between the Selwyn Basin, Pelly Cassiar Platform, and Yukon Crystalline Terrane in the Pelly Mountains, Yukon. *In*. Report of Activities, Part A: Geol. Surv. Can., Paper 76-1A. 223-227.

Tempelman-Kluit, D.J. (1976) The Yukon Crystalline terrane: Enigma in the Canadian Cordillera. Geol. Soc. Am. Bull. **87**. 1343-1357.

Tempelman-Kluit, D.J. (1972) Geology and origin of the Faro, Vangorda and Swim concordant zinc-lead deposits, central Yukon Territory. Geol. Surv. Canada, Bull. **208**. 73 p.

Tempelman-Kluit, D.J. (1970) The relationship between sulphide grain size and metamorphic grade of host rocks in some stratabound pyritic ores. Can. J. Earth Sci. **7**. 1339-45.

Tempelman-Kluit, D.J., Gordey, S.P., & Read, B.C. (1976) Stratigraphic and structural studies in the Pelly Mountains, Yukon Territory. Geol. Surv. Can., Paper 76-1A, 97-106

Thompson, B., Mercier, E., & Roots, C. (1987) Extension and its influence on Canadian Cordilleran passive-margin evolution. *In*. Continental Extensional Tectonics. (M.P. Coward, J.F. Dewey, & P.L. Hancock eds). Geol. Soc. Special Pub. No. 28. 409-417.

Toulmin, P. III, & Barton, P.B. (1964) A thermodynamic study of pyrite and pyrrhotite. Geochim. Cosmochim. Acta. **28**. 641-671.

Van den Driessche, J. & Brun, J.P. 1987. Rolling structures at large shear strain. J. Struct. Geol. **9**, 691-704.

Vokes, F.M. (1969) A review of the metamorphism of sulphide deposits. Earth-Sci. Rev. **95**. 403-406.

Wheeler, J.O., & McFeely, P. (1991) Tectonic assemblage map of the Canadian Cordillera and adjacent parts of the United States of America. Geol. Surv. Can. Map 1712A.

APPENDIX 1

Sample locations

Appendix 1

Diamond drill core sample locations

Sample no.	drill section	DDH	depth (m)	litho-facies	polish/ thin
90-1	9+00E	90-85	33	4A	polished
90-2	9+00E	90-85	37.5	4A	thin
90-3	9+00E	90-85	49.5	4A	thin
90-4	9+00E	90-85	60	4C	polished
90-5	9+00E	90-85	61	4E	polished
90-6	9+00E	90-86	78	3	polished
90-7	7+00E	90-59	27	3	polished
90-8	7+00E	90-59	30	4H	polished
90-9	7+00E	90-59	42	3	polished
90-10	7+00E	90-59	59.5	4A	polished
90-11	13+00E	90-77	33.2	3	polished
90-12	13+00E	90-77	40	3	polished
90-13	13+00E	90-77	41	3	polished
90-14	13+00E	90-77	44.8	3	polished
90-15	13+00E	90-77	44.9	4H	polished
90-16					
90-17					
90-18					
90-19	15+00E	90-75	59	4G	polished
90-20	9+00E	90-96	82.5	3	polished
90-21	9+00E	90-96	97.5	4H	polished
90-22	7+00E	90-84	25.5	4G	polished
90-23	7+00E	90-84	34.5	4G	polished
90-24	7+00E	90-84	37.8	4H	polished
90-25	7+00E	90-84	41.2	4A	polished
90-26	7+00E	90-84	47	4G	polished
90-27	7+00E	90-84	52.7	4C	polished
90-28	7+00E	90-84	65	4C	thin
90-29	6+00E	90-67	46.7	4A	thin
90-30	6+00E	90-67	52.8	4A	thin
90-31	6+00E	90-67	70	4C	polished
90-32	6+00E	90-67	78.6	4G	polished
90-33	6+00E	90-67	80	4G	polished
90-43	6+00E	90-67	84	4H	polished
90-35	6+00E	90-67	87	4H	polished
90-36	6+00E	90-67	88	4G	polished
90-37	6+00E	90-67	94	4E	polished
90-38	6+00E	90-67	96.7	4E	polished
90-39	6+00E	90-67	101	4E	polished
90-40	6+00E	90-67	106.8	4C	polished
90-41	6+00E	90-67	112.5	4C	polished
90-42	4+00E	90-116	34	3	thin
90-43	4+00E	90-116	38.2	4H	polished
90-44	4+00E	90-116	39.8	4A	polished
90-45	4+00E	90-116	49	4A	polished
90-46	4+00E	90-116	63.8	4E	polished

Appendix 1

Diamond drill core sample locations

90-47	4+00E	90-116	67.2	4G	polished
90-48	4+00E	90-116	71.2	4H	polished
90-49	4+00E	90-116	91.4	4C	polished
90-50	4+00E	90-116	109	4E	polished
90-51	4+00E	90-115	44	4H	polished
90-52	4+00E	90-115	53	4E	polished
90-53	4+00E	90-115	72.5	4C	polished
90-54	4+00E	90-115	98.5	4C	polished
90-55	4+00E	90-115	112	4H	polished
90-56	4+00E	90-118	33.4	4G	polished
90-57	4+00E	90-118	34	4G	polished
90-58	4+00E	90-118	47.5	4G	polished
90-59	4+00E	90-118	50.1	4H	polished
90-60	4+00E	90-118	66	4H	polished
90-61	4+00E	90-118	71	4C	polished
90-62	4+00E	90-108	20	4G	polished
90-63	4+00E	90-108	25	4G	polished
90-64	4+00E	90-108	29.5	4G	thin
90-65	4+00E	90-108	33.5	4H	polished
90-66	4+00E	90-108	46.5	4A	polished
90-67	4+00E	90-108	54.4	4E	polished
90-68	4+00E	90-108	69.5	4H	polished
90-69	17+00E	90-134	18	4E	polished
90-70	17+00E	90-134	23.2	4C	thin
90-71	17+00E	90-134	37.3	4E	polished
90-72	1+00E	90-131	38	4A	polished
90-73	1+00E	90-131	49	4A	thin
90-74	1+00E	90-131	57	4E	polished
90-75	1+00E	90-131	60.4	3	polished
90-76	1+00E	90-131	64	4G	polished
90-77	1+00E	90-131	65	3	thin
90-78	1+00E	90-131	70.7	4H	polished
90-79	1+00E	90-131	71.5	4G	polished
90-90	1+00E	90-131	73.2	4E	polished
90-81	1+00E	90-131	74.2	4G	polished
90-82	1+00E	90-131	77	4E	polished
90-83	1+00E	90-131	78.3	4G	polished
90-84	1+00E	90-131	84	4C	polished
90-85	3+00E	90-122	11.5	3	polished
90-86	3+00E	90-122	22.3	4A	polished
90-87	3+00E	90-122	27	4G	polished
90-88	3+00E	90-122	28.3	4H	polished
90-89	3+00E	90-122	29	4G	polished
90-90	3+00E	90-122	32	4G	polished
90-91	3+00E	90-122	33	4A	polished
90-92	3+00E	90-122	35.5	3	polished
90-93	3+00E	90-122	46.4	4A	polished
90-94	3+00E	90-122	49.3	4C	polished
90-95	3+00E	90-122	50.3	4E	polished
90-96	3+00E	90-122	53.5	4G	polished
90-97	3+00E	90-122	62.5	4C	polished
90-98	3+00E	90-122	72	4H	polished
90-99	3+00E	90-122	76	3	thin

Appendix 1

Diamond drill core sample locations

90-100	3+00E	90-122	83.4	4C	thin
90-101	3+00E	90-122	90	4C	polished
90-102	25+00E	90-32	13	4G	polished
90-103	25+00E	90-32	13.5	4G	thin
90-104	25+00E	90-32	15.7	4C	polished
90-105	25+00E	90-32	17	4C	polished
90-106	25+00E	90-32	19	4C	polished
90-107	25+00E	90-32	22	4G	polished
90-108	25+00E	90-32	24.5	4E	polished
90-109	25+00E	90-32	26.5	4E	polished
90-110	25+00E	90-32	28	4E	thin
90-111	25+00E	90-32	29	4C	polished
90-112	6+00E	79-95	49	4G	thin
90-113	6+00E	79-95	52	4G	polished
90-114	6+00E	79-95	53	4C	polished
90-115	6+00E	79-95	54	4H	polished
90-116	6+00E	79-95	55	4G	thin
90-117	6+00E	79-95	56	4H	polished
90-118	6+00E	79-95	58	4G	polished
90-119	6+00E	79-95	60	4H	polished
90-120	6+00E	79-95	61	4E	thin
90-121	6+00E	79-95	65	4E	polished
90-122	6+00E	79-95	68	4E	polished
90-123	6+00E	79-95	69.5	4E	polished
90-124	6+00E	79-95	71	4E	polished
90-125	6+00E	79-95	74.5	4H	polished
90-126	6+00E	79-95	75	4H	polished
90-127	6+00E	79-95	76.5	4G	polished
90-128	6+00E	79-95	82	4C	polished
90-129	6+00E	79-95	87	4C	polished
90-130	6+00E	79-95	98	4E	polished
90-131	8+00E	79-302	42.5	4G	polished
90-132	8+00E	79-302	44	4E	polished
90-133	8+00E	79-302	45	4G	thin
90-134	8+00E	79-302	48	4G	polished
90-135	8+00E	79-302	48.5	4G	polished
90-136	8+00E	79-302	50.3	4E	polished
90-137	8+00E	79-302	51.5	4G	polished
90-138	8+00E	79-302	52.7	4G	polished
90-139	8+00E	79-302	55.5	4C	thin
90-140	8+00E	79-302	56	4C	polished
90-141	8+00E	79-302	57	4E	polished
90-142	8+00E	79-302	58	4E	polished
90-143	8+00E	79-302	59.5	4C	polished
90-144	8+00E	79-302	61.2	4C	polished
90-145	8+00E	79-302	62.5	4G	polished
90-146	8+00E	79-302	66	4C	polished
90-147	8+00E	79-302	68	4C	polished
90-148	8+00E	79-302	70	4G	thin
90-149	8+00E	79-302	72	4C	polished
91-01	12+00E	V-63	38	4H	polished
91-02	12+00E	V-63	47.5	4C	polished
91-03	12+00E	V-63	56	4C	polished

Appendix 1

Diamond drill core sample locations

91-04	12+00E	V-63	86	4H	polished
91-05	8+00E	88-49	55.5	4E	polished
91-06	8+00E	88-49	62	4H	polished
91-07	8+00E	88-49	67.5	4E	polished
91-08	8+00E	88-49	87	4E	polished
91-09	12+00E	88-06	45	4H	polished
91-10	12+00E	88-06	51	4C	thin
91-11	12+00E	88-06	55.5	4G	polished
91-12	12+00E	88-06	76	4E	polished
91-13	12+00E	88-06	78	4H	polished
91-14	12+00E	88-06	79.5	4H	polished
91-15	2+00E	79-115	45	4G	polished
91-16	2+00E	79-115	50	4H	polished
91-17	2+00E	79-115	51	4G	thin
91-18	2+00E	79-115	55	4E	polished
91-19	2+00E	79-115	59	4G	thin
91-20	2+00E	79-115	61	4G	polished
91-21	2+00E	79-115	62.5	4H	polished
91-22	2+00E	79-115	64	4E	polished
91-23	2+00E	79-115	65	4E	polished
91-24	2+00E	79-115	74	4G	polished
91-25	2+00E	79-115	75.5	4C	polished
91-26	2+00E	79-115	82	3	thin
91-27	2+00E	79-115	84.5	4H	polished
91-28	2+00E	79-115	118	3	thin
91-29	2+00E	79-119	55	4G	polished
91-30	2+00E	79-119	56	4G	thin
91-31	2+00E	79-119	64.5	4E	polished
91-32	2+00E	79-119	70.5	4E	polished
91-33	2+00E	79-119	76	4E	polished
91-34	2+00E	79-119	78.5	4C	polished
91-35	2+00E	79-119	87	3	thin
91-36	6+00E	79-94	26	4G	polished
91-37	6+00E	79-94	27	4G	polished
91-38	6+00E	79-94	29.5	4E	polished
91-39	6+00E	79-94	32	4H	polished
91-40	6+00E	79-94	32.5	3	polished
91-41	6+00E	79-94	38	4A	thin
91-42	6+00E	79-94	52	4H	polished
91-43	6+00E	79-94	52.1	4H	polished
91-44	6+00E	79-94	53.5	4G	thin
91-45	6+00E	79-94	57	4C	polished
91-46	6+00E	79-94	61	4C	polished
91-47	6+00E	79-94	65	4C	polished
91-48	6+00E	79-94	63.5	4E	polished
91-49	6+00E	79-94	68.5	4C	polished
91-50	6+00E	79-94	70	4C	thin
91-51	6+00E	79-94	78	4C	thin
91-52	6+00E	79-94	88	4C	polished
91-53	6+00E	79-94	95	3	thin
91-54	6+00E	V-126	30	4C	polished
91-55	6+00E	V-126	34	4A	thin
91-56	6+00E	V-126	48	3	thin

Appendix 1

Diamond drill core sample locations

91-57	6+00E	V-126	54	3	thin
91-58	6+00E	V-126	59.5	4A	polished
91-59	6+00E	V-126	64	3	thin
91-60	6+00E	V-126	69	4C	polished
91-61	6+00E	V-126	82	4C	thin
91-62	6+00E	79-47	41	4G	polished
91-63	6+00E	79-47	42	4C	polished
91-64	6+00E	79-47	43	4E	polished
91-65	6+00E	79-47	44.5	4C	polished
91-66	6+00E	79-47	45	4G	polished
91-67	6+00E	79-47	45.5	4H	polished
91-68	6+00E	79-47	47	3	thin
91-69	6+00E	79-47	50	3	thin
91-70	6+00E	79-47	51	4E	polished
91-71	6+00E	79-47	53	4G	thin
91-72	6+00E	79-47	57	4E	polished
91-73	6+00E	79-47	58.5	4G	thin
91-74	6+00E	79-47	67	4E	polished
91-75	6+00E	79-47	72.5	4C	thin
91-76	6+00E	79-47	76.5	4C	polished
91-77	6+00E	79-47	78	4C	thin
91-78	6+00E	79-47	81.5	4C	polished
91-79	6+00E	79-47	85	4E	thin
91-80	6+00E	79-47	89	4C	polished
91-81	6+00E	79-47	104	3	thin
91-82	6+00E	79-47	115.5	3	polished
91-83	6+00E	79-47	125	4H	polish/thin
91-84	6+00E	79-47	164.8	3	polished
91-85	8+00E	79-45	32	4G	thin
91-86	8+00E	79-45	44	4G	thin
91-87	8+00E	79-45	44	4G	thin
91-88	8+00E	79-45	44	4G	polished
91-89	8+00E	79-45	44	4G	polished
91-90	8+00E	79-45	47.8	4G	polish/thin
91-91	8+00E	79-45	48.3	4C	polished
91-92	8+00E	79-45	48.5	4C	polished
91-93	8+00E	79-45	48.9	4E	polished
91-94	8+00E	79-45	49.5	4C	polished
91-95	8+00E	79-45	51	4E	polished
91-96	8+00E	79-45	50.8	4C	polished
91-97	8+00E	79-45	54	4E	polished
91-98	8+00E	79-45	57	4E	polished
91-99	8+00E	79-45	59	4C	thin
91-100	8+00E	79-45	61.5	4A	thin
91-101	8+00E	79-45	64.5	4C	thin
91-102	8+00E	79-45	73	4D	polished
91-103	8+00E	79-45	76	4C	polished
91-104	8+00E	79-45	78	4C	polished
91-105	8+00E	79-45	79.5	4C	polished
91-106	8+00E	79-45	82.5	4C	polished
91-107	8+00E	79-45	84.5	4C	polished

Appendix 1

Diamond drill core sample locations

91-108	8+00E	79-45	87	4C	thin
19-109	8+00E	79-45	89	3	thin
91-110	8+00E	79-45	139.5	3	polished
91-111	8+00E	79-45	162	3	thin
91-112	8+00E	79-45	165.5	4C	polished
91-113	8+00E	79-45	167	4C	polished
91-114	8+00E	79-45	169	4C	polished
91-115	8+00E	79-45	171	4A	thin
91-116	8+00E	79-45	173	4C	polished
91-117	8+00E	79-45	176	4A	polished
91-118	8+00E	79-45	178	4E	thin
91-119	8+00E	79-45	183	3	thin
91-120	8+00E	79-45	199	3	thin
91-121	8+00E	79-303	29.5	4H	polished
91-122	8+00E	79-303	30	4A	thin
91-123	8+00E	79-303	31.5	4C	polished
91-124	8+00E	79-303	32	4C	thin
91-125	8+00E	79-303	32.8	4G	thin
91-126	8+00E	79-303	36.5	4C	thin
91-127	8+00E	79-303	38	4A	thin
91-128	8+00E	79-303	40.5	4C	polished
91-129	8+00E	79-303	44.5	4E	polished
91-130	8+00E	79-303	45.5	4G	polished
91-131	8+00E	79-303	47.5	4C	polished
91-132	8+00E	79-303	49.5	4C	thin
91-133	8+00E	79-303	54.5	4H	polished
91-134	8+00E	79-303	57	4C	polished
91-135	8+00E	79-303	64.5	4C	thin
91-136	8+00E	79-303	65	4C	thin
91-137	8+00E	79-303	69	4C	polished
91-138	8+00E	79-303	82	3	thin
91-139	8+00E	79-303	111	4E	polished
91-140	4+00E	79-33	29	4G	thin
91-141	4+00E	79-33	34.5	4G	thin
91-142	4+00E	79-33	36	4E	polished
91-143	4+00E	79-33	43.5	4C	polished
91-144	4+00E	79-33	46	4G	thin
91-145	4+00E	79-33	47.5	4G	polished
91-146	4+00E	79-33	50	4C	polished
91-147	4+00E	79-33	53	4G	thin
91-148	4+00E	79-33	61.5	3	thin

4A = ribbon-banded, carbonaceous quartzite
4C = pyritic quartzite

Appendix 1

Diamond drill core sample locations

4E = massive pyritic sulphides

4G = baritic, massive pyritic sulphides

4H = pyrrhotite - sphalerite -galena massive sulphides

APPENDIX 2

Thermobarometry Calculations

Appendix 2

Thermobarometry calculations

A2.1 Chlorite thermometry

Chlorite thermometry is based on the cation site occupancy as a function of temperature, in particular the increase of $Al_{(IV)}$ on the tetrahedral site with an increase in temperautre (Cathelineau & Nieva 1985; Cathelineau 1988). The equation used to calculate temperature from chlorite composition is based on the systematic increase of the tetrahedral $Al_{(IV)}$ occupancy with temperature is;

$$T\ (^{\circ}C) = -61.92 + 321.98Al_{(IV)} \quad \text{(Cathelineau 1988)}$$

(on the basis of 18 O, OH)

A2.2 Arsenopyrite thermometry

Arsenopyrite thermometry is based on the increase in atomic% As in arsenopyrite buffered by pyrite + pyrrhotite or pyrrhotite and can be solved graphically using the method outlined by Kretschmar & Scott (1976). Similarly the log fS_2 can be solved graphically following the procedure of Kretschmar & Scott (1976) and Sharp *et al.* (1985).

The fugacity of S_2 and the activity of FeS in pyrrhotite used in the pyrrhotite-indicator method are calculated as;

$$\log fS_2 = (70.03 - 85.83N)(1000/T - 1) + 39.30\sqrt{(1 - 0.9981N)} - 11.91 \quad \text{(Toulmin \& Barton 1966)}$$

A2.3 Sphalerite + hexagonal pyrrhotite (+ pyrite) barometry

The sphalerite geobarometer is based on the decreasing content of FeS in sphalerite with increasing pressure when buffered by pyrite + hexagonal pyrrhotite or by hexagonal

pyrrhotite (Barton & Toulmin 1966; Scott & Barnes 1971; Scott 1971, 1976; Hutchison & Scott 1981; Bryndzia *et al.* 1988, 1990). For the purpose of this study two equations were used;

For the sphalerite + hexagonal pyrrhotite + pyrite barometer

$$P\ (kb) = 42.30 - 32.10 \log \text{mole } \%FeS_{(sp)} \quad \text{(Hutchison \& Scott 1981)}$$

where mole % FeS used in this equation in this paper is calculated to be

$$\text{Mol}\%_{FeS} = [(Fe/(Fe + S))/(S/(Fe + S))]$$

and for the sphalerite + hexagonal pyrrhotie barometer

$$P(kb) = 27.982 \log \gamma_{FeS}^{sp} - 8.549\ (\pm 0.5kb) \quad \text{(Bryndzia } et\ al. \text{ 1990)}$$

where γ, the activity coefficient, is calculated by

$$a_{FeS}/X_{FeS}^{sp},\ (X_{FeS}^{sp} = M_{FeS}/100)$$

and

$$\log a_{FeS} = 85.83(1000/T - 1)(1 - N + \ln N) + 39.30\sqrt{(1 - 09981N)} - 39.23\tanh^{-1}\sqrt{(1 - 0.9981N)} - 0.002 \quad \text{(Toulmin \& Barton 1966)}$$

where

$$N_{FeS} = 2(Fe/(Fe + S))$$

similarly a_{FeS} can be calculated as;

$$\ln a_{FeS} = -\{\ln r + B((r - 1)/r)^2\} \qquad \text{(Rau 1976)}$$

$$B = 3.160 + 22269/T$$

Temperature in all these calculations is in °K.

APPENDIX 3

Microprobe Data

Chlorite Sample 90-110

	A1-A1	A1-A2	A1-A3	A1-A4	A1-B1	A1-B2
SiO2	25.90	23.73	26.27	24.66	26.04	24.72
TiO2	0.04	0.05	0.05	0.07	0.03	0.08
Al2O3	18.95	21.70	18.62	20.67	18.64	20.87
FeO	26.61	30.91	29.54	31.20	29.63	30.71
MnO	0.55	0.59	0.42	0.62	0.38	0.48
MgO	12.32	11.09	13.20	11.68	13.06	11.35
CaO	0.03	0.04	0.01	0.01	0.00	0.00
Na2O	0.00	0.03	0.00	0.03	0.01	0.04
K2O	0.00	0.00	0.05	0.00	0.00	0.00
TOTAL	84.40	88.14	88.16	88.94	87.79	88.25
Si IV	2.81	2.58	2.82	2.65	2.81	2.67
Al IV	1.19	1.42	1.18	1.35	1.19	1.33
T site	4.00	4.00	4.00	4.00	4.00	4.00
Al VI	1.23	1.36	1.18	1.28	1.18	1.33
Ti	0.00	0.00	0.00	0.01	0.00	0.01
Fe +2	2.69	2.81	2.65	2.81	2.68	2.78
Mn	0.05	0.05	0.04	0.06	0.03	0.04
Mg	1.99	1.80	2.11	1.88	2.10	1.83
Ca	0.00	0.00	0.00	0.00	0.00	0.00
Na	0.00	0.00	0.00	0.01	0.00	0.01
K	0.00	0.01	0.01	0.00	0.00	0.00
O site	5.97	6.03	6.00	6.03	6.00	6.00
O	9.87	9.93	9.95	10.01	9.91	9.95
OH	8.13	8.07	8.05	7.99	8.09	8.05
Charge	0.13	0.07	0.05	0.01	0.09	0.05

	A1-B2*	A1-C1	A1-C2	A1-C3	A1-D1	A1-D2
SiO2	25.41	26.06	24.76	24.04	25.95	23.78
TiO2	0.06	0.08	0.08	0.06	0.05	0.02
Al2O3	21.74	19.15	19.90	21.46	19.21	21.61
FeO	29.22	28.66	31.26	30.84	29.59	31.16
MnO	0.39	0.04	0.30	0.50	0.57	0.42
MgO	11.52	12.54	10.34	11.00	13.00	10.83
CaO	0.04	0.00	0.04	0.00	0.03	0.05
Na2O	0.03	0.01	0.02	0.00	0.01	0.08
K2O	0.03	0.02	0.01	0.02	0.00	0.00
TOTAL	88.44	86.56	86.71	87.92	88.41	87.95
Si IV	2.71	2.83	2.74	2.61	2.78	2.59
Al IV	1.29	1.17	1.26	1.39	1.22	1.41
T site	4.00	4.00	4.00	4.00	4.00	4.00
Al VI	1.44	1.27	1.33	1.36	1.21	1.37
Ti	0.00	0.01	0.01	0.01	0.00	0.00
Fe +2	2.60	2.60	2.89	2.81	2.65	2.84
Mn	0.04	0.04	0.03	0.05	0.05	0.04
Mg	1.83	2.03	1.70	1.78	2.08	1.76
Ca	0.00	0.00	0.00	0.00	0.00	0.01
Na	0.01	0.00	0.01	0.00	0.00	0.02
K	0.00	0.00	0.00	0.00	0.00	0.00
O site	5.93	5.95	5.97	6.01	6.00	6.03
O	9.97	9.84	98.00	9.91	9.97	9.91
OH	8.03	8.16	8.20	8.09	8.03	8.09
Charge	0.03	0.16	0.20	0.09	0.03	0.09

Chlorite Sample 90-110

	A2-A1	A2-A1*	A2-A2	A2-A3	A2-A4	A2-A6
SiO2	25.19	26.98	23.37	26.60	25.28	28.16
TiO2	0.07	0.07	0.09	0.05	0.00	0.07
Al2O3	19.87	21.16	21.65	21.67	19.41	22.24
FeO	30.57	28.43	31.17	28.48	31.38	25.99
MnO	0.48	0.47	0.46	0.38	0.51	0.47
MgO	11.72	11.07	10.47	10.80	12.05	9.49
CaO	0.00	0.00	0.00	0.00	0.00	0.07
Na2O	0.05	0.00	0.03	0.03	0.00	0.01
K2O	0.03	0.00	0.00	0.01	0.02	0.03
TOTAL	87.98	88.18	87.24	88.02	88.65	86.53
Si IV	2.73	2.86	2.57	2.82	2.73	2.98
Al IV	1.27	1.14	1.43	1.18	1.27	1.02
T site	4.00	4.00	4.00	4.00	4.00	4.00
Al VI	1.27	1.50	1.38	1.54	1.20	1.76
Ti	0.01	0.01	0.01	0.00	0.00	0.01
Fe +2	2.77	2.52	2.87	2.53	2.84	2.30
Mn	0.04	0.04	0.04	0.03	0.05	0.04
Mg	1.89	1.75	1.72	1.71	1.94	1.50
Ca	0.00	0.00	0.00	0.00	0.00	0.01
Na	0.01	0.00	0.01	0.01	0.00	0.00
K	0.00	0.00	0.00	0.00	0.00	0.00
O site	6.00	5.82	6.02	5.82	6.03	5.63
O	9.92	9.96	9.85	9.94	9.99	9.82
OH	8.08	8.04	8.15	8.06	8.01	
Charge	0.08	0.04	0.15	0.06	0.01	0.18

Chlorite Sample 90.28

	B1-A1	B1-B1	B1-C1	B1-C2	B1-E1	B1-E2
SiO2	23.73	23.93	24.60	24.50	24.55	23.94
TiO2	0.07	0.07	0.09	0.05	0.09	0.08
Al2O3	19.84	19.84	20.05	19.53	19.45	20.13
FeO	35.65	35.16	34.07	34.82	34.17	34.87
MnO	1.86	1.83	1.87	1.67	1.74	1.57
MgO	7.32	7.33	7.48	7.79	7.76	7.23
CaO	0.02	0.10	0.11	0.10	0.03	0.07
Na2O	0.00	0.02	0.00	0.01	0.00	0.05
K2O	0.04	0.01	0.13	0.02	0.05	0.03
TOTAL	88.53	88.29	88.40	88.49	87.84	87.97
Si IV	2.66	2.68	2.73	2.73	2.74	2.68
Al IV	1.34	1.32	1.27	1.27	1.26	1.32
T site	4.00	4.00	4.00	4.00	4.00	4.00
Al VI	1.28	1.30	1.35	1.28	1.30	1.34
Ti	0.01	0.01	0.01	0.00	0.01	0.01
Fe +2	3.34	3.29	3.16	3.24	3.19	3.27
Mn	0.18	0.17	0.18	0.16	0.17	0.15
Mg	1.22	1.22	1.24	1.29	1.29	1.21
Ca	0.00	0.01	0.01	0.01	0.00	0.01
Na	0.00	0.00	0.00	0.00	0.00	0.01
K	0.01	0.00	0.02	0.00	0.01	0.00
O site	6.03	6.01	5.96	5.99	5.97	5.99
O	9.94	9.92	9.94	9.94	9.88	9.89
OH	8.06	8.08	8.06	8.06	8.12	8.11
Charge	0.06	0.08	0.06	0.06	0.12	0.11

	B1-F1	B1-F2	B1-G1	B2-A1	B2-A2	B2-C1
SiO2	23.72	23.56	23.61	24.90	23.72	24.19
TiO2	0.00	0.01	0.01	0.06	0.09	0.04
Al2O3	20.59	20.95	21.00	20.76	20.53	20.35
FeO	35.14	35.70	35.10	34.26	34.52	36.10
MnO	2.02	1.77	1.86	1.23	1.42	1.64
MgO	7.12	6.91	6.99	6.90	6.88	7.35
CaO	0.00	0.00	0.00	0.02	0.01	0.00
Na2O	0.01	0.01	0.04	0.00	0.01	0.00
K2O	0.03	0.08	0.23	1.09	0.25	0.09
TOTAL	88.63	88.99	88.84	89.22	87.43	89.76
Si IV	2.64	2.62	2.63	2.74	2.67	2.67
Al IV	1.36	1.38	1.37	1.26	1.33	1.33
T site	4.00	4.00	4.00	4.00	4.00	4.00
Al VI	1.35	1.37	1.38	1.43	1.39	1.31
Ti	0.00	0.00	0.01	0.00	0.01	0.00
Fe +2	3.28	3.32	3.29	3.15	3.25	3.33
Mn	0.19	0.17	0.16	0.11	0.14	0.15
Mg	1.18	1.15	1.14	1.13	1.15	1.21
Ca	0.00	0.00	0.00	0.00	0.00	0.00
Na	0.00	0.00	0.00	0.00	0.00	0.00
K	0.00	0.01	0.01	0.15	0.04	0.01
O site	6.01	6.01	6.00	5.99	5.98	6.01
O	9.95	9.98	9.96	10.01	9.84	10.05
OH	8.05	8.02	8.04	7.99	8.16	7.95
Charge	0.05	0.02	0.04	0.01	0.16	0.00

Chlorite Sample 90.28

	B2-C2	B2-D1	B2-D2	B2-E1	B2-E2
SiO2	24.17	24.11	25.83	23.89	24.39
TiO2	0.03	0.00	0.34	0.01	0.00
Al2O3	19.48	19.90	20.13	20.63	19.88
FeO	35.27	34.81	33.73	34.50	35.21
MnO	1.69	1.55	1.18	1.70	1.36
MgO	7.61	7.76	6.48	7.57	7.65
CaO	0.01	0.00	0.03	0.00	0.00
Na2O	0.01	0.00	0.00	0.03	0.00
K2O	0.02	0.00	1.74	0.12	0.03
TOTAL	88.29	88.13	89.46	88.45	88.52
Si IV	2.70	2.69	2.83	2.66	2.71
Al IV	1.30	1.31	1.17	1.34	1.29
T site	4.00	4.00	4.00	4.00	4.00
Al VI	1.27	1.31	1.43	1.36	1.32
Ti	0.00	0.00	0.03	0.00	0.00
Fe +2	3.30	3.25	3.09	3.21	3.27
Mn	0.16	0.15	0.11	0.16	0.13
Mg	1.27	1.29	1.06	1.25	1.27
Ca	0.00	0.00	0.00	0.00	0.00
Na	0.00	0.00	0.00	0.01	0.00
K	0.00	0.00	0.24	0.02	0.00
O site	6.01	6.00	5.96	6.00	5.99
O	9.92	9.91	10.03	9.94	9.94
OH	8.08	8.09	7.97	8.06	8.06
Charge	0.08	0.09	0.00	0.06	0.06

Chlorite Sample 90-128

	C1-A1	C1-A2	C1-B1	C1-B2	C1-C1	C1-D1
SiO2	23.97	24.58	24.15	24.53	23.67	24.33
TiO2	0.02	0.00	0.11	0.21	0.18	0.16
Al2O3	22.00	21.21	21.30	21.62	22.14	21.30
FeO	29.04	29.19	29.14	28.96	28.62	28.83
MnO	0.27	0.21	0.17	0.25	0.18	0.32
MgO	12.33	12.55	12.46	12.36	11.75	12.65
CaO	0.05	0.03	0.04	0.00	0.02	0.17
Na2O	0.02	0.01	0.02	0.00	0.00	0.00
K2O	0.04	0.00	0.00	0.02	0.02	0.06
TOTAL	87.78	87.39	87.95	86.58	87.82	87.05
Si IV	2.58	2.65	2.62	2.63	2.58	2.62
Al IV	1.42	1.35	1.38	1.37	1.42	1.38
T site	4.00	4.00	4.00	4.00	4.00	4.00
Al VI	1.38	1.34	1.33	1.37	1.43	1.32
Ti	0.00	0.00	0.01	0.02	0.01	0.01
Fe +2	2.62	2.63	2.64	2.60	2.61	2.60
Mn	0.03	0.02	0.02	0.02	0.02	0.03
Mg	1.98	2.01	2.01	1.98	1.91	2.03
Ca	0.01	0.00	0.00	0.00	0.00	0.02
Na	0.00	0.00	0.00	0.00	0.00	0.00
K	0.01	0.00	0.00	0.00	0.00	0.01
O site	6.02	6.01	6.02	5.99	5.98	6.02
O	9.91	9.91	9.88	9.93	9.80	9.91
OH	8.09	8.09	8.12	8.07	8.20	8.09
Charge	0.09	0.09	0.12	0.07	0.20	0.09

	C1-E1	C1-E2	C1-F1	C1-F2	C1-G1	C2-A1
SiO2	24.35	23.87	23.92	24.46	23.89	25.24
TiO2	0.09	0.11	0.06	0.03	0.14	0.17
Al2O3	21.24	21.70	21.55	21.04	21.65	20.57
FeO	28.67	28.77	29.19	28.22	29.27	28.35
MnO	0.26	0.29	0.27	0.22	0.25	0.25
MgO	12.37	12.30	12.47	12.39	12.44	13.23
CaO	0.06	0.00	0.00	0.00	0.00	0.09
Na2O	0.00	0.05	0.00	0.01	0.01	0.02
K2O	0.01	0.00	0.00	0.01	0.00	0.00
TOTAL	87.09	87.46	86.38	87.65	87.92	87.46
Si IV	2.64	2.59	2.59	2.67	2.58	2.70
Al IV	1.36	1.41	1.41	1.33	1.42	1.30
T site	4.00	4.00	4.00	4.00	4.00	4.00
Al VI	1.36	1.37	1.34	1.37	1.34	1.29
Ti	0.01	0.01	0.01	0.00	0.01	0.01
Fe +2	2.60	2.61	2.64	2.57	2.65	2.54
Mn	0.02	0.03	0.02	0.02	0.02	0.02
Mg	2.00	1.99	2.01	2.01	2.00	2.11
Ca	0.01	0.00	0.00	0.00	0.00	0.01
Na	0.00	0.01	0.00	0.00	0.00	0.00
K	0.00	0.00	0.00	0.00	0.00	0.00
O site	6.00	6.02	6.03	5.98	6.03	5.99
O	9.85	9.85	9.88	9.78	9.90	9.93
OH	8.15	8.15	8.12	8.22	8.10	8.07
Charge	0.15	0.15	0.12	0.22	0.10	0.07

Chlorite Sample 90-128

	C2-A2	C2-B1	C2-B2	C2-C1	C2-C2	C2-D1	C2-D2
SiO2	24.66	24.09	25.78	23.84	24.57	24.70	25.18
TiO2	0.17	0.12	0.24	0.12	0.26	0.09	0.22
Al2O3	21.04	21.66	20.45	21.60	21.05	21.08	19.92
FeO	28.42	28.77	28.78	28.26	28.07	28.84	28.15
MnO	0.20	0.33	0.26	0.28	0.31	0.19	0.10
MgO	12.91	12.13	12.92	12.36	12.46	12.98	13.56
CaO	0.05	0.04	0.08	0.05	0.06	0.13	0.08
Na2O	0.00	0.02	0.00	0.02	0.00	0.01	0.00
K2O	0.01	0.01	0.00	0.00	0.00	0.05	0.00
TOTAL	87.17	88.51	86.53	86.78	88.07	87.21	87.21
Si IV	2.66	2.61	2.74	2.60	2.66	2.65	2.71
Al IV	1.34	1.39	1.26	1.40	1.34	1.35	1.29
T site	4.00	4.00	4.00	4.00	4.00	4.00	4.00
Al VI	1.33	1.38	1.30	1.37	1.35	1.31	1.25
Ti	0.01	0.01	0.02	0.01	0.02	0.01	0.02
Fe +2	2.56	2.61	2.56	2.58	2.55	2.58	2.54
Mn	0.02	0.03	0.02	0.03	0.03	0.02	0.01
Mg	2.07	1.96	2.05	2.01	2.01	2.07	2.18
Ca	0.01	0.01	0.01	0.01	0.01	0.01	0.01
Na	0.00	0.00	0.00	0.00	0.00	0.00	0.00
K	0.00	0.00	0.00	0.00	0.00	0.01	0.00
O site	6.00	6.00	5.96	6.01	5.97	6.02	6.00
O	9.89	9.86	9.98	9.80	9.82	9.94	9.86
OH	8.11	8.14	8.02	8.20	8.18	8.06	8.14
Charge	0.11	0.14	0.02	0.20	0.18	0.06	0.14

Arsenopyrite Sample 90-125

	A1 AS1 CORE		A1 AS2 RIM		A1 AS2 CORE	
	wt. %	at. %	wt. %	at. %	wt. %	at. %
Cu	0.01	0.01	0.00	0.00	.O47	0.04
Fe	35.70	34.06	34.95	33.72	36.10	34.20
S	20.90	34.72	20.91	35.14	21.30	35.14
As	43.83	31.17	43.14	31.03	43.19	30.50
Co	0.00	0.00	0.00	0.00	0.00	0.00
Ni	0.00	0.00	0.12	0.11	0.09	0.08
Au	0.14	0.04	0.00	0.00	0.00	0.00
Zn	0.00	0.00	0.00	0.00	0.02	0.02
Ag	0.02	0.01	0.00	0.00	0.03	0.02
Pb	0.00	0.00	0.00	0.00	0.00	0.00
Total	100.59	100.00	99.11	100.00	100.77	100.00

	A1 AS3 CORE		A1 AS4 RIM		A1 AS5 CORE	
	wt. %	at. %	wt. %	at. %	wt. %	at. %
Cu	0.13	0.11	0.05	0.04	0.15	0.12
Fe	35.84	34.08	35.73	33.96	35.56	33.90
S	21.42	35.47	21.43	35.47	21.35	35.44
As	42.73	30.28	43.06	30.50	42.80	30.41
Co	0.01	0.01	0.01	0.01	0.00	0.00
Ni	0.00	0.00	0.00	0.00	0.14	0.12
Au	0.04	0.01	0.09	0.02	0.00	0.00
Zn	0.00	0.00	0.00	0.00	0.01	0.00
Ag	0.08	0.04	0.00	0.00	0.00	0.00
Pb	0.00	0.00	0.00	0.00	0.00	0.00
Total	100.25	100.00	100.37	100.00	99.99	100.00

	A1 AS6 RIM		A1 AS7 CORE		A1 AS8 RIM	
	wt. %	at. %	wt. %	at. %	wt. %	at. %
Cu	0.00	0.00	0.00	0.00	0.01	0.01
Fe	35.39	33.99	36.18	34.11	35.45	33.80
S	21.31	35.64	21.61	35.49	21.60	35.87
As	42.20	30.20	43.08	30.27	42.46	30.18
Co	0.01	0.01	0.03	0.02	0.02	0.02
Ni	0.06	0.06	0.07	0.06	0.03	0.03
Au	0.00	0.00	0.18	0.00	0.00	0.00
Zn	0.12	0.10	0.00	0.00	0.11	0.09
Ag	0.00	0.00	0.00	0.00	0.03	0.01
Pb	0.00	0.00	0.00	0.00	0.00	0.00
Total	99.09	100.00	101.14	100.00	99.70	100.00

	A1 AS9 CORE		A1 AS10 CORE		A1 AS11 CORE	
	wt. %	at. %	wt. %	at. %	wt. %	at. %
Cu	0.02	0.01	0.01	0.01	0.00	0.00
Fe	35.60	34.09	35.99	34.38	35.13	33.65
S	20.76	34.63	21.31	35.46	21.31	35.56
As	43.78	31.26	42.31	30.13	43.01	30.71
Co	0.00	0.00	0.00	0.00	0.01	0.01
Ni	0.00	0.00	0.00	0.00	0.00	0.00
Au	0.00	0.00	0.00	0.00	0.00	0.00
Zn	0.00	0.00	0.04	0.03	0.09	0.07
Ag	0.00	0.00	0.00	0.00	0.01	0.00
Pb	0.00	0.00	0.00	0.00	0.00	0.00
Total	100.16	100.00	99.66	100.00	99.56	100.00

Arsenopyrite Sample 90-131

	B1 AS1 CORE		B1 AS2 RIM		B1 AS3 CORE	
	wt. %	at. %	wt. %	at. %	wt. %	at. %
Cu	0.00	0.00	0.10	0.09	0.00	0.00
Fe	36.46	34.45	35.89	34.35	35.71	34.13
S	22.12	36.40	20.85	34.74	21.43	35.67
As	41.33	29.11	43.13	30.77	42.24	30.09
Co	0.03	0.02	0.00	0.00	0.02	0.02
Ni	0.00	0.00	0.03	0.03	0.00	0.00
Au	0.00	0.00	0.09	0.02	0.05	0.01
Zn	0.02	0.01	0.00	0.00	0.03	0.03
Ag	0.01	0.00	0.00	0.00	0.00	0.00
Pb	0.00	0.00	0.00	0.00	0.21	0.05
Total	99.96	100.00	100.10	100.00	99.70	100.00

	B1 AS4 RIM		B1 AS5 CORE		B1 AS6 CORE	
	wt. %	at. %	wt. %	at. %	wt. %	at. %
Cu	0.02	0.01	0.10	0.08	0.01	0.01
Fe	35.62	33.92	35.65	34.04	35.64	34.04
S	21.35	35.41	21.02	34.96	21.18	35.25
As	43.11	30.60	43.29	30.81	43.03	30.64
Co	0.06	0.05	0.01	0.01	0.03	0.02
Ni	0.00	0.00	0.04	0.03	0.00	0.00
Au	0.00	0.00	0.00	0.00	0.00	0.00
Zn	0.00	0.00	0.07	0.06	0.00	0.00
Ag	0.00	0.00	0.02	0.01	0.08	0.04
Pb	0.00	0.00	0.00	0.00	0.00	0.00
Total	100.17	100.00	100.19	100.00	99.97	100.00

	B1 AS7 CORE		8 CORE		B1 AS9 CORE	
	wt. %	at. %	wt. %	at. %	wt. %	at. %
Cu	0.00	0.00	0.05	0.04	0.15	0.12
Fe	36.15	34.54	35.47	33.84	35.87	34.18
S	21.05	35.03	21.08	35.02	21.15	35.11
As	42.70	30.41	43.49	30.93	42.96	30.52
Co	0.02	0.02	0.00	0.00	0.01	0.01
Ni	0.00	0.00	0.17	0.15	0.00	0.00
Au	0.00	0.00	0.00	0.00	0.08	0.02
Zn	0.00	0.00	0.00	0.00	0.04	0.04
Ag	0.00	0.00	0.03	0.01	0.00	0.00
Pb	0.00	0.00	0.00	0.00	0.00	0.00
Total	99.92	100.00	100.30	100.00	100.30	100.00

	B1 AS10 CORE		B1 AS11 RIM		B1 AS12 CORE	
	wt. %	at. %	wt. %	at. %	wt. %	at. %
Cu	0.17	0.14	0.13	0.11	0.00	0.00
Fe	35.78	33.99	35.89	34.06	35.77	34.22
S	21.51	35.60	21.37	35.32	20.97	34.93
As	42.66	30.21	43.11	30.50	43.17	30.79
Co	0.06	0.06	0.00	0.00	0.06	0.00
Ni	0.00	0.00	0.00	0.00	0.00	0.00
Au	0.00	0.00	0.03	0.01	0.00	0.00
Zn	0.00	0.00	0.00	0.00	0.04	0.03
Ag	0.00	0.00	0.02	0.01	0.06	0.03
Pb	0.00	0.00	0.00	0.00	0.00	0.00
Total	100.18		100.53		100.01	

	B1 AS13 CORE		B1 AS14 CORE		B1 AS15 CORE	
	wt. %	at. %	wt. %	at. %	wt. %	at. %
Cu	0.10	0.09	0.00	0.00	0.00	0.00
Fe	35.74	34.09	35.81	34.20	36.28	34.45
S	20.89	34.71	21.38	35.57	21.10	34.88
As	43.54	30.96	42.41	30.19	43.11	30.51
Co	0.04	0.04	0.03	0.03	0.01	0.01
Ni	0.08	0.08	0.00	0.00	0.12	0.11
Au	0.15	0.04	0.01	0.00	0.00	0.00
Zn	0.00	0.00	0.00	0.00	0.05	0.04
Ag	0.00	0.00	0.01	0.01	0.00	0.00
Pb	0.00	0.00	0.00	0.00	0.00	0.00
Total	100.56	100.00	99.66	100.00	100.67	100.00

	B1 AS16 CORE		B1 AS17 CORE		B1 AS18 RIM	
	wt. %	at. %	wt. %	at. %	wt. %	at. %
Cu	0.06	0.05	0.12	0.10	0.02	0.02
Fe	36.00	34.05	36.35	34.64	35.82	34.25
S	21.56	35.51	20.93	34.74	20.94	34.87
As	43.10	30.38	42.94	30.50	43.12	30.73
Co	0.00	0.00	0.02	0.02	0.02	0.02
Ni	0.00	0.00	0.00	0.00	0.08	0.08
Au	0.00	0.00	0.00	0.00	0.00	0.00
Zn	0.05	0.00	0.00	0.00	0.03	0.02
Ag	0.01	0.00	0.00	0.00	0.02	0.01
Pb	0.00	0.00	0.00	0.00	0.00	0.00
Total	100.73	100.00	100.37	100.00	100.06	100.00

	B1 AS19 CORE		AS20 RIM		B1 AS21 CORE	
	wt. %	at. %	wt. %	at. %	wt. %	at. %
Cu	0.12	0.10	0.07	0.06	0.10	0.08
Fe	35.79	34.24	35.70	34.02	35.31	34.02
S	20.92	34.86	21.46	35.62	20.86	35.01
As	43.11	30.74	42.63	30.28	42.91	30.82
Co	0.04	0.03	0.03	0.02	0.03	0.03
Ni	0.00	0.00	0.00	0.00	0.00	0.00
Au	0.01	0.00	0.00	0.00	0.04	0.01
Zn	0.03	0.02	0.00	0.00	0.02	0.02
Ag	0.00	0.00	0.00	0.00	0.03	0.02
Pb	0.02	0.01	0.00	0.00	0.00	0.00
Total	100.01	100.00	99.89	100.00	99.29	100.00

	B1 AS22 CORE		B1 AS23 CORE		B1 AS24 CORE	
	wt. %	at. %	wt. %	at. %	wt. %	at. %
Cu	0.08	0.07	0.04	0.03	0.00	0.00
Fe	36.66	34.50	36.27	34.49	36.73	34.61
S	22.29	36.53	21.45	35.53	21.68	35.59
As	40.95	28.72	42.18	29.90	42.15	29.61
Co	0.00	0.00	0.01	0.00	0.02	0.02
Ni	0.10	0.09	0.00	0.00	0.18	0.16
Au	0.02	0.01	0.01	0.00	0.01	0.00
Zn	0.10	0.08	0.05	0.04	0.03	0.02
Ag	0.02	0.01	0.02	0.01	0.00	0.00
Pb	0.00	0.00	0.00	0.00	0.00	0.00
Total	100.21	100.00	100.02	100.00	100.79	100.00

Arsenopyrite Sample 90-131

	B2 AS1 CORE		B2 AS2 RIM		B2 AS3 CORE	
	wt. %	at. %	wt. %	at. %	wt. %	at. %
Cu	0.10	0.08	0.00	0.00	0.03	0.02
Fe	34.48	33.52	36.23	34.47	36.13	34.55
S	20.83	35.28	21.14	35.04	20.88	34.79
As	42.92	31.10	42.85	30.39	42.80	30.51
Co	0.00	0.00	0.00	0.00	0.00	0.00
Ni	0.00	0.00	0.08	0.08	0.07	0.06
Au	0.00	0.00	0.01	0.00	0.05	0.01
Zn	0.02	0.02	0.02	0.02	0.04	0.03
Ag	0.00	0.00	0.00	0.00	0.03	0.02
Pb	0.00	0.00	0.00	0.00	0.00	0.00
Total	98.35		100.34		100.02	

	B2 AS4 RIM		B2 AS5 CORE		B2 AS6 RIM	
	wt. %	at. %	wt. %	at. %	wt. %	at. %
Cu	0.00	0.00	0.01	0.01	0.10	0.08
Fe	35.98	34.01	36.39	34.39	35.19	33.76
S	21.74	35.79	21.55	35.47	21.26	35.53
As	42.46	29.91	42.72	30.09	42.75	30.57
Co	0.03	0.03	0.05	0.05	0.01	0.01
Ni	0.28	0.25	0.00	0.00	0.05	0.04
Au	0.05	0.01	0.00	0.00	0.00	0.00
Zn	0.00	0.00	0.00	0.00	0.00	0.00
Ag	0.00	0.00	0.00	0.00	0.01	0.01
Pb	0.00	0.00	0.00	0.00	0.00	0.00
Total	100.54		100.72		99.37	

	B2 AS7 CORE		B2 AS8 CORE		B2 AS9 CORE	
	wt. %	at. %	wt. %	at. %	wt. %	at. %
Cu	0.12	0.10	0.05	0.04	0.00	0.00
Fe	35.56	33.91	36.06	34.36	35.85	34.50
S	21.61	35.89	21.89	36.33	20.83	34.92
As	42.18	29.98	41.16	29.23	42.57	30.54
Co	0.00	0.00	0.02	0.02	0.04	0.04
Ni	0.09	0.08	0.00	0.00	0.00	0.00
Au	0.00	0.00	0.00	0.00	0.01	0.00
Zn	0.03	0.03	0.00	0.00	0.00	0.00
Ag	0.02	0.01	0.00	0.00	0.00	0.00
Pb	0.00	0.00	0.04	0.01	0.00	0.00
Total	100.72		99.23		99.31	

	B2 AS10 CORE	
	wt. %	at. %
Cu	0.00	0.00
Fe	35.61	33.96
S	21.82	36.23
As	41.77	29.69
Co	0.02	0.02
Ni	0.13	0.11
Au	0.00	0.00
Zn	0.00	0.00
Ag	0.02	0.00
Pb	0.00	0.00
Total	99.35	

Sphalerite compositions

	90-132Asp8	90-132A2sp1	90-132A2sp2	90-132A2sp3	90-132A2sp6
	at. %	at. %	at. %	at. %	at. %
Cu	0.00	0.02	0.00	0.08	0.03
Fe	9.22	9.27	10.06	9.52	8.60
S	50.01	48.90	50.41	48.95	49.09
As	0.00	0.04	0.00	0.01	0.03
Co	0.00	0.01	0.01	0.01	0.01
Ni	0.03	0.00	0.00	0.03	0.00
Au	0.00	0.00	0.00	0.00	0.00
Zn	40.74	41.75	39.51	41.40	42.23
Ag	0.00	0.00	0.02	0.00	0.00
Pb	0.00	0.00	0.00	0.00	0.00
Total	100.00	100.00	100.00	100.00	100.00

	90-132A2sp7	90-129B2aS1	90-129B2aS2	90-129B2as3	90-129B2as4
	at. %	at. %	at. %	at. %	at. %
Cu	0.01	0.03	0.00	0.00	0.00
Fe	8.87	8.17	8.91	6.01	5.66
S	49.12	49.47	48.90	49.22	49.62
As	0.02	0.00	0.00	0.00	0.00
Co	0.02	0.01	0.00	0.01	0.00
Ni	0.02	0.00	0.00	0.06	0.00
Au	0.00	0.00	0.00	0.00	0.00
Zn	41.94	42.31	42.19	44.69	44.69
Ag	0.00	0.01	0.00	0.02	0.02
Pb	0.00	0.00	0.00	0.00	0.00
Total	100.00	100.00	100.00	100.00	100.00

	90-129B2as5	90-129B2bs1	90-129B2bs2	90-129B2bs3	90-129B2cs1
	at. %	at. %	at. %	at. %	at. %
Cu	0.01	0.03	0.00	0.00	0.01
Fe	5.80	7.85	5.40	6.70	9.21
S	49.31	49.24	49.47	49.10	49.73
As	0.00	0.00	0.06	0.03	0.00
Co	0.00	0.01	0.00	0.01	0.00
Ni	0.00	0.05	0.00	0.02	0.00
Au	0.00	0.00	0.00	0.00	0.00
Zn	44.88	42.82	45.06	44.14	41.05
Ag	0.00	0.01	0.01	0.00	0.00
Pb	0.00	0.00	0.00	0.00	0.00
Total	100.00	100.00	100.00	100.00	100.00

Sphalerite compositions

	90-129B2cs2	90-129B2cs3	90-129B1as1	90-129B1as2	90-129B1as3
	at. %	at. %	at. %	at. %	at. %
Cu	0.03	0.00	0.01	0.05	0.01
Fe	6.76	7.03	7.84	5.44	8.35
S	49.16	49.51	48.48	48.23	49.22
As	0.00	0.04	0.03	0.00	0.01
Co	0.00	0.00	0.00	0.01	0.00
Ni	0.06	0.00	0.00	0.00	0.00
Au	0.00	0.00	0.00	0.00	0.00
Zn	43.97	43.42	43.62	46.26	42.40
Ag	0.02	0.00	0.02	0.00	0.01
Pb	0.00	0.00	0.00	0.00	0.00
Total	100.00	100.00	100.00	100.00	100.00

	90-129B1bs1	90-129B1bs2	90-129B1cs3	90-68a2s1	90-68A2s2
	at. %	at. %	at. %	at. %	at. %
Cu	0.02	0.07	0.00	0.03	0.02
Fe	6.48	8.53	6.03	8.42	8.90
S	48.16	48.46	48.83	52.22	51.56
As	0.00	0.00	0.04	0.02	0.00
Co	0.00	0.01	0.00	0.03	0.03
Ni	0.09	0.05	0.00	0.00	0.00
Au	0.00	0.00	0.00	0.00	0.00
Zn	45.25	42.87	45.10	39.28	39.49
Ag	0.00	0.02	0.00	0.00	0.00
Pb	0.00	0.00	0.00	0.00	0.00
Total	100.00	100.00	100.00	100.00	100.00

	90-68A2s4	90-68A2s5	90-68A2s7	90-68A2s8	90-68A2s9
	at. %	at. %	at. %	at. %	at. %
Cu	0.00	0.04	0.03	0.10	0.04
Fe	8.55	8.55	8.39	8.32	8.60
S	51.92	52.06	52.11	51.82	51.24
As	0.00	0.01	0.02	0.02	0.02
Co	0.01	0.01	0.03	0.02	0.03
Ni	0.00	0.01	0.00	0.00	0.00
Au	0.00	0.00	0.00	0.00	0.00
Zn	39.52	39.31	39.42	39.71	40.06
Ag	0.00	0.00	0.00	0.00	0.00
Pb	0.00	0.00	0.00	0.00	0.00
Total	100.00	100.00	100.00	100.00	100.00

Sphalerite compositions

	90-68A2s10	90-68A2s11	90-68A2s12	90-68A2s13	90-68A2s14
	at. %	at. %	at. %	at. %	at. %
Cu	0.00	0.00	0.00	0.07	0.00
Fe	8.41	8.35	8.35	8.26	8.37
S	51.72	51.97	51.70	51.93	51.64
As	0.00	0.00	0.02	0.00	0.00
Co	0.04	0.02	0.03	0.02	0.03
Ni	0.05	0.04	0.00	0.13	0.00
Au	0.00	0.00	0.00	0.00	0.00
Zn	39.77	39.62	39.90	39.59	39.95
Ag	0.00	0.00	0.00	0.00	0.00
Pb	0.00	0.00	0.00	0.00	0.00
Total	100.00	100.00	100.00	100.00	100.00

	90-68A2s15	90-68A216	90-68a2s17	90-68A2s18	90-68A2s19
	at. %	at. %	at. %	at. %	at. %
Cu	0.03	0.01	0.03	0.02	0.00
Fe	8.50	8.18	8.41	8.25	8.48
S	51.99	52.11	51.89	52.08	51.80
As	0.03	0.00	0.00	0.00	0.00
Co	0.02	0.01	0.00	0.02	0.03
Ni	0.07	0.02	0.06	0.00	0.01
Au	0.00	0.00	0.00	0.00	0.00
Zn	39.36	39.66	39.61	39.62	39.68
Ag	0.00	0.00	0.00	0.00	0.00
Pb	0.00	0.00	0.00	0.00	0.00
Total	100.00	100.00	100.00	100.00	100.00

	90-68a2s20	90-68A2s21	90-68A2s22	90-68A2s23	90-68A2s24
	at. %	at. %	at. %	at. %	at. %
Cu	0.05	0.03	0.05	0.00	0.01
Fe	9.26	8.33	8.05	8.41	8.44
S	51.04	51.61	51.87	51.90	52.06
As	0.03	0.00	0.00	0.00	0.03
Co	0.00	0.04	0.01	0.02	0.02
Ni	0.03	0.00	0.00	0.00	0.00
Au	0.00	0.00	0.00	0.00	0.00
Zn	39.59	39.98	40.02	39.67	39.44
Ag	0.00	0.00	0.00	0.00	0.00
Pb	0.00	0.00	0.00	0.00	0.00
Total	100.00	100.00	100.00	100.00	100.00

Sphalerite compositions

	90-68A2s25	90-68A2s26	90-68A2s27	90-54A1s4	90-54A1s5
	at. %	at. %	at. %	at. %	at. %
Cu	0.07	0.00	0.02	0.01	0.00
Fe	8.37	8.09	8.59	7.50	7.64
S	52.10	52.04	51.61	49.88	49.56
As	0.00	0.01	0.00	0.03	0.01
Co	0.00	0.01	0.01	0.01	0.00
Ni	0.00	0.00	0.03	0.00	0.03
Au	0.00	0.00	0.00	0.00	0.00
Zn	39.45	39.85	39.75	42.57	42.75
Ag	0.00	0.00	0.00	0.00	0.00
Pb	0.00	0.00	0.00	0.00	0.00
Total	100.00	100.00	100.00	100.00	100.00

	90-54A1s6	90-54a1s7	90-54A1s8	90-54A1s9	90-54A1s11
	at. %	at. %	at. %	at. %	at. %
Cu	0.02	0.03	0.00	0.01	0.05
Fe	7.44	7.52	7.51	7.78	7.63
S	49.55	49.22	49.66	49.79	49.61
As	0.02	0.01	0.03	0.01	0.06
Co	0.00	0.01	0.01	0.00	0.01
Ni	0.00	0.02	0.05	0.01	0.00
Au	0.00	0.00	0.00	0.00	0.00
Zn	42.96	43.21	42.72	42.38	42.63
Ag	0.00	0.00	0.02	0.02	0.01
Pb	0.00	0.00	0.00	0.00	0.00
Total	100.00	100.00	100.00	100.00	100.00

	90-54A1s12	90-54A1s13	90-54A1s15	90-54A1s16	90-54A1s18
	at. %	at. %	at. %	at. %	at. %
Cu	0.01	0.02	0.01	0.03	0.02
Fe	8.15	7.85	7.74	8.13	7.54
S	49.62	49.82	49.26	48.91	49.64
As	0.01	0.03	0.00	0.02	0.00
Co	0.00	0.01	0.00	0.00	0.01
Ni	0.00	0.00	0.01	0.02	0.00
Au	0.00	0.00	0.00	0.00	0.00
Zn	42.21	42.27	42.98	42.89	42.80
Ag	0.00	0.00	0.00	0.00	0.00
Pb	0.00	0.00	0.00	0.00	0.00
Total	100.00	100.00	100.00	100.00	100.00

Sphalerite compositions

	90-54A1s19	90-54A1s20	90-54A1s21	909-54A1s22	90-54A1s23
	at. %	at. %	at. %	at. %	at. %
Cu	0.00	0.04	0.02	0.00	0.02
Fe	7.29	7.61	7.44	8.10	7.96
S	49.45	49.48	49.25	49.17	49.71
As	0.01	0.04	0.02	0.00	0.00
Co	0.00	0.01	0.01	0.02	0.00
Ni	0.05	0.00	0.00	0.02	0.00
Au	0.00	0.00	0.00	0.00	0.00
Zn	43.18	42.82	43.13	42.68	42.30
Ag	0.02	0.00	0.00	0.01	0.00
Pb	0.00	0.00	0.11	0.00	0.00
Total	100.00	100.00	100.00	100.00	100.00

	90-54A2s2	90-54A2s3	90-54a2s4	90-54A2s5	90-54A2s6
	at. %	at. %	at. %	at. %	at. %
Cu	0.03	0.02	0.05	0.01	0.06
Fe	7.52	7.70	7.56	8.00	7.81
S	49.43	49.03	49.52	48.95	49.55
As	0.03	0.00	0.00	0.02	0.00
Co	0.00	0.02	0.00	0.00	0.00
Ni	0.00	0.00	0.00	0.00	0.00
Au	0.00	0.00	0.00	0.00	0.00
Zn	42.99	43.23	42.87	43.02	42.58
Ag	0.00	0.00	0.00	0.00	0.00
Pb	0.00	0.00	0.00	0.00	0.00
Total	100.00	100.00	100.00	100.00	100.00

	90-54A2s7	90-54A2s8	90-54A2s9	90-54A2s10	90-54A2s11
	at. %	at. %	at. %	at. %	at. %
Cu	0.01	0.01	0.00	0.02	0.03
Fe	7.95	7.63	7.45	7.48	7.16
S	49.16	49.26	49.84	49.84	49.64
As	0.02	0.00	0.02	0.05	0.01
Co	0.00	0.00	0.01	0.01	0.00
Ni	0.00	0.01	0.00	0.03	0.01
Au	0.00	0.00	0.00	0.00	0.00
Zn	42.85	43.09	42.68	42.58	43.15
Ag	0.00	0.00	0.00	0.00	0.00
Pb	0.00	0.00	0.00	0.00	0.00
Total	100.00	100.00	100.00	100.00	100.00

Sphalerite compositions

	90-54A2s12	90-54A2s15	90-54A2s17	90-24b1s1	90-24B1s4
	at. %	at. %	at. %	at. %	at. %
Cu	0.00	0.03	0.00	0.01	0.03
Fe	7.64	7.45	7.38	8.07	7.81
S	49.55	49.42	49.59	50.23	50.45
As	0.01	0.04	0.03	0.01	0.00
Co	0.00	0.00	0.00	0.00	0.01
Ni	0.01	0.00	0.00	0.00	0.00
Au	0.00	0.00	0.00	0.00	0.00
Zn	42.79	43.06	43.00	41.67	41.69
Ag	0.00	0.00	0.00	0.00	0.00
Pb	0.00	0.00	0.00	0.00	0.00
Total	100.00	100.00	100.00	100.00	100.00

	90-24B1s5	90-24B1s6	90-24B2s10	90-24B2s12	90-24B2s15
	at. %	at. %	at. %	at. %	at. %
Cu	0.03	0.01	0.01	0.00	0.00
Fe	7.78	8.18	7.93	7.81	7.92
S	50.33	50.23	49.20	49.51	49.54
As	0.01	0.02	0.00	0.00	0.00
Co	0.00	0.00	0.01	0.00	0.00
Ni	0.05	0.00	0.00	0.06	0.01
Au	0.00	0.00	0.00	0.00	0.00
Zn	41.79	41.56	42.86	42.62	42.52
Ag	0.00	0.00	0.00	0.00	0.02
Pb	0.00	0.00	0.00	0.00	0.00
Total	100.00	100.00	100.00	100.00	100.00

	90-24B2s18	90-24B2s20
	at. %	at. %
Cu	0.00	0.03
Fe	7.59	7.78
S	49.39	49.31
As	0.01	0.00
Co	0.00	0.00
Ni	0.00	0.00
Au	0.00	0.00
Zn	43.02	42.88
Ag	0.00	0.00
Pb	0.00	0.00
Total	100.00	100.00

Sample		Atm. %	N FeS
90-68 A1po3	Fe	46.57	0.93
	S	53.37	
90-68A1po4	Fe	47.45	0.95
	S	52.42	
90-68A1po6	Fe	47.30	0.95
	S	52.66	
90-68A1po7	Fe	47.57	0.95
	S	52.35	
90-68A1po8	Fe	46.85	0.94
	S	53.09	
90-68A1po9	Fe	47.05	0.94
	S	52.70	
90-68A1po10	Fe	47.29	0.95
	S	52.51	
90-68A1po11	Fe	46.73	0.94
	S	53.22	
90-68A1po12	Fe	47.49	0.95
	S	52.36	
90-68A1po13	Fe	47.42	0.95
	S	52.52	
90-68A1po14	Fe	47.16	0.95
	S	52.62	
90-68A1po16	S	47.36	0.95
		52.46	
90-68A2po2	Fe	47.07	0.94
	S	52.60	
90-68A2po3	Fe	47.12	0.95
	S	52.49	
90-68A2po4	Fe	46.77	0.94
	S	53.06	
90-68A2po5	Fe	46.69	0.93
	S	53.19	
90-68A2po6	Fe	47.21	0.95
	S	52.60	
90-68A2po7	Fe	46.77	0.94
	S	53.15	
90-68A2po8	Fe	46.68	0.94
	S	53.12	
90-68A2po9	Fe	47.39	0.95
	S	52.44	
90-68A2po10	Fe	47.58	0.95
	S	52.33	
90-68A1po15	Fe	47.15	0.94
	S	52.66	

Sample		Atm. %	N FeS
90-68A2po11	Fe	46.67	0.93
	S	53.26	
90-68AA2po12	Fe	46.59	0.93
	S	53.19	
90-68A2po13	Fe	46.44	0.93
	S	53.44	
90-68A2po14	Fe	47.40	0.95
	S	52.42	
90-68A2po15	Fe	46.60	0.94
	S	53.06	
90-68A2po16	Fe	46.97	0.94
	S	52.94	
90-68A2po16	Fe	47.22	0.95
	S	52.45	
90-132Apo1	Fe	46.61	0.93
	S	53.19	
90-132Apo2	Fe	46.70	0.93
	S	53.20	
90-132Apo3	Fe	46.06	0.93
	S	53.06	
90-132Apo4	Fe	46.91	0.94
	S	52.75	
90-132Apo5	Fe	46.97	0.94
	S	52.93	
90-129B1po1	Fe	46.84	0.94
	S	53.01	
90-129B1po2	Fe	46.66	0.93
	S	53.21	
90-129B1po3	Fe	47.01	0.94
	S	52.93	
90-129B1po4	Fe	46.85	0.94
	S	52.84	
90-131B1po1	Fe	46.03	0.92
	S	53.62	
90-131B1po2	Fe	46.31	0.93
	S	53.38	
90-131B1po3	Fe	46.56	0.93
	S	53.22	
90-131B1po4	Fe	46.36	0.93
	S	53.51	
90-131B1po5	Fe	46.43	0.93
	S	53.46	
90-54A1po12	Fe	46.53	0.93
	S	53.32	

Sample		Atm. %	N FeS
90-131B1po6	Fe	47.16	0.95
	S	52.62	
90-131B1po1	Fe	46.70	0.93
	S	53.24	
90-131B2po2	Fe	46.94	0.94
	S	52.93	
90-131B2po3	Fe	46.96	0.94
	S	52.73	
90-54A1po4	Fe	47.07	0.94
	S	52.78	
90-54A1po5	Fe	46.70	0.94
	S	53.15	
90-54A1po6	Fe	46.96	0.94
	S	52.81	
90-54A1po7	Fe	47.04	0.94
	S	52.65	
90-54A1po8	Fe	46.54	0.93
	S	53.25	
90-54A1po10	Fe	47.55	0.95
	S	52.28	
90-54A1po11	Fe	46.88	0.94
	S	52.84	
90-54A2po2	Fe	47.37	0.95
	S	52.54	
90-54A2po3	Fe	47.57	0.95
	S	52.30	
90-54A2po5	Fe	47.23	0.95
	S	52.64	
90-54A2po6	Fe	46.62	0.93
	S	53.23	
90-54A2po7	Fe	47.17	0.94
	S	52.75	
90-54A2po8	Fe	46.94	0.94
	S	52.82	
90-54A2po9	Fe	47.27	0.95
	S	52.62	
90-54A2po10	Fe	47.42	0.95
	S	52.39	
90-54A2po11	Fe	47.21	0.95
	S	52.47	
90-54A2po12	Fe	47.41	0.95
	S	52.31	

Sample		Atm. %	N FeS
90-54A1po13	Fe	46.83	0.94
	S	52.94	
90-54a1po14	Fe	46.55	0.93
	S	53.27	
90-54A1po15	Fe	46.44	0.93
	S	53.29	
90-54A1po16	Fe	46.49	0.93
	S	53.20	
90-54A1po17	Fe	47.10	0.94
	S	52.73	
90-54A1po18	Fe	46.24	0.93
	S	53.66	
90-54A1po19	Fe	46.85	0.94
	S	53.05	
90-54A121	Fe	46.51	0.93
	S	53.32	
90-54A1po22	Fe	46.60	0.93
	S	53.22	
90-54A2po1	Fe	47.34	0.95
	S	52.50	
90-54A2po14	Fe	46.70	0.94
	S	53.16	
90-24B1po1	Fe	45.98	0.93
	S	52.74	
90-24B1po2	Fe	46.53	0.93
	S	53.26	
90-24B1po3	Fe	46.76	0.94
	S	53.13	
90-24B1po5	Fe	46.92	0.94
	S	52.98	
90-24B1po6	Fe	46.44	0.93
	S	53.37	
90-24B1po7	Fe	47.24	0.95
	S	52.55	
90-24B1po9	Fe	47.78	0.96
	S	52.06	
90-24B1po10	Fe	47.32	0.95
	S	52.48	
90-24B2po11	Fe	46.73	0.94
	S	53.19	
90-24B2po12	Fe	46.56	0.93
	S	53.15	

Sample		Atm. %	N FeS
90-24B2po13	Fe	46.96	0.94
	S	52.81	
90-24B2po14	Fe	46.58	0.93
	S	53.24	
90-24B2po15	Fe	46.75	0.94
	S	53.04	
90-24B2po16	Fe	47.04	0.94
	S	52.86	
90-24B2po17	Fe	46.83	0.94
	S	53.00	
90-24B2po18	Fe	46.95	0.94
	S	53.01	
90-24B2po20	Fe	46.98	0.94
	S	52.81	
90-54A2po13	Fe	47.34	0.95
	S	52.38	

APPENDIX 4

Pressure and Temperature Data

SAMPLE 90-110

point	Al+4(tet)	T (C)	average	2σ
A1-A1	1.19	321	352	29
A1-A2	1.42	395		
A1-A3	1.18	318		
A1-A4	1.35	373		
A1-B1	1.19	321		
A1-B2	1.33	366		
A1-B2?	1.29	353		
A1-C1	1.17	315		
A1-C2	1.26	344		
A1-C3	1.39	386		
A1-D1	1.22	331		
A1-D2	1.41	392		
A2-A1	1.27	347		
A2-A2	1.43	399		
A2-A3	1.18	318		
A2-A4	1.27	347		

SAMPLE 90-28

point	Al+4(tet)	T (C)	average	2σ
B1-A1	1.34	370	360	17
B1-B1	1.32	363		
B1-C1	1.27	347		
B1-C2	1.27	347		
B1-E1	1.26	344		
B1-E2	1.32	363		
B1-F1	1.36	376		
B1-F2	1.38	382		
B1-G1	1.37	379		
B1-G2	1.39	386		
B2-A1	1.26	344		
B2-A2	1.33	366		
B2-C1	1.33	366		
B2-C2	1.30	357		
B2-D1	1.31	360		
B2-D2	1.17	315		
B2-E1	1.34	370		
B2-E2	1.29	353		

SAMPLE 90-120

point	Al+4(tet)	T (C)	average	2σ
C1-A1	1.42	395	378	14
C1-A2	1.35	373		
C1-B1	1.38	382		
C1-B2	1.37	379		
C1-C1	1.42	395		
C1-D1	1.38	382		
C1-E1	1.36	376		
C1-E2	1.41	392		
C1-F1	1.41	392		
C1-F2	1.33	366		
C1-G1	1.42	395		
C2-A1	1.30	357		
C2-A2	1.34	370		
C2-B1	1.39	386		
C2-B2	1.26	344		
C2-C1	1.40	389		
C2-C2	1.34	370		
C2-D1	1.35	373		
C2-D2	1.29	353		
C2-E1	1.39	386		
C2-E2	1.41	392		

Arsenopyrite Sample 90-131

	comp. (wt. %)			total	comp. (at. %)			mineral assemblage	T (C)*	log f (S2)*	T (C)	log$f$S2
	Fe	S	As		Fe	S	As					
As. 2 rim	35.89	20.85	43.13	99.87	34.35	34.74	30.77	po - py(?)	349	-8.62	336	-8.99
As. 3 core	35.71	21.43	42.24	99.38	34.13	35.67	30.09	po - py(?)	306	-9.83	$2\sigma = 17$	$2\sigma = 0.465$
As. 4 rim	35.62	21.35	43.11	100.08	33.92	35.41	30.61	po - py(?)	339	-8.91	n = 26	n = 26
As. 5	35.65	21.02	43.29	99.96	34.04	34.96	30.81	po - py(?)	352	-8.55		
As. 6	35.64	21.18	43.03	99.85	34.04	35.25	30.64	po - py(?)	341	-8.85		
As. 7	36.15	21.05	42.71	99.91	34.54	35.03	30.41	po - py(?)	326	-9.26		
As. 8	35.47	21.08	43.49	100.04	33.84	35.02	30.93	po - py(?)	359	-8.34		
As. 9	35.87	21.15	42.96	99.98	34.18	35.11	30.52	po - py(?)	333	-9.07		
As. 10 core	35.78	21.51	42.66	99.95	33.99	35.61	30.21	py - po(?)	314	-9.62		
As. 11 rim	35.89	21.37	43.11	100.37	34.06	35.32	30.51	py - po(?)	333	-9.09		
As. 12	35.77	20.97	43.17	99.91	34.22	34.93	30.79	po - py(?)	350	-8.59		
As. 13	35.74	20.89	43.54	100.17	34.09	34.71	30.96	po - py(?)	361	-8.28		
As. 14	35.81	21.38	42.41	99.60	34.21	35.57	30.19	po - py(?)	312	-9.66		
As. 15	36.28	21.09	43.11	100.48	34.45	34.88	30.51	po - py(?)	333	-9.09		
As. 16	36.01	21.56	43.11	100.68	34.05	35.51	30.38	po - py(?)	324	-9.32		
As. 17 core	36.35	20.93	42.94	100.22	34.64	34.74	30.51	py - po(?)	333	-9.09		
As. 18 rim	35.82	20.94	43.12	99.88	34.25	34.87	30.73	py - po(?)	347	-8.69		
As. 19 core	35.79	20.92	43.11	99.82	34.24	34.86	30.74	py - po(?)	347	-8.68		
As. 20 rim	35.71	21.46	42.63	99.80	34.02	35.62	30.28	py - po(?)	318	-9.50		
As. 21	35.31	20.86	42.91	99.08	34.02	35.01	30.82	py - po(?)	352	-8.53		
As. 25 core	34.48	20.83	42.92	98.23	33.52	35.28	31.11	po - py(?)	371	-8.02		
As. 26 rim	36.23	21.14	42.85	100.22	34.47	35.04	30.39	po - py(?)	325	-9.30		
As. 27 core	36.13	20.88	42.81	99.82	34.55	34.79	30.51	po - py(?)	333	-9.09		
As. 29 core	36.39	21.55	42.72	100.66	34.39	35.47	30.09	po + py	306	-9.83		
As. 30 rim	35.19	21.26	42.75	99.20	33.76	35.53	30.57	po + py	336	-8.98		
As. 33	35.85	20.83	42.57	99.25	34.51	34.92	30.54	po - py(?)	335	-9.03		

Arsenopyrite Sample 90-125

	comp. (wt. %)				comp. (at. %)			mineral assemblag	T (C)*	log f (S2)*	T (C)	log f(S2)
	Fe	S	As	total	Fe	S	As					
As. 1 Cor	35.71	20.91	43.83	100.45	34.06	34.72	31.17	po - py(?)	375	-7.91	335	-9.00
As. 2 Rim	34.95	20.91	43.14	99.00	33.72	35.14	31.03	po - py(?)	366	-8.16	2σ= 25.33	2σ = 0.709
As. 3 Cor	35.84	21.42	42.73	99.99	34.08	35.47	30.28	py - po(?)	318	-9.50	11	n = 11
As. 4 Rim	35.73	21.43	43.06	100.22	33.96	35.47	30.51	py - po(?)	333	-9.09		
As. 5 Cor	35.56	21.35	42.79	99.70	33.91	35.44	30.41	py - po(?)	326	-9.26		
As. 6 Rim	35.39	21.31	42.21	98.91	33.99	35.64	30.21	py - po(?)	314	-9.62		
As. 7 Cor	36.17	21.61	43.08	100.86	34.11	35.49	30.27	py - po(?)	317	-9.51		
As. 8 Rim	35.45	21.59	42.46	99.50	33.81	35.87	30.18	py - po(?)	312	-9.67		
As. 9	35.61	20.76	43.78	100.15	34.09	34.63	31.26	py - po(?)	380	-7.75		
As. 10	35.99	21.31	42.31	99.61	34.38	35.46	30.13	po + py	308	-9.76		
As. 11	35.13	21.31	43.01	99.45	33.65	35.56	30.71	po + py	345	-8.73		

*Calculated using the calibration of Sharp et al. (1985)

Sphalerite inclusions in pyrite

Sample 90-129

sp	Mol% FeS	P (kb)*	average	2σ
b2as1	16.52	3.20	5.15	2.46
b2as2	18.22	1.84		
b2as3	12.21	7.42		
b2as4	11.41	8.36		
b2as5	11.76	7.94		
b2bs1	15.94	3.70		
b2bs2	10.92	8.97		
b2bs3	13.65	5.86		
b2cs1	18.52	1.61		
b2cs2	13.75	5.76		
b2cs3	14.20	5.31		
b1as1	16.17	3.50		
b1as2	11.28	8.52		
b1as3	16.96	2.84		
b1bs1	13.46	6.06		
b1bs2	17.60	2.32		
b1cs3	12.35	7.26		
b1cs4	17.62	2.30		

Sample 90-132

sp	Mol% FeS	P (kb)*	average	2σ
a2sp8	18.44	1.67	1.46	0.61
a2sp1	18.96	1.28		
a2sp2	19.96	0.56		
a2sp3	19.45	0.93		
a2sp6	17.52	2.38		
a2sp7	18.06	1.96		

*Calculated using the equation of Hutchison and Scott (1981)

SAMPLE 90-68

po	sp	a FeS po*	a FeS po~	Mol% FeS	γ	P (kb)	mean	2σ
a2po4	a2s17	0.49	0.52	16.21	3.02	4.85	5.73	1.49
a2po4	a2s18	0.49	0.52	15.84	3.09	5.13		
a2po3	a2s7	0.58	0.60	16.10	3.60	6.98		
a2po6	a2s24	0.58	0.60	16.21	3.58	6.89		
a2po7	a2s23	0.48	0.51	16.20	2.96	4.61		
a2po8	a2s19	0.47	0.50	16.37	2.87	4.23		
a2po9	a2s20	0.61	0.63	18.14	3.36	6.14		
a2po9	a2s21	0.61	0.63	16.14	3.78	7.56		
a2po13	a2s16	0.42	0.45	15.70	2.68	3.37		
a2po11	a2s11	0.46	0.49	16.07	2.86	4.19		
a2po12	a2s10	0.46	0.49	16.26	2.83	4.05		
a2po10	a2s8	0.64	0.66	16.06	3.99	8.20		
a2po16	a2s15	0.52	0.55	16.35	3.18	5.47		
a2po5	a2s13	0.52	0.55	15.91	3.27	5.80		
a2po5	a2s24	0.47	0.50	16.07	2.92	4.45		
a2po14	a2s27	0.62	0.64	16.15	3.84	7.75		
a2po14	a2s14	0.62	0.64	16.21	3.82	7.70		

SAMPLE 90-24

po	sp	a FeS po*	a FeS po~	Mol% FeS				
b1po5	b1s1	0.51	0.54	16.07	3.17	5.44	6.51	1.37
b1po7	b1s4	0.59	0.61	15.48	3.81	7.66		
b1po9	b1s5	0.69	0.71	15.46	4.46	9.57		
b1po10	b1s6	0.60	0.62	16.29	3.68	7.24		
b2po5	b2s10	0.49	0.51	16.12	3.04	4.92		
b2po16	b2s12	0.54	0.56	15.77	3.42	6.36		
b2po17	b2s15	0.50	0.53	15.99	3.13	5.26		
b2po18	b2s18	0.51	0.54	15.37	3.32	5.98		
b2po20	b2s20	0.53	0.56	15.78	3.36	6.13		

SAMPLE 90-54

po	sp	a FeS po*	a FeS po~	Mol% Fes				
a1po4	a1s1	0.55	0.57	15.04	3.66	7.16	6.25	1.70
a1po5	a1s5	0.47	0.50	15.42	3.05	4.95		
a1po6	a1s6	0.53	0.56	15.02	3.53	6.72		
a1po7	a1s7	0.55	0.58	15.28	3.60	6.97		
a1po8	a1s8	0.45	0.48	15.12	2.98	4.66		
a1po11	a1s11	0.52	0.55	15.38	3.38	6.21		
a1po13	a1s12	0.51	0.53	16.42	3.11	5.18		
a1po15	a1s13	0.44	0.46	15.76	2.79	3.89		
a1po16	a1s15	0.45	0.48	15.71	2.86	4.20		
a1po17	a1s18	0.55	0.58	15.19	3.62	7.04		
a1po18	a1s19	0.39	0.42	14.74	2.65	3.24		
a1po19	a1s20	0.50	0.52	15.38	3.25	5.73		
a1po21	a1s21	0.44	0.47	15.11	2.91	4.40		
a1po22	a1s23	0.46	0.48	16.01	2.87	4.24		
a2po2	a2s2	0.60	0.62	15.21	3.94	8.08		
a2po3	a2s3	0.64	0.67	15.70	4.08	8.47		
a2po5	a2s4	0.58	0.60	15.27	3.80	7.62		
a2po6	a2s5	0.46	0.49	16.34	2.82	3.99		
a2po7	a2s6	0.56	0.58	15.76	3.55	6.81		
a2po8	a2s7	0.53	0.55	16.17	3.28	5.83		
a2po9	a2s8	0.58	0.61	15.49	3.74	7.44		
a2po10	a2s9	0.62	0.64	14.95	4.15	8.68		
a2po11	a2s10	0.59	0.61	15.01	3.93	8.03		
a2po12	a2s11	0.63	0.65	14.42	4.37	9.31		
a2po13	a2s15	0.61	0.63	15.07	4.05	8.39		
a2po14	a2s17	0.47	0.50	14.88	3.16	5.38		

* Calculated using the equation of Toulmin and Barton (1964).
~ Calculated using the equation of Rau (1976).

Low temperature, low pressure deformation and metamorphism of the Vangorda massive sulphide orebody, Yukon, Canada

Dennis Brown

Department of Geology, Royal Holloway, University of London, Egham, Surrey, TW20 OEX, U.K.

Abstract

The Vangorda orebody a small stratiform massive sulphide orebody located in Anvil District, Yukon, Canada. The orebody consists of fine- to medium-grained semi-massive and massive sulphides with a common sulphide mineralogy of pyrite, pyrrhotite, sphalerite, galena, and minor chalcopyrite. The host rocks and the sulphide lithofacies have been complexly deformed during two phases of deformation (D_1 and D_2) and associated metamorphism (M_1 and M_2). The effects of D_1 and M_1 are penetratively overprinted by D_2 and M_2. D_2 and M_2 resulted in tight to isoclinal F_2 folding of the orebody, remobilisation of the sulphides, recrystallisation and development of shear zones along the limbs of the F_2 folds.

Chlorite thermometry and sulphide thermobarometry have been carried out on the host phyllites and on the sulphides. Chlorite was analysed from the S_1 and S_2 foliations in the phyllites to determine M_1 and M_2 temperatures, respectively. However, no difference was found between chlorite compositions in these foliations and a mean temperature of 363 °C was calculated from the tetrahedral Al_{IV} occupancy. Arsenopyrite thermometry yielded a comparable mean temperature of 336 °C. Sphalerite inclusions in M_2 pyrite porphyroblasts from D_2 shear zones were analysed for pressure using the sphalerite + hexagonal pyrrhotite + pyrite barometer. Inclusions were analysed in an attempt to determine if relic M_1 sphalerite, and hence pressure signature, was preserved. Inclusion compositions appear to reflect only M_2 conditions and yielded a mean pressure of 4.0 kb. Sphalerite + hexagonal pyrrhotite assemblages were analysed from D_2 shear zones to determine the M_2 pressure using the sphalerite + hexagonal pyrrhotite barometer. These calculations yielded a mean pressure of 6.1 kb. The M_2 temperatures and pressures calculated using these calibrations are in good agreement with those estimated from petrogenetic relationships.

Introduction

The Vangorda orebody is a polydeformed and polymetamorphosed (Brown and McClay, 1992, 1993a,b; Jennings and Jilson 1986; Tempelman-Kluit 1972), SEDEX-type (Carne and Cathro 1982) Pb-Zn-Ag massive sulphide deposit in the Anvil Mining District of Yukon, Canada (Fig. 1). The deposit had geological reserves of 7.1 million tonnes with a combined Pb + Zn grade of 7.7% (Jennings and Jilson 1986) and was mined as an open pit operation, from 1990 to 1992 by Curragh Inc. The dominant sulphide mineralogy consists of pyrite, sphalerite, galena, and pyrrhotite, with minor chalcopyrite and arsenopyrite. Magnetite is an important constituent locally. The deposit is hosted by muscovite + chlorite $\pm$ biotite phyllites. The orebody has been deformed and metamorphosed during two major deformation and metamorphic events.

In recent years there have been several calibrations of the pressure-temperature response of sulphide ores in hydrothermal systems and metamorphic terranes. These have incorporated either an empirical approach (e.g. Hutchison and Scott 1981) or a more rigorous thermodynamic approach (e.g. Bryndzia et al. 1988, 1990). Both these approaches have stemmed from a significant amount of research into the Fe - Zn - Cu - As - S systems (e.g. Toulmin and Barton 1964; Barton and Toulmin 1966; Barton 1969; Scott and Barnes 1971; Craig and Scott 1974; Rau 1976; Kretchmar and Scott 1976; Hutchison and Scott; Scott 1983; Sharp et al. 1985; Bryndzia et al. 1988). However, sulphides, because of their refractive nature, are often unreliable indicators of hydrothermal and metamorphic pressure and temperature conditions, and require careful petrographic and petrological analysis and cautious application of quantitative analysis to thermobarometry.

The phyllite hosting the Vangorda orebody do not have silicate mineral assemblages that can be used for thermobarometry. However, recent empirical calibrations of the $Al_{(IV)}$ tetrahedral site occupancy of chlorite as a function of temperature (Cathelineau and Nieva 1985, Cathelineau 1988) allows a determination of temperature conditions. Significantly, analyses of chlorite grains from within different textural locations (i.e. different foliations) can be made.

This paper provides the first detailed analyses of the pressure and temperature conditions of the deformation and metamorphic events affecting a orebody within the Anvil District during. Chlorite and sulphide assemblages are analysed from a number of textural relationships in an attempt to determine differences between the D_1/M_1 and D_2/M_2 events. This study is based on detailed, 1:200 scale, mapping of the orebody during its development as an open pit mine and 1:100 scale logging of diamond drill core.

Geological setting

The Anvil District (Fig. 1) is hosted by the Selwyn Basin (Jennings and Jilson 1986) in the northwestern Canadian Cordillera. Rocks in the Anvil District consist of late Precambrian to upper Paleozoic metasedimentary and metavolcanic rocks that have been intruded by mid-Cretaceous granitoid rocks of the Anvil Plutonic Suite (Pigage and Anderson 1985; Jennings and Jilson 1986). These rocks are structurally overlain by the allochthonous Yukon-Tanana terrane (Tempelman-Kluit 1979; Coney et al. 1980) and are adjacent to a major orogen-scale dextral strike-slip fault, the Tintina Fault.

Five deformation events (D_1 - D_5) have been recognised in the Anvil District, the first two of which (D_1 and D_2) are regionally extensive (Jennings and Jilson 1986). D_1 is interpreted to be related to the pre- to mid-Cretaceous docking of the allochthonous Yukon-Tanana terrane onto the continental margin (Tempelman-Kluit 1979), causing northeast-directed nappe emplacement, folding, thrusting and metamorphism (M_1) of the continental margin. D_1 deformation resulted in the development of northeast-verging F_1 folds and a penetrative regional foliation (S_1), and regional M_1 metamorphism to at least greenschist facies. D_2 deformation is related to emplacement, uplift, and unroofing of the Anvil Batholith (Jennings and Jilson 1986) causing southwest-directed folding, the development of a wavy, gently southwest-dipping, penetrative crenulation foliation (S_2), and greenschist to amphibolite facies metamorphism (M_2) (Smith and Erdmer 1990; Jennings and Jilson 1986; Pigage and Anderson 1985). Northwest or southeast - dipping, brittle to ductile extensional faults, related to

unroofing of the Anvil Batholith, are late- to post-D_2 folding (Pigage and Jilson 1985; Brown and McClay 1992, 1993b). Other many faults in the district have subhorizontal to shallowly-plunging slickensides, indicating at least a late phase of strike-slip movement (Brown and McClay 1992). The D_3 to D_5 deformation events produced minor folding and steeply dipping crenulation foliations that overprint the D_1 and D_2 structural elements, locally.

The lithostratigraphy of the Anvil District consists of polydeformed metasedimentary and metavolcanic rocks with a structural thickness of up to 5 km that have been intruded by Cretaceous granites. The massive sulphide deposits are hosted by, or straddle the boundary between two lithostratigraphic units, the Mt. Mye formation and the overlying Vangorda formation (Jennings and Jilson 1986). The Mount Mye formation consists of noncalcareous schist and phyllite and has a minimum structural thickness of 2 km, though its base is not exposed. The Vangorda formation consists of calcareous schist and phyllite and ranges from 0.5 to 2 km in structural thickness.

Metamorphism

Metamorphism in the Anvil District occurred during both the regional D_1 and D_2 deformation events (Tempelman-Kluit 1972; Jennings and Jilson 1986). Within the district, D_2 and M_2 have penetratively overprinted D_1 and M_1 structures and mineral assemblages. However, mineral assemblages that may represent M_1 are found in D_2 lithons, between the S_2 foliation, where they define the S_1 foliation (see Fig. 4a). The common mineral assemblage that defines S_1 is muscovite + chlorite + quartz, the same as that defining S_2, suggesting either comparable M_1 and M_2 conditions or recrystallisation of S_1 minerals during M_2.

The M_2 regional metamorphic grade in the Anvil District decreases outward from the Anvil Batholith in a Buchan-type facies series in which the biotite, garnet, andalusite, staurolite, and sillimanite isograds in the metapelites are concentric to the batholith (Tempelman-Kluit 1972; Smith and Erdmer 1990) (Fig. 2). An andalusite + staurolite + garnet + biotite + muscovite + quartz + plagioclase mineral assemblage is locally developed in the metapelites immediately

adjacent the batholith contact. Locally andalusite has altered to sillimanite (Pigage and Anderson 1985) and sillimanite is abundant in a roof pendant (Smith and Erdmer 1990). The absence of kyanite indicates pressure conditions of less than 4 kb. Along the northeast margin of the Anvil Batholith, the isograds are closely spaced and cut straight across topography, suggesting a steeply dipping contact. In the southwest, in the area encompassing the Vangorda deposit, the isograds are more widely spaced suggesting that the contact dips more shallowly.

Using petrogenetic relations Smith and Erdmer (1990) determined pressures and temperatures of the M_2 metamorphism of 3 kb and 400 - 500 °C for the chlorite + biotite zone and 600 - 620 °C for the biotite + almandine + sillimanite zone. However, pressure - temperature estimates using thermobarometry give spurious results, with pressure ranging from 2.8 - 10 kb and garnet + biotite temperatures ranging from 509 - 872 °C (Smith and Erdmer 1990). Limited sphalerite barometry by Kuo (1976) yielded a pressure of approximately 3 kb.

The Vangorda orebody

The Vangorda orebody consists of fine- to medium-grained semi massive and massive sulphides. Five sulphide lithofacies have been identified within the orebody with a typical sulphide mineralogy of pyrite, sphalerite, pyrrhotite, and galena (Brown and McClay 1993a; Jennings and Jilson 1986). The Vangorda orebody has an overall tabular shape, is elongate in a northwest-southeast orientation and plunges gently northwest, parallel to the regional F_2 fold axes. The orebody is approximately 900 m long by 200 m wide and varies in thickness from 20 m to 60 m.

The orebody has been penetratively deformed and metamorphosed during the regional D_1 and D_2 deformation and M_1 and M_2 metamorphic events and all ore lithofacies are tectonised (Brown and McClay in press). The Vangorda ores have been extensively recrystallised and the only primary depositional features found are rare colloform and framboidal pyrite textures

preserved in the cores of metamorphic pyrite porphyroblasts (Brown and McClay 1993a). The sulphide lithostratigraphic sequence in the Vangorda orebody is developed in the massive sulphide deposits throughout the district and may be a primary depositional feature (c.f. Jennings and Jilson 1986)

The oldest structure in the orebody is a penetrative S_1 muscovite $\pm$ chlorite + quartz foliation in both the host phyllite and the sulphides. F_1 folds have not been identified. The S_1 foliation is folded by southwest-verging, F_2 folds that plunge shallowly northwest or southeast. An axial planar S_2 muscovite + chlorite + quartz foliation is widespread in the phyllite and semi-massive sulphide but is only locally developed in the massive sulphide lithofacies. In the phyllite S_2 is defined by metamorphic muscovite and/or chlorite suggesting that peak D_2 deformation and M_2 metamorphism were coeval. Thickened hinges of F_2 folds suggest that remobilisation of the ore is common (Brown and McClay 1993b, Brown and McClay in press). Along the overturned limbs of F_2 folds and at lithofacies contacts, centimetre to metre-scale zones enriched in pyrrhotite, sphalerite, and galena are developed. Pyrite in these zones is typically retrograde euhedral porphyroblasts or rounded to subhedral porphyroclasts. These areas are commonly very-fine grained, have a well developed sulphide foliation and numerous shear-sense indicators such as winged and rotated clasts and inclusions and locally form 'durchbewegung' (Brown and McClay in press).

The orebody is cut by several extensional faults (Brown and McClay 1993b). It is truncated in the northwest by a steeply southeast-dipping post-F_2 extensional fault and in the southeast by a moderately to steeply south-dipping extensional fault. The orebody is cut approximately in half by a steeply to moderately northwest-dipping extensional fault. Late D_2 strike-slip faults offset all earlier structures.

The Vangorda orebody has macroscale and mesoscale geometries and textures that reflect extensive D_2 deformation, M_2 metamorphism and remobilisation (Brown and McClay 1992, 1993a,b). Drill holes cross sections through the orebody show a macroscale F_2 fold structure

with significant limb thinning and hinge zone thickening (Fig. 3). Extensive remobilisation appears to be dominant in the baritic massive sulphides which have deformed by cataclastic and plastic processes (Brown and McClay in press). As well, the fine grained pyrrhotite, sphalerite and galena -rich zones along the limbs and hinges of folds (Fig. 3) have a widespread occurrence of 'durchbewegung', shear-sense indicators such as σ and δ clasts and a well-developed pyrrhotitic foliation that provide strong evidence for their interpretation as shear zones (Brown and McClay in press). The position of these shear zones, in the limbs of F_2 folds, makes them favourable for the study D_2 deformation and M_2 metamorphic effects.

Thermobarometry

Microprobe operating conditions

All data were acquired by wave-length dispersive analyses using a Cameca SX50 automated electron microprobe at the University of Oviedo, Spain. Chlorite analyses were carried out using a natural standard with a beam current of 15nA, an accelerating voltage of 20 kV and a count time of 15 seconds. Sulphide analyses were carried out using synthetic pyrite, sphalerite, pyrrhotite, and arsenopyrite standards with a beam current of 30 nA, an accelerating voltage of 20 kV and a count time of 15 seconds. Data was corrected using ZAF corrections.

The equations used in the various temperature and pressure calculations in this paper are given in Appendix A.

Chlorite thermometry

Chlorite thermometry was carried out on phyllite from the Mount Mye formation to determine if a temperature difference exists between M_1 and M_2. For this purpose, samples were probed in which there was within-lithon S_1 chlorite and chlorite defining the S_2 crenulation foliation (Fig.

4a). Temperature estimates were calculated using the empirical equation derived by Cathelineau (1988).

Chlorite in lithons (i.e. defining S_1) have a mean tetrahedral site $Al_{(IV)}$ occupancy of 1.29 ($2\sigma = \pm 0.08$), corresponding to a mean temperature of 355 °C ($2\sigma = \pm 27$ °C) (Table 1). Chlorite defining the S_2 foliation have a mean tetrahedral site $Al_{(IV)}$ occupancy of 1.34 ($2\sigma = \pm 0.06$), corresponding to a mean temperature of 372 °C ($2\sigma = \pm 18$°C).

Arsenopyrite thermometry

Arsenopyrite forms subhedral to euhedral, 0.01 to 0.1 mm grains in grain-grain contact with pyrite and/or pyrrhotite (Fig. 4b). This provides an effective assemblage to buffer S_2 (Barton 1969). In several places, arsenopyrite forms overgrowths on pyrite. However, there is no increase in the As content in pyrite adjacent to the overgrowth. Arsenopyrite shows little compositional variation, with a mean of 30.60 ($2\sigma = \pm 0.30$) atomic % As (Table 2). Core - rim analyses and grain traverses show no appreciable variation in composition across grains.

Arsenopyrite temperatures calculated using the pyrrhotite + arsenopyrite + pyrite buffering curve are consistent with $Al_{(IV)}$ temperatures in chlorite, with a mean of 336 °C ($2\sigma = \pm 20$ °C) (Fig. 5a) and show no systematic variation related to the buffering assemblage or phase. Mean log fS_2 values of -8.99 ($2\sigma = \pm 0.55$) (Table 2) are obtained using the po - asp + py sulfidation curve of Barton (1969) at 336 °C. However, the fS_2 calculated using the pyrrhotite-indicator methods of Toulmin and Barton (1964) (Appendix A) for pyrrhotite of composition $Fe_{0.93}S$ co-existing with arsenopyrite, by both their equation and that of Rau (1976) gives mean log fS_2 values of -7.54 ($2\sigma = \pm 0.84$) and -7.34 ($2\sigma = \pm 0.78$), respectively. These latter fugacities at least one log unit less than that estimated for arsenopyrite and outside the stability range of

arsenopyrite in the Fe-As-S system (Fig. 5b).

Kretschmar and Scott (1976) pointed out that the application of arsenopyrite thermometry requires an estimate of $a\,S_2$. The mean log $a\,S_2$ at 336 °C was calculated using the equation of Rau (1976) to be -3.67 ($2\sigma = \pm 0.41$); this is outside the stability field of arsenopyrite (Fig. 5b).

Sphalerite + hexagonal pyrrhotite (+ pyrite) barometry

Sphalerite was analysed in two different textural relationships; as inclusions in pyrite using the sphalerite + hexagonal pyrrhotite + pyrite barometer (Hutchison and Scott 1981) and coexisting with hexagonal pyrrhotite using the sphalerite + hexagonal pyrrhotite barometer (Bryndzia *et al.* 1988, 1990). The only locations in which the correct mineral assemblages were found was D_2 sulphide shear zones along the limbs of F_2 folds (see Fig. 3). The minor element composition of all sphalerite analysed, including copper, is negligible.

Sphalerite inclusions in pyrite are generally 0.01 mm to 0.03 mm sized grains totally encapsulated by subhedral to euhedral pyrite (Fig. 4c). Pyrrhotite inclusions accompanying sphalerite were not found. However, sphalerite inclusions were selected in which pyrrhotite was in contact with the pyrite porphyroblast and in which pyrrhotite formed a significant proportion of the sample. These sphalerite grains have a mean mol% FeS of 15.62 ($2\sigma = \pm 2.87$) (Table 3) corresponding to a mean pressure of 3.98 kb ($2\sigma = \pm 2.7$) (Table 3).

Sphalerite + hexagonal pyrrhotite occur together in shear zones within the massive sulphide body as 0.02 to 0.1 mm subhedral to euhedral grains (Fig. 4d) commonly accompanied by galena. Locally, rare, fine-grained, retrograde equant to euhedral pyrite occurs but was avoided in these analyses. Chalcopyrite is rare in these shear zones and in general does not form an exsolved phase in sphalerite and so is easily avoided. Etched pyrrhotite grains locally have thin overgrowths to which a magnetitic colloid does not readily adhere suggesting they may be non-magnetic monoclinic pyrrhotite (c.f. Scott 1974). To avoid any possibility of the monoclinic

phase only pyrrhotite cores were analysed.

Pyrrhotite grains in the D_2 shear zones have a mean composition of $Fe_{0.94}S$ (Table 4) and coexist with sphalerite with a mean mole % FeS of 15.75 ($2\sigma = \pm 0.63$). The activity of FeS was calculated at 363 °C to be 0.53 ($2\sigma = \pm 0.07$) and 0.57 ($2\sigma = \pm 0.06$) using the equations of Toulmin and Barton (1964) and Rau (1976), respectively (Table 4). The composition of pyrrhotite and the low a_{FeS} indicate that pyrrhotite deviates from stochiometric FeS and lies on or near the pyrite + pyrrhotite solvus, although within the pyrite + pyrrhotite field at 5 kb (Fig. 6). The composition of pyrrhotite and the a_{FeS} in the Vangorda orebody D_2 shear zones are at the lower limit of the values used in the experiments of Bryndzia et al. (1988). However, the absence of pyrite suggests that the assemblage is applicable to the sphalerite + hexagonal pyrrhotite barometer.

Following Bryndzia et al. (1988, 1990) only the a_{FeS} of Toulmin and Barton (1964) was used in determining the activity coefficients. The mean activity coefficient (γ) in the sphalerite + hexagonal pyrrhotite assemblage is 3.38 ($2\sigma = + 0.443$) corresponding to a mean pressure of 6.1 kb ($2\sigma = \pm 1.58$ kb) (Table 4).

Discussion

The calibrations used to determine the temperature and pressure of metamorphism of the Vangorda orebody provide consistent values. The M_2 temperatures of 336 °C to 363 °C at pressures of 4 - 6 kb are in good agreement with those derived from petrogenetic relationships by Smith and Erdmer (1990). They provide quantitative evidence that the D_2 deformation and M_2 metamorphism occurred at low temperature and low pressure. Analyses of S_1 chlorite and of inclusions in pyrite yield temperatures and pressures similar to those that are unambiguously M_2 and suggest that the pressure and temperature conditions during M_1 may have been similar

to those during M_2 and the two cannot be distinguished. Alternatively, M_1 assemblages may have re-equlibrated during M_2 and reflect only M_2 temperature and pressure.

Chlorite temperatures determined from both S_1 and S_2 are similar and it is thought that compositions of chlorite grains in lithons (S_1) represent M_2 conditions. The average formula for the Vangorda chlorites is $(Fe_{2.83}Mg_{1.71}Al_{1.34}Mn_{0.07}Ti_{0.01})[(Al_{1.31}Si_{2.68})O_{9.95}](OH_{8.04})$ and the average temperature given by the total chlorite population is 363 °C ($2\sigma = \pm$ 24 °C). The S_2 foliation in the phyllite is defined by the chlorite and there is no evidence to suggest that it is a retrograde phases after biotite. The S_2 chlorite is therefore interpreted to represent a peak M_2 silicate mineral phase in the Vangorda orebody and 363 °C to be the peak M_2 temperature.

Temperatures of 336 °C estimated for arsenopyrite buffered by pyrite and/or pyrrhotite are consistent with those calculated for chlorite. The textural relationships of the arsenopyrite coexisting with pyrite (i.e. as overgrowths) indicate that it grew late it the metamorphic cycle, possibly during waning of the temperature and 336 °C is therefore interpreted to be a cooling temperature. The fS_2 and $a\ S_2$ calculated for pyrrhotite coexisting with arsenopyrite falls outside of the stability fields for these phases. This may be the result of re-equilibration of the pyrite + pyrrhotite assemblage and the decomposition and decrease in sulphur content of pyrrhotite during cooling (c.f. Craig and Vokes 1993).

Sphalerite inclusions in pyrite have a wide ranging mol% FeS composition that provide a widely varying pressure value. The variation in mol% FeS is likely due to the absence of the buffering assemblage of pyrite + hexagonal pyrrhotite or to departure from equilibrium during cooling. Since there is no bimodal distribution of mol% FeS it is not thought that these values represent different metamorphic events (i.e. M_1 and M_2). Nor is there any consistent change in sphalerite composition from core to rim of the enveloping pyrite grains to suggest changing pressure conditions during M_2. The pressure of 4.0 kb calculated from this method is in good agreement with the pressure determined from petrogenetic relationships (Smith and Erdmer 1990).

Sphalerite + hexagonal pyrrhotite pairs in the D_2 shear zones also appear to be a reliable assemblage for determining metamorphic pressures in the Vangorda orebody. Despite the fact that pyrrhotite lies approximately on the pyrite + pyrrhotite solvus or in the pyrite + pyrrhotite field (Fig. 6) the assemblage provides a tightly bracketed mol% FeS in sphalerite (Table 4) that yields a geologically reasonable pressure of 6.1 kb. However, 6.1 kb is a somewhat higher pressure than expected for the Anvil District (Fig. 7). The absence of kyanite in silicate assemblages adjacent to the contact with the Anvil Batholith and the fact that near the contact andalusite alters to sillimanite (Pigage and Anderson 1985, Smith and Erdmer 1990) suggests that M_2 took place at pressures of less than 4 kb. These higher pressures indicate that regional uplift in the district may exceed the 10 km suggested by the lower pressure mineral assemblages. Note that with the exception of the presence of kyanite the sequence of metamorphic reactions that have taken place in the aureole would be similar at 4 to 6 kb as a 3 kb (Fig. 7).

The low a_{FeS} in pyrrhotite may be a retrograde effect in which it is on the verge of altering to pyrite during waning of the metamorphic conditions (c.f. Graig and Vokes 1993). This is possibly reflected in the position of pyrrhotite on or near the pyrite + pyrrhotite solvus (Figure 6) and in the occurrence of rare, retrograde pyrite overgrowing the sphalerite + pyrrhotite assemblage.

These pressures and temperatures determined for the Vangorda orebody are in the lower portion of the 350° to 500 °C suggested by Marshall and Gilligan (1993) as being the most effective temperature range for ductile mechanical and chemical remobilisation of massive sulphides. However, the penetrative nature of deformation and metamorphism affecting the Vangorda orebody at these low temperatures and low pressures suggests that, under upper crustal conditions, massive sulphide deposits undergo extensive deformation, shearing, remobilisation and recrystallisation and formation of 'durchbewegung'. As a result any primary textural features that reflect the genesis of such a deposit may be completely overprinted by deformation and metamorphic effects. For instance, because of the extensive deformation the genesis of the

Vangorda orebody as a SEDEX (Carne and Cathro 1982) deposit can only be interpreted in view of the the well-developed, district-wide sulphide lithostratigraphic sequence, the restricted stratigraphic position of the massive sulphide deposits in the district and their occurrence along a curvilinear trend and association with a carbonaceous pelite unit that may indicate a reduced basinal margin (Jennings and Jilson 1986). Similarly the pervasive recrystallisation of sulphide grains suggest that the isotopic signature may be extensively reset and any analyses must be viewed with caution.

Conclusions

The Vangorda orebody has been penetratively deformed and metamorphosed during two deformation and metamorphic events, D_1/M_1 and D_2/M_2, respectively.. Thermometry carried out on a M_2 arsenopyrite + pyrrhotite $\pm$ pyrite assemblage provides a cooling temperature of 336° C. Thermometry carried out on chlorite grains defining both the S_1 and S_2 foliations result in a similar temperature of 363° C which is interpreted to represent the peak M_2 temperature. Barometry was carried out on samples taken from D_2 shear zones along the limbs of F_2 folds using sphalerite inclusions in pyrite and the sphalerite + hexagonal pyrrhotite + pyrite barometer and on sphalerite coexisting with hexagonal pyrrhotite using the sphalerite + hexagonal pyrrhotite barometer. These barometers provide D_2/M_2 pressures of 4 and 6 kilobars, respectively. Pressures of 4 to 6 kb are higher than those determined petrogenetically and suggest that regional uplift in the Anvil District may exceed 10 km. This study has shown that at the low pressures and temperatures massive sulphides undergo extensive and penetrative deformation and metamorphism that results in mechanical and chemical remobilisation of the ore and recrystallisation of the sulphide minerals.

Appendix A

Chlorite thermometry

Chlorite thermometry is based on the cation site occupancy as a function of temperature, in particular the increase of $Al_{(IV)}$ on the tetrahedral site with an increase in temperature (Cathelineau and Nieva 1985; Cathelineau 1988). The equation used to calculate temperature from chlorite composition is ;

$$T\ (°C) = -61.92 + 321.98Al_{(IV)} \quad \text{(Cathelineau 1988)}$$

(on the basis of 14 O)

Arsenopyrite thermometry

Arsenopyrite thermometry is based on the increase in atomic% As in arsenopyrite buffered by pyrite + pyrrhotite or pyrrhotite and can be solved graphically using the method outlined by Kretschmar and Scott (1976). Similarly the log fS_2 can be solved graphically following the procedure of Kretschmar and Scott 91976) and Sharp *et al.* (1985).

Sphalerite + hexagonal pyrrhotite (+ pyrite) barometry

The sphalerite geobarometer is based on the decreasing content of FeS in sphalerite with increasing pressure when buffered by pyrite + hexagonal pyrrhotite or by hexagonal pyrrhotite alone (Barton and Toulmin 1966; Scott and Barnes 1971; Scott 1971, 1976; Hutchison and Scott 1981; Bryndzia et al. 1988, 1990). The pressure equation for the sphalerite + hexagonal pyrrhotite + pyrite calibration is;

$$P\ (kb) = 42.30 - 32.10 \log \text{mole } \%FeS_{(sp)} \quad \text{(Hutchison and Scott 1981)}$$

where mole % FeS_{sp} is calculated to be

$$\text{Mol\% } FeS_{sp} = [(Fe/(Fe + S))/(S/(Fe + S))]$$

and the equation for the sphalerite + hexagonal pyrrhotite calibration is;

$$P(kb) = 27.982 \log \gamma_{FeS}^{sp} - 8.549 \ (\pm 0.5kb) \quad \text{(Bryndzia } et\ al.\text{ 1990)}$$

where γ, the activity coefficient, is calculated by

$$a_{FeS}/X_{FeS}^{sp}, \ (X_{FeS}^{sp} = \text{Mol\% } FeS_{sp}/100)$$

The fugacity of S_2 and the activity of FeS in pyrrhotite used in the pyrrhotite-indicator method are calculated as;

$$\log fS_2 = (70.03 - 85.83N)(1000/T - 1) + 39.30\sqrt{(1 - 0.9981N)}$$

$$- 11.91 \quad \text{(Toulmin and Barton 1966)}$$

and

$$\log a_{FeS} = 85.83(1000/T - 1)(1 - N + \ln N) + 39.30\sqrt{(1 - 09981N)} -$$

$$39.23\tanh^{-1}\sqrt{(1 - 0.9981N)} - 0.002 \quad \text{(Toulmin and Barton 1966)}$$

where

$$N_{FeS}^{po} = 2(Fe/(Fe + S))$$

similarly a_{FeS} can be calculated as;

$$\ln a_{FeS} = -\{\ln r + B((r - 1)/r)^2\} \qquad \text{(Rau 1976)}$$

where r = S/Fe (atom ratio) in pyrrhotite

and

$$B = 3.160 + 22269/T$$

Temperature in all these calculations is in K.

Acknowledgements

Funding for this project was provided in part by the Rothemere Foundation, and by the Special Scholarship for Students doing Research in Resource Development administered by Memorial University of Newfoundland. Fieldwork was supported by Curragh Inc., Department of Indian and Northern Affairs Canada (Whitehorse), Geological Survey of Canada (Vancouver), and by the Industry Association (RHUL). Ken McClay is thanked for his supervision and support of this research. Dave Alderton, Joel Baker, Ian Fitzsimons and Tony Hall are thanked for reviewing early drafts of the manuscript. Philippe Erdmer and Taras Bryndzia provided careful and insightful reviews that greatly improved the manuscript.

References

Barker, W.W., Parks, T.C. (1986) The thermodynamic properties of pyrrhotite and pyrite: A re-evaluation. Geochim. Cosmochim. Acta. 50: 2185-2194.

Barton, P.B. (1969) Thermochemical study of the system Fe - As - S. Geochim. Cosmochim. Acta. 33: 841-857.

Barton, P.B., Toulmin, P. III (1966) Phase relations involving sphalerite in the Fe - Zn - S system. Econ. Geol. 61: 815-849.

Brown, D., McClay, K. (1992) Structure of the Vangorda Pb-Zn-Ag deposit, Anvil Range, Yukon Territory. Current Research, Part A; Geol. Surv. of Canada, Paper 92-1A: 121-128

Brown, D., McClay, K. (1993a). Deformation textures in pyrite from the Vangorda Pb - Zn - Ag deposit, Yukon, Canada. Min. Mag. 57: 55-66.

Brown, D., McClay, K. (1993b) The Vangorda deposit. Yukon Exploration and Geology, 1992. Exploration and Geological Services Division, Yukon, Indian and Northern Affairs Canada. 25-32.

Brown, D., McClay, K. (in press) Structural geology of the Vangorda Pb-Zn-Ag orebody, Yukon, Canada. Ore Geol. Reviews.

Bryndzia, L.T., Scott, S.D., Spry, P.G. (1988) Sphalerite and hexagonal pyrrhotite geobarometer: experimental calibration and application to the metamorphosed sulphide ores of Broken Hill, Australia. Econ. Geol. 83: 1193-1204.

Bryndzia, L.T., Scott, S.D., Spry, P.G. (1990) Sphalerite and hexagonal pyrrhotite

geobarometer: correction in calibration and application. Econ. Geol. 85: 408-411.

Carne, R.C., Cathro, R.J. (1982) Sedimentary exhalative (sedex) zinc - lead - silver deposits, northern Canadian Cordillera. The Canadian Mining and Metallurgical Bull. 75: 66-75.

Cathelineau, M. (1988) Cation site occupancy in chlorites and illites as a function of temperature. Clay Minerals. 23: 471-485.

Cathelineau, M., Nieva, D. (1985) A chlorite solid solution geothermometer, the Los Azufres (Mexico) geothermal system. Contrib. Mineral. Petrol. 91: 235-244.

Coney, P.J., Jones, D.L., Monger, J.W.H. (1980) Cordilleran suspect terranes. Nature. 288: 329-333

Craig, J.R., Vokes, F.M. (1993) The metamorphism of pyrite and pyritic ores: an overview. Min. Mag. 57: 3-18.

Craig, J.R., Scott, S.D. (1974) Sulphide phase equilibria. In: Ribbe, P.H. (ed.) Sulphide Mineralogy. Mineral. Soc. Amer. Short Course Notes, Vol. 1.

Hutchison, M.N., Scott, S.D. (1981) Sphalerite geobarometry in the Cu-Fe-Zn-S system. Econ. Geol. 76:143-153.

Jennings, D.S., Jilson, G.A. (1986) Geology and sulphide deposits of the Anvil Range, Yukon. In: Morin, J.A.(ed.) Mineral Deposits of Northern Cordillera. Canadian Ins. of Mining and Metallurgy, Special Paper 37: 319-361

Kretschmar, U., Scott, S.D. (1976) Phase relations involving arsenopyrite in the system Fe - As - S and their application. Canadian Min. 14: 364-386.

Kuo, S.L. (1976) Geology and geochemistry of stratabound ore deposits in south central Yukon Territory and southwestern District of Mackenzie, Northwest Territories. Unpubl. Ph.D. thesis, University of Alberta, Edmonton, Canada.

Marshall, B. and Gilligan, L.B. (1993) Remobilization, syn-tectonic processes and massive sulphide deposits. Ore Geol. Reviews, 8: 39-64.

Pigage, L.C., Anderson, R.G. (1985) The Anvil Plutonic suite, Faro, Yukon Territory. Canadian J. of Earth Sciences, 22: 1204-1216

Pigage, L.C., Jilson, G.A. (1985) Major extensional faults, Anvil Pb-Zn district, Yukon (abstract). Geol. Soc. of Amer., Cordilleran Section Annual Meeting, Abstracts with Programmes, 17: 400

Rau, H. (1976) Energetics of defect formations and interaction in pyrrhotite $Fe_{1-x}S$ and its homogeneity range. J. Phys. Chem. Solids. 37: 425-429.

Scott, S.D. (1983) Chemical behaviour of sphalerite and arsenopyrite in hydrothermal and metamorphic environments. Min. Mag. 47: 427-435.

Scott, S.D., Barnes, H.L. (1971) Sphalerite geothermometry and geobarometry. Econ. Geol. 66: 653-669.

Sharp, Z.D., Essene, E.J., Kelly, W.C. (1985) A re-examination of the arsenopyrite geothermometer: pressure considerations and applications to natural assemblages. Canadian Min. 23: 517-534.

Smith, J.M., Erdmer, P (1990) The Anvil aureole, an atypical mid-Cretaceous culmination

in the northern Canadian Cordillera. Canadian J. of Earth Sciences, 27: 344-356

Tempelman-Kluit, D.J. 1972. Geology and origin of the Faro, Vangorda, and Swim concordant zinc-lead deposits, central Yukon Territory. Geol. Survey. of Canada, Bull. 208, 73p.

Tempelman-Kluit, D.J. 1979. Transported cataclasite, ophiolite and granodiorite in Yukon Territory. Geol. Surv. Can., paper 79-14: 27 p.

Toulmin, P. III, Barton, P.B. (1964) A thermodynamic study of pyrite and pyrrhotite. Geochim. Cosmochim. Acta. 28: 641-671.

Vaughan, D.J. and Craig, J.R. (1978) Mineral Chemistry of Metal Sulphides. Cambridge University Press. 493p.

Figure Captions

Fig. 1. Generalised geological map and cross section of the Anvil District. Location map is in the inset. The mineral deposits occur along a curvilinear trend on the southwest side of the Anvil Plutonic Suite (Redrafted from Jennings and Jilson 1986).

Fig. 2. Schematic map of the Anvil District showing the concentric distribution of the metamorphic isograds around the Anvil Batholith. The Vangorda deposit is located on the biotite 'in' isograd. Isograds are taken from Tempelman-Kluit (1972) and Smith and Erdmer (1990).

Fig. 3. Drill hole cross section through the sulphide lithofacies sequence in the Vangorda deposit. The pyrrhotite, sphalerite, galena massive sulphide shear zones (in black) along the limbs of the large scale F_2 folds provide sulphide mineral assemblages that can be used to unambiguously define the D_2 metamorphic conditions.

Fig. 4. A). Photomicrograph of chlorite defining the S_1 and S_2 foliations that were used for thermometry. B) Photomicrograph of arsenopyrite porphyroblasts coexisting with pyrrhotite and as overgrowths on pyrite that were used for thermometry. C) Sphalerite inclusions in a M_2 pyrite porphyroblast used for sphalerite + hexagonal pyrrhotite + pyrite barometry. D) Photomicrograph of coexisting M_2 sphalerite and pyrrhotite used for sphalerite + hexagonal pyrrhotite barometry.

Fig. 5. A) Position of the Vangorda arsenopyrite on a T-X diagram. Buffering curves are from Kretschmar and Scott (1976) The edges of the box represents 2σ for both X_{As} and T. B) Position of the Vangorda arsenopyrite and coexisting pyrrhotite on the sulfidation curves in the Fe-As-S system (after Barton 1969). The stability field of arsenopyrite is shaded. Log fS_2 in pyrrhotite was calculated using a mean temperature of 336 °C. Edges of boxes represent 2σ.

Fig. 6. Activity of FeS in pyrrhotite as a function of temperature and N_{FeS} and the location of the pyrite + pyrrhotite solvus at 1 bar. The thick dashed line is the position of the solvus at 5 kb. The a_{FeS} in pyrrhotite from D_2 shear zones in the Vangorda orebody plot within the pyrite + pyrrhotite field at 5 kb and touch the solvus at a bar. The edges of the shaded box represents 2σ. (Taken from Vaughan and Graig 1978).

Fig. 7. Petrogenetic grid showing the metamorphic reactions interpreted to have taken place in the contact aureole around the Anvil Batholith (arrow indicates the sequence of reactions towards the batholith). A = chlorite - biotite zone, B = biotite - andalusite zone, C = biotite - andalusite - staurolite zone, D = biotite - sillimanite - staurolite zone, E = biotite - almandine - sillimanite zone and the black dots indicate the position of zone boundaries (from Smith and Erdmer 1990). The Vangorda orebody records a lower temperatures and a higher pressure than determined petrogenetically.

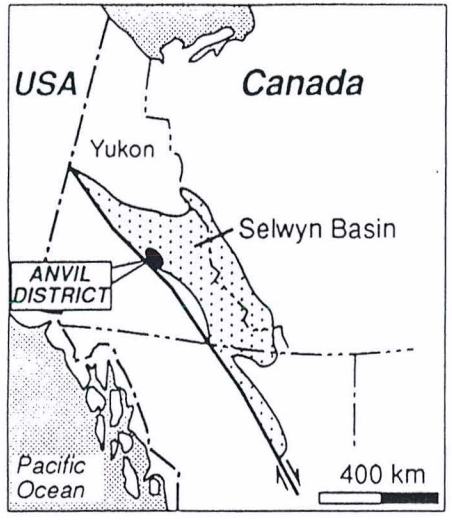

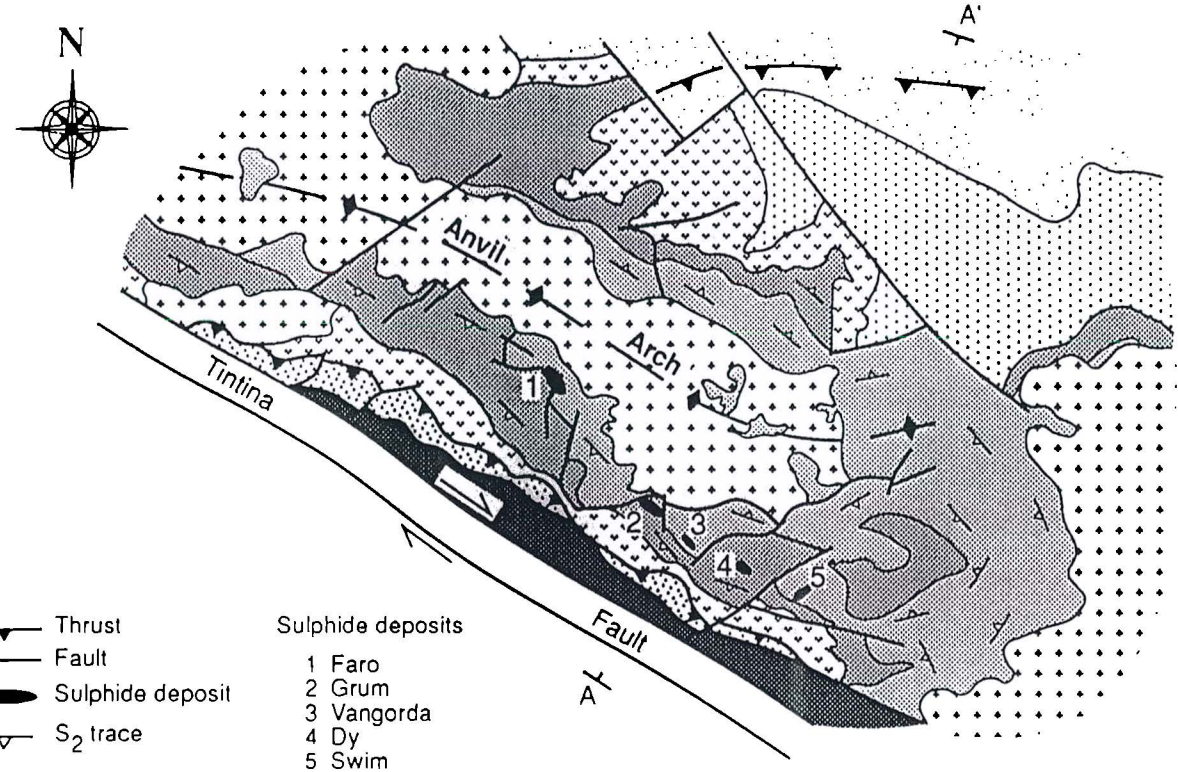

LEGEND

- Anvil Plutonic Suite
- Menzie Creek formation
- Vangorda formation
- Mt. Mye formation
- Anvil Group
- Earn Group?
- Road River Group?
- Yukon-Tanana Terrane

- Thrust
- Fault
- Sulphide deposit
- S_2 trace

Sulphide deposits

1 Faro
2 Grum
3 Vangorda
4 Dy
5 Swim

Scale

0 km — 20 km

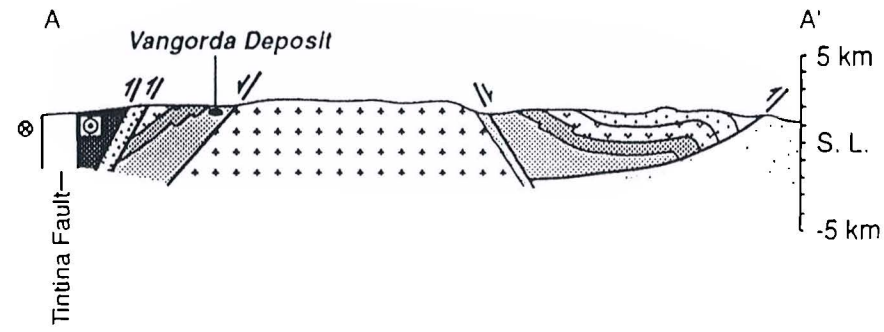

Brown Fig. 1

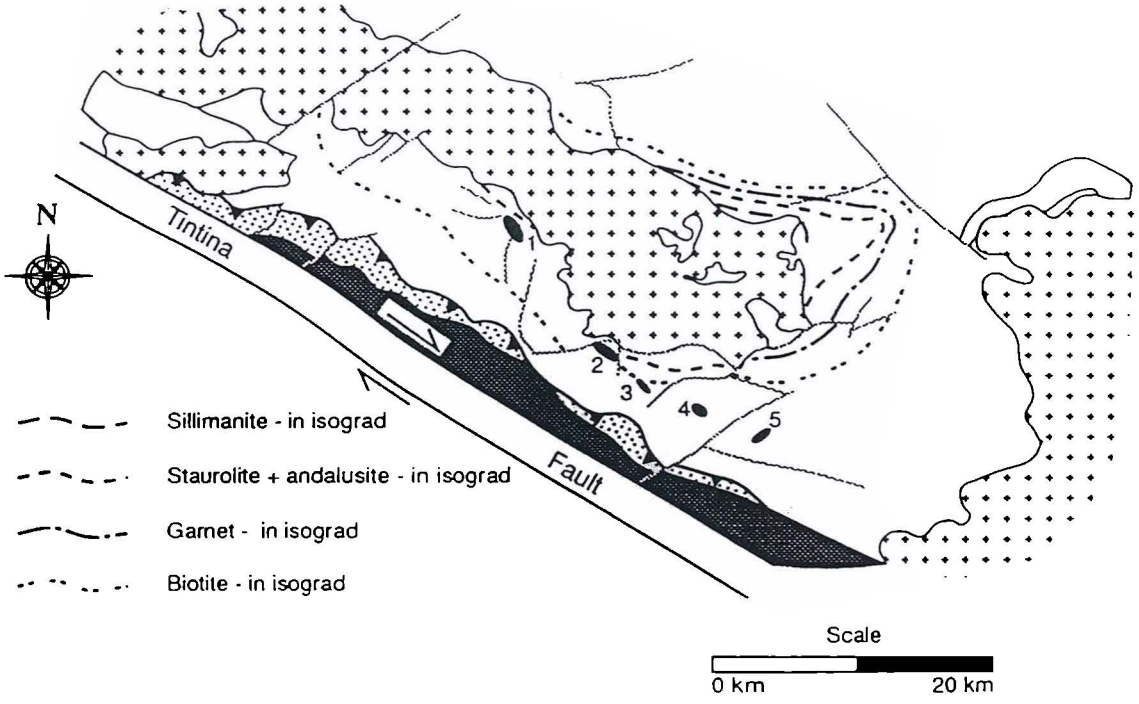
N
Tintina
Fault
1
2
3
4
5
Sillimanite - in isograd
Staurolite + andalusite - in isograd
Garnet - in isograd
Biotite - in isograd
Scale
0 km
20 km

Brown Fig. 2

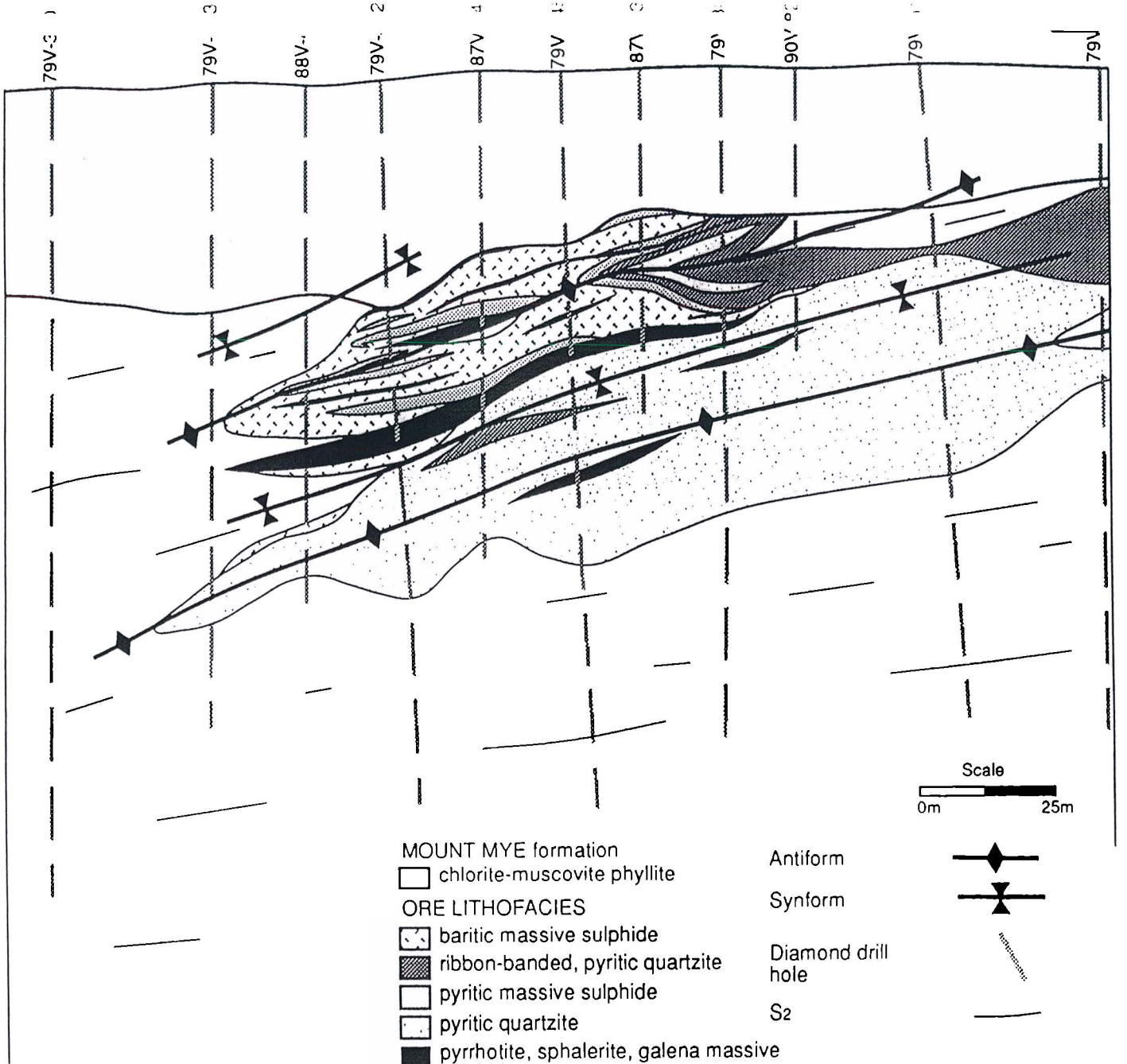
Scale
0m
25m
MOUNT MYE formation
chlorite-muscovite phyllite
ORE LITHOFACIES
baritic massive sulphide
ribbon-banded, pyritic quartzite
pyritic massive sulphide
pyritic quartzite
pyrrhotite, sphalerite, galena massive sulphide
Antiform
Synform
Diamond drill hole
S2

Brown Fig. 3

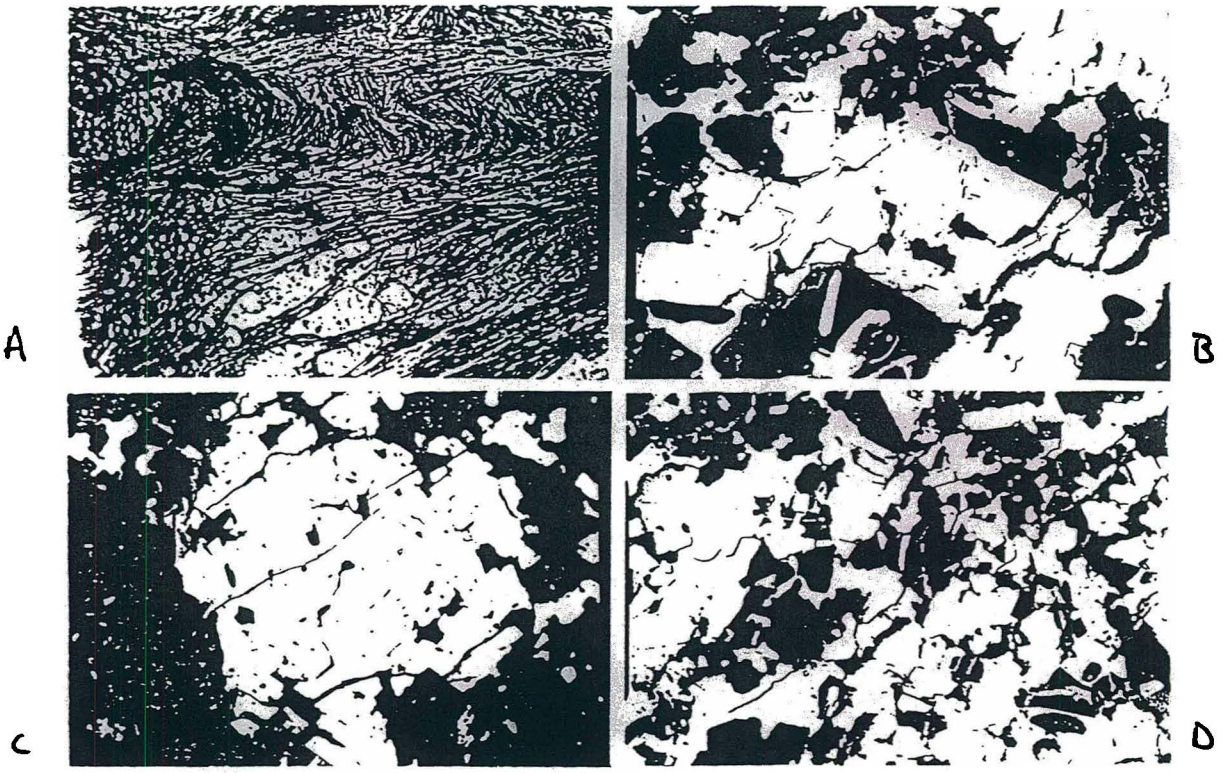

Fig 4.

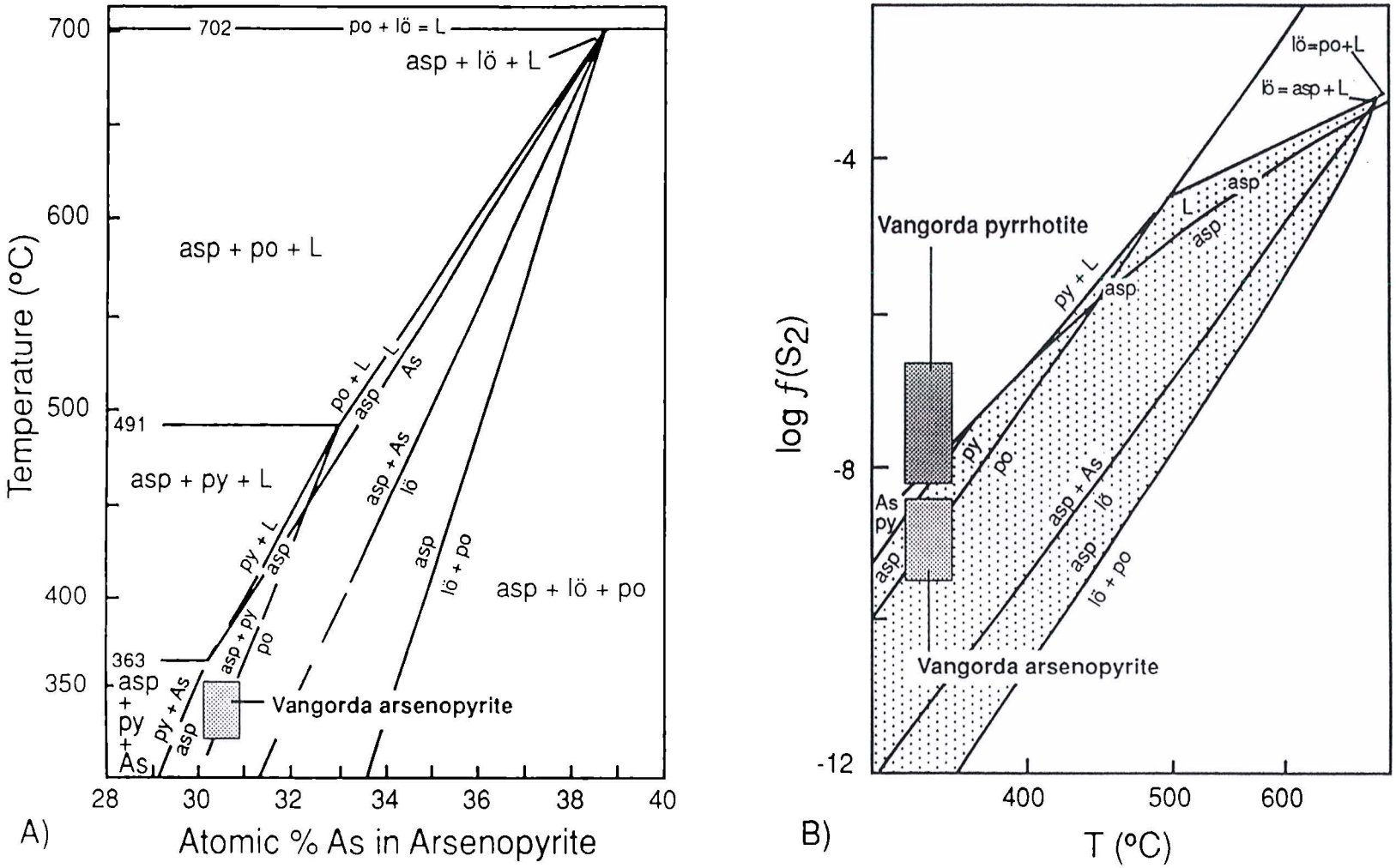
700
600
500
400
350
Temperature (°C)
702
po + lö = L
asp + lö + L
asp + po + L
491
asp + py + L
asp + lö + po
363
asp + py + As
Vangorda arsenopyrite
po + L
asp + As
py + L
asp + py
lö + po
28
30
32
34
36
38
40
Atomic % As in Arsenopyrite
A)
lö=po+L
lö = asp + L
-4
-8
-12
log f(S2)
Vangorda pyrrhotite
Vangorda arsenopyrite
400
500
600
T (°C)
B)

Brown Fig. 5

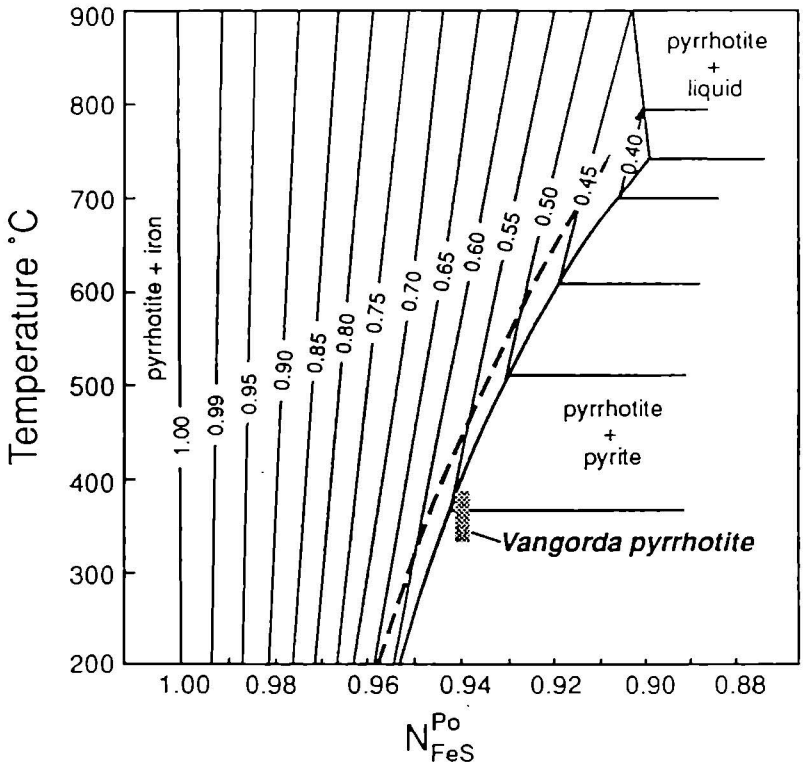
900
800
700
600
500
400
300
200
Temperature °C
1.00
0.98
0.96
0.94
0.92
0.90
0.88
N_{FeS}^{Po}
pyrrhotite + iron
1.00
0.99
0.95
0.90
0.85
0.80
0.75
0.70
0.65
0.60
0.55
0.50
0.45
0.40
pyrrhotite + liquid
pyrrhotite + pyrite
Vangorda pyrrhotite

Brown Fig. 6

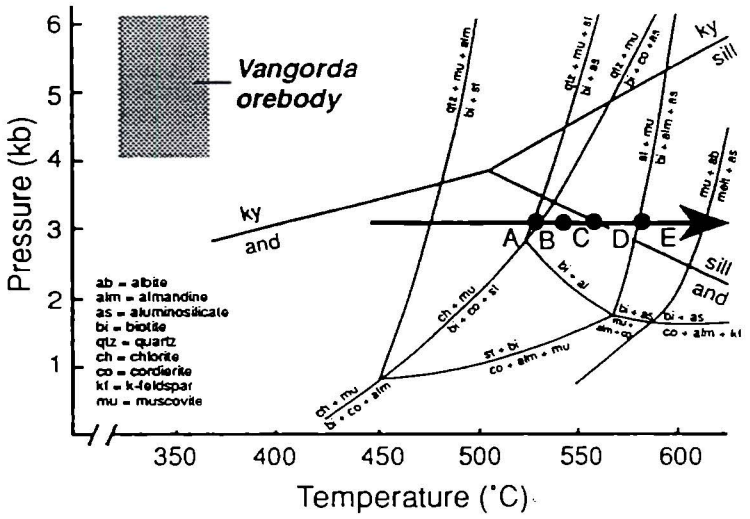
Vangorda orebody
Pressure (kb)
Temperature (°C)
6
5
4
3
2
1
350
400
450
500
550
600
ky
and
sill
A
B
C
D
E
ab = albite
alm = almandine
as = aluminosilicate
bi = biotite
qtz = quartz
ch = chlorite
co = cordierite
kf = k-feldspar
mu = muscovite

Brown Fig. 7

Table 1. Representative chlorite analyses and compositions.

wt. %	S_1	S_1	S_1	S_1	S_2	S_2	S_2	S_2
SiO_2	23.73	24.50	23.72	23.73	24.17	24.11	23.97	23.92
Al_2O_3	19.84	19.53	20.59	21.70	19.48	19.90	22.00	21.55
TiO_2	0.07	0.05	0.00	0.05	0.03	0.00	0.02	0.06
FeO	35.65	34.82	35.14	30.91	35.27	34.81	29.04	29.19
MnO	1.86	1.67	2.02	0.59	1.69	1.55	0.27	0.27
MgO	7.32	7.79	7.12	11.09	7.61	7.76	12.33	12.47
CaO	0.02	0.10	0.00	0.04	0.01	0.00	0.05	0.00
Na_2O	0.00	0.01	0.01	0.03	0.01	0.00	0.02	0.00
K_2O	0.04	0.02	0.03	0.00	0.02	0.00	0.04	0.00
Sum	88.53	88.49	88.63	88.14	88.29	88.13	87.78	86.38
Si_{IV}	2.66	2.73	2.64	2.58	2.70	2.69	2.58	2.59
Al_{IV}	1.34	1.27	1.36	1.42	1.30	1.31	1.42	1.41
T - site	4.00	4.00	4.00	4.00	4.00	4.00	4.00	4.00
Al_{VI}	1.28	1.28	1.35	1.36	1.27	1.31	1.38	1.34
Ti	0.01	0.00	0.00	0.00	0.00	0.00	0.00	0.01
Fe	3.34	3.24	3.28	2.81	3.30	3.25	2.62	2.64
Mn	0.18	0.16	0.19	0.05	0.16	0.15	0.03	0.02
Mg	1.22	1.29	1.18	1.80	1.27	1.29	1.98	2.01
Ca	0.00	0.01	0.00	0.00	0.00	0.00	0.01	0.00
Na	0.00	0.00	0.00	0.00	0.00	0.00	0.00	0.00
K	0.01	0.00	0.00	0.01	0.00	0.00	0.01	0.00
O - site	6.03	5.99	6.01	6.03	6.01	6.00	6.02	6.03
O	9.94	9.94	9.95	9.93	9.92	9.91	9.91	9.88
OH	8.06	8.06	8.05	8.07	8.08	8.09	8.09	8.12

General formula $(Fe_{2.83}Mg_{1.71}Al_{1.34}Mn_{0.07}Ti_{0.01})[(Al_{1.31}Si_{2.68})O_{9.95}](OH_{8.04})$

S_1 Tet. Al_{IV}	1.29 (2σ = +/- 0.08)	n = 27
S_2 Tet. Al_{IV}	1.34 (2σ = +/- 0.06)	n = 29
S_1 T (°C)	355 (2σ = +/- 27)	
S_2 T (°C)	372 (2σ = +/- 18)	
Mean T (°C)	363 (2σ = +/- 24)	n = 56

Table 2. Representative arsenopyrite analyses.

At. %	core	rim	core	rim	core	rim	core	rim	core	rim
As	31.17	31.03	30.28	30.50	29.11	30.77	30.09	30.60	30.21	30.50
Fe	34.06	33.72	34.08	33.96	34.45	34.35	34.13	33.92	33.99	34.06
S	34.72	35.14	35.47	35.47	36.40	34.74	35.68	35.41	35.60	35.32
Sum	99.95	99.89	99.83	99.93	99.96	99.86	99.80	99.93	99.80	99.88

At. % As 30.60 (2σ = +/- 0.0.30) n = 46

log $f S_2$ -8.99 (2σ + +/- -0.55)

Mean T (°C) 336 (2σ = +/- 20)

Table 3. Representative analyses of sphalerite inclusions in pyrite.

At %	1	2	3	4	5	6	7	8	9	10
Fe	9.22	10.06	9.27	8.60	8.91	6.01	5.66	7.85	5.40	9.21
Zn	40.74	39.51	41.75	42.23	42.19	44.69	44.69	42.82	45.06	41.05
S	50.01	50.41	48.90	49.09	48.90	49.22	49.62	49.24	49.47	49.73
Sum	99.97	99.98	99.93	99.92	100.00	99.92	99.97	99.91	99.93	99.99

Mol% FeS 15.62 (2σ = +/- 2.78) n = 24

$P_{(kb)}$ 3.98 (2σ = +/- 2.68)[1]

[1] Equation of Hutchison and Scott (1981)

Table 4. Representative analyses for co-existing pyrrhotite and sphalerite pairs.

At. %	Pyrrhotite									
Fe	46.92	46.95	46.98	46.96	46.83	46.85	46.94	47.12	46.77	46.97
S	52.98	53.01	52.81	52.81	52.94	53.05	52.82	52.49	53.15	52.94
Sum	99.99	99.96	99.79	99.77	99.77	99.90	99.76	99.61	99.92	99.91
At. %	Sphalerite									
Fe	8.07	7.59	7.78	7.44	8.15	7.61	7.95	8.39	8.41	8.50
Zn	41.67	43.02	42.88	42.96	42.21	42.82	42.85	39.52	39.67	39.36
S	50.23	49.39	49.31	49.55	49.62	49.48	49.16	52.11	51.90	51.99
Sum	99.97	100.00	99.97	99.95	99.98	99.91	99.96	100.02	99.98	99.95

^{a} FeS	0.53 (2σ = +/- 0.07)[1]	0.57 (2σ = +/- 0.06)[2]	n = 49
$Mol\%_{FeS}$	15.75 (2σ = +/- 0.63)		
N_{FeS}	0.94 (2σ = +/- 0.03)[1]		
γ	3.38 (2σ = +/- 0.44)[1]		
$P_{(kb)}$	6.11 (2σ = +/- 1.58)[3]		

[1] Equation of Toulmin and Barton (1964)

[2] Equation of Rau (1976)

[3] Equation of Bryndzia et al. (1988, 1990)

LSET06 OREGEXS219

Ore Geology Reviews, 00 (1993) 00–00

ORE GEOLOGY REVIEWS

Structural geology of the Vangorda Pb–Zn–Ag orebody, Yukon, Canada

Dennis Brown, Ken McClay

Department of Geology, Royal Holloway, University of London, Egham, Surrey, TW20 OEX, England

(Received May 13, 1993; revised version accepted September 20, 1993)

Abstract

The Vangorda Pb–Zn–Ag orebody is a 7.1 M tonne, polydeformed, polymetamorphosed stratiform massive sulphide orebody in the Anvil mining district, Yukon, Canada. The orebody consists of fine- to medium-grained semi-massive and massive sulphides with a dominant sulphide mineralogy of pyrite, pyrrhotite, sphalerite, galena and minor chalcopyrite. Five sulphide lithofacies have been identified within the orebody; ribbon-banded, carbonaceous, pyritic quartzite; pyritic quartzite; massive pyritic sulphides; baritic, massive pyritic sulphides; and pyrrhotite-sphalerite massive sulphides. The orebody is elongate in a northwest–southeast orientation and plunges shallowly towards the northwest. The host rocks and the various sulphide lithofacies have been complexly deformed during two penetrative phases of deformation (D_1 and D_2, respectively) and associated metamorphism (M_1 and M_2).

M_2 metamorphism resulted in extensive recrystallisation and subsequent grain growth of sulphide minerals. M_2 metamorphic grade recorded by arsenopyrite and chlorite thermometry and sphalerite + hexagonal pyrrhotite barometry is of mid-greenschist facies with temperatures of 336° to 363°C, respectively, and a pressure of 4 kb.

The earliest structure that can be recognised in the orebody is a penetrative S_1 spaced cleavage that is well-developed in the host phyllites and a differentiated layering in the semi-massive and massive sulphides. However, F_1 folds have not been identified in the orebody, although they do occur within the Anvil District. The S_1 cleavage has been deformed into downward-facing, southwest-verging, recumbent F_2 folds that plunge shallowly northwest–southeast. A penetrative axial planar S_2 crenulation cleavage is developed in the phyllites and ribbon-banded, carbonaceous, pyritic quartzite, but is found only locally in the massive sulphide lithofacies. In the baritic lithofacies, F_2 folds have thickened hinges suggesting remobilisation of the ore. Along the overturned limbs of the F_2 folds and at lithofacies contacts centimetric to metric-scale zones enriched in pyrrhotite, sphalerite and galena are developed. These areas commonly have a significantly reduced grain size, a well-developed sulphide foliation and numerous shear indicators such as winged and rotated clasts. F_2 folds and the S_2 form surfaces are cut by syn- to post-D_2 NW–SE-dipping extensional faults. Minor strike-slip faults cut D_1 and D_2 structures.

1. Introduction

The Anvil District is the largest Pb–Zn mining camp in northwestern Canada with estimated geological reserves (before mining) of 120 million tonnes at a combined Pb + Zn grade of 9.3% (Jennings and Jilson, 1986). The district contains five Cambrian to early Ordovician SEDEX-type (Carne and Cathro, 1981) Pb–Zn–Ag (barite) deposits of economic significance that lie along a curvilinear trend on the southwest flank of the Anvil Batholith (Fig. 1). The deposits are interpreted to have formed in terraced, extensional rift basins (Jennings and Jilson, 1986;

0169-1368/93/$06.00 © 1993 Elsevier Science Publishers B.V. All rights reserved
SSDI 0169-1368(93) E0024-4

...nks et al., 1987), similar to those described ...lsewhere in the Selwyn Basin and Kechika ... ugh by McClay (1991) and MacIntyre ... 92). The Anvil District has been affected by ...ive deformation events (D_1–D_5) and metamor...hosed to greenschist to amphibolite facies dur... ...he D_2 event (M_2).

...he Vangorda orebody is a small (7.1 million ...onne), Pb–Zn–Ag (barite) massive sulphide ... ...ody within the Anvil District. The orebody ... ...ists of several southwest-dipping, north... ...est-plunging lenses of fine- to medium-grained ...assive sulphides and semi-massive sulphides, ...ed by muscovite-chlorite phyllites. Five sul...hide lithofacies have been identified in the ore...ody. However, no feeder zone has been estab... ...d. The orebody has been by the D_1–D_5 ... ...rmation events that affected the Anvil Dis...ict and metamorphosed to lower-greenschist ... ...s during M_2 (Tempelman-Kluit, 1972; Jen... ... s and Jilson, 1986).

...ne Vangorda orebody was developed as an ...pen pit mine from 1990 to 1993 by Curragh Inc., ...ucing approximately 13,000 tonnes of ore ... ...lay with an average combined Pb + Zn grade ... 7.7%. During this time all the final mine walls ... mapped. This paper documents the various ... ...tural features of the Vangorda orebody ...apped in the mine, together with quantitative ...ermobarometric analysis of the metamor... ...n, and places them in the regional context ... ...ne Anvil District geology. The mesoscopic ...formation textures and deformation mecha... ...s active within the deforming sulphide ... ...age are described in an attempt to better un...erstand how the massive sulphides responded ... ...e regional deformation.

Regional geology

... e Anvil District (Fig. 1) is part of the Sel...yn Basin of the western Canadian Cordillera ... ...h formed part of the ancient North Ameri... ...r miogeocline until the Early Cretaceous ...Tempelman-Kluit, 1972; Abbott et al., 1986). ...he Anvil District is underlain by late Precam... ...i to upper Paleozoic metasedimentary and metavolcanic rocks (Jennings and Jilson, 1986). These rocks have been intruded by mid-Cretaceous granitoids of the Anvil Plutonic Suite (Jennings and Jilson, 1986; Pigage and Anderson, 1985). The district is structurally overlain by the allochthonous Yukon–Tanana terrane (Tempelman-Kluit, 1972) and is adjacent to a major orogen-scale dextral strike-slip fault, the Tintina Fault (Fig. 1).

2.1. Lithostratigraphy

The lithostratigraphy of the Anvil District consists of up to 5 km of metasedimentary and metavolcanic rocks that have been intruded by Cretaceous granites. The Anvil massive sulphide deposits are hosted by, or straddle the boundary between, two lithostratigraphic units of importance to this paper, the Mt. Mye formation and the overlying Vangorda formation (informal district names; see Fig. 2). Both the Mt. Mye and Vangorda formations have been interpreted to represent sediments deposited in a rift basin into which the Anvil District ore-bearing fluids were also being deposited (cf. Jennings and Jilson, 1986; Shanks et al., 1987). The Vangorda orebody occurs entirely within Mount Mye formation phyllites, 50–100 m below the contact with the Vangorda formation.

In the vicinity of the Vangorda orebody, the Mount Mye formation consists of light to medium grey noncalcareous, weakly carbonaceous, quartz + muscovite + chlorite ± biotite phyllite with lesser, interlayered, carbonaceous phyllite, calcareous phyllite, and metabasite. The Mount Mye formation has an apparent structural thickness of at least 2 km, though its base is not exposed (Jennings and Jilson, 1986).

The overlying Vangorda formation consists of light to medium grey, calcareous, weakly carbonaceous light grey, calcareous quartz + calcite (± dolomite) + muscovite + chlorite ± biotite phyllite with interbanded metabasite, carbonaceous phyllite, and phyllitic limestone. It varies from between 0.5 and 2 km in structural thickness (Jennings and Jilson, 1986).

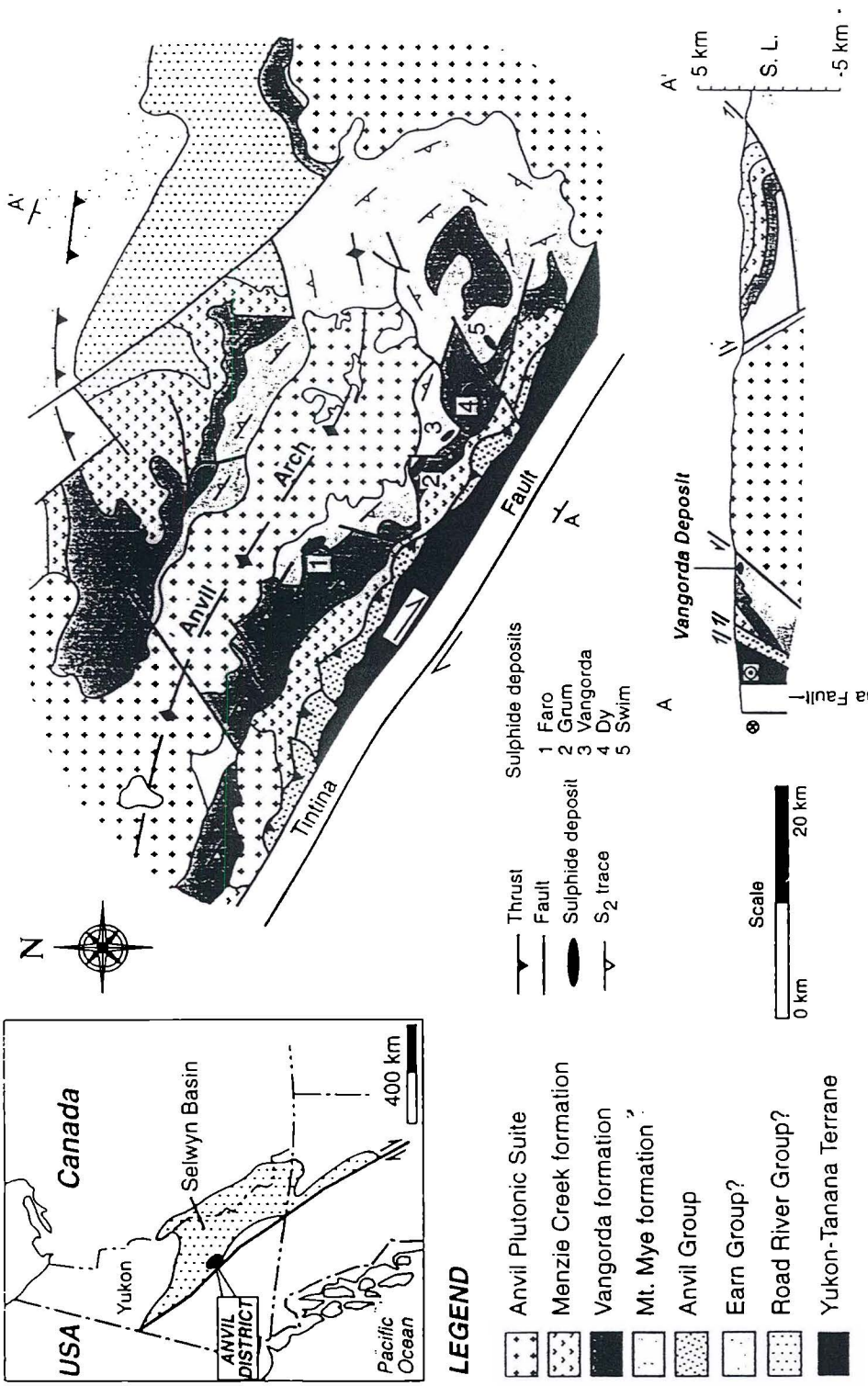

Fig. 1. Generalised geological map and cross-section of the Anvil District. The mineral deposits occur on a curvilinear trend along the south margin of the Anvil Arch (redrafted from Jennings and Jilson, 1986).

Schematic lithostratigraphic column of the Anvil District. The Anvil Cycle lithofacies represents a vertical and lateral sequence of semi-massive and massive sulphides that is persistent in all deposits in the Anvil District (redrafted from Jennings and Jilson, 1986).

2.2. Deformation events

Five deformation events (D_1 to D_5) have been recognised in the Anvil District, the first two of which (D_1 and D_2) are regionally significant (Jennings and Jilson, 1986). D_1 is interpreted to be related to the pre- to mid-Cretaceous collision of the allochthonous Yukon–Tanana terrane with the continental margin (Tempelman-Kluit, 1979) causing northeast-directed nappe emplacement, folding, thrusting and regional metamorphism of the continental margin sediments. D_1 deformation resulted in development of northeast-verging F_1 folds and a penetrative regional schistosity to spaced cleavage (S_1) axial planar to F_1 folds. D_1 was accompanied by greenschist to amphibolite facies metamorphism (M_1). D_2 deformation is related to emplacement, uplift, and unroofing of the Anvil Batholith (Jennings and Jilson, 1986). D_2 involved southwest-directed folding (F_2) and development of a shallowly southwest-dipping, penetrative schistosity to crenulation cleavage (S_2) axial planar to the F_2 folds. D_2 was accompanied by greenschist to amphibolite facies metamorphism (M_2) (Jennings and Jilson, 1986; Smith and Erdmer, 1989). F_2 folds are nearly coaxial with F_1 and, where seen, the interference pattern is typically type 3 (Ramsay, 1967; see fig. 21 in Jennings and Jilson, 1986). Brittle to ductile extensional faulting, related to unroofing of the Anvil Batholith, is late- to post-D_2 (Pigage and Jilson, 1985; Brown and McClay, 1992). Many post-F_2 faults in the Anvil District have subhorizontal to shallowly plunging slickensides indicating at least a late phase of strike-slip faulting (Jennings and Jilson, 1986; Brown and McClay, 1992). The D_3 to D_5 deformation events produced minor folding and steeply dipping crenulation cleavages that locally overprint the D_1 and D_2 structural elements.

Both the regional D_1 and D_2 deformation events were accompanied by metamorphism (M_1 and M_2, respectively; Tempelman-Kluit, 1972; Jennings and Jilson, 1986; Smith and Erdmer, 1990). The phyllites hosting the Vangorda orebody have a chlorite + muscovite + quartz assemblage in the S_1 cleavage and chlorite + muscovite + quartz ± biotite assemblage in the S_2 cleavage. The appearance of biotite in the M_2 assemblage corresponds to the M_2 Buchan series biotite isograd in the district (Tempelman-Kluit, 1972). The M_1 metamorphic grade in the district appears to be similar to that of M_2 since the S_1 and S_2 mineral assemblage are essentially the same.

D_2 regional metamorphic grade in the Anvil District decreases outward from the Anvil Batholith in a Buchan-type facies series in which the biotite, garnet, andalusite, staurolite and sillimanite isograds occur concentrically around the batholith (Tempelman-Kluit, 1972; Smith and Erdmer, 1990). In pelitic schists adjacent to the contact the common mineral assemblage is andalusite + staurolite + garnet + biotite + muscovite + quartz + plagioclase with local sillimanite (Pigage and Andersen, 1985). The absence of kyanite indicates pressure conditions of less than 4 kb. Smith and Erdmer (1990) determined pressures and temperatures of the D_2 metamorphism from petrogenetic relations to in the order of 3 kb and 400°–500°C for the chlorite + biotite zone and 600°–620°C for the biotite + almandine + sillimanite zone.

3. The Vangorda orebody

3.1. Ore lithofacies

The Vangorda orebody consists of five sulphide lithofacies of varying thickness and bulk sulphide composition. Both in the Vangorda orebody and in the other deposits in the district, there is a distinct vertical and lateral arrangement of ore lithofacies which Jennings et al. (1980) termed the Anvil Cycle (Fig. 2). Contacts between the sulphide lithofacies are commonly sharp but often display a complete gradation from one to another. The sulphide lithofacies are often accompanied by, and interlayered with, a chlorite-muscovite alteration zone.

Ribboned-banded, carbonaceous, pyritic quartzites: these are fine-grained, carbonaceous, phyllitic to siliceous quartzites with 0.2–5.0 mm thick ribbons of sulphide-bearing (10–30% py-

..., sphalerite and galena) coarsely crystalline quartzite. Sphalerite minerals in this lithofacies consist of fine- to medium-grained, subhedral to ...edral porphyroblasts of pyrite, sphalerite and ...alena. This lithofacies attains ore grade locally.

Pyritic quartzite: this consists predominantly of quartz with up to 40% fine- to medium-grained, euhedral to subhedral pyrite, sphalerite, galena, and minor pyrrhotite, magnetite and chalcopyrite. These rocks have a moderately to ...ly-developed differentiated layering consisting of nearly massive pyrite with minor magnetite and sulphide-bearing quartzite. Locally, a ...losilicate (muscovite-chlorite) preferred orientation is well-developed. The pyritic quartzites are gangue, though they do contain ...able Pb–Zn grade locally.

...assive pyritic sulphides: this lithofacies consists of fine- to medium-grained, euhedral to ...edral pyrite, sphalerite, galena, pyrrhotite ... minor magnetite and chalcopyrite. Total pyrite content varies from between 60% to close to 100%. Quartz, barite and carbonates are dissem...ed throughout the massive pyrite. A differ...iated layering is developed on a scale of millimetres as alternating massive pyrite (with ...or magnetite + elongate pyrrhotite + quartz) ... pyritic quartzite. The massive pyritic sulphide lithofacies is gangue.

...ritic, massive pyritic sulphides: these consist ...ominantly of barite with fine- to medium-grained, euhedral to subhedral pyrite, sphalerite ...d galena, with minor pyrrhotite, and magnetite. Quartz and carbonate are common gangue ...erals. Millimetre- to centimetre-scale differentiated layering of pyrite-rich and barite-rich ...y is ubiquitous. Clasts of massive pyrite and ...ite are common. Total barite content varies ...t may be has high as 50%. Massive barite does ...t occur. There is complete gradation between ...e baritic massive sulphide ores and the massive pyritic ore. This lithofacies is the major ore ...ck in the orebody.

...rrhotite-sphalerite massive sulphides: these ...st predominantly of fine-grained, euhedral ... elongate pyrrhotite and sphalerite with lesser, ...hedral to subhedral magnetite, galena, and pyrite. This lithofacies is highly strained, with well developed tailed pyrite porphyroblasts and winged inclusions of quartz or massive pyrite. This lithofacies commonly forms very high grade ore.

3.2. Metamorphism

Quantitative geothermometry was done on the chlorite from S_1 and S_2 mineral assemblages in the phyllites hosting the orebody to try and determine if a temperature difference existed. No temperature difference was found between the S_1 and S_2 mineral assemblages. Chlorite temperatures were calculated on the basis of Al_{IV} in the tetrahedral site using the equation of Cathelineau (1988) and are estimated to be 363°C ($2\sigma = \pm 24$°C).

Sulphide minerals in the orebody have undergone extensive deformation and recrystallisation during the D_2 tectonothermal event (cf. Brown and McClay, 1993). The common mineral assemblages found in these rocks that can be used to quantitatively estimate conditions of metamorphism are sphalerite + hexagonal pyrrhotite ± pyrite, arsenopyrite + pyrite and arsenopyrite + pyrrhotite. Grains in these assemblages form subhedral to euhedral porphyroblasts with well-developed 120° triple junctions. Euhedral pyrite porphyroblasts commonly grew across the S_2 foliation in the ribbon-banded, carbonaceous quartzite and overgrew sulphide minerals in other lithofacies, incorporating them as inclusions.

Arsenopyrite thermometry provides a temperature of 336°C ($2\sigma = \pm 20$°C) using the calibration of Sharp et al. (1985). A sphalerite + hexagonal pyrrhotite ± pyrite pressure of 4 kb ($2\sigma = \pm 0.5$ kb) was determined using the calibration of Hutchison and Scott (1981) and Bryndzia et al. (1988, 1990). These temperatures and pressure are in very good agreement with those calculated from silicate assemblages by Smith and Erdmer (1990), and further attest to the D_2 metamorphic conditions affecting the Vangorda orebody to be mid-greenschist facies.

A sphalerite + hexagonal pyrrhotite (+ pyrite) pressure of 4 and 6 kb was determined using the calibration of Hutchison and Scott (1981) and Bryndzia et al. (1988, 1990), respectively.

3.3. Structure

The Vangorda orebody has an overall tabular shape, elongate in a northwest–southeast orientation and plunges shallowly northwest, parallel to the regional F_2 fold axes. The orebody is approximately 900 m long by 200 m wide and varies in thickness from 20 to 60 m (Fig. 3). The orebody is subdivided into three major sulphide-bearing fault blocks and two phyllite-bearing fault blocks (Fig. 4), each with different structural features but similar structural styles.

The orebody is truncated in the northwest by the steeply southeast-dipping Northwest Fault which puts older sulphide-bearing Mt. Mye formation rocks in its hanging wall against younger Vangorda formation rocks in its footwall (Fig. 3). In the southeast, the moderately to steeply south-dipping Sump Fault truncates the thinning orebody. The Sump Fault is cut by the SE-dipping Overburden Fault. The orebody is cut approximately in half by the steeply to moderately northwest-dipping Cross Fault which juxtaposes the northwest part of the orebody against the southeast part, dividing the orebody into two distinct structural units. A late strike-slip fault, the Creek fault, offsets the Northwest Fault sinistrally approximately 30 to 40 m (Fig. 3).

The most northwesterly sulphide-bearing fault block (fault block 4) contains a thick sulphide package that makes up the bulk of the mineable reserves. This fault block is bound by the Northwest Fault and the Cross Fault and individual structural features and sulphide lithostratigraphic units cannot be traced into the fault blocks to the southeast. Southeast of the Cross Fault, two fault blocks contain a much thinner sulphide package (fault blocks 2 and 3). These are bound by the Sump Fault and the Cross Fault. The two phyllite-bearing fault blocks (Figs. 3 and 4) are partially exposed in the open pit, in the footwall to the Northwest Fault and in the hangingwall of the Sump Fault (fault blocks 5 and 1, respectively).

Structural orientation data from within each fault block (Fig. 4) shows an overall similar trend for the various structural elements. The F_2 folds in fault blocks 1, 2 and 3 plunge gently WNW–ESE and in fault blocks 4 and 5 they have a more NW–SE plunge. The S_2 in all fault blocks has an overall shallowly southwest-dipping orientation. The S_1 has two dominant trends which we interpret as reflecting a macroscopic F_2 fold. The S_1 in the normal limbs of F_2 folds dips predominantly towards the southwest to west, whereas in the overturned limbs it dips towards the north to northeast. Deviations from these trends, such as S_1 in fault block 2 and S_2 in fault block 5, are caused by complications arising from late faulting. This is discussed in more detail in the following text.

3.4. D_1 structural elements

The earliest structural element that can be recognised is a chlorite-muscovite spaced cleavage preserved in D_2 lithons in the phyllites (Fig. 5a). The occurrence of F_1 folding in rocks in close proximity to the orebody (see fig. 21 in Jennings and Jilson, 1986) with an axial planar cleavage indicates that the spaced cleavage in the orebody corresponds to the regional S_1 of Jennings and Jilson (1986). In the sulphide lithofacies a differentiated layering is well developed on a scale of millimetres to centimetres (Fig. 5b,c). Locally there is a marked angular relationship between the differentiated layering, the unfaulted sulphide/phyllite contact (S_0?), and S_2, suggesting that the layering is not a primary feature. The differentiated layering is pervasively folded by the same fold systems that resulted in the development of D_2 lithons, suggesting that both it and the within-lithon cleavage are syn-D_1 features (i.e., S_1).

The widespread presence of S_1 in the ore lithofacies and surrounding phyllites, and the evidence for F_1 folding in the district indicate the relative importance of F_1. The local angular relationship mapped between S_0, S_1 and S_2 indicates an overprinting relationship that suggests the possibility of large-scale F_1 folding affecting the orebody. However, F_1 folds have not been identified in the orebody. Several localised examples of mesoscopic refolded folds have been found in pit wall exposures but the fold evolution is ambiguous and it is thought that they may

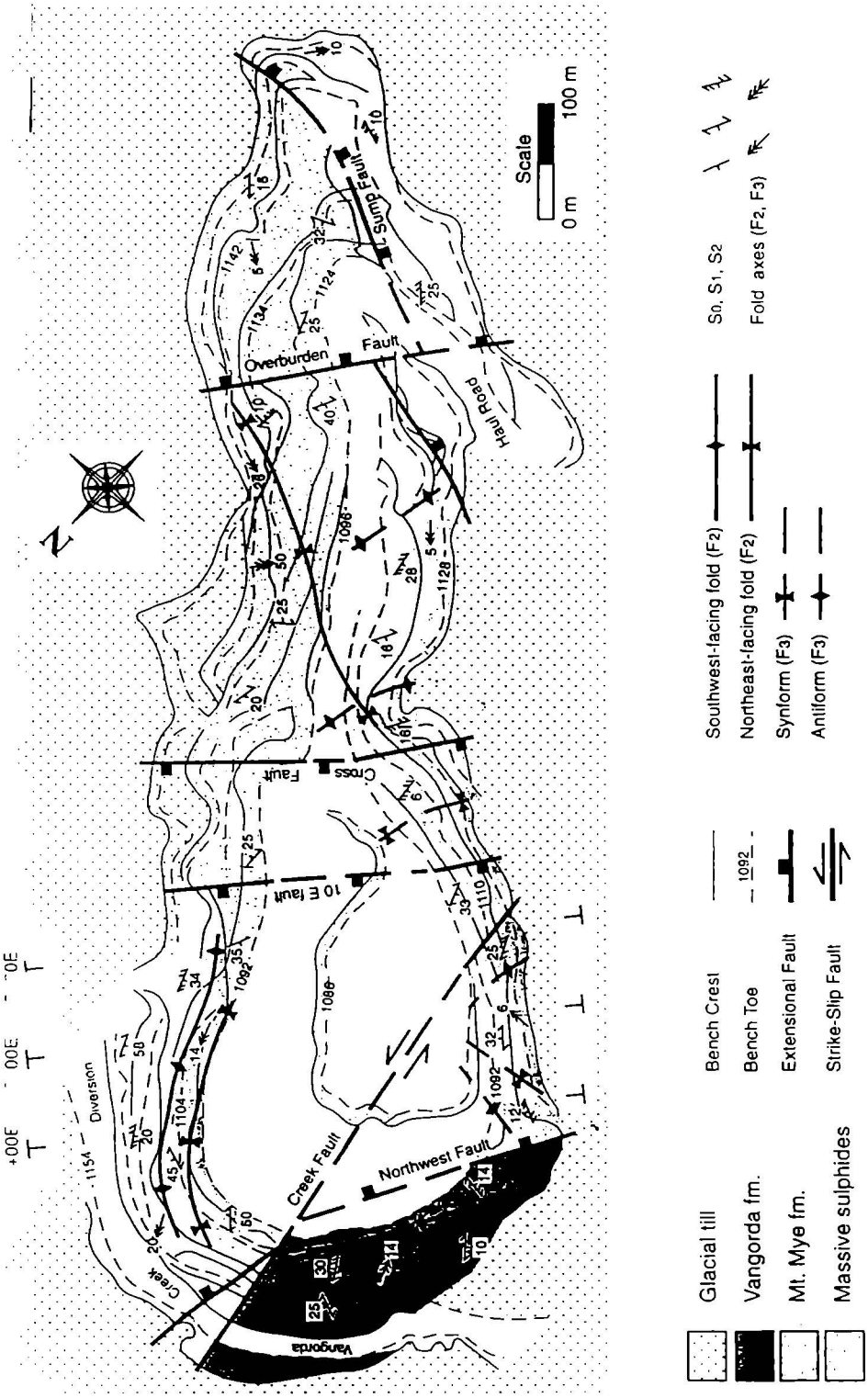

Simplified geological map of the Vangorda open pit mine, based on 1:500 scale mapping, showing the distribution of the major structural featur
the distribution of the lithofacies in the pit walls. Only representative structural element orientations are shown. Location of the diamond drill co
ections in Fig. 7 are also shown.

Fig. 4. Structural element orientation data for the individual fault blocks (see text). The location of each fault block is shown in the inset.

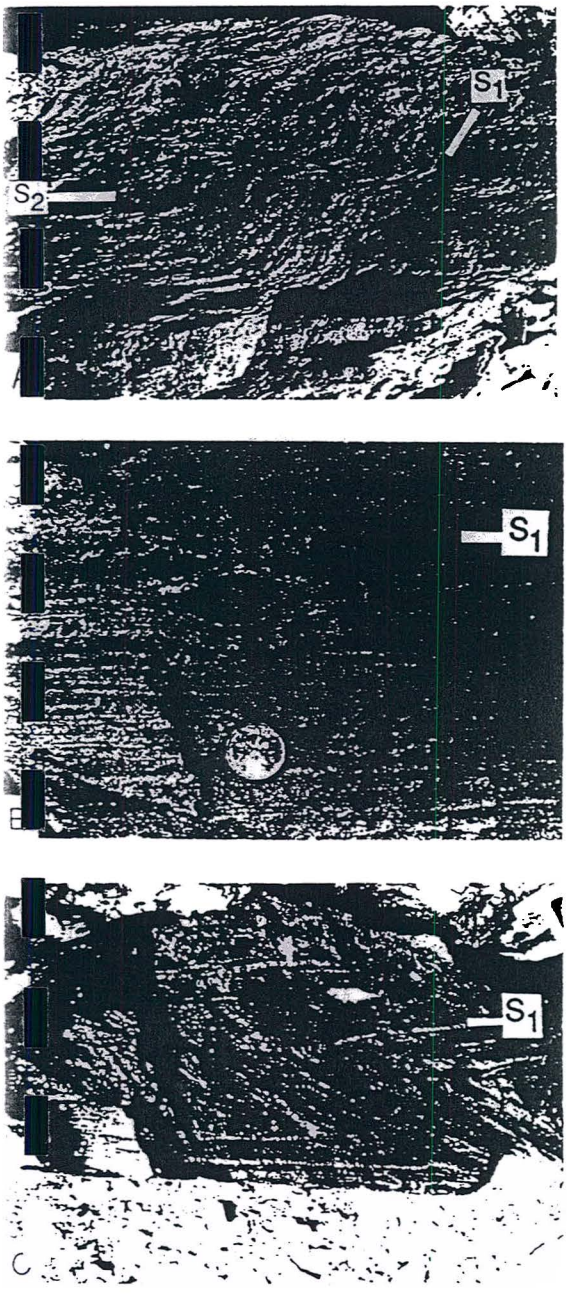

5(A). Field photograph showing F_2 crenulations in the nt Mye formation phyllites. (B) S_1 differentiated layer- a baritic massive sulphide. Note the winged inclusion of massive pyrite. (C) F_2-folded differentiated layering (S_1) in bbon-banded, carbonaceous quartzite.

have formed as a result of progressive folding during D_2, and not by F_1/F_2 interference.

3.5. D_2 structural elements

Throughout the orebody, the host phyllites have a predominantly southwest-dipping, penetrative, millimetre- to centimetre-scale carbonaceous, chlorite-muscovite crenulation to domainal cleavage (S_2). In most sulphide lithofacies S_2 is found only rarely, in high strain zones where shearing and pressure solution have resulted in the formation of a new, inhomogeneous S_2 cleavage (Brown and McClay, 1993). This is particularly the case for the baritic massive sulphides and the pyrrhotite-sphalerite massive sulphides. However, in the ribboned-banded, carbonaceous quartzite, a differentiated axial planar S_2 cleavage is well developed.

The dominant fold phase in the Vangorda orebody clearly folds the S_1 foliation and is therefore F_2. F_2 folds are often tight to isoclinal similar folds (Fig. 5c) but within the different sulphide lithofacies the F_2 fold style is variable as a result of the different rheological properties. In general the similar style is maintained. Many mesoscale folds outcropping in the sulphides, especially those affecting the baritic lithofacies, show considerable thickening in the hinge zone.

The large-scale fold structure of the orebody has been constructed from the relationships between the S_1 and S_2 form traces mapped in open pit exposures (Fig. 6a). Fault blocks 2 and 3 (sections A–A′ and B–B′, respectively) contain a southwest-facing and northeast-facing recumbent fold pair (Fig. 6b), cut by the Overburden Fault and the Sump Fault. Fault block 2 (section A–A′) contains the west- to northwest-dipping overturned limb and part of the southwest-facing fold closure. The overturned limb has been folded by movement along the Sump Fault which accounts for the spread and re-orientation of S_1 shown in Fig. 4. Fault block 3 contains the northeast-facing closure and southwest- to west-dipping normal limb and northeast-facing closure of the same structure (section B–B′).

The S_1/S_2 relationships in fault block 4 (section C–C′) defines a southwest-facing and

northeast-facing recumbent fold pair (Fig. 6b). The overturned limbs of these folds dip predominantly towards the north to northeast and the normal limbs dip southwest to west. This structure is cut by the Northwest Fault which juxtaposes it against a northeast-facing recumbent fold in its footwall (Fig. 6a) and by the Creek fault. The S_1/S_2 relationship between the hangingwall of the Northwest Fault and the Creek fault along the southwestern side of the mine is complicated by tight F_3 folding related to movement along these faults. However, the geometry is that of an overturned F_2 limb. The more NNW-plunge of fold axes in fault block 4 compared to those in other fault blocks (Fig. 4) indicates some block rotation has likely occurred. The orientation of fold axes in fault block 5 are probably the result of bending of structures into the Northwest Fault.

The S_2 form surface traces are openly warped to tightly folded near major faults (Fig. 6a). In pit wall exposures, this is manifested as local broad warping of S_2 and is interpreted to be the result of south- to southwest-plunging, open F_3 folds. The proximity of the folded S_2 form surface traces with faults in the orebody and the orientation of F_3 axes (Fig. 3), suggests F_3 may be related to post-S_2 faulting.

All faults examined in open pit exposures truncate the S_2 cleavage and F_2 folds and, therefore, post-date or are late D_2. Faults generally dip towards the northwest or southeast to south and form graben and half-graben systems. The amount of offsets along most faults is difficult to determine because of the lack of marker horizons. However, the phyllite sulphide contact is affected many small-scale faults that are coeval with the larger faults. These minor faults have offsets of centimetres to several metres. Offsets on the major faults, such as the Northwest Fault and Cross Fault are impossible to determine but are thought to be on the order of several tens of metres (Cross Fault) to hundreds of metres (Northwest Fault). Faults are commonly segmented and overlapping, forming fault zones rather than discrete fault surfaces. Within the sulphide lithofacies rocks, faults form wide, steeply dipping zones of intense fracturing and cataclasis. In phyllites they are shallower dipping and form discrete gouge zones. Locally, faults are sealed by phyllosilicates, quartz and calcite and, in some instances, by pyrite.

Paucity of marker horizons and kinematic indicators make it difficult to accurately determine the kinematics of most faults in the orebody. However, many faults have slickensided fault surfaces and are accompanied by bending of the S_2 cleavage in close proximity to faults that can be used to indicate at least a final phase of fault movement. Slickensides have a varying array of orientations, ranging from downdip to a high pitch angle in the fault plane, as in the case of the Northwest, Sump and Cross faults, to subhorizontal, as in the case of the Creek fault. Individual faults also display sets of variably oriented slickensides ranging from down-dip to subhorizontal. The complete spectrum of slickenside orientations attest to a complicated fault kinematic history. Strike-slip reactivation of extensional faults, or vice versa, is possible.

3.6. Diamond drill core analysis

The diamond drill core cross sections through fault block 4 (Fig. 7) show a number of complexly folded lenses of massive and disseminated sulphides and baritic massive sulphides in host phyllites. The overall fold style and fold geometry and location is partially constrained by open pit mapping. Section 6+00E (Fig. 7) corresponds to section C–C′ (Fig. 6b). The extreme fold complexity apparent in these sections is due in part to the lensoidal nature of the sulphide lithofacies involved, to minor faulting and to unconstrained orientation of the marker structural element (S_2) in drill core.

The hanging wall and footwall phyllite and sulphide lithofacies contact is faulted locally, but is generally gradational, marked by an increase in chlorite/muscovite content in the phyllites and concomitant decrease in quartz and sulphide content, similar to that mapped in the mine. The sulphide lithostratigraphic sequence and host phyllites are folded by southwest-verging, tight, symmetric to slightly asymmetric F_2 folds with a wavelength of 50–75 m. The folds are signifi-

Fig 6(A) & B. For caption see p. 13.

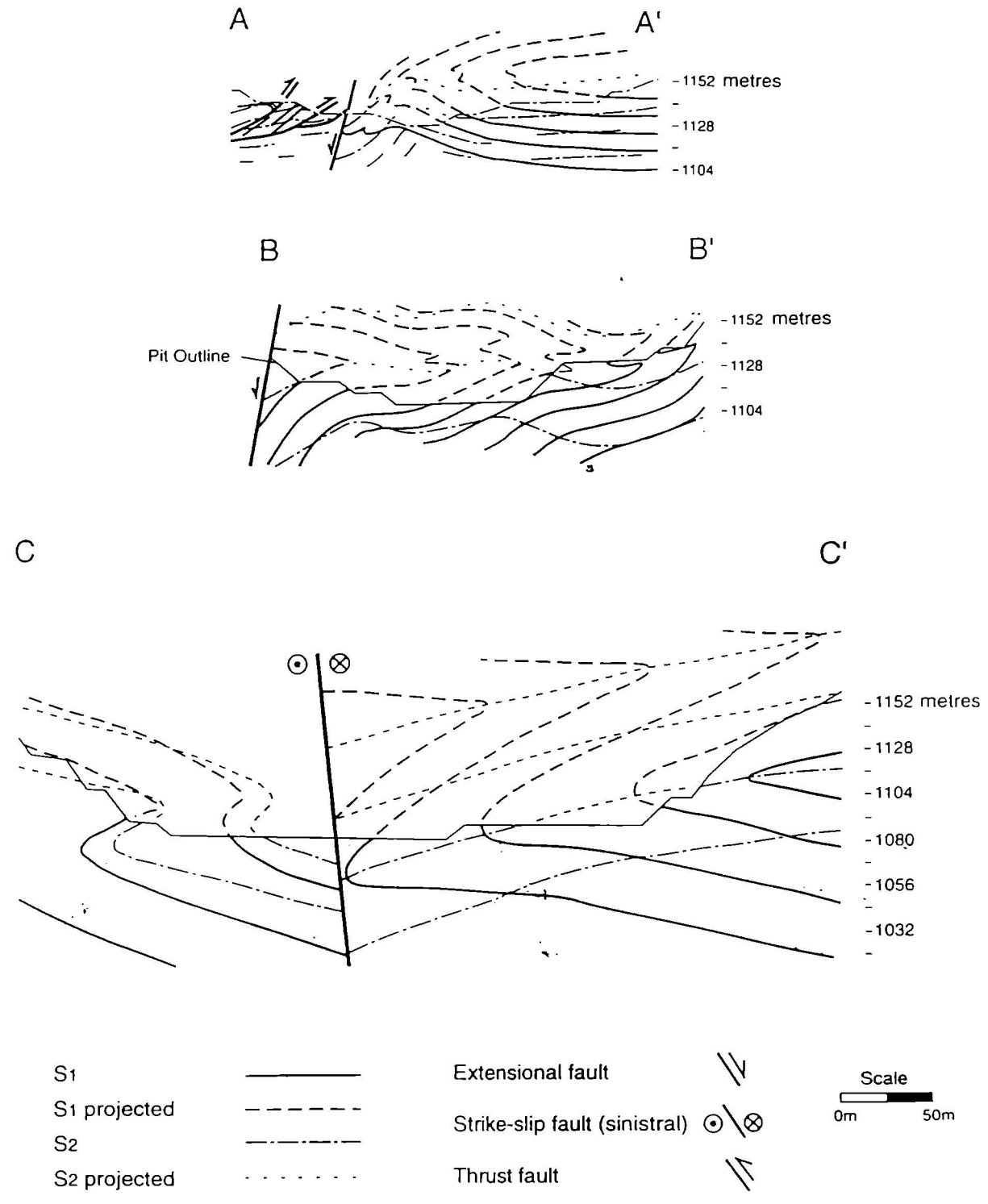

Fig. 6(A). Map of the Vangorda open pit showing the S_1 and S_2 form surface traces compiled from a 1:500 scale map. Note the sharp bends in the S_2 trace adjacent to the Cross Fault and the Northwest Fault. (B) Schematic S_1/S_2 cross-sections through fault blocks two, three and four (locations are shown on Fig. 6A).

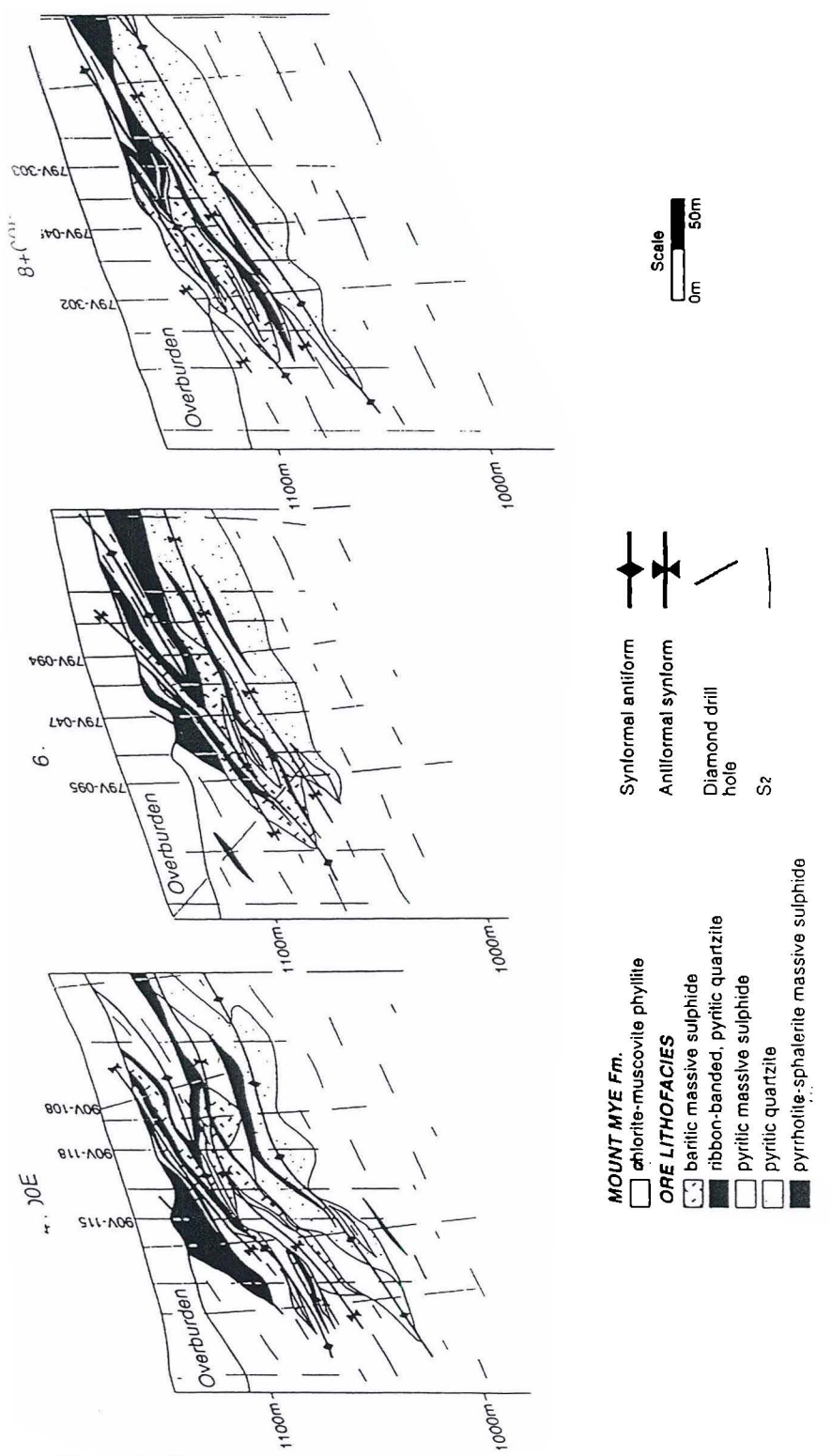

g. 7. Diamond drill core cross-sections through fault block four (locations are shown in Fig. 4). Fault block four makes up the bulk of the mineabi serves and also provides the best example of the F_2 fold style affecting the sulphides. Note the position of the pyrrhotite, sphalerite, galena massiv i des (shear zones) along the limbs of the F_2 folds, subparallel to the fold axial surface. These shear zones pinch out laterally.

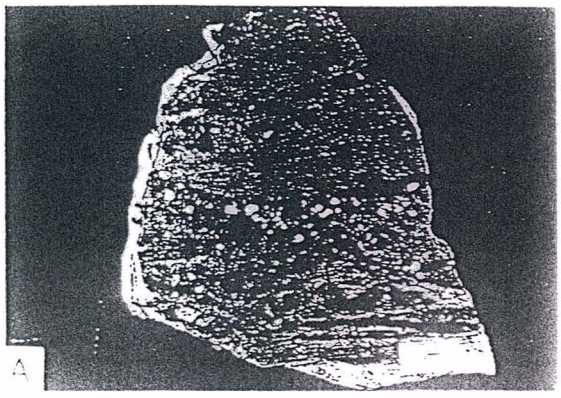
A

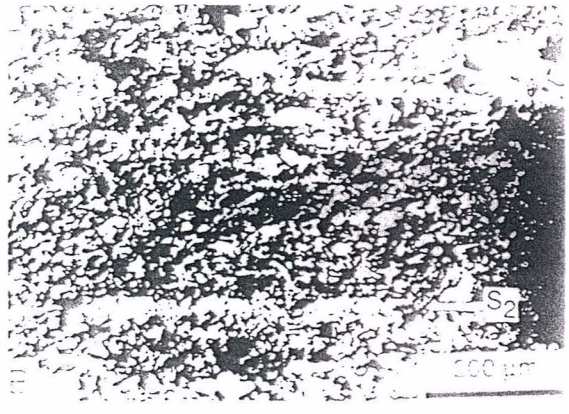
B
S_2
200 μm

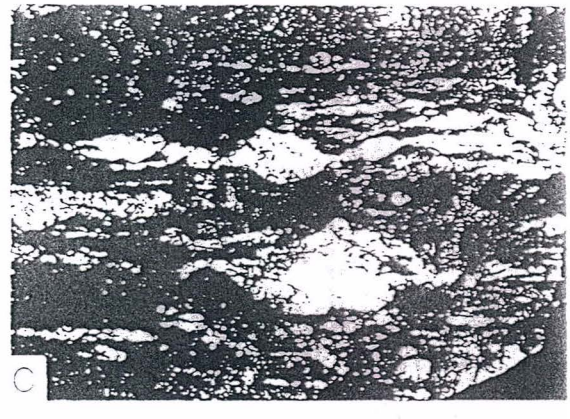
C

abundant broad, parallel-sided growth twinning and 120° triple junctions. However, the widespread presence of strongly lobate grain boundaries may indicate strain-induced grain boundary migration processes were active. The higher modal abundance of sphalerite and galena in these areas has resulted in an increase Pb+Zn grade.

Discussion

This paper discusses the deformation and metamorphism that affects the Vangorda orebody. The angular relationships between the phyllite/sulphide contact (S_0), S_1 and S_2 suggests the presence of a macroscopic D_1 structure, possibly an F_1 fold. However, it is not possible to further elucidate the nature or effects of D_1 other than that it resulted in the development of a penetrative S_1 cleavage and metamorphism, possibly to a similar grade as M_2. Only the D_2 and post-D_2 structures can be determined with any degree of confidence and they provide the main structural control on the geometry and metamorphic textures of the orebody. Quantitative thermobarometry shows that M_2 metamorphism was low temperature and low pressure (i.e., 336°C to 363°C at 4 kb).

The Vangorda orebody has macroscale and mesoscale geometries and textures that reflect extensive D_2 deformation, metamorphism and remobilisation of the orebody. Diamond drill-core cross-sections through the orebody (Fig. 7) show significant limb thinning and hinge zone thickening of the macroscale F_2 fold structure. Large-scale mobilisation appears to be focused in the rheologically less competent baritic massive sulphides which have deformed by cataclastic and plastic processes. Similar remobilisation of sulphides into areas of low relative strain such as fold closures, fractures and boudin necks has been widely documented (e.g., Pedersen, 1980; Vaiden et al., 1986; Skinner and Johnson, 1987; De Roo et al., 1991).

The pyrrhotite-sphalerite lithofacies occurs along the limbs and hinges of folds within the baritic lithofacies and along the limbs of the macroscopic fold structure, commonly at the contact with the pyritic quartzite and other lithofacies. In these areas the widespread occurrence of shear indicators, the well-developed pyrrhotitic foliation, and the significantly reduced grain size provide strong evidence for the interpretation of these as shear zones situated in areas of high shear strain (i.e., along the limbs of folds). The occurrence of magnetite inclusions in pyrrhotite and pyrrhotite inclusions in magnetite suggests this process may have been accompanied by complex activity and fugacity interaction of sulphur and oxygen.

A possible mechanism for development of these shear zones involves strain localisation combined and resultant cataclasis of the host lithofacies. Solute mass transfer processes result in an increase in the modal abundance of pyrrhotite, sphalerite and galena in the shear zone. The increase in modal abundance of the rheologically weak sulphides is accompanied by a switch in the mode of deformation from cataclasis of the host to plastic processes focused in the sulphide grains. This switch in deformation processes resulted in extensive shearing of the breccia clasts to form asymmetric and symmetric winged and tailed inclusions, formation of pyrrhotitic ribbons with weak crystallographic preferred orientation and reduced grain size. The small grain size and subhedral to euhedral grain shape of the sulphides, together with strain-induced grain boundary processes such as bulging, suggests deformation in these areas took place under steady state conditions in which deformation and recrystallisation processes where proceeding at roughly the same rate. A process involving cataclastic flow and reaction-enhanced deformation softening has been described in silicate rocks by Kronenburg and Tullis (1984), Koons et al. (1987), Brodie and Rutter (1988) and bears similarities to the processes that took place in the shear zones in the Vangorda orebody.

The pyrrhotite-sphalerite massive sulphides described in this paper are interpreted to be shear zones along which deformation is localised. A similar relationship between the increased strain and pyrrhotite content discussed here has been noted in the Ducktown massive sulphide mine

in Tennessee by Brooker et al. (1987). The processes active within these zones facilitate the mechanical and chemical remobilisation of the sulphides within the shear zones by solution and strain-induced plastic deformation processes. They also facilitate mechanical remobilisation of material within the orebody by providing weakened areas along which the orebody can move. Other than a moderate increase in the Pb+Zn grade associated with the shear zones and concentration of the baritic massive sulphides in the hinges of the folds there appears to be very little structural control on the distribution of any of the elements assayed in the orebody.

The Vangorda orebody is cut by a number of post-F_2 extensional faults that dip steeply towards the northwest or southeast to south. These faults have similar orientations and characteristics to those described elsewhere in the Anvil District as being related to unroofing of the Anvil Batholith (Jennings and Jilson, 1986; Pigage, 1990). Extensional faults in the Vangorda orebody are likewise interpreted to be related to unroofing of the batholith. These faults have folded the S_2 foliation in close proximity to them. A final phase of faulting in the mine is strike-slip. Strike-slip faults may also be related to unroofing of the batholith. An alternative explanation is that they are related to movement along the Tintina Fault. However, both these explanations cannot be proved for the Vangorda orebody.

Acknowledgements

This work forms part of D. Browns Ph.D. research. Brown is funded in part by the Rothemere Foundation, and by the Special Scholarship for Students doing Research in Resource Development administered by Memorial University of Newfoundland. Fieldwork was supported by Curragh Resources, Department of Indian and Northern Affairs Canada (Whitehorse), Geological Survey of Canada (Vancouver), and by the Industry Association (RHUL). Gregg Jilson and Lee Pigage are thanked for their help during the course of fieldwork. Reviews by Joaquina Alvarez-Marrón, Daniel Arias and Andrés Pérez-Estaún greatly improved the manuscript. Journal referees K. Sundblad and J. De Roo provided insightful comments.

References

Abbott, J.G., Gordey, S.P. and Tempelman-Kluit, D.J., 1986. Setting of stratiform, sediment-hosted lead-zinc deposits in Yukon and northeastern British Columbia. In: J.A. Morin (Editor), Mineral Deposits of Northern Cordillera. Can. Inst. Min. Metall., Spec. Pap., 37: 1–18.

Brodie, K.H. and Rutter, E.H., 1985. On the relationship between deformation and metamorphism with special reference to the behaviour of basic rocks. In: A.B. Thompson and D.C. Rubie (Editors), Advances in Physical Geochemistry 4. Springer, Berlin, pp. 138–179.

Brooker, D.D., Craig, J.R. and Rimstidt, 1987. Ore metamorphism and pyrite porphyroblast development at the Cherokee mine, Ducktown, Tennessee. Econ. Geol., 82: 72–86.

Brown, D. and McClay, K., 1992. Structure of the Vangorda Pb–Zn–Ag orebody, Anvil Range, Yukon Territory. In: Current Research, Part A. Geol. Surv. Can., Pap. 92-1A: 121–128.

Brown, D. and McClay, K., 1993. Deformation textures in pyrite from the Vangorda Pb–Zn–Ag orebody, Yukon, Canada. Min. Mag.

Bryndzia, L.T., Scott, S.D. and Spry, P.G., 1988. Sphalerite and hexagonal pyrrhotite geobarometer: experimental calibration and application to the metamorphosed sulphide ores of Broken Hill, Australia. Econ. Geol., 83: 1193–1204.

Bryndzia, L.T., Scott, S.D. and Spry, P.G., 1990. Sphalerite and hexagonal pyrrhotite geobarometer: correction in calibration and application. Econ Geol., 85: 408–411.

Carne, R.C. and Cathro, R.J., 1981. Sedimentary exhalative (sedex) zinc-lead-silver deposits northern Canadian Cordillera. Can. Min. Metall. Bull., 75: 66–75.

Cathelineau, M., 1988. Cation site occupancy in chlorites and illites as a function of temperature. Clay Miner., 23: 471–485.

De Roo, J.A., Williams, P.F. and Moreton, C., 1991. Structure and evolution of the Heath Steele base metal sulphide orebodies, Bathurst Camp, New Brunswick, Canada. Econ. Geol., 86: 927–943.

Hutchison, M.N. and Scott, S.D., 1981. Sphalerite geobarometry in the Cu–Fe–Zn–S system. Econ. Geol., 76: 143–153.

Jennings, D.S. and Jilson, G.A., 1986. Geology and sulphide deposits of the Anvil Range, Yukon. In: J.A. Morin (Editor), Mineral Deposits of Northern Cordillera. Can. Inst. Min. Metall., Spec. Pap., 37: 319–361.

Jennings, D.S., Jilson, G.A. and Pigage, L.C., 1980. Anvil Range stratigraphy, south-central Yukon Territory (ab-

itract). Geol. Assoc. Can., Cordilleran Sect., Progr. Abstr., pp. 16–17.

Koons, P.O., Rubie, D.C. and Frueh-Green, G., 1987. The effects of disequilibrium and deformation on the mineralogical evolution of quartz diorite during metamorphism in eclogite facies. J. Petrol., 28: 679–700.

Kronenberg, A.K. and Tullis, J., 1984. Flow strengths of quartz aggregates: grain size and pressure effects due to hydrolitic weakening. J. Geophys. Res., 89: 4281–4297.

McIntyre, D.G., 1992. Geological setting and genesis of sedimentary exhalative barite and barite-sulphide deposits, Cataga District, Northeastern British Columbia. Explor. Min. Geol., 1: 1–20.

McClay, K.R., 1991. Deformation of stratiform Zn–Pb(–barite) deposits in the northern Canadian Cordillera. Ore Geol. Rev., 6: 435–462.

Mien, K.J., Chimimba, L.R. and Smalley, T.J., 1986. Cusate ore-wall rock interfaces, piercement structures, and the localization of some sulphide ores in deformed sulphide deposits. Econ. Geol., 81: 1464–1472.

Nilsen, F.D., 1980. Remobilization of the massive sulfide ore of the Black Angel Mine, central west Greenland. Econ. Geol., 75: 1022–1041.

Pigage, L.C., 1990. Field Guide Anvil Pb–Zn–Ag District, Yukon Territory, Canada. In: J.G. Abbott and R.J.W. Turner (Editors), Mineral Deposits of the Northern Canadian Cordillera, Yukon—Northeastern British Columbia. Geol. Surv. Can., Open File Rep., 2169: 283–308.

Pigage, L.C. and Jilson, G.A., 1985. Major extensional faults, Anvil Pb–Zn district, Yukon (abstract). Geol. Soc. Am., Cordilleran Sect. Annu. Meet., Abstr. Progr., 17: 400.

Pigage, L.C. and Anderson, R.G., 1985. The Anvil Plutonic suite, Faro, Yukon Territory. Can. J. Earth Sci., 22: 1204–1216.

Ramsay, J.G., 1967. Folding and Fracturing of Rocks. McGraw-Hill, New York, N.Y., 568 pp.

Shanks, W.C. III, Woodruff, L.G., Jilson, G.A., Jennings, D.S., Modene, J.S. and Ryan, B.D., 1987. Sulfur and lead isotope studies of stratiform Zn–Pb–Ag deposits, Anvil Range, Yukon: basinal brine exhalation and anoxic bottom-water mixing. Econ. Geol., 82: 600–634.

Sharp, Z.D., Essene, E.J. and Kelly, W.C., 1985. A re-examination of the arsenopyrite geothermometer: pressure considerations and applications to natural assemblages. Can. Mineral., 23: 517–534.

Skinner, B.J. and Johnson, C.A., 1987. Evidence for movement of ore materials during high-grade metamorphism. Ore Geol. Rev., 2: 191–204.

Smith, J.M. and Erdmer, P., 1990. The Anvil aureole, an atypical mid-Cretaceous culmination in the northern Canadian Cordillera. Can. J. Earth Sci., 27: 344–356.

Tempelman-Kluit, D.J., 1972. Geology and origin of the Faro, Vangorda, and Swim concordant zinc-lead deposits, central Yukon Territory. Geol. Surv. Can. Bull., 208, 73 pp.

Tempelman-Kluit, D.J., 1979. Transported cataclasite, ophiolite and granodiorite in Yukon Territory. Geol. Surv. Can., Pap. 79-14, 27 pp.

THE VANGORDA DEPOSIT

Dennis Brown and Ken McClay
Department of Geology, Royal Holloway, University of London, Egham, Surrey, U.K., TW20 OEX

BROWN, D., and MCCLAY, K.R., 1993. The Vangorda deposit. In: Yukon Exploration and Geology, 1992, Exploration and Geological Services Division, Yukon, Indian and Northern Affairs Canada, p.27-32.

NTS map sheet: 105 K/6
Coordinates: 62° 15' N, 133° 12' W
Area: Anvil District
Access: Robert Campbell Highway
MINFILE #: 55
Company: Curragh Inc.
Commodities: Zinc, Lead, (Silver, Gold)

INTRODUCTION

The Vangorda deposit is a small (7.1 million tonne), SEDEX-type, Pb-Zn-Ag (barite) massive sulphide ore body, in the Anvil district, Yukon, Canada (Figure 1). The deposit is currently being open pit mined at approximately 13,000 tonnes per day by Curragh Inc. A project was begun at the start of mine development in 1990 in order to define the deformational style of the deposit and, by extrapolation, that of the other massive sulphide deposits in the Anvil District. In addition, the detailed understanding of the structural controls on the ore body are beneficial during development stages for grade control, and for short-term planning during mining. The sulphide textures that result from deformation, metamorphism, and remobilsation are important metallurgical factors that have significant effects on the milling properties of sulphide ores.

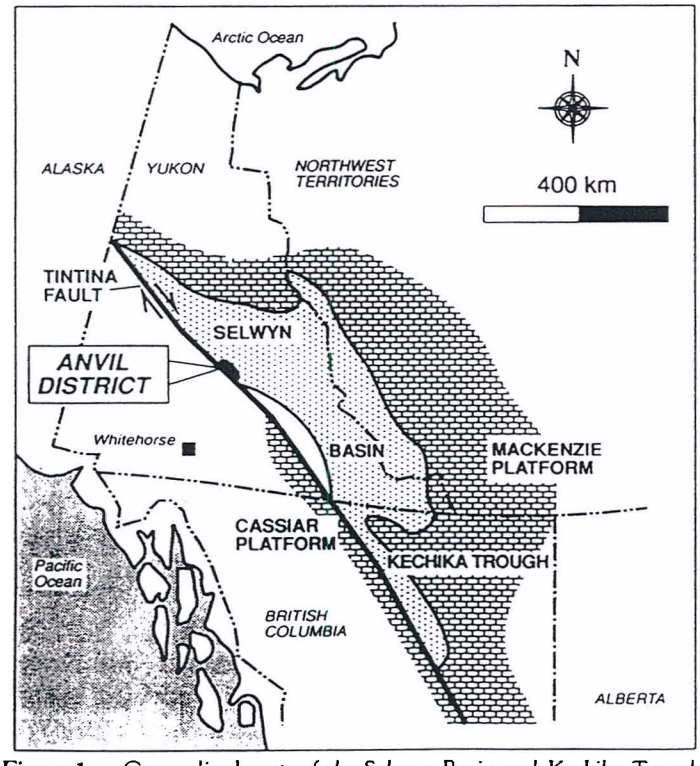

Figure 1. Generalised map of the Selwyn Basin and Kechika Trough showing the location of the Anvil District.

REGIONAL GEOLOGY

The Anvil District (Figure 2) is part of the Omineca Crystalline Belt of the western Canadian Cordillera (Monger et al. 1982). The district is structurally overlain by the allochthonous Yukon-Tanana terrane (Coney et al. 1980) and is adjacent to a major orogen-scale dextral strike-slip fault, the Tintina Fault. Rocks in the Anvil District consist of late Precambrian to upper Paleozoic metasedimentary and metavolcanic rocks that are correlated with Selwyn Basin stratigraphy (Jennings and Jilson 1986) which formed part of the ancient North American miogeocline until the Early Cretaceous. These rocks have been intruded by mid-Cretaceous granitoid rocks of the Anvil Plutonic Suite (Pigage and Anderson 1985; Jennings and Jilson 1986).

Five deformation events have been recognised in the Anvil District, the first two of which (D_1 and D_2) are regionally significant (Jennings and Jilson 1986). D_1 is interpreted to be related to the pre- to mid-Cretaceous docking of the allochthonous Yukon-Tanana terrane onto the continental margin (Tempelman-Kluit 1979) causing inversion of the rift basin, northeast-directed nappe emplacement, folding, thrusting and metamorphism of the continental margin sediments. D_1 deformation resulted in the development of northeast-verging F_1 folds and a penetrative regional foliation (S_1), and regional metamorphism. D_2 deformation is related to emplacement, uplift, and unroofing of the Anvil Batholith (Jennings and Jilson 1986). D_2 resulted in southwest-directed folding, development of a wavy, shallowly southwest-dipping, penetrative foliation (S_2), and greenschist to amphibolite facies metamorphism (Jennings and Jilson 1986; Smith and Erdmer 1989). F_2 folds are nearly coaxial with F_1 and, where seen, the interference pattern is typically type 3 (Ramsay, 1967; see Jennings and Jilson 1986, figure 21). Northwest-southeast - dipping, brittle to ductile extensional faulting, related to unroofing of the Anvil Batholith, is late- to post-D_2 folding (Pigage and Jilson 1985; Brown and McClay 1992). However, many faults in the district have subhorizontal to shallowly-plunging slickensides indicating at least a late phase of strike-slip movement (Brown and McClay, 1992, in press). The D

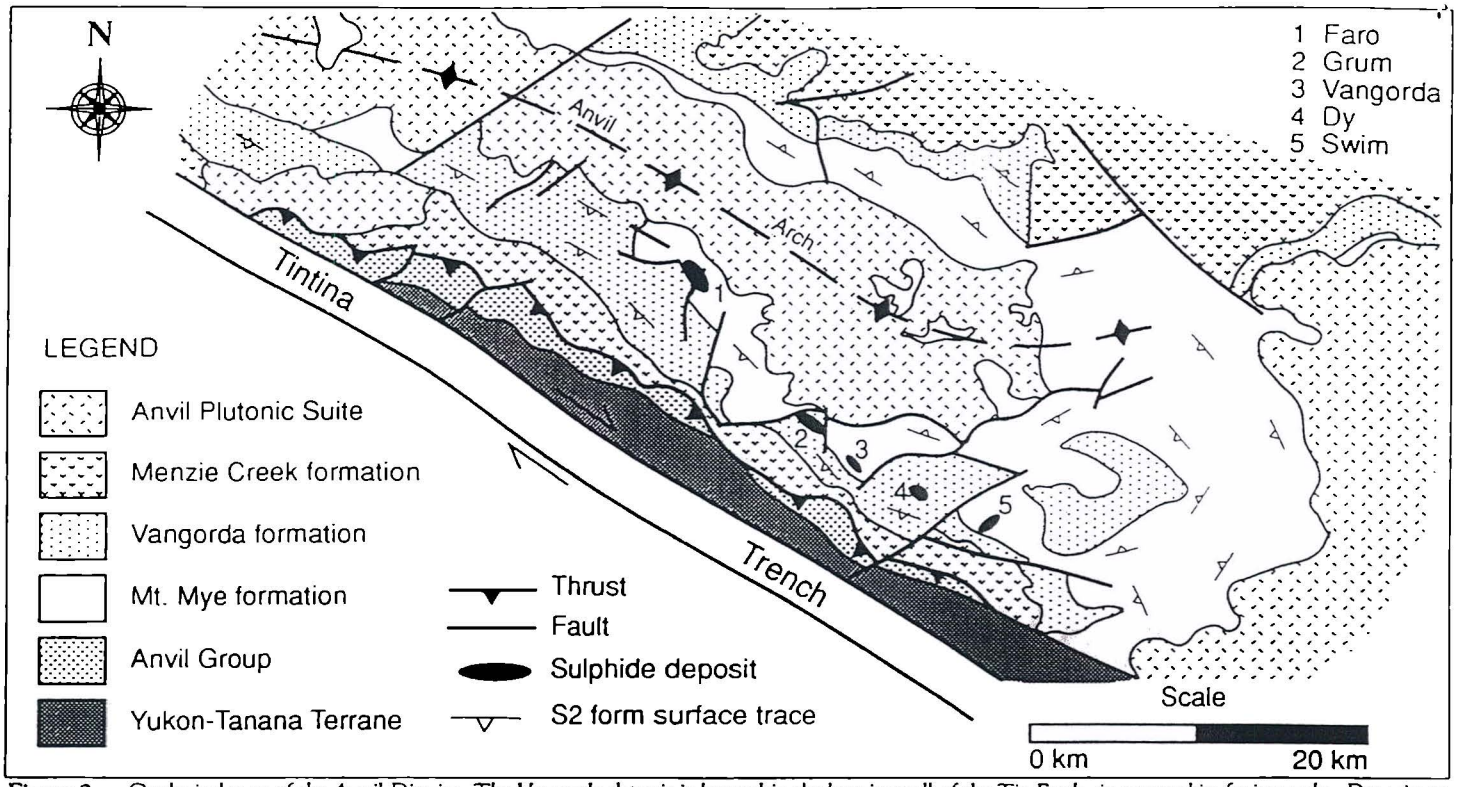

Figure 2. Geological map of the Anvil District. The Vangorda deposit is located in the hangingwall of the Tie Fault, in greenschist facies rocks. Deposits to the northwest are Faro and Grum, respectively. The large deposit immediately southeast of Vangorda is Dy.

to D_5 deformation events produced minor folding and steeply dipping crenulation foliations that locally overprint the D_1 and D_2 structural elements.

The lithostratigraphy of the Anvil District consists of up to 5 km of polydeformed metasedimentary and metavolcanic rocks that have been intruded by Cretaceous granites (Figure 3). The massive sulphide deposits are hosted by, or straddle the boundary between two lithostratigraphic units of importance to this paper, the Mt. Mye formation and the overlying Vangorda formation. The Mount Mye formation consists of noncalcareous schists and phyllites and has an apparent structural thickness of at least 2 km, though its base is not exposed. The Vangorda formation consists of calcareous schists and phyllites and varies from between 0.5 to 2 km in structural thickness.

The Anvil mining district, is the largest Pb-Zn play in northern Canada with estimated geological reserves before mining of 120 million tonnes with a combined Pb + Zn grade of 9.3% (Jennings and Jilson 1986). The district contains five SEDEX-type Pb-Zn-Ag (barite) deposits (Carne and Cathro 1981) of economic significance that lie along a curvilinear trend on the southwest flank of the Anvil Batholith (Figure 2). The deposits are interpreted to have formed in second and third order extensional rift basins (Jennings and Jilson 1986; Shanks et al. 1987), similar to those described elsewhere in Selwyn Basin and Kechika Trough by McClay (1991) and MacIntyre (1992). The massive sulphide deposits are variably affected by the deformation events, with D_1 and D_2 being dominant (Jennings and Jilson 1986). The Faro deposit is deformed by D_1 through to and D_4 and metamorphosed to amphibolite facies. Grum, Vangorda, and Dy are mostly affected by D_1 and D_2, with only minor F_3 crenulation folding, and reach greenschist facies metamorphism.

THE VANGORDA DEPOSIT

Lithostratigraphy

The Vangorda deposit is hosted by the Mount Mye formation which consists of greenschist facies, light to medium grey noncalcareous, weakly carbonaceous, muscovite-chlorite phyllite with lesser, interlayered, carbonaceous phyllite, calcareous phyllite, and metabasite. The overlying Vangorda formation, which is exposed in the northwest end of the open pit, consists of light to medium grey, calcareous, weakly carbonaceous muscovite-chlorite phyllite and light grey, calcareous quartz-calcite (+ dolomite) phyllite with interbanded metabasite, carbonaceous phyllite, and phyllitic limestone.

Ore lithofacies

The Vangorda deposit consists of a number of stacked sulphide lenses of varying thickness and bulk sulphide composition. Ore lithofacies are interbanded on a scale of centimetres to metres and commonly display a complete gradation from one to another. These are accompanied by, and interbanded with, Mount Mye formation phyllites. A footwall biased muscovite alteration zone is also developed but is not continuous.

Ribbon-banded, carbonaceous, pyritic quartzite: these are well banded, fine grained, carbonaceous, phyllitic to siliceous quartzite and interbanded, sulphide-bearing (pyrite, sphalerite, and galena) coarsely crystalline quartzite. Banding ranges from 0.2 mm to 2.0 mm in thickness and typically contains 10% to 30% sulphides. This lithofacies is typically low grade ore.

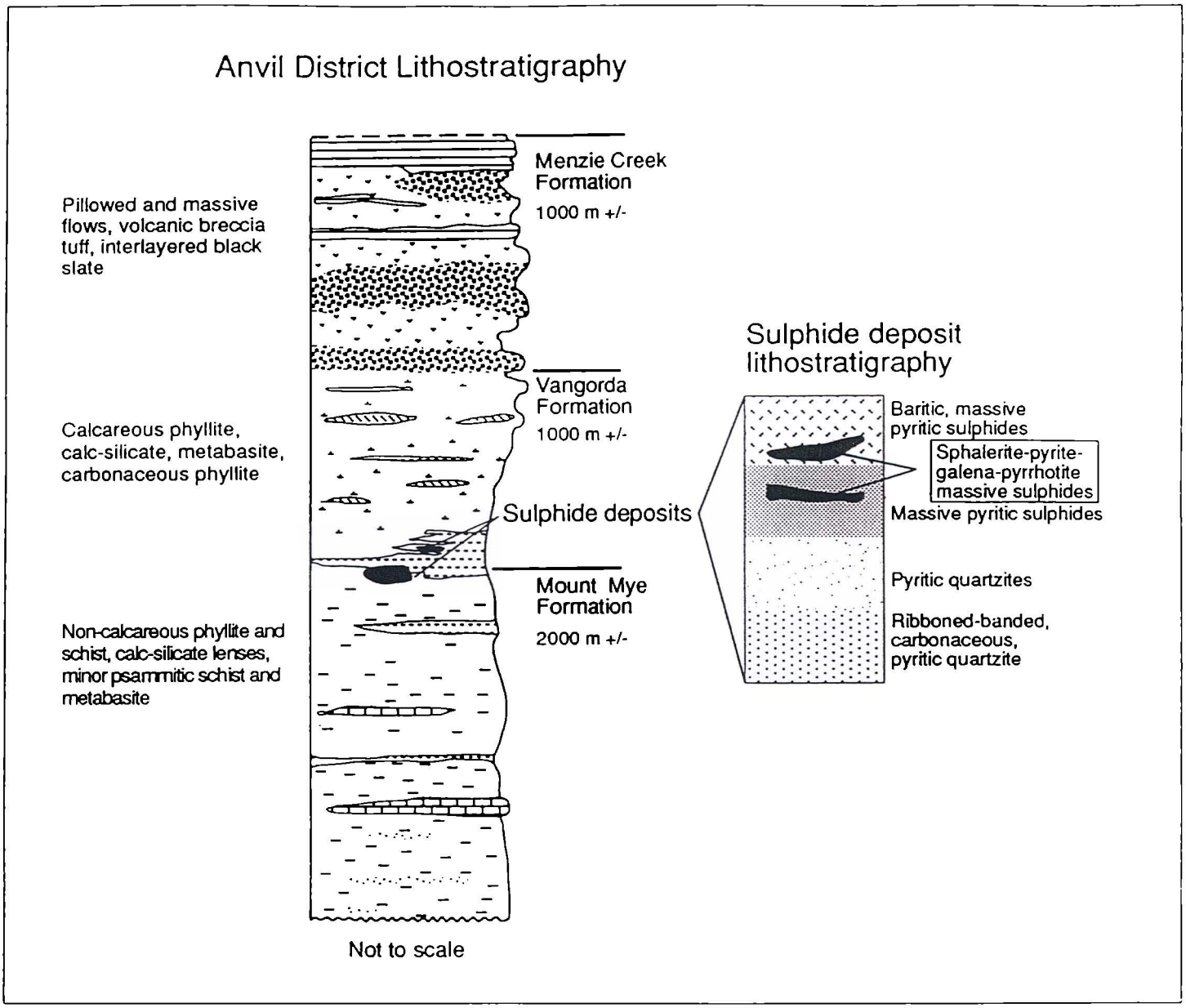

Figure 3. Lithostratigraphic column of the Anvil District with the generalised ore lithostratigraphic sequence of the Vangorda deposit (modified from Jennings and Jilson, 1986).

Pyritic quartzite: consists predominantly of quartz with up to 40% pyrite with subordinate sphalerite and galena. These rocks are moderately to poorly banded with, locally, a well developed micaceous (muscovite-chlorite) foliation. Chalcopyrite + pyrrhotite infills subvertical fractures. The pyritic quartzite is commonly gangue but may locally attain ore grades.

Massive pyritic sulphides: these are typically massive pyrite with subordinate sphalerite, galena, pyrrhotite, and minor magnetite and chalcopyrite. Quartz, barite, and carbonates are disseminated throughout or occur in aggregates. Total sulphide content varies from between 60% to nearly 100%. Banding is developed on a scale of centimetres to metres as alternating massive pyrite and of pyritic quartzite, often grading from one to the other. A muscovite-chlorite foliation is common. The massive pyrite lithofacies is gangue.

Baritic, massive pyritic sulphides: these consist of up to 50 % barite with pyrite, sphalerite, galena, together with minor pyrrhotite and magnetite. Quartz and carbonate are major gangue components. Clasts of pyrite and phyllite are common within the banded sulphide. Total barite content varies but may be has high as 50 %. Millimetre- to centimetre-scale interbanding of pyrite-rich and barite-rich layers is ubiquitous. Massive barite has not been observed. There is a complete gradation between the baritic massive sulphide ores and the massive pyritic ore. This lithofacies is the major ore type in the Vangorda deposit.

Pyrrhotite-sphalerite-pyrite-magnetite-galena (breccia): this lithofacies consists predominantly of pyrrhotite and sphalerite with subordinate pyrite, magnetite, and galena. This lithofacies is typically highly strained with a well developed foliation in both the sulphide- and the micaceous sulphides. These rocks often contain breccia clasts of other rock types around which the foliation anastomoses. Tailed

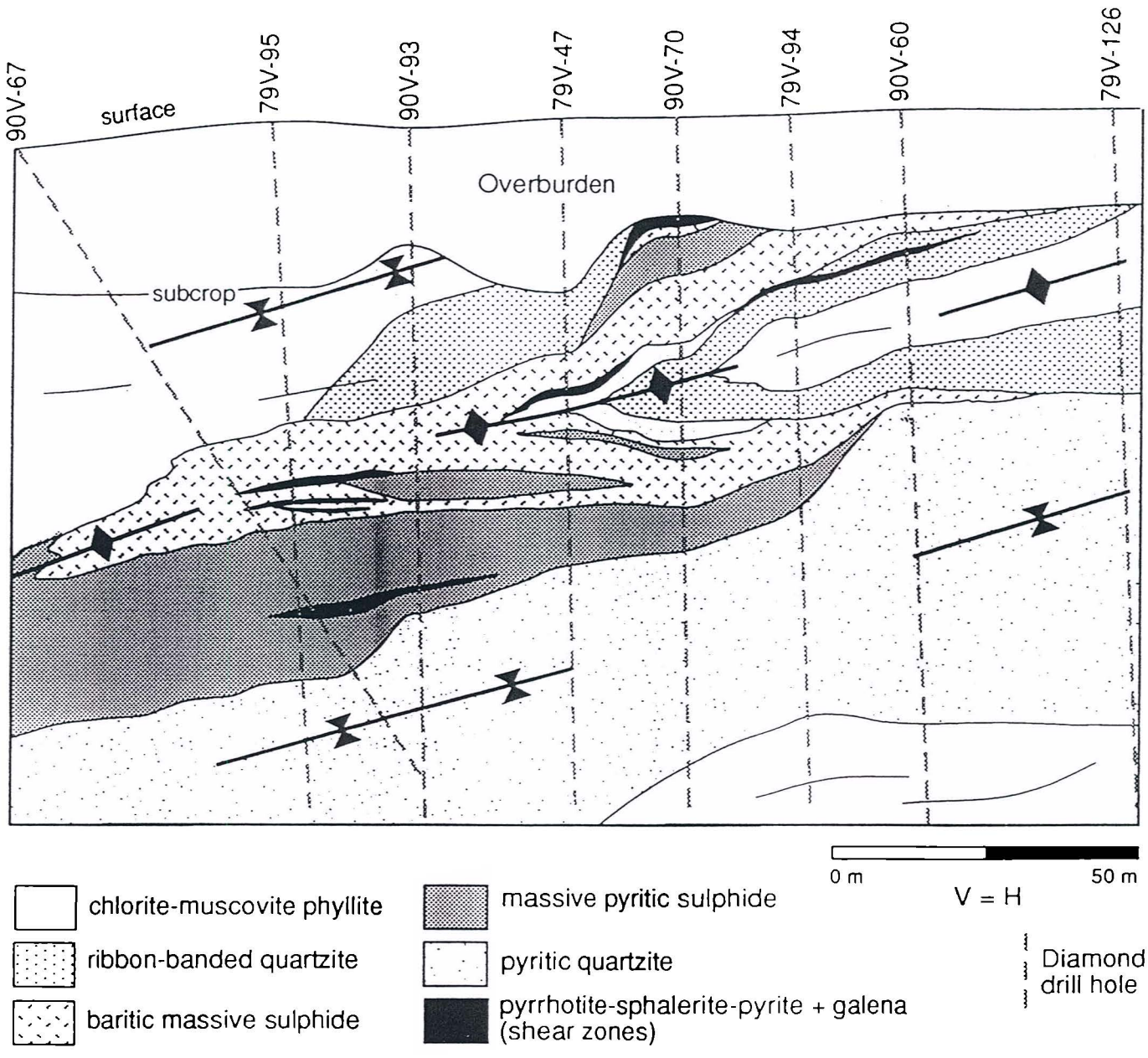

Figure 4. Detail of cross section 6 through the Vangorda deposit. The baritic lithofacies shows extensive mobilisation into the hinge zone of the F2 structure. The major structure containing the ore deposit is a southwest-facing synformal-antiform. High strain zones denoted by the pyrrhotite-sphalerite-pyrite-galena lithofacies occur along the fold limbs and in the hinge zone.

porphyroblasts, winged inclusions, foliation boudins, and rolling structures are common. This lithofacies, though relatively minor, is typically high grade ore.

Metamorphism

Both the regional D_1 and D_2 deformation events were accompanied by metamorphism in the Vangorda deposit. D1 metamorphic mineral assemblages found in lithons in phyllites (see below) in the Vangorda deposit consist of chlorite + muscovite with, locally, biotite.-chlorite intergrowths. These assemblages broadly indicate that the D_1 metamorphic grade was low to mid-greenschist facies. D_2 regional metamorphic grade in the Anvil District decreases outward from the Anvil Batholith in a Buchan-type facies series (Jennings and Jilson 1986; Smith and Erdmer 1989). In the Vangorda deposit, D_2 silicate assemblages in phyllites consist of transposed and recrystallised muscovite and chlorite, suggesting

there may not have been any significant new mineral growth during the D_2 event. The D_2 metamorphic grade is also interpreted to be lower greenschist facies.

Structure

All sulphide lithofacies and phyllites in the Vangorda deposit have been penetratively deformed by the D_1 and D_2 deformation events, making definition of any primary depositional features difficult on a scale other than microscopic (c.f. Brown and McClay 1992, in press). However, the Anvil District macro-scale sulphide lithostratigraphic sequence defined by Jennings and Jilson (1986) may be a relic primary feature. The hangingwall and footwall, phyllite and sulphide lithofacies contacts are locally faulted, but are generally gradational.

The Vangorda deposit has an overall elongate shape in a northwest-southeast orientation and plunges shallowly northwest, parallel to the regional F_2 fold axes. The orebody is approximately 900 m long by 200 m wide and varies in thickness from 20 m to 60 m. It consists of a number of complexly folded and faulted lenses of massive and disseminated sulphides and baritic massive sulphides in quartzitic and graphitic phyllites. In cross section the deposit is folded by a series of southwest-verging, northwest-plunging, tight, symmetric to slightly asymmetric F_2 folds (Figure 4). These folds have a wavelength of 50 m to 75 m. The cross section shows a thickening and concentration of baritic massive sulphides in hinge zone of a SW-verging synform-antiform fold pair. Relatively thin pyrrhotite, sphalerite, pyrite, and galena-rich zones occur along the limbs of the folds and in the baritic rocks in the hinge, parallel to the F_2 axial surface.

F_1 folds are rarely observed in the Vangorda deposit, possibly as a result of the penetrative overprinting by the F_2 folding. Lithons in the phyllites and the ribbon-banded, carbonaceous quartzite are interpreted to contain a S_1 foliation (Figure 5a). Banding in the sulphide lithofacies is locally at a moderate to high angle to the phyllite contacts and is generally pervasively folded by F_2 folds, suggesting that it is also S_1.

The dominant fold phase in the Vangorda deposit is F_2. F_2 folds are typically east-west- to northwest-southeast-plunging, tight to isoclinal (interlimb angle is commonly between 5o to 25_) similar style folds (Figure 5b). Within the different sulphide lithofacies the F_2 fold morphology is variable, but, in general, a similar style is maintained.

In the surrounding phyllites there is a penetrative, wavy, predominantly southwest-dipping F_2 axial planar crenulation foliation (S_2). S_2 is defined by transposed chlorite/muscovite porphyroblasts and remobilised carbon. In the ribboned-banded, carbonaceous quartzite, a differentiated axial planar S_2 foliation is also well developed. However, S_2 in other sulphide lithofacies is found only rarely in fold hinges and high strain zones. In high strain zones, shearing has disrupted the S_1 banding and a new, inhomogeneous foliation is developed, parallel to the F_2 axial surface.

Steeply south- to southwest-plunging to subvertical, open F_3 folds refold the S_2 foliation and tighten F_2 folds. There is only a minor crenulation foliation associated with the F_3 folding.

Within the ore lithofacies rocks there are zones characterised by well foliated pyrrhotite + sphalerite + magnetite + galena and pyrite

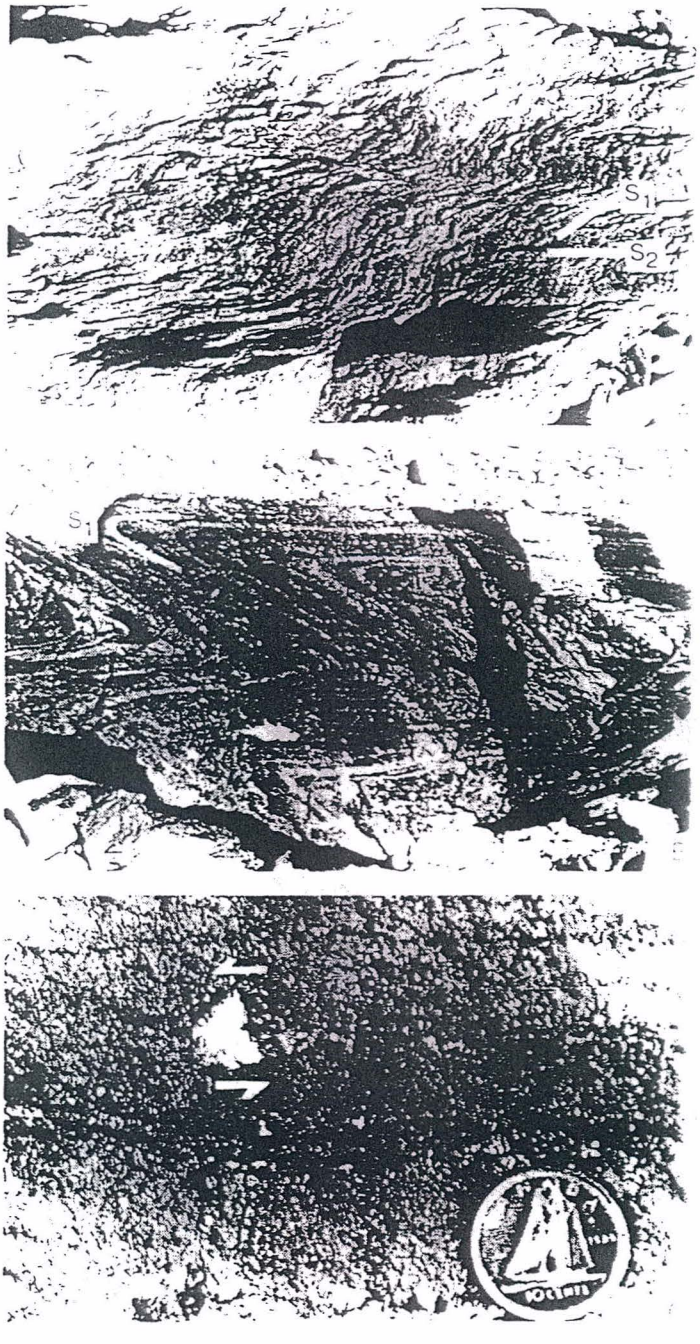

Figure 5 *(a) Lithon texture defined by S1 and S2 in Mt. Mye formation phyllites. Coin provides scale. (b) F2 fold folding S1 banding in ribbon-banded, carbonaceous quartzite. Hammer in bottom left corner provides scale (c) Winged quartz inclusion in massive pyritic sulphides. Arrows indicate a sinistral sense of shear (note, however, that this sample is not in situ.)*

with angular to rounded inclusions of brecciated quartz, phyllite and sulphides. These zones display textures such as winged inclusions (Hanmer and Passchier 1991), tailed and rotated clast-foliation boudins, and brecciation (Figure 5). These structures indicate very high strains and are interpreted to be the product of shearing within sulphide shear zones. The shear zones occur along the limbs of F_2 folds, and range in width from several millimetres to several metres thick and clearly show an increase in pyrrhotite

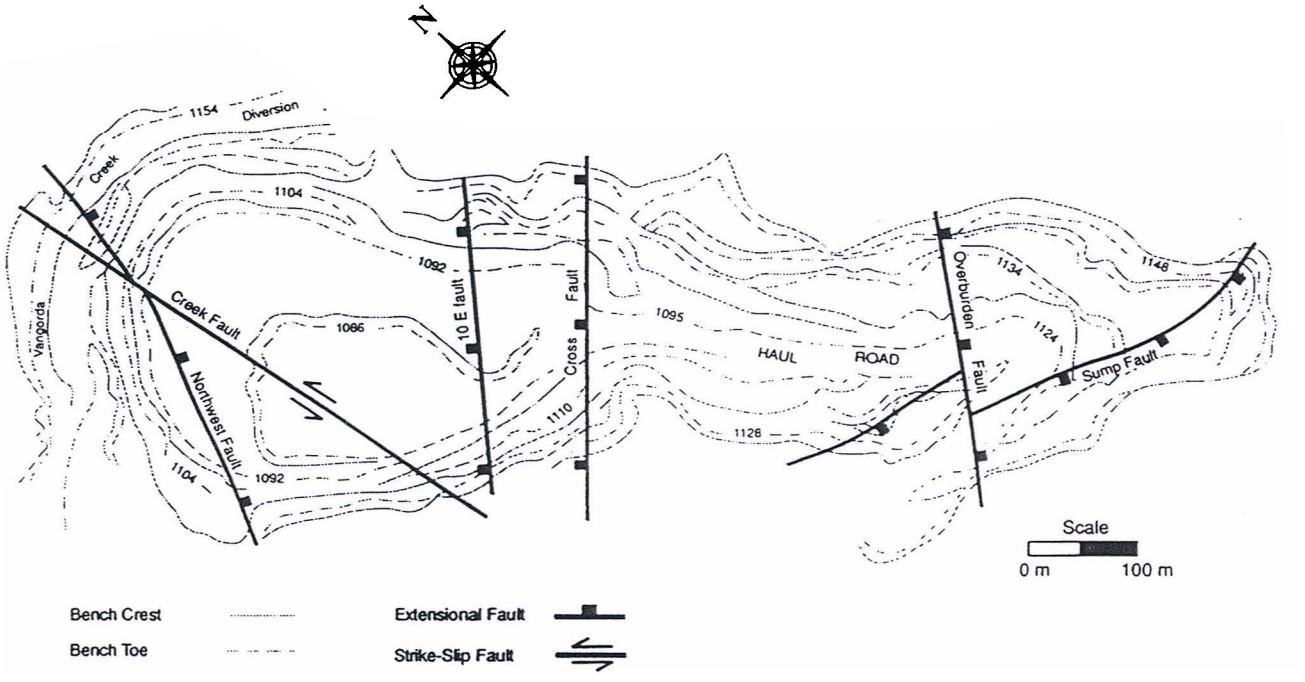

Figure 6. Generalised status map of the Vangorda open pit showing the locations of the major faults.

similar increase in pyrrhotite content in high strain zones was also noted in the Ducktown deposit of Tennessee by Brooker et al. (1987)

The present down-plunge extent of the ore body is controlled by faulting. All faults examined in open pit exposures truncate the S_2 foliation and the F_2 folds and the sulphide shear zones, and therefore clearly post-date or are late D_2 folding. The deposit is truncated in the northwest by the steeply southeast-dipping Northwest fault, and in the southeast by the moderately to steeply south-dipping Sump fault (Figure 6). The deposit is cut in half by the steeply to moderately north-northwest-dipping Cross fault. Smaller faults, with offsets up to 5 m, commonly form graben and half-graben structures. Slickensides on these fault surfaces are steeply-plunging indicating a final phase of extensional movement.

However, there are also subhorizontal to shallowly plunging slickensides on many fault surfaces, thus indicating a late stage of strike-slip to oblique-slip movement (Figure 6). In the northern end of the deposit the Creek fault offsets the Northwest fault by approximately 50 metres. Sets of variably oriented slickensides attest to a complicated kinematic history for many of these faults, and a strike-slip reactivation of previously formed extensional faults is possible. In open pit exposures there is clear evidence of strike-slip faults cutting extensional fault structures. In the northern end of the open pit, minor NE-directed thrusting appears related to the strike-slip faulting. Thrusting may be the result of a transpressional component to the strike-slip movement.

At the southern end of the deposit, in the hangingwall of the Sump fault, low-angle, post-D_2, northeast-directed thrusts occur within phyllites, cutting the S_2 foliation. Displacement along these thrust may be up to 10 m.

DISCUSSION

This paper illustrates the macroscopic deformational style of the Vangorda deposit. The deposit is deformed by four significant and one minor phase of deformation. The first two phases, D_1 and D_2, resulted in ductile and brittle deformation (i.e. folding and development of sulphide shear zones, fracturing), metamorphism, and remobilisation. These were followed by brittle extensional faulting and brittle strike-slip faulting, respectively. Minor F_3 folding has also been observed but its relationship with post D_2 faulting is unclear.

Though there is a very good correlation in macroscopic structural style between the host phyllites and the sulphides, the Vangorda deposit has mesoscale textures that reflect extensive shearing of the orebody, especially in the baritic and pyrrhotitic massive sulphides. There are abundant shear indicators such as tailed and winged clasts and inclusions and pressure solution fabrics in these lithofacies. These, together with other common features such as piercement veins, rootless folds, limb thinning and hinge zone thickening of folds, point to extensive mechanical mobilisation of the sulphide in the Vangorda deposit. The location of the pyrrhotitic (breccia) in the large-scale folds indicate significant shearing along the limbs. These shear zones may provide a mechanism by which large-scale mobilisation occurs in massive sulphide deposits.

Faults in the Vangorda deposit clearly offset F_2 and S_2 and therefore post-date or are late D_2. Major faults (i.e. Northwest fault, Cross fault, and Sump fault) dip steeply towards the northwest or southeast and have moderate to steeply-plunging slickensides. Slickensides indicate a final oblique- to dip-slip component of movement. The lack of marker horizons make it difficult to impossible to determine the exact amount of offset on many faults

or to determine their kinematic history. A post-extensional phase of strike-slip faulting strikes NE-SW and N-S. The Creek fault offsets the Northwest fault sinistrally approximately 50 metres. It is not clear if strike-slip faults are reactivated extensional faults.

The tight to isoclinal, similar fold style and complex internal deformation indicates that the Vangorda deposit has undergone significantly high strains. Strain partitioning has produced breccia zones and shear zones in part controlled by the sulphide and matrix rheologies. Shear zones in particular are localised in the baritic massive sulphide facies or along lithofacies boundaries, commonly along the limbs of the large F_2 fold structure.

An understanding of the location, orientation, and expression of structures and structural elements within a deformed and metamorphosed deposit are of interest to the mine geologists and engineers in the day to day operations of the mine. For instance, the orientation and location of features such as faults, joints, and various foliations provide important information that can be used to help predict and assess pit wall stability, potential problems with water, location of road access to the active mining area, and to predict loading pattern and charge of blasts. Likewise, an enhanced understanding of the location and orientation of folds and faults, and which are major and which minor, are of importance in grade control during mining. By paying careful attention to these factors dilution of the ore can be significantly reduced and mine development factors can be more efficiently assessed and the costs of mine operations reduced. These and other aspects of a structural analysis of a developing mine are beyond the scope of this paper but point to the importance of continuous and detailed mapping during mine operation.

ACKNOWLEDGEMENTS

Fieldwork for this project was jointly supported by DIAND (Geology Section, Whitehorse) and by Curragh Inc. Successful completion of fieldwork could not have been achieved without the help of the people at the Faro mine site, especially those in the Geology and Engineering departments. The G.S.C. (Vancouver) is thanked for field support during the 1991 field season. The Industry Association, Royal Holloway College, is thanked for logistical support during the 1991/92 field seasons. Brown is funded in part by the Rothemere Foundation (University of London) and by a Newfoundland Provincial Government "Special scholarship for studies in the sciences related to resource development" issued through Memorial University of Newfoundland.

REFERENCES

BROOKER, D.D., CRAIG, J.R., RIMSTIDT. (1987) Ore metamorphism and pyrite porphyroblast development at the Cherokee mine, Ducktown, Tennessee. Econ. Geol. 82, p. 72-86

BROWN, D., MCCLAY, K. (1992) Structure of the Vangorda Pb-Zn-Ag deposit, Anvil Range, Yukon Territory. In Current Research, Part A; Geol. Surv. of Can., Paper 92-1A, p. 121-128

BROWN, D., MCCLAY, K. (in press) Deformation textures in pyrite from the Vangorda Pb-Zn-Ag deposit, Yukon, Canada. Mineralogical Magazine.

CONEY, P.J., JONES, D.L., MONGER, J.W.H. (1980) Cordilleran suspect terranes. Nature. 288, p. 329-333

HANMER, S; PASSCHIER, C. (1991) Shear sense indicators: a review. Geological Survey of Canada, Paper 90-17, 72 p.

JENNINGS, D.S., JILSON, G.A. (1986) Geology and sulphide deposits of the Anvil Range, Yukon. In Mineral Deposits of Northern Cordillera (J.A. Morin, ed.). Canadian Institute of Mining and Metallurgy, Special Paper 37, p. 319-361

JENNINGS, D.S., JILSON, G.A., PIGAGE, L.C. (1980) Anvil Range stratigraphy, south-central Yukon Territory (abstract). Geological Association of Canada, Cordilleran Section, Programme and Abstracts, p. 16-17

MACINTYRE, D.G. (1992) Geological setting and genesis of sedimentary exhalative barite and barite-sulphide deposits, Gataga District, Northeastern British Columbia. Exploration and Mining Geology. 1, p. 1-20

MCCLAY, K.R. (1991) Deformation of stratiform Zn-Pb (-barite) deposits in the northern Canadian Cordillera. Ore Geology Reviews. 6, p. 435-462

MONGER, J.W.H., PRICE, R.A., TEMPELMAN-KLUIT, D.J. (1982) Tectonic accretion and the origin of the two major metamorphic and plutonic belts in the Canadian Cordillera. Geology. 10, p. 70-75.

PIGAGE, L.C. (1990) Field Guide Anvil Pb-Zn-Ag District, Yukon Territory, Canada. In Mineral Deposits of the Northern Canadian Cordillera, Yukon-Northeastern British Columbia (J.G. Abbott & R.J.W. Turner, eds.), Geological Survey of Canada, Open File 2169, p. 283-308

PIGAGE, L.C., JILSON, G.A. (1985) Major extensional faults, Anvil Pb-Zn district, Yukon (abstract). Geological Society of America, Cordilleran Section Annual Meeting, Abstracts with Programmes, 17, p. 400

PIGAGE, L.C., ANDERSON, R.G. (1985) The Anvil Plutonic suite, Faro, Yukon Territory. Canadian Journal of Earth Sciences, 22, p. 1204-1216

RAMSAY, J.G. (1967) Folding and Fracturing of Rocks. New York, McGraw-Hill, 567 p.

SHANKS, W.C. III, WOODRUFF, L.G., JILSON, G.A., JENNINGS, D.S., MODENE, J.S., RYAN, B.D.. (1987) Sulphur and lead isotope studies of stratiform Zn-Pb-Ag deposits, Anvil Range Yukon: Basinal brine exhalation and anoxic bottom-water mixing. Economic Geology, 82, p. 600-634.

SMITH, J.M., ERDMER, P (1989) The Anvil aureole, an atypical mid-Cretaceous culmination in the northern Canadian Cordillera. Canadian Journal of Earth Sciences, 27, p. 344-356

TEMPELMAN-KLUIT, D.J. (1979) Transported cataclasite, ophiolite and granodiorite in Yukon Territory. Geological Survey of Canada, Paper 79-14, 27 p.

Structure of the Vangorda Pb-Zn-Ag deposit, Anvil Range, Yukon Territory

Dennis Brown[1] and Ken McClay[1]
Cordilleran Division, Vancouver

Brown, D. and McClay, K., 1992: Structure of the Vangorda Pb-Zn-Ag deposit, Anvil Range, Yukon Territory; in Current Research, Part A; Geological Survey of Canada, Paper 92-1A, p. 121-128.

Abstract

The Vangorda Pb-Zn-Ag deposit is a small polydeformed, polymetamorphosed sedex-type massive sulphide deposit in the Anvil Mining District of the Selwyn Basin, Yukon Territory. The ore body consists of a number of banded, gently southwest-dipping lenses of sulphide lithofacies in the hinge and overturned limb of a southwest verging F_2 fold. Banding in the sulphide lithofacies occurs on a scale of millimetres to centimetres interpreted to be S_1. The S_1 banding is folded by mesoscopic northwest- to southeast-plunging, tight to nearly isoclinal, class 2 similar style F_2 folds. The deposit is cut by northwest- and northeast-dipping extensional faults with a final stage of strike-slip to oblique-slip movement. F_2-folded ductile shear zones occur in the sulphide lithofacies.

Preliminary microstructural work indicates that pyrite in the Vangorda deposit deformed by both ductile and brittle mechanisms. Subsequent annealing textures are common.

Résumé

Le gisement à Pb-Zn-Ag de Vangorda est un petit gisement de sulfures massifs de type SEDEX, polydéformé et polymétamorphisé, contenu dans le district minier d'Anvil du bassin de Selwyn (Yukon). Le massif minéralisé est composé d'un certain nombre de lentilles rubanées à lithofaciès sulfuré plongeant faiblement vers le sud-ouest dans la charnière et le flanc déversé d'un pli F_2 à vergence sud-ouest. Le rubanement observé dans le lithofaciès sulfuré est d'échelle millimétrique à centimétrique, interprété comme étant de type S_1. Le rubanement S_1 est déformé par des plis F_2 mésoscopiques, semblables, de classe 2, à plongement de nord-ouest à sud-est et dont l'aspect varie de serrés à quasi isoclinal. Le gisement est limité par des failles de distension plongeant vers le nord-ouest et le nord-est qui témoignent d'un stade final de décrochement ou de mouvement oblique. Des zones de cisaillement ductile à plis F_2 sont présentes dans le lithofaciès sulfuré.

Des études microstructurales préliminaires indiquent que la pyrite contenue dans le gisement de Vangorda a été déformée à la fois par des mécanismes ductiles et cassants. Les textures dues à des recristallisations par recuit sont courantes.

[1] Department of Geology, Royal Holloway and Bedford New College, University of London, Egham, Surrey, TW20 OEX, United Kingdom

INTRODUCTION

ıe Vangorda Pb-Zn-Ag deposit is a small (6.9 million tons), dex-type massive sulphide ore body in the Anvil Mining District of the Selwyn Basin, Yukon Territory (Fig. 1). The deposit is currently being developed as an open pit mine oducing approximately 13 500 tonnes of ore per day. The e body consists of several lenses of fine- to medium-grained pyrite-sphalerite-galena-barite-quartz within the Lower Paleozoic upper Mt. Mye phyllite of the Anvil District. The :posit is polydeformed and polymetamorphosed to ...id-greenschist facies. During the 1990 and 1991 field seasons detailed mapping and drill core logging were ıdertaken to carry out a structural analysis of the Vangorda :posit. The aim of this research is to establish the 3D geometry of the deposit, to define the structural evolution of the orebody and host rocks, and to define the effects of formation and metamorphism in the sulphides. This paper esents the preliminary results.

EGIONAL GEOLOGY

ıne Anvil Range lead-zinc-silver district is located within the Omineca Crystalline Belt of the northern Canadian ɔrdillera, approximately 200 km northeast of Whitehorse, ıkon (Fig. 1). The district lies immediately north of the Cretaceous-Tertiary Tintina fault, a major dextral strike-slip fault in the northern Cordillera (Fig. 2). Rocks in the Anvil ıstrict consist of a structurally thickened sequence of upper ·oterozoic to lower Paleozoic polydeformed, polymetamorphosed, metasedimentary and metavolcanic

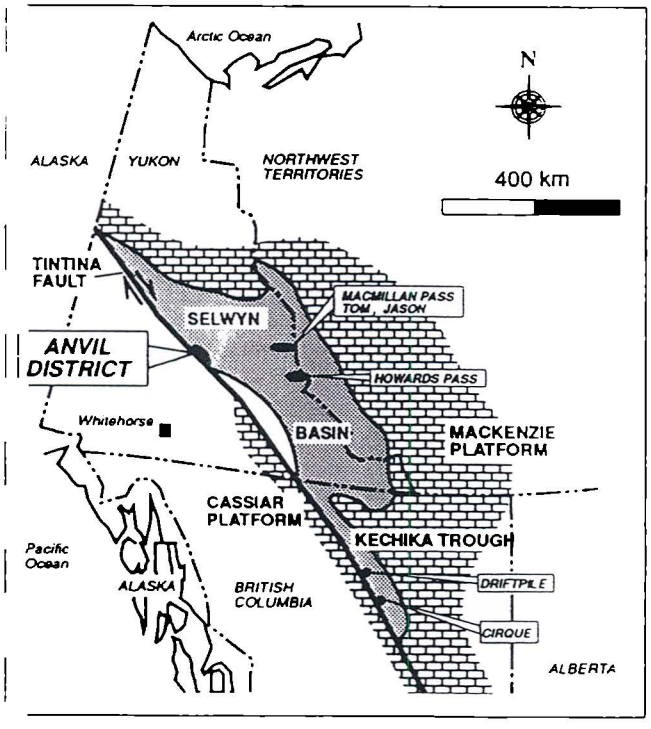

gure 1. Generalized geological map showing the location of major mineral occurrences in the Selwyn Basin.

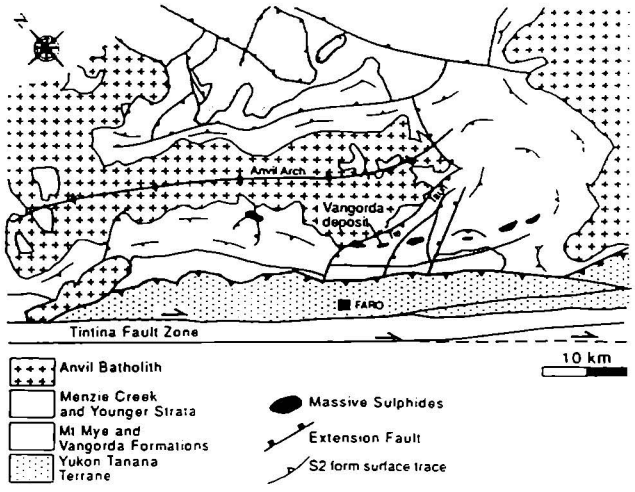

Figure 2. Schematic geological map of the Anvil District. Note the curvilinear distribution of the sulphide deposits. (Redrafted from Jennings and Jilson, 1986).

schist and phyllite (Jennings and Jilson, 1986) interpreted as part of the ancient western North American margin. These rocks are intruded by Cretaceous granite (Pigage and Anderson, 1985) and granodiorite of the Anvil plutonic suite. The dominant structural feature in the district, the Anvil Arch, has a northwest-southeast structural grain outlined by foliation form-surface traces, and is related to uplift during intrusion of the Anvil plutonic suite. Late extensional faults such as the Tie fault (Fig. 2) are interpreted to be related to emplacement and unroofing of the Anvil Batholith (Jennings and Jilson, 1986).

Five ductile deformation events have been recognized in the Anvil district (Jennings and Jilson, 1986). The first two are penetrative and form the dominant structural elements of the district. The first phase, D_1, is interpreted to be related to northeast-directed folding, thrusting, and nappe emplacement during the pre- to mid-Cretaceous docking of outboard terranes onto the ancient North American continent (Tempelman-Kluit, 1979; Mortensen and Jilson, 1985). D_1 resulted in the development of a penetrative regional foliation (S_1), and regional metamorphism reaching greenschist to amphibolite facies (Jennings and Jilson, 1986).

The second deformation event, D_2, is probably related to emplacement of the Anvil plutonic suite. D_2 resulted in southwest-directed folding, development of a penetrative foliation (S_2), greenschist to amphoblite facies contact metamorphism, and extensional faulting. The structural enviroment of D_2 is essentially that of a metamorphic core complex. The fold overprinting style between F_1 and F_2 is that of a type 3 hook structure (cf. Ramsay, 1967; Jennings and Jilson, 1986). D_3 to D_5 deformation events produced minor folds and steeply dipping crenulation foliations that overprint the D_1 and D_2 structural elements.

The Anvil district is host to five stratiform, massive sulphide deposits with an estimated geological reserve of 120 million tonnes (Jennings and Jilson, 1986) (Fig. 2). The five deposits lie along a northwest-southeast curvilinear trend,

parallel to the regional structural grain of the district (Fig. 2). Ore rocks in the deposits are variably recrystallized metamorphic tectonites (Pigage, 1990) that display deformation textures that can be related to D_1 and D_2, and locally D_3 to D_5 (cf. Jennings and Jilson, 1986).

LITHOSTRATIGRAPHY

The lithostratigraphy of the Anvil District consists of up to 5 km of polydeformed, late Precambrian to upper Paleozoic metasedimentry and metavolcanic rocks intruded by Cretaceous granites (Jennings and Jilson, 1986) (Fig. 3). Within it are two lithostratigraphic units important to this paper, the lower non-calcareous, carbonaceous Mt. Mye formation and the overlying calcareous, variably carbonaceous Vangorda formation. Near the Vangorda deposit these rocks are chlorite-muscovite phyllite that, in the case of the Vangorda formation, contain calcite and/or dolomite. The Anvil District deposits straddle the boundary between the Mt. Mye and the Vangorda formations, or occur up to 150 m below the stratigraphic contact between the two (Jennings and Jilson, 1986). Ore rocks in the Vangorda deposit are part of the synsedimentary, stratiform Anvil cycle (Fig. 3) as defined by Jennings et al. (1980) and Jennings and Jilson (1986). These authors envision the Anvil cycle to have formed from hot metalliferous brines discharged along a synsedimentary fault in a terraced fault system.

The Vangorda deposit occurs in the uppermost section of Mt. Mye phyllite directly below the Vangorda formation. The deposit appears to consist of lenses of varying thicknesses and bulk sulphide compositions and are typically accompanied by a footwall biased phyllitic, muscovite-chlorite alteration zone that grades into the ore lithofacies. The salient features of each ore lithofacies in the Vangorda deposit are outlined below.

Ribboned-banded, carbonaceous, pyritic quartzite: these are well banded, sulphide-bearing quartzite, with lesser sphalerite and galena. Bands are on a millimetre- to centimetre-scale and consist of quartz-sulphide and carbonaceous, phyllitic quartzite. Where F_2 folding occurs, S_1 is typically preserved in millimetre- to centimetre-scale lithons. Detailed mapping and drillcore logging shows that this lithofacies may occur alone or be absent from the previously defined Anvil cycle.

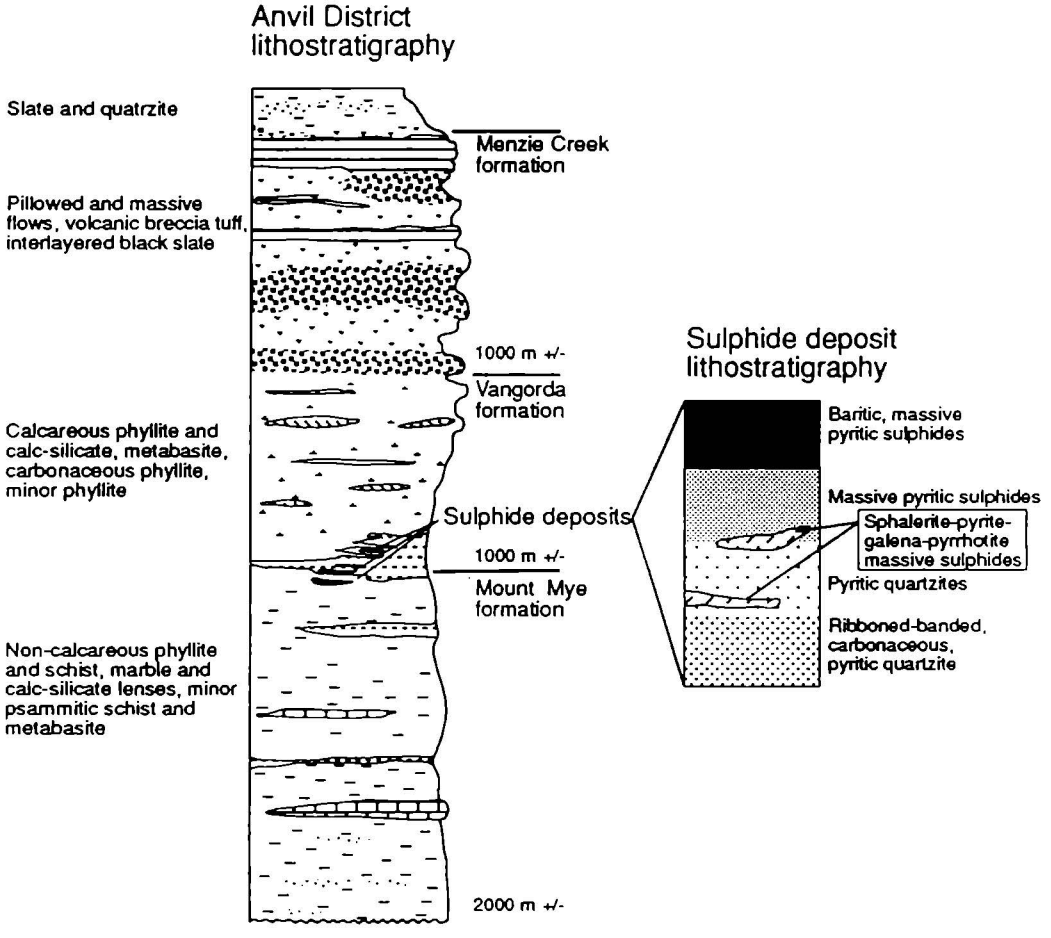

Figure 3. A schematic column of a portion of the Anvil District lithostratigraphy and the sulphide deposit lithostratigraphy. The sulphide deposits occur as lenses in the upper Mt. Mye formation, lower Vangorda formation. (Redrafted from Jennings and Jilson, 1986).

Pyritic quartzite: this consists predominantly of quartz with up to 40% pyrite and minor sphalerite and galena. These cks are moderately to poorly banded with, locally, a well veloped micaceous (muscovite) foliation. Sulphides are typically fine- to medium-grained (0.2-1 mm) , with local coarse-grained patches (1-2 mm). Galena, and less mmonly sphalerite, may occur in coarse grained gregates.

Massive pyritic sulphides: these are typically fine- to edium-grained (0.1-1 mm) massive pyrite with less halerite, galena, pyrrhotite, and minor magnetite. Quartz, barite, and carbonate are disseminated throughout or occur in aggregates. Total sulphide content ranges from 60% to 100%. xturally the massive pyritic rocks are homogeneous to nded. Banding is developed on a scale of millimetres to centimetres as alternating thick bands of pyrite and thin bands sphalerite + magnetite + galena. This lithofacies may be interbanded with the pyritic quartzites on a scale of centimentres to metres and commonly grades laterally into it. A foliation, defined by chlorite + carbon occurs locally.

Baritic, massive pyritic sulphides: these consist predominantly of barite with fine- to coarse-grained (0.1-2 mm) pyrite, sphalerite, galena, with minor magnetite. Quartz and carbonate are major matrix components. Clasts of pyrite and phyllite are common. Total barite content may be has high as 50%. Millimetre- to centimetre-scale interbanding of pyrite-rich and barite-rich layers is ubiquitous.

As well as the above lithofacies, whose distribution are believed to be relicts of primary depositional ore types, two lithofacies occur in areas of high strain and are interpreted as the result of metamorphic reactions and mobilization during deformation.

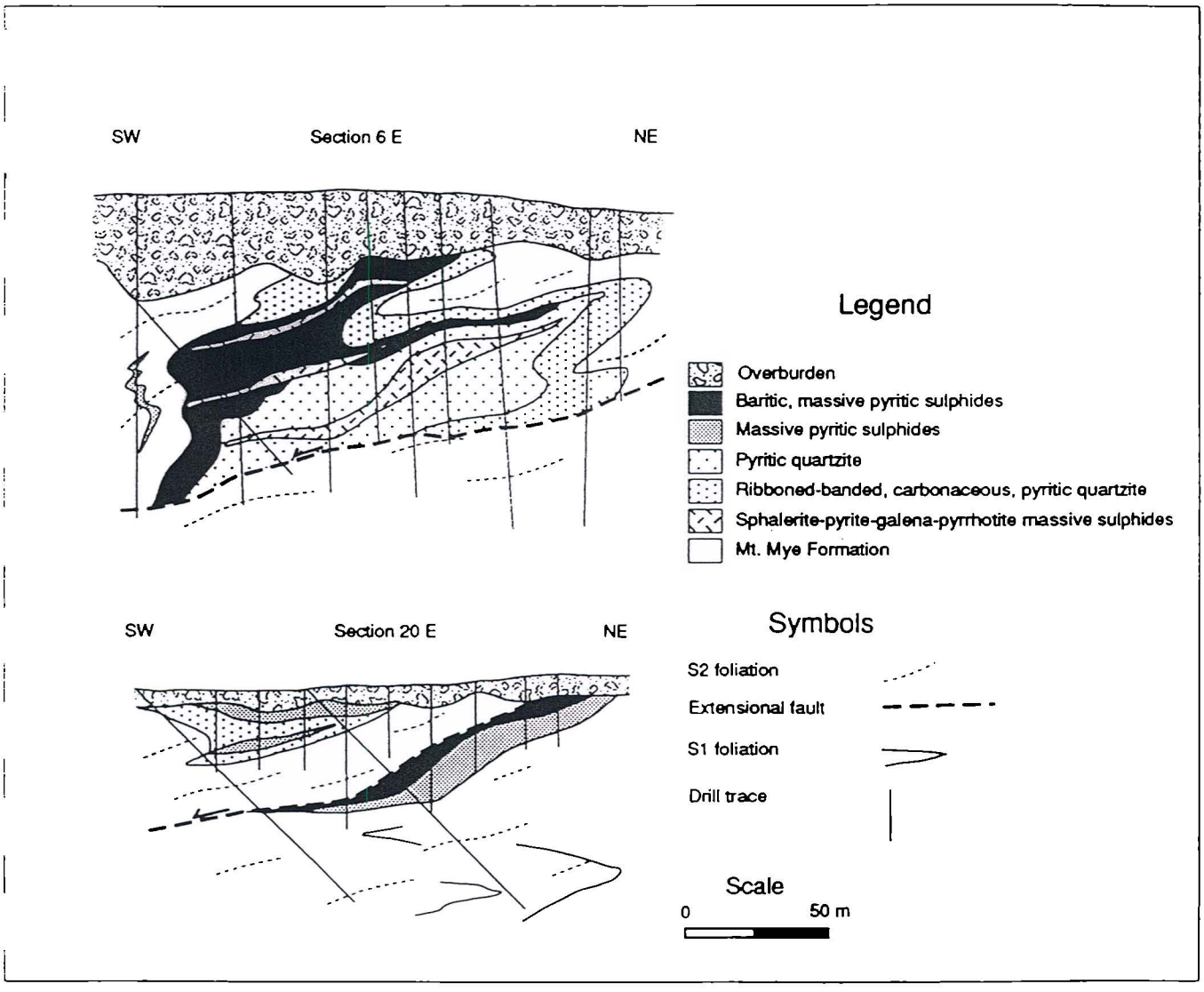

Figure 4. Cross-sections through the Vangorda deposit. Section 6 E contains the complete ore lithostratigraphy. Section 20 E consists of several lenses of sulphide lithofacies that are possibly separated by a fault. Sections were constructed using diamond drillhole data.

Pyrite-sphalerite-galena-pyrrhotite quartzite: this lithofacies is a variant of the pyritic quartzite in which the dominant sulphide is pyrite and sphalerite with lesser galena, and pyrrhotite. Grain sizes range from 0.01 to 2 mm and coarse (2-3 mm) patches of sphalerite or galena are common. Pyrite typically occurs as medium to coarse grained, submillimetre- to millimetre-sized porphyroblasts in an inhomogeneous, discontinuous foliation, or in isolated breccia clasts. These rocks are typically highly strained and commonly contain clasts of other rock types around which a well developed foliation anastomoses. Tailed clasts and rolling structures are common.

Pyrrhotitic massive sulphides: these contain predominantly fine-grained (0.05-1 mm) pyrrhotite with lesser pyrite, sphalerite, galena, and chalcopyrite. Pyrite is commonly porphyroblastic, reaching grain sizes of up to 1 mm. These rocks are typically highly strained and brecciated. Breccia clasts are rounded to angular, and generally have an internal foliation. Clasts may have symmetric or asymmetric tails and rolling structures are common.

THE VANGORDA DEPOSIT

The Vangorda deposit occurs 50 to 120 m beneath the carbonaceous base of the Vangorda formation. It consists of a number of gently northwest-plunging lenses and is elongated northwest-southeast. The deposit is interpreted to lie in the hinge and overturned limb of a macroscopic F_2 fold (Jennings and Jilson, 1986; Pigage, 1990). However, contrary to its structural position the overall lithostragraphy in this part of the deposit appears to consist of a single, right way up, idealized Anvil cycle (Fig. 4). An extensional fault of unknown offset truncates the orebody to the northwest, and in the southeast the deposit also appears to be truncated by extensional faulting. The deposit is cut approximately in half by a northwest-dipping extensional fault of unknown throw which juxtaposes two fault blocks of contrasting structural and lithostratigraphic styles. Northwest of this fault (Fig. 4, section 6 E) the deposit consists of a thick body of sulphide displaying one complete lithostratigraphic sequence, whereas southeast of the fault (Fig. 4, section 20 E) the orebody consists of thin lenses of individual lithofacies or group of lithofacies.

Regional D_2 metamorphic grade in the area decreases outward from the Anvil Batholith and metamorphism in the Vangorda deposit is thought to be due to contact metamorphism related to intrusion of the batholith (Jennings and Jilson, 1986). Metamorphic grade, recorded by muscovite-chlorite assemblages in wall rock phyllite, is sub- to mid-greenschist facies. The D_1 metamorphic grade regionally reached greenschist to amphibolite facies and in the orebody likely did not exceed greenschist facies.

Rocks in the Vangorda deposit are penetratively deformed by the D_1 and D_2 deformation events, making definition of any primary depositional features on a scale other than microscopic (see below) ambiguous at best. In most lithofacies in the deposit, banding is well developed on a scale of millimetres to centimetres. This banding is commonly folded by south- to southwest-verging folds presently accepted to be F_2 and is therefore taken to define S_1. Throughout the deposit, S_1 is commonly preserved as lithons in the hinges of F_2 folds in phyllite and the ribbon banded, carbonaceous quartzite. In sulphide-rich lithofacies S_1 is typically transposed into the F_2 axial surface. S_1 is used throughout this paper as the datum for determining the relative ages of the structural elements of the Vangorda deposit.

F_1 folds have not been identified in the Vangorda deposit previously because of penetrative overprinting by F_2 and because exposure was poor before mine development. This study identifies several examples of refolded folds in drill core and in pit wall exposures, indicating that F_1 folding may be important in the present geometry of the deposit. The widespread presence of S_1 in the ore lithofacies, and the evidence for F_1 folding in rocks near the deposit (e.g., Jennings and Jilson, 1986) also point to the relative importance of F_1 folding.

The dominant fold phase in the Vangorda deposit is F_2. F_2 folds are typically east-west- to northwest-southeast-plunging, tight to near isoclinal (interlimb angle is commonly 5-25°) similiar folds. F_2 fold morphology changes as a result of relative competency and ductility contrasts between the different lithofacies, but the similar fold style is maintained. Where competency contrast is high, F_2 folds become somewhat disharmonic.

In the surrounding phyllite, a penetrative shallowly southwest-dipping, wavy D_2 axial planar cleavage (S_2) is developed. In some sulphide lithofacies, such as the ribboned-banded, carbonaceous quartzite, a differentiated axial planar S_2 cleavage is well developed. However, S_2 appears to be non-penetrative in the sulphides and is only rarely found in fold hinges. In general, the S_1 banding is transposed into the S_2 orientation, and is easily mistaken for S_2. In high strain zones, such as the overturned limbs of macroscopic folds, S_1 banding in the sulphide lithofacies is discontinuous as a result of shearing and a new, inhomogeneous S_2 foliation is developed.

There is little evidence for the relationship between F_1 and F_2 folds in the Vangorda deposit, but the rare occurrence of refolded folds indicates that the style of overprinting is the same as that recorded regionally, (i.e. type 3 of Ramsay, 1967) (cf. Jennings and Jilson, 1986, Fig. 21).

Locally, steeply south- to southwest-plunging to subvertical, open folds fold the S_2 cleavage and tighten F_2 folds. These folds are here termed F_3. F_3 folds are of minor importance and a local crenulation cleavage is associated with them.

The Vangorda deposit is strongly faulted by brittle extensional faults that, together with F_2 folding, provide the dominant control on the geometry of the orebody. Extensional faults examined truncate the S_2 cleavage and F_2 folds and postdate or are late D_2. Faults in the deposit are typically steeply northwest- to southeast-dipping gouge zones consisting of phyllosilicate and/or sulphide-quartz sand and/or breccia. Locally, these are cemented by a matrix

of quartz and calcite and, in some instances, by pyrite. Breccias contain angular clasts of phyllite and sulphide ranging in size from several millimetres to several centimetres. Clasts are strongly broken and, in many cases, can be fitted back together. Pyrite slickensides on polished fault surfaces are typically subhorizontal or have a shallow pitch angle, indicating a late phase of strike-slip to oblique-slip movement. Faults have an offset of centimetres to several tens of metres. Paucity of marker horizons precludes measurement of exact offset on any fault.

Another type of fault common in the sulphide rocks is characterized by tectonic mixing of angular to rounded clasts of brecciated quartz, phyllite, and sulphide in a ductilely formed, well foliated, and recrystallized pyrrothite-rich or sphalerite and galena-rich matrix (Fig. 5a). These faults range in size from several millimetres up to several tens of centimetres wide, generally with sharp boundaries. Clasts are rolled or rotated (5b), and internally folded, with the foliation flowing around them. Pyrite porphyroblasts are common in the matrix and in sulphide clasts. In several instances shear zones are folded by F_2 folds. These shear zones appear to be the extremely high strain end-member of a durchbewegung structure (see review by Marshall and Gilligan, 1989) and may represent discrete faults or zones of shearing. Thin breccias and ductile faults are common along boundaries between sulphide lithofacies indicating layer parallel shearing during deformation.

Several low-angle, post-D_2, northeast-directed thrusts occur within phyllite in the southeast end of the deposit. These cut the S_2 cleavage and have offsets ranging from centimetres up to several tens of metres.

MICROSTRUCTURE

Preliminary studies were carried out on several microstructural aspects of ore rocks from the Vangorda deposit. To date, deformation textures in pyrite have received the bulk of the attention. Selected polished sections were etched with warm, 30% nitric acid (HNO_3) to study growth features (e.g., grain boundaries and overgrowths), mineral phases, and deformation textures (e.g., dislocation structures).

Relict, primary colloform pyrite grains, although rare, occur in the massive pyrite and pyritic quartzite lithofacies within the Vangorda deposit. These are typically 0.05-0.5 mm-sized, equant to xenoblastic grains that occur alone or as cores with overgrowths of secondary, metamorphic pyrite.

Medium- to coarse-grained (0.25-2 mm), secondary, metamorphic pyrite, identifiable by its massive, typically inclusion-poor, equant to idioblastic nature, exhibits both brittle and ductile deformation textures. Zones of intense cataclasis have produced aggregates of angular comminuted grains. Within these zones a foliation, defined by micas and aligned quartz, anastomose around pyrite porphyroblasts. Indentation and axial cracking of large porphyroblasts is common (Fig. 5c).

One sample from the massive pyrite lithofacies shows an excellent example of grain shape preferred orientation of pyrite (Fig. 5d). These elongate grains typically show little or no evidence of brittle deformation, and only minor dislocation microstructure. Grain boundaries are straight to slightly curved, mildly sutured, and lightly indented. No overgrowths are apparent but pressure solution is the likely mechanism responsible for the preferred shape orientation.

Pyrite porphyroblasts commonly have overgrowths, either on relict colloform grains or on secondary metamorphic grains. In some cases numerous phases of grain growth can be recognized in one porphyroblast. These multiple phases of grain growth are evidence of a complex pyrite formation history.

Pyrite also shows annealing textures from metamorphism. In the massive pyritic lithofacies, grains are commonly submillimetre- to millimetre-sized, equant grains with straight to mildly sutured boundaries with 120° triple junctions. In quartz-rich areas and in the pyritic quartzite lithofacies, pyrite commonly forms larger (up to 3 mm locally), equant to idioblastic porphyroblasts.

Etched pyrite grains show dislocation microstructures which are characterized by straight to slightly curved, stepped, or branching dislocation walls and tangles.The dislocation walls and tangles commonly form grid-like arrays denoting the onset of polygonization and subgrain formation and incipient dynamic recrystallization (Fig. 5e).

Subgrain formation is common throughout the samples examined in this study. Subgrains are typically 5-50 mm, equant grains with straight to slightly curved grain boundaries that meet at 120° triple junctions. Subgrain formation commonly occurs along the boundaries of parent grains (Fig. 5f) resulting in a core-mantle texture.

Pyrite textures such as preferred grain shape orientation, subgrain formation, pressure solution, and dislocation structures indicate pyrite was deformed both by ductile and brittle mechanisms. Many ductile features outlined above have been studied experimentally (cf. Cox et al., 1981) and occur at temperatures of 500 to 650 °C and pressures of ~300 MPa.

CONCLUSIONS

This paper illustrates characteristics of the deformational style in the ore rocks of the Vangorda deposit. The dominant fabric element in the deposit is a penetratively developed banding and/or foliation, S_1, which can be used as a datum for determining the relative age of structural elements.

S_1 is folded by tight to near isoclinal, east-west-plunging F_2 folds with a class 2 similar geometry. In host rocks and some sulphide lithofacies, S_1 is preserved as lithons in the hinge zones of F_2 folds, whereas in fold limbs S_1 has been transposed into the F_2 axial surface. S_2 is typically poorly, or not developed in massive pyritic rocks. The widespread occurrence of S_1 and the relative rarity of S_2 suggests that D_1 played an important role in the deformation and remobilization of the orebody and may be responsible for the

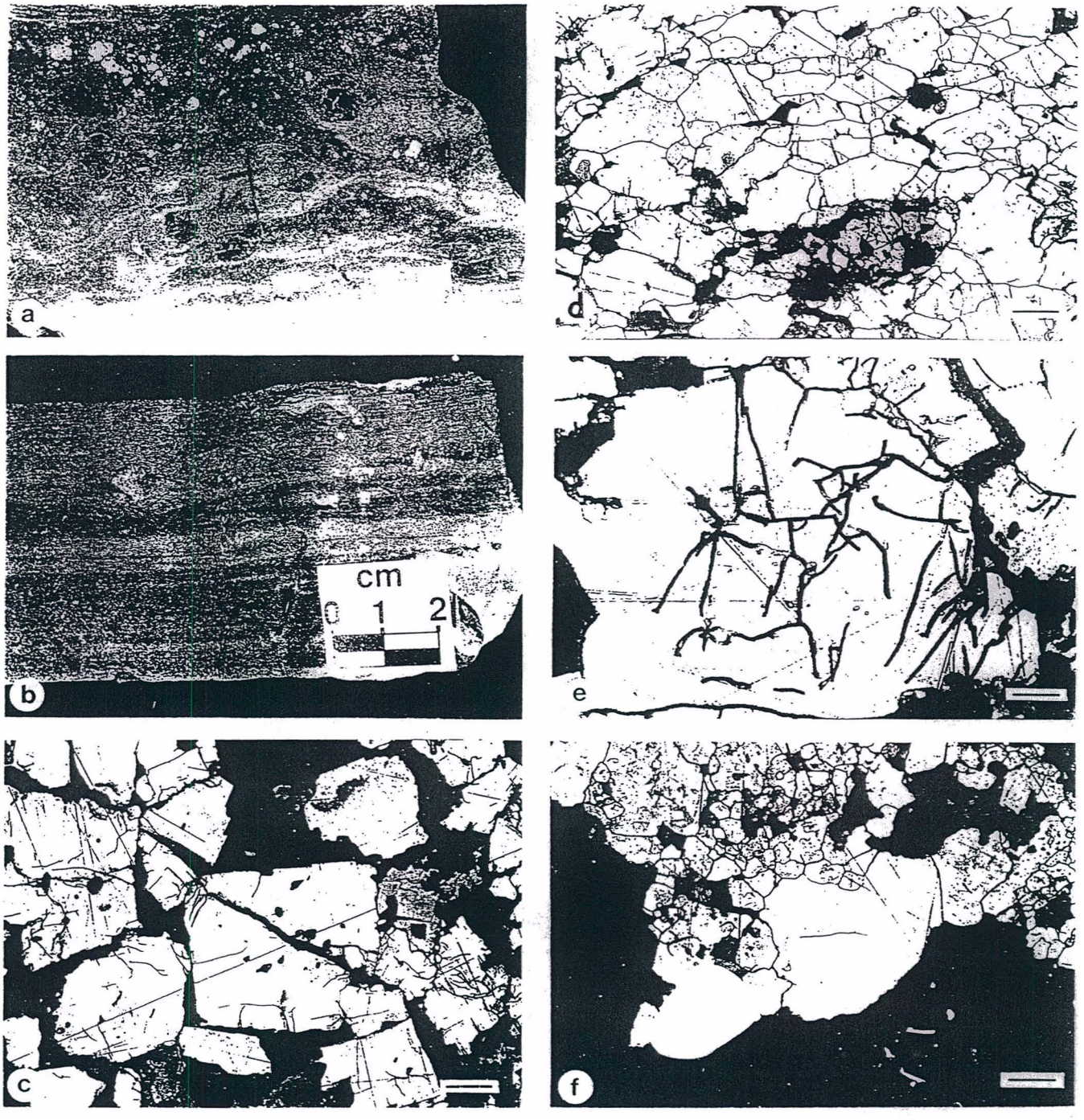

Figure 5(a) Ductile fault zone in massive sulphide. Matrix consists of sphalerite, pyrrhotite, and galena. (b) Sulphide mylonite with tailed, a-type porphyroclasts of quartz. (c) Pyrite porphyroblasts displaying indentation and marked axial cracking. Scale bar is 1.0 mm. d) Preferred grain-shape orientation in pyrite. Grain boundaries are straight to moderately serate and meet at 120° triple junctions. Scale bar is 1.0 mm. (e) Dislocation walls and tangles marking the onset of polygonization in pyrite. Scale bar is 0.25 mm. (f) Grain boundary recrystallization and subgrain formation in pyrite. Scale bar is 0.5 mm.

bulk of deformation textures in the sulphides. Strong evidence for this is the occurence of F_2 folded sulphide shear zones. The D_1 distribution of sulphide lithofacies is tightly folded by F_2 folds.

The geometric relationship between F_1 and F_2 folds remains to be defined. The examples discussed above indicate that the refolding pattern is likely to be a type 3 (or hook structure), similiar to that recorded regionally.

Shear zones in the sulphides are complex and may result from D_1. Some appear to be geometrically related to F_2 folds.

Extensional faults in the Vangorda deposit appear to postdate or are late D_2 and clearly offset earlier D_2 features such as S_2 and F_2 folds. The amount of throw on these faults is generally not known. Determination of offset is further complicated by a late strike-slip to oblique-slip component of movement.

Pyrite in the Vangorda deposit ranges in grain size from 0.1 to 3 mm. Pyrite grains are deformed by ductile and brittle mechanisms. Ductile features include formation of dislocation walls and tangles, polygonization and subgrain formation. A preferred grain-shape orientation is developed locally. Annealing features such as grain-boundary bulging are common. Pyrite grains are also indented, cracked, and strongly disaggregated. Primary colloform pyrite still occurs locally.

ACKNOWLEDGMENTS

This project is funded in part by Curragh Resources, D.I.A.N.D., Whitehorse, Yukon, the Geological Survey of Canada (Vancouver), and the Industrial Association, Royal Holloway and Bedford New College. We would like to personally thank Greg Jilson, Lee Pigage, Cam Reed, Mitch Wasel, Steve Morrison, Grant Abbott, and Dirk Tempelman-Kluit. We would also like to thank the people at the Faro mine for their help. Brown is sponsored in part by the Rothemere Foundation and by the Special Scholarship for Students doing Research in Resource Development administered by Memorial University of Newfoundland. Brenda Fediuk is thanked for her help in getting this paper written.

REFERENCES

Cox, S.F., Etheridge, M.A., and Hobbs, B.E.
1981: The experimental ductile deformation of polycrystalline and single crystal pyrite; Economic Geology, v. 76, p. 2105 - 2117.

Jennings, D.S. and Jilson, G.A.
1986: Geology and sulphide deposits of the Anvil Range, Yukon; in Mineral Deposits of Nothern Cordillera, (ed.) J.A. Morin; Canadian Institute of Mining and Metallurgy, Special Paper 37, p. 319-361.

Jennings, D.S., Jilson, G.A., and Pigage, L.C.
1980: Anvil Range stratigraphy, south-central Yukon Territory (abstract); Geological Association of Canada, Cordilleran Section, Programme and Abstracts, p. 16-17.

Marshall, B. and Gilligan, L.B.
1989: Durchbewegund structure, piercement cusps, and piercement veins in massive sulphide deposits: formation and interpretation; Economic Geology, v. 84, p. 2311-2319.

Mortensen, J.K. and Jilson, G.A.
1985: Evolution of the Yukon-Tanana terrane: evidence from southeastern Yukon Territory; Geology, v. 13, p. 806-810.

Pigage, L.C.
1990: Field guide Anvil Pb-Zn-Ag district, Yukon Territory, Canada; in Mineral Deposits of the Northern Canadian Cordillera, Yukon-Northeastern British Columbia, (ed.) J.G. Abbott and R.J.W. Turner; Geological Survey of Canada, Open File 2169, p. 283-308.

Pigage, L.C. and Anderson, R.G.
1985: The Anvil Plutonic Suite, Faro, Yukon Territory; Canadian Journal of Earth Sciences, v. 22, p. 1204-1216.

Ramsay, J.G.
1967: Folding and Fracturing of Rocks; New York, McGraw-Hill, 568 p.

Tempelman-Kluit, D.J.
1979: Transported cataclasite, ophiolite and granodiorite in Yukon Territory: evidence of arc-continent collision; Geological Survey of Canada, Paper 79-14.

Geological Survey of Canada Project 820015

Deformation textures in pyrite from the Vangorda Pb–Zn–Ag deposit, Yukon, Canada

D. Brown and K. R. McClay

Department of Geology, Royal Holloway, University of London, Egham, Surrey TW20 0EX, U.K.

Abstract

The Vangorda Pb–Zn–Ag orebody is a 7.1 M tonne, polydeformed stratiform massive sulphide deposit in the Anvil mining district, Yukon, Canada. Five sulphide lithofacies have been identified within the desposit with a typical mineralogy of pyrite, sphalerite, galena, and barite. Pyrrhotite–sphalerite–magnetite assembalges are locally developed. Etched polished sections of massive pyrite ores display relict primary depositional pyrite textures such as colloform growth zoning and spheroidal/framboidal features. A wide variety of brittle deformation, ductile deformation, and annealing textures have been identified. Brittle deformation textures include thin zones of intense cataclasis, grain indentation and axial cracking, and grain boundary sliding features. Ductile deformation textures include strong preferred grain shape orientations, dislocation textures, grain boundary migration, dynamic recrystallisation and pressure solution textures. Post deformational annealing has produced grain growth with lobate grain boundaries, 120° triple junctions and idioblastic pyrite porphyroblasts. The distribution of deformation textures within the Vangorda orebody suggests strong strain partitioning along fold limbs and fault/shear zones. It is postulated that focussed fluid flow in these zones had significant effects on the deformation of these pyritic ores.

Keywords: pyrite, deformation, textures, Vangorda deposit, Yukon, Canada.

Introduction

The Vangorda deposit is a 7.1 million tonne (Jennings and Jilson, 1986), SEDEX-type (Carne and Cathro, 1982) massive sulphide orebody in the Anvil Pb–Zn–Ag District, Yukon Territory, Canada (Fig. 1). The deposit has a combined Pb + Zn grade of 7.7%. It has been polydeformed and polymetamorphosed under mid-greenschist facies conditions (Tempelman-Kluit, 1972; Jennings and Jilson, 1986). The Vangorda orebody is shallowly southwesterly dipping, with complex and folded lenses of massive and disseminated sulphides and barite approximately 900 m long, 100 m wide and varying in thickness from 20 to 60 m. The orebody is currently being mined in a 10000 tonne per day open pit operation by Curragh Resources. The deposit consists of lenses of baritic-pyritic massive sulphides, pyritic massive sulphides, pyritic quartzites, and ribbon banded carbonaceous quartzites in quartz–chlorite–muscovite phyllites. Five distinct sulphide lithofacies with varying modal abundances of pyrite have been identified. Pyrite within these display a variety of brittle and ductile deformation features, together with recrystallisation, and annealing textures (Brown and McClay, 1992).

Pyrite in many deformed and metamorphosed ore-bodies, as well as in controlled experiments, has been shown to deform by brittle mechanisms over a wide range of geological conditions (e.g. Vokes, 1969, 1971; Ramdohr, 1969; Graf and Skinner, 1970; Atkinson, 1975; Mookherjee, 1976; McClay, 1983). It has further been demonstrated that both experimentally and naturally deformed pyrite also deforms by crystal plastic mechanisms, and diffusive mass transfer coupled with grain boundary sliding (Mookherjee, 1971; Natale, 1971; Couderc *et al.*, 1980; Graf *et al.*, 1981; Cox *et al.* 1981; McClay and Ellis, 1983; Brill, 1989). Cox *et al.* (1981) experimentally determined the onset of crystal plastic mechanisms in pyrite to occur at approximately 450 °C at 300 MPa. Dynamic recrystallisation, though not a widely reported feature in naturally deformed pyrites, has also been found to occur (e.g. Cox *et al.*, 1981). This paper examines deformation and annealing textures in pyrite from

Mineralogical Magazine, March 1993, Vol. 57, pp. 55–66
© *Copyright the Mineralogical Society*

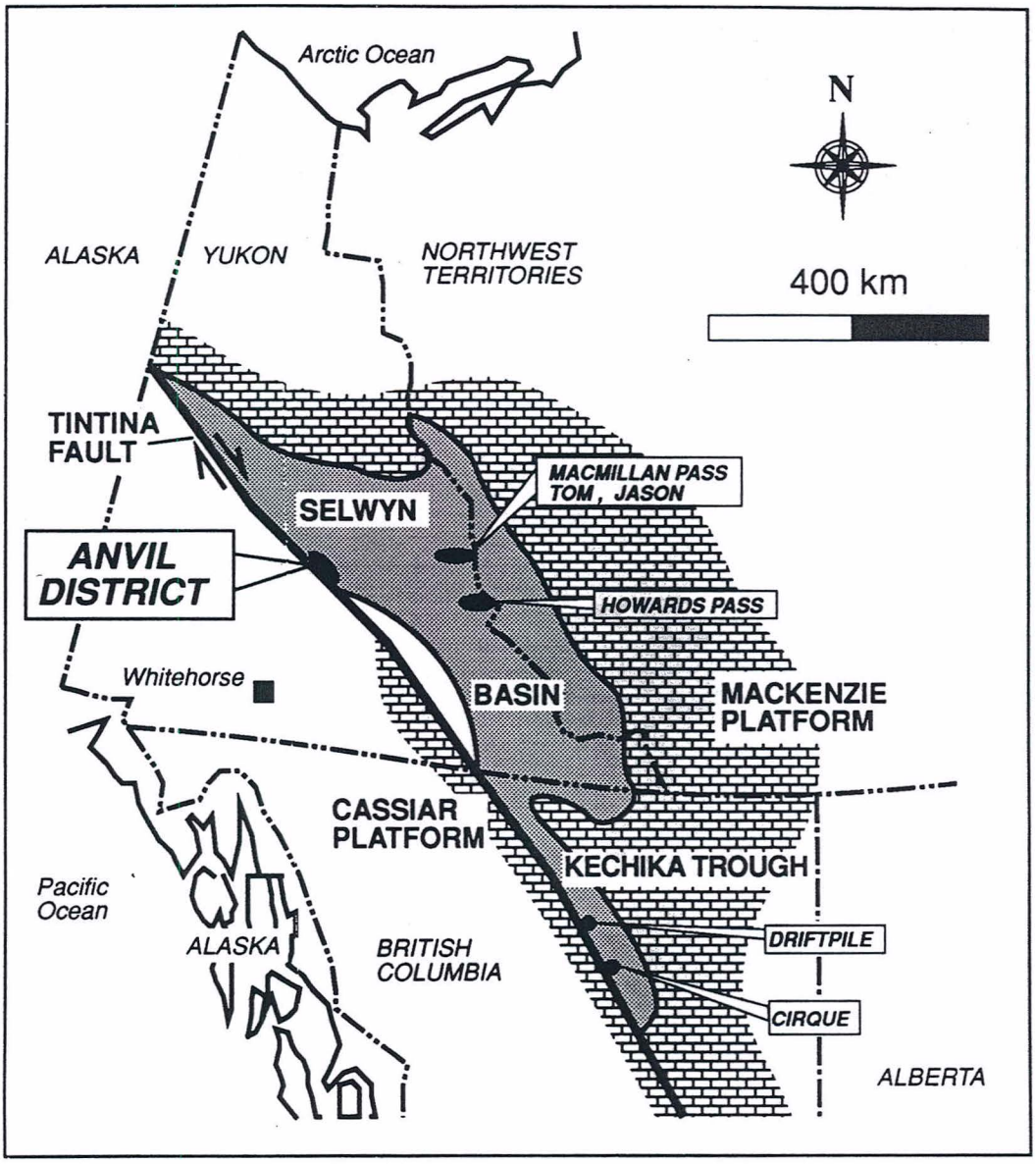

FIG. 1. Location of the Anvil District in the Northern Canadian Cordillera (after McClay, 1991).

the Vangorda deposit. Data for this study comes from logged diamond drill holes and from detailed mapping and sampling of the open pit.

Regional geology

The Anvil lead–zinc–silver district is located within the Omineca Crystalline Belt of the northern Canadian Cordillera, approximately 200 km northeast of Whitehorse, Yukon (Fig. 1). Rocks in the Anvil District consist of a structurally thickened sequence of late Precambrian to upper Palaeozoic polydeformed, polymetamorphosed, metasedimentary and metavolcanic schists and phyllites (Jennings and Jilson, 1986). These have been intruded by Cretaceous granites and granodiorites (Pigage and Anderson, 1985). The Anvil District is host to seven major stratiform, massive sulphide deposits that lie along a

northwest-southeast curvilinear trend, parallel to the regional structural grain of the district (Fig. 2).

Lithostratigraphy

The lithostratigraphy of the Anvil District is shown in Fig. 3. Precise thickness and age determinations are difficult because of the penetrative deformation and metamorphism. Within the Anvil District two lithostratigraphic units, the lower non-calcareous Mt. Mye Formation phyllites and the overlying calcareous Vangorda Formation phyllites are regionally significant as the sulphide deposits straddle the boundary between them (Fig. 3). The Vangorda orebody occurs in the Mount Mye Formation immediately below the base of the Vangorda Formation. In the vicinity of the Vangorda deposit the Mt. Mye and Vangorda Formations are typically mid-greenschist facies chlorite–muscovite phyllites.

Deformation events

Five deformation events have been recognised in the Anvil District, the first two of which (D_1 and D_2) are regionally significant (Jennings and Jilson, 1986). D_1 is interpreted to be related to northeast-directed folding, thrusting, and nappe emplacement during the pre- to mid-Cretaceous docking of allochthonous terranes from the southwest onto the ancestral margin of North America (Jennings and Jilson, 1986). D_1 deformation resulted in the development of NE-verging F_1 folds and a penetrative regional foliation (S_1), and regional metamorphism. The D_2 tectonic setting appears to be similar to that of a metamorphic core complex and is related in southwest-directed folding, development of a shallowly SW-dipping, penetrative foliation (S_2), and greenschist to amphibolite facies metamorphism (Jennings and Jilson, 1986; Smith and Erdmer, 1990). Brittle to ductile extensional faulting, related to unroofing of the Anvil Batholith, is late- to post-D_2 folding (Pigage and Jilson, 1985). D_3 to D_5 deformation events produced minor folding and steeply dipping crenulation foliations that variably overprint the D_1 and D_2 structural elements.

The Vangorda Deposit

The Vangorda deposit occurs 50 to 120 metres beneath the base of the Vangorda Formation

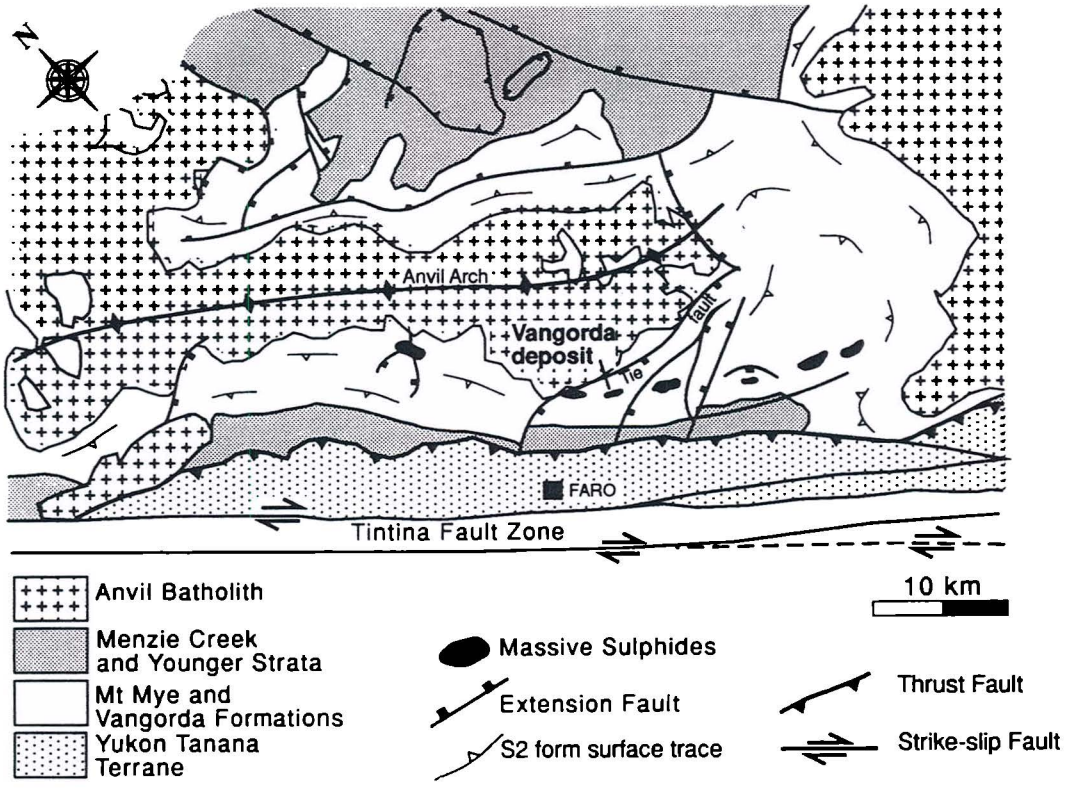

FIG. 2. Regional geology of the Anvil District showing the location of the Vangorda deposit (after Brown and McClay, 1992).

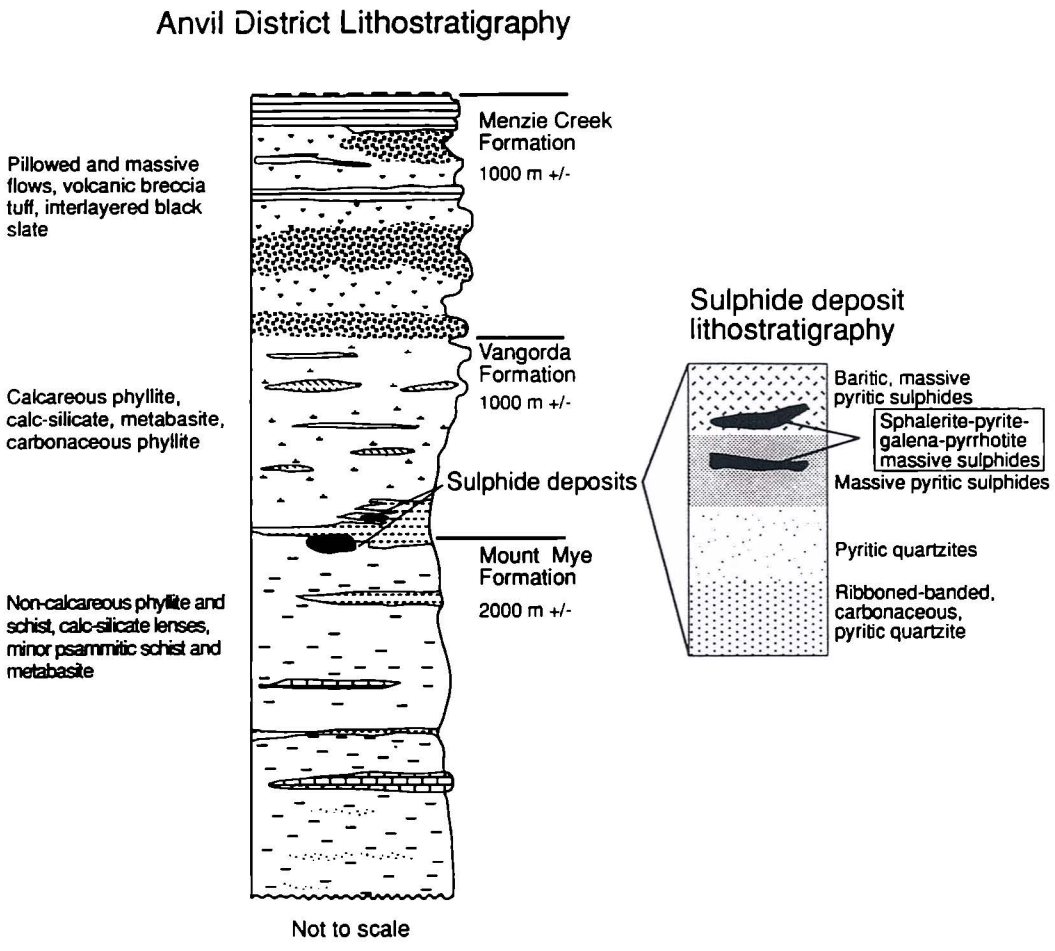

FIG. 3. Lithostratigraphy of the Anvil District (after Brown and McClay, 1992).

(Fig. 3). The orebody plunges shallowly towards the northwest and is interpreted to occur in the hinge and the under limb of an overturned large-scale F_2 fold (Fig. 4) (Jennings and Jilson, 1986; Pigage, 1990). Syn- to post D_2 NW–SE oriented extensional faults truncate the deposit to the northwest and southeast (Pigage, 1990; Brown and McClay, 1992).

Ore lithofacies

The Vangorda orebody consists of a number of sulphide lenses of varying thickness (1–30 m) and varying sulphide composition that are typically accompanied by a footwall biased phyllitic, muscovite–chlorite alteration zone. In any one section or drill hole the entire ore sequence as shown in Fig. 3 may or may not be developed. The salient features of each ore lithofacies in the Vangorda deposit are outlined below.

Ribbon-banded, carbonaceous, pyritic quartzite: This is a well banded, sulphide-bearing quartzite, with minor sphalerite and galena. Bands are on a millimetre- to centimetre-scale and consist of fine-grained, carbonaceous quartzite to siliceous phyllite, interbanded with more coarsely-grained sulphide-rich quartzite. Pyrite grain size ranges from 0.1 mm to 1.0 mm.

Pyritic quartzite: This consists predominantly of quartz with up to 40% pyrite and minor sphalerite and galena. These rocks have a moderate to poorly developed pyrite banding with, locally, a well developed micaceous (muscovite) foliation. Pyrite typically forms 0.1 mm–1 mm sized subhedral to euhedral porphyroblasts, with local coarse grained patches in which grain size

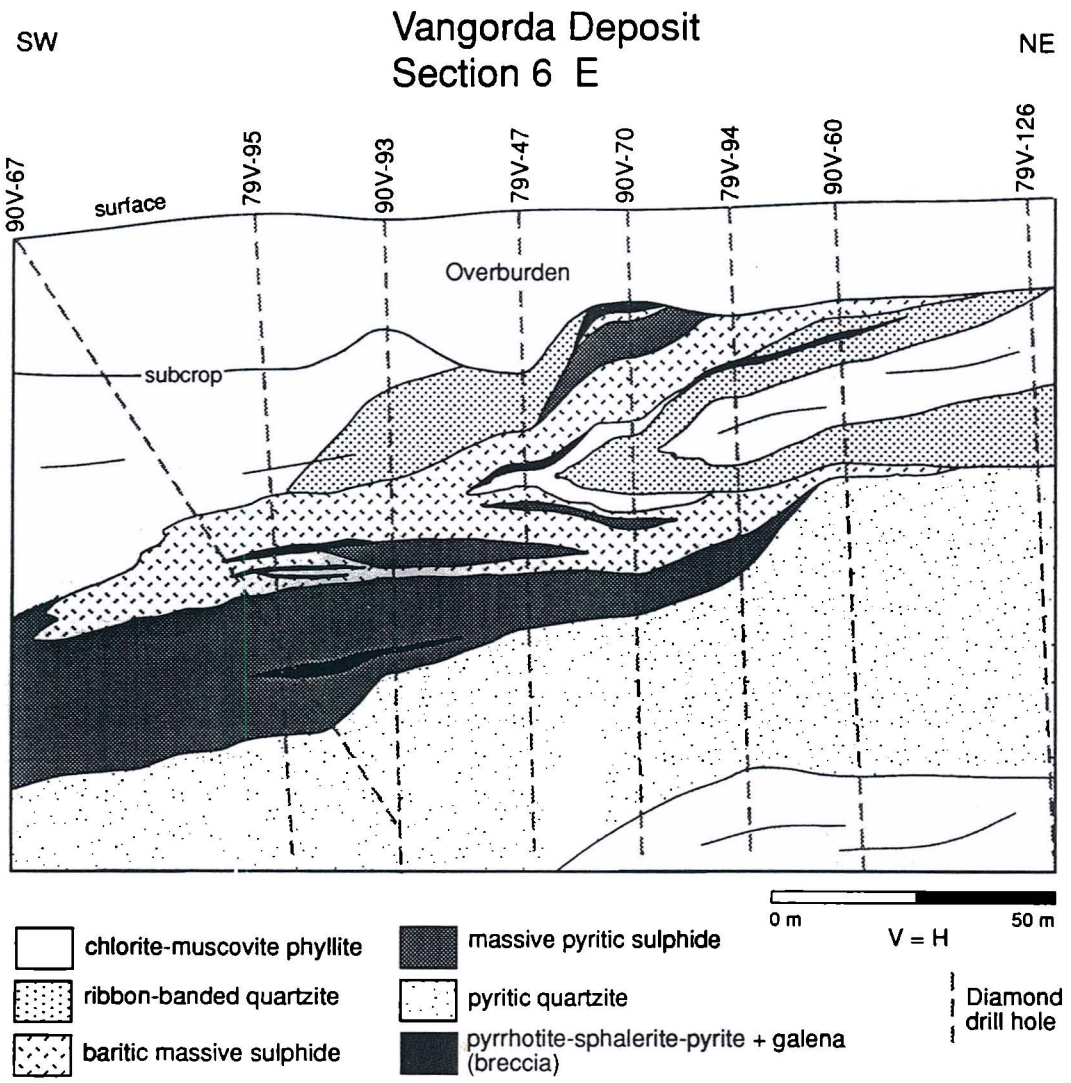

FIG. 4. Cross-section 6E, Vangorda deposit showing the tight to near isoclinal, similar fold, and the distribution of the ore lithofacies.

reaches approximately 3.0 mm. Galena, and less commonly sphalerite, occur in coarse-grained patches with grain sizes ranging from 0.05 to 0.5 mm.

Massive pyritic sulphides: These are typically massive pyrite with minor sphalerite, galena, pyrrhotite, and magnetite. Quartz, barite, and carbonates are disseminated throughout or occur in coarse aggregates. Total pyrite content varies from between 60% to close to 100% with grain size ranging from 0.1 to 1.5 mm.

Baritic, massive pyritic sulphides: These consist predominantly of barite with pyrite, sphalerite, galena, with minor magnetite. This lithofacies appears to be interbanded with the pyritic massive sulphides on a scale of centimetres to metres. Quartz and carbonate are major matrix components. Clasts of massive pyrite and phyllite are common. Total barite content varies but may be as high as 50%.

As well as the above lithofacies, the distribution of which is interpreted to reflect primary depositional ore types, another lithofacies occurs in areas of high strain and is interpreted to be the result of metamorphic reactions and strain related mobilisation during deformation.

Pyrrhotite–sphalerite–pyrite–galena (breccia): This lithofacies is a variant of the pyritic quartzite in which the dominant sulphides are pyrrhotite and sphalerite with lesser pyrite, and galena. Coarse patches of sphalerite or galena are common. Pyrite typically occurs as 0.1 to 1.5 mm-sized porphyroblasts and as isolated breccia clasts. This lithofacies is typically highly strained and often contains clasts of other rock types and a well developed anastomosing foliation. Tailed clasts and rolling structures are common.

The baritic massive sulphides, pyrrhotite–sphalerite–pyrite–galena (breccia), and locally the ribbon-banded, carbonaceous, pyritic quartzite form the principal ore rocks. The pyritic quartzite and massive pyritic sulphides are typically gangue.

Deformation of the Vangorda deposit

All rocks in the Vangorda deposit have been penetratively deformed and metamorphosed by D_1 and D_2 deformation events, making definition of any primary depositional features on a scale other than microscopic (see below) ambiguous at best. Direct evidence of F_1 folding is restricted to refolded folds in drill core and in pit wall exposures, suggesting that F_1 folding may have played an important role in the present geometry of the deposit. In most of the ore lithofacies, an S_1 pyritic banding is well developed on a scale of millimetres to centimetres. In the phyllites and in the ribbon banded, carbonaceous quartzite, S_1 is commonly preserved as lithons in the hinges of F_2 folds. In the more sulphide-rich lithofacies, however, S_1 is typically transposed into sub-parallelism with the F_2 axial surfaces.

The dominant fold phase in the Vangorda deposit is F_2. F_2 folds are shallowly east-west to northwest-southeast-plunging, tight to near-isoclinal (interlimb angle is commonly between 5° to 25°) similar style folds. F_2 fold morphology varies according to lithofacies as a result of different rheologies, but in general a similar style is maintained.

In the surrounding phyllites, a penetrative sub-horizontal, wavy F_2 axial surface foliation (S_2) is developed. In some sulphide lithofacies, such as the ribbon-banded, carbonaceous quartzite, a differentiated axial planar S_2 foliation is also well developed. However, S_2 appears to be non-penetrative in the sulphides and is only found rarely in fold hinges. In high strain zones, S_1 banding in the sulphide lithofacies is discontinuous as a result of shearing and a new, inhomogeneous S_2 foliation is developed. In ore rocks with an S_2 foliation (such as the ribbon-banded, carbonaceous quartzite) pyrite porphyroblasts often grow across the foliation indicating post-S_2 pyrite growth.

Thin, discontinuous, anastomosing shear zones are widespread in the deposit, and are typically parallel to the S_2 orientation (pyrrhotite–sphalerite–magnetite breccia, Figs. 4 and 5). Within these zones, massive pyrite has deformed by brecciation whereas other sulphides, such as pyrrhotite, sphalerite, and galena, have deformed by ductile mechanisms.

The Vangorda deposit is very strongly faulted by steeply northwest- to southeast-dipping brittle extensional faults that, together with F_2 folding, provide the dominant structural control on the present geometry of the orebody. All extensional faults examined truncate the S_2 foliation and F_2 folds and therefore clearly post-date or are late D_2 (Brown and McClay, 1992). Faults have an apparent offset of centimetres to (tens) of metres but, due to paucity of marker horizons, it is often impossible to determine the exact amount of offset on any one fault. Pyrite slickensides on polished fault surfaces typically have a shallow pitch angle suggesting a late stage strike-slip to oblique-slip phase of fault movement.

A number of low-angle, post-D_2, northeast-directed thrusts occur within phyllites in the southeast end of the deposit. These thrusts cut the S_2 foliation, and locally the extensional faults, and have offsets ranging from centimetres up to several metres.

Microstructures

Representative samples were taken from each lithofacies to determine the deformation mechanisms active on a mesoscopic and microscopic scale and their relationship to structural position. For the purpose of this study, selected polished sections of pyrite were etched with warm 20% HNO_3 to study growth features (e.g. grain boundaries and overgrowths), different mineral phases, and deformtaion textures (e.g. dislocation, diffusion and recrystallisation structures).

Tempelman-Kluit (1970) and McClay and Ellis (1983) noted a crude correlation between pyrite grain-size and metamorphic grade in the Anvil District deposits. McClay and Ellis (1983) also noted a number of other factors that affect grain-size, including primary/depositional and post-depositional/metamorphic effects as well as the nature of the matrix, the nature of grain boundaries, and pyrite chemistry. In the Vangorda orebody pyrite porphyroblasts exhibit both brittle and ductile deformation textures as well as post-deformation annealing features, all of which

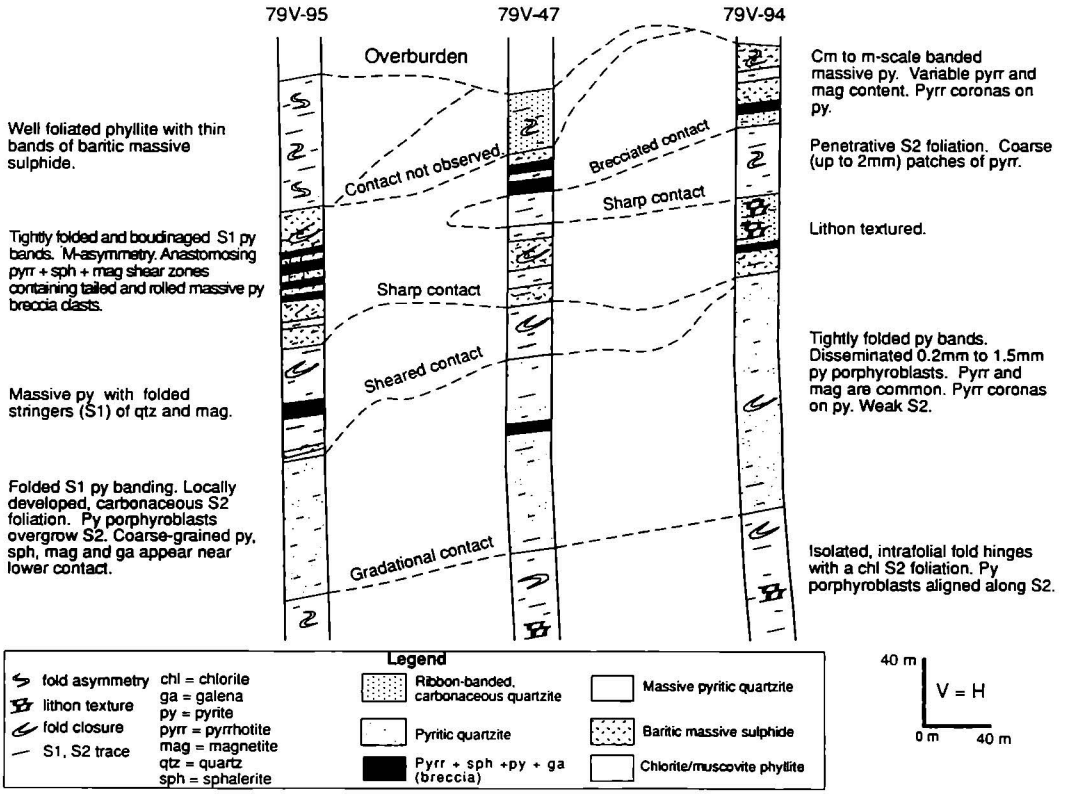

FIG. 5. Detailed logs through the sulphide stratigraphy, section 6E, Vangorda deposit.

affect grain-size to varying degrees. Sulphide grain-sizes and textures are significant metallurgical factors affecting the milling properties of massive sulphide ores. Rigorous textural analysis using etched sections is of fundamental importance for understanding the depositional and metamorphic evolution of the deposit.

Pyrite grain-size in the Vangorda deposit ranges from 0.1 mm to 1.5 mm, with an average grain-size of between 0.5 mm and 1.0 mm. Large grains (i.e. in the 0.5 mm to 1.0 mm range) are typically equant to idioblastic porphyroblasts. However, relict, primary colloform pyrite grains and relict spheroids and framboids, although rare, can still be found. The colloform and zoned grains are typically 0.1 mm to 0.25 mm sized, equant to xenoblastic and occur alone or, more commonly, as cores in metamorphic porphyroblasts (Fig. 6*a*).

Brittle deformation textures

Deformation of single grains and massive pyrite in the Vangorda deposit occurred mainly by cataclasis, resulting in an overall reduction in grain-size. Cataclastic textures, in the form of brittle shear zones in massive pyrite and fracturing and grain boundary sliding are found throughout the deposit, regardless of structural position. Zones of intense brittle shearing are common in polycrystalline pyrite and form aggregates of finely crushed, angular grains (Fig. 6*b*). These zones are commonly sealed by quartz, carbonate, and mica. In places, smaller fractures, oriented approximately 30° to the shear zone boundary, cross-cut the shear zone.

On a grain scale, where pyrite grains impinge upon each other, indentation and dissolution, axial cracking and microfracturing occur (Fig. 6*c*). Locally, pyrite displays internal microfracturing, suggesting inelastic strain accommodation in the core of the grains. Grain boundary sliding, which is geometrically necessary to accommodate diffusional deformation, is usually difficult to document. Microfracturing along and parallel to grain boundaries where two grains impinge upon each other indicates that grain boundary sliding was active (Fig. 6*d*).

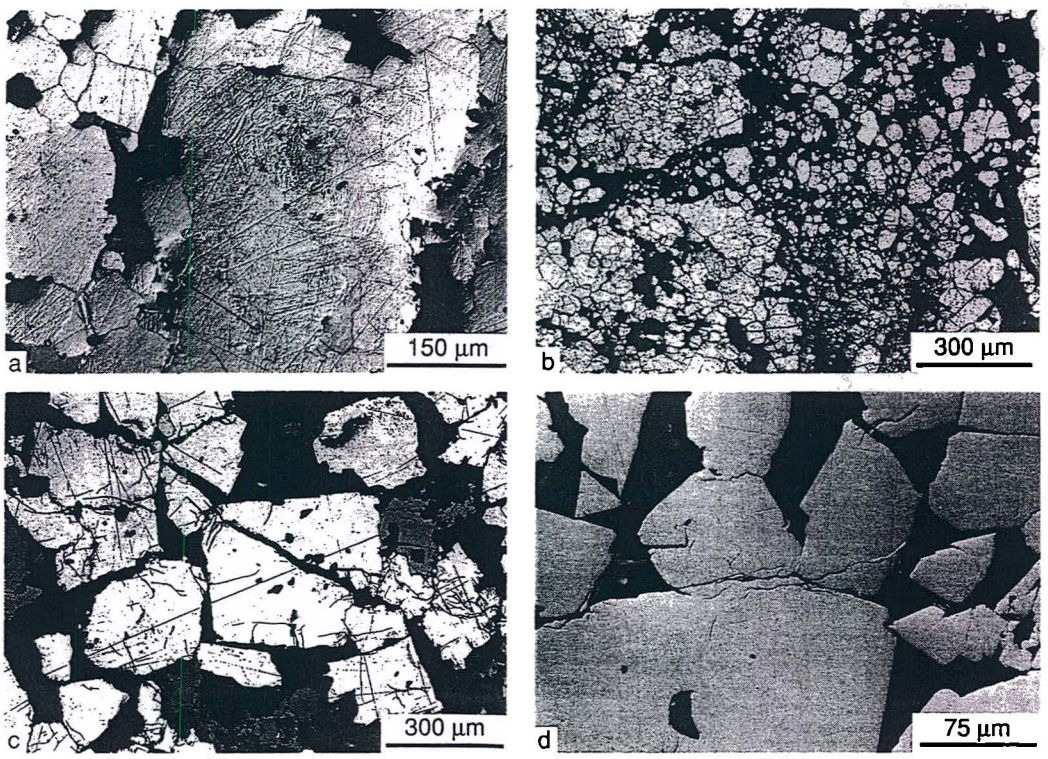

FIG. 6. Pyrite textures in the Vangorda deposit. All photomicrographs are of polished sections etched with HNO_3. (*a*) Relict primary colloform texture in the cores of metamorphic porphyroblasts. Nomarski interference contrast, section 90–52, DDH 90V–115. (*b*) Pyrite cataclasite in a shear zone. Note the comminution of pyrite grains and the disaggregation of clusters of pyrite grains. Nomarski interference contrast, section 90–46, DDH 90V-116. (*c*) Indentation and axial cracking of subhedral pyrite porphyroblasts. Plane polarised light, section 90-37, DDH 90V-67. (*d*) Microfracturing sub-parallel to grain boundaries indicating grain boundary sliding during deformation. Nomarski interference contrast, section 90-121, DDH 79V-95.

Ductile deformation features

Readily identifiable ductile deformation textures in pyrite in the Vangorda deposit are not widespread but are found locally, commonly in zones of high bulk strain such as the overturned limbs of folds. The lack of ductile deformation features is most likely a result of strong post-deformation annealing, that produced grain growth and an increase in grain-size.

Dislocation microstructures in pyrite are characterised by straight to slightly curved, stepped, or branching dislocation etch pits that outline dislocation tangles and walls forming parallel to <100> and <110> (cf. Cox *et al.*, 1981; Graf *et al.*, 1981). Movement of dislocations through the crystals, possibly along the {100} <001> slip plane, is evidenced by slip lines (Fig. 7*a*), here bent to form kink bands. Etch pits commonly intersect to form grid-like arrays that mark subgrain boundaries and the onset of polygonisation (Fig. 7*b*). The subgrains are 1–10 μm in size.

Dynamically recrystallised grains are common in the samples looked at in this study. Subgrain formation commonly occurs along the boundaries of parent grains (Fig. 7*c*) and in extreme cases results in the formation of a core–mantle texture. Recrystallised grains are typically 5–50 μm, equant grains with straight to slightly curved grain boundaries. Post-recrystallisation grain growth has likely resulted in an increase in grain size from the smaller subgrains.

Preferred grain shape orientation in pyrite (Fig. 7*d*) occurs in areas of high bulk strain in which thin, discontinuous, often anastomosing zones define a crude S_2 foliation. Grains are elongate with straight to slightly curved, mildly sutured, and lightly indented grain boundaries. Within individual grains there is little or no evidence of brittle deformation, and dislocation textures are rare. These features are particularly well dis-

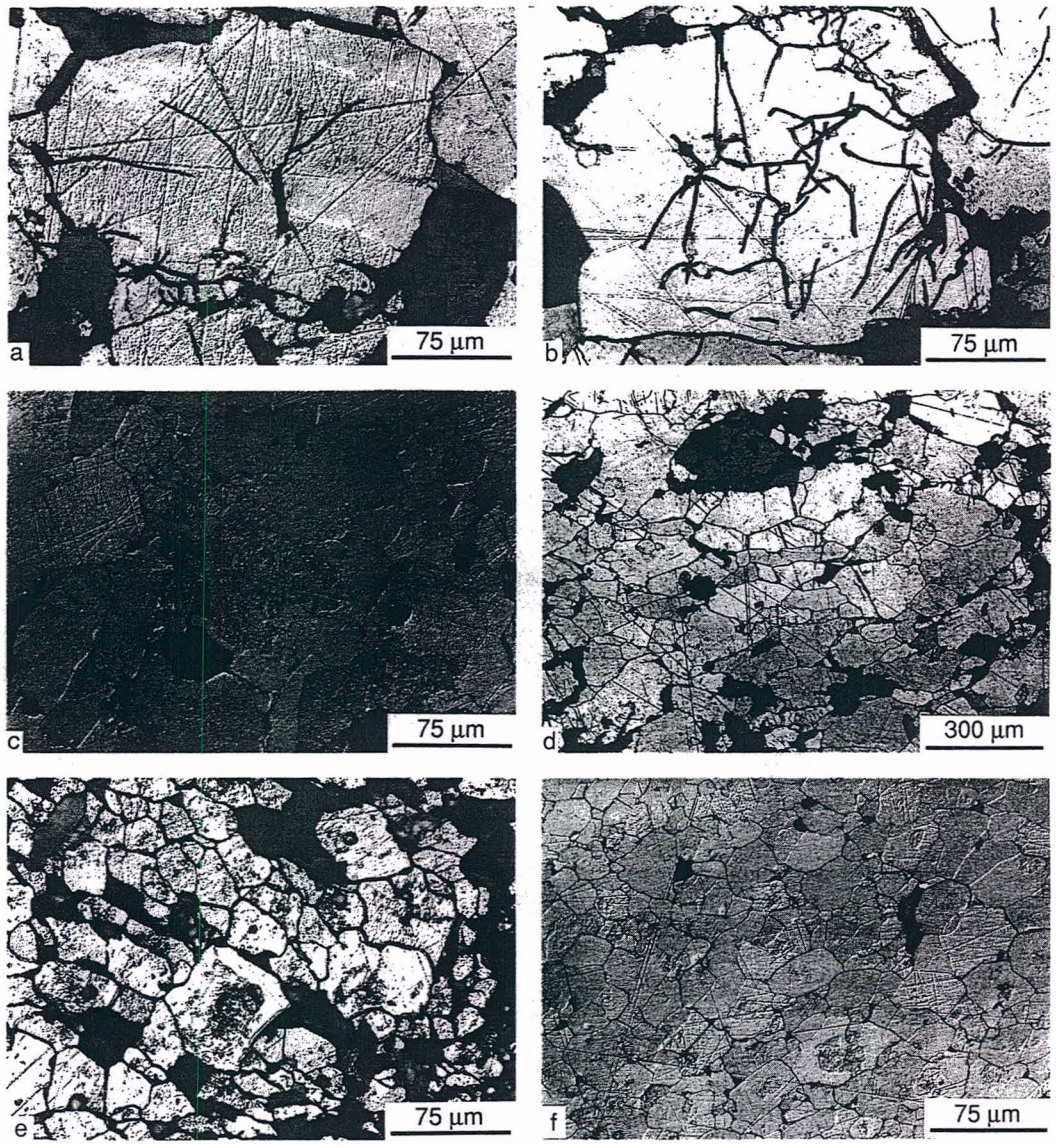

FIG. 7. Pyrite textures in the Vangorda deposit. All photomicrographs are of polished sections etched with HNO_3. (*a*) Etched pyrite porphyroblast showing kink bands that bend slip lines. Straight lines of etch pits that traverse whole grains or several grains are surface scratches on the specimen. Nomarski interference contrast, section 90-41, DDH 90V-67. (*b*) Arrays of etch pits that form subgrain walls indicating the onset of polygonisation. Plane polarised light, section 90-39, DDH 90V-67. (*c*) Dynamically recrystallised grains formed at the margin of large old grains. Plane polarised light, section 90-46, DDH 90V-116. (*d*) Recrystallised pyrite showing preferred shape orientation. Plane polarised light, section 90-39, DDH 90V-67. (*e*) Pressure solution texture showing truncated grain boundaries and a preferred shape orientation. Nomarski interference contrast, section 90-41, DDH 90V-67. (*f*) Annealed grains showing lobate grain boundaries and 120° triple junctions. Nomarski interference contrast, section 90-46, DDH 90V-116.

played in aggregates of small grains which have relict spheroidal and framboidal cores (Fig. 7*e*). In addition, overgrowths are not apparent on elongate grains, but pyrite porphyroblasts else-

where in these samples commonly do have overgrowths. Fluid-assisted diffusive mass transfer (pressure solution) is thought to be the likely mechanism responsible for formation of this preferred grain shape fabric (cf. McClay and Ellis, 1984). These features suggest dissolution and mobilisation have occurred, at least on a grain scale.

Annealing textures

As well as deformation textures, pyrite shows a number of annealing and grain growth textures due to metamorphism. In the massive pyritic lithofacies, grains are commonly 0.2 mm to 1.5 mm in size, equant with straight to mildly sutured grain boundaries that meet at 120° triple junctions (Fig. 7*f*). Strongly lobate grain boundaries are indicative of grain growth during annealing. Other sulphide phases, as well as quartz and carbonate, are commonly trapped along grain boundaries and at triple junctions. Concentric inclusion patterns in pyrite grains suggest multiple phases of grain growth. Rare, helicitic inclusion patterns indicate either porphyroblast rotation (Craig *et al.*, 1991) or multi-stage porphyroblast growth overgrowing successive foliations (cf. Bell, 1985).

Discussion

The Vangorda orebody has undergone polyphase deformation and metamorphism under greenschist facies conditions. Five distinct sulphide lithofacies have been recognised (Brown and McClay, 1992) and their textures reflect the response of the sulphides to various degrees of brittle and ductile deformation.

Primary depositional pyrite textures such as colloform and growth banded grains together with relict spheroidal and framboidal aggregates are only rarely preserved in the Vangorda sulphides. Deformation, recrystallisation and grain growth textures predominate. Pyrite deformation textures identified in this study include brecciation in cataclastic shear zones, grain fracturing, grain boundary sliding, preferred pyrite grain shape orientations, pressure solution, dislocation structures (slip lines and dislocation walls), subgrain formation and dynamic recrystallisation. These textures indicate that the pyrite in the Vangorda deposit deformed by both brittle and ductile mechanisms. The deformation processes, in general, have led to an overall reduction in grain-size. Post-deformation annealing has resulted in an increase in relative grain-size, formation of equant grains and development of pyrite porphyroblasts.

Grain fragmentation and axial cracking indicate that brittle deformation of pyrite grains and of the massive pyrite has occurred throughout the deposit. Breccia textures and pyrrhotite–magnetite–sphalerite shear zones are localised in high-strain zones (Fig. 5) that appear to be anastomosing D_2 fault zones on the limbs of the D_2 fold (Fig. 4). Similarly, textures indicating strong plastic deformation of pyrite (bands of dynamically recrystallised grains and preferred grain-shape textures) are also restricted to localised areas. The partitioning of deformation textures, both brittle and ductile, within the Vangorda orebody may be interpreted to indicate local strain or strain-rate partitioning during deformation. As the orebody and host rocks appear to be uniformly metamorphosed at mid-greenschist facies conditions, the brittle and ductile strain partitioning indicates local variations in sulphide/matrix rheologies. High strain zones may be localised on the limbs of D_2 folds or along D_2 fault zones. Reaction enhanced ductility may have been produced by the formation of pyrrhotite–sphalerite–magnetite assemblages in shear zones. D_2 fault zones may also have been the locus of transient high pore-fluid pressures that permitted the deformation to occur well into the cataclastic deformation regime thus producing the breccia textured pyrites.

The plastic deformation textures in pyrite found in this study (slip lines, kink bands, subgrains, dynamically recrystallised grains and preferred grain shape orientations) also indicate that, at geological strain rates, plastic deformation of pyrite occurs well below the threshold of 450 °C at 300 MPa confining pressure determined experimentally in the laboratory (Cox *et al.*, 1981). In addition relict deformed spheroidal and framboidal textures (Fig. 7*e*) together with overgrowth features indicate that pressure solution played an important role in the deformation of pyrite in the Vangorda deposit.

Post-deformational thermal annealing in the Vangorda deposit, as in the other Anvil District deposits (e.g. Faro—McClay and Ellis, 1983), resulted in the formation of foam textures with 120° triple junctions together with grain boundary migration, grain growth and porphyroblast formation. The annealing event has largely obscured and destroyed the earlier depositional, diagenetic, overgrowth and deformation textures tending to increase the grain size and produce homogeneous granoblastic pyrite ores.

The tight to isoclinal, similar, fold style and complex internal deformation indicates that the

Vangorda deposit has undergone significantly high strains. Strain partitioning has produced breccia zones and shear zones in part controlled by the sulphide and matrix rheologies. Shear zones in particular are localised in the baritic massive sulphide facies. Shear zones have long been known to act as conduits for fluids during deformation (e.g. Carter *et al.*, 1990, and references therein), and fluids are well known to affect the mechanical response of rocks during deformation (e.g. Hubbert and Rubey, 1959; Handin *et al.*, 1963; Atkinson, 1984). To date, a full appreciation of the role of a fluid in the deforming Vangorda deposit has not been assessed. However, sealing of cataclastic zones and fractures by quartz, carbonate, and often pyrite, together with the occurrence of overgrowths on grains indicates that fluid infiltration and mobilisation did occur, and likely played an important role in the mechanical response of the sulphide rocks.

The precise effects of pore fluids on the ductile deformation of pyrite is largely unknown, and is beyond the scope of this paper. Textural evidence, however, indicates that pressure solution is an important deformation mechanism in naturally deformed pyrite (McClay and Ellis, 1983; McClay, 1991). It may be expected that the focussing of a fluid phase along zones of increased strain (i.e. shear zones) may significantly reduce the flow stress required to induce crystal plastic deformation in pyrite, in much the same way it affects the mechanical response of quartz and olivine (Blacic, 1972; Kirby, 1984; Kirby and Kronenberg, 1987). The effects of fluid chemistry on rock and mineral deformation are not well understood, although Hobbs (1981, 1984) suggests that deformation and metamorphic reactions are closely tied. The deformation of pyrite in deposits such as Vangorda may be expected to have not only dramatically changed the textural characteristics of the ore but may also be expected to have affected the chemical and isotopic signatures.

Acknowledgements

This study forms part of D. Brown's Ph.D research program. Brown is funded in part by the Rothemere Foundation and by the Special Scholarship for Students doing Research in Resource Development administered by Memorial University of Newfoundland. Fieldwork was supported in part by Curragh Resources, Department of Indian and Northern Affairs, Whitehorse, Geological Survey of Canada, Vancouver, and by the Industry Association, R.H.B.N.C., University of London. Lee Pigage and two journal referees are thanked for reviewing this manuscript.

References

Atkinson, B. K. (1975) Experimental deformation of polycrystalline pyrite: effects of temperature, confining pressure, strain rate and porosity. *Econ. Geol.*, **70**, 473–87.

—— (1984) Subcritical crack growth in geological materials. *J. Geophysical Res.*, **89**, 4077–114.

Bell, T. H. (1985) Deformation partitioning and porphyroblast rotation in metamorphic rocks: a radical reinterpretation. *J. Metamorphic Geol.*, **3**, 109–18.

Blacic, J. D. (1972) Effect of water on the experimental deformation of olivine. *Am. Geophysical Union Mono.* **16**, 109–15.

Brill, B. A. (1989) Deformation and recrystallisation microstructures in deformed ores from the CSA mine, Cobar, N.S.W., Australia. *J. Struct. Geol.*, **11**, 591–601.

Brown, D. and McClay, K. R. (1992) Structure of the Vangorda Pb–Zn–Ag deposit, Anvil Range, Yukon Territory. In *Current Research, Part A*. Geol. Sur. of Canada, Paper 92-1A, 121–8.

Carne, R. C. and Cathro, R. J. (1982) Sedimentary exhalative (SEDEX) zinc–lead–silver deposits, northern Canadian Cordillera. *Canadian Institute Mining and Metallurgy Bull.*, **75**, no. 840, 66–78.

Carter, N. L., Kronenberg, A. K., Ross, J. V., and Wiltschko, D. V. (1990) Control of fluids on deformation of rocks. In *Deformation Mechanisms, Rheology and Tectonics* (R. J. Knipe and E. H. Rutter, eds.). Geol. Soc. Special Pub., **54**, 1–13.

Couderc, J.-J., Bras, J., Fagot, M., and Levade, C. (1980) Etude par microscopie electronique en transmission de l'etat de deformation de pyrite de differentes provences. *Bull. Mineral.*, **103**, 547–57.

Cox, S. F., Etheridge, M. A., and Hobbs, B. E. (1981) The experimental ductile deformation of polycrystalline and single crystal pyrite. *Econ. Geol.*, **76**, 2105–18.

Craig, J. R., Vokes, F. M., and Simpson, C. (1991) Rotational fabrics in pyrite from Ducktown, Tennessee. Ibid., **86**, 1737–46.

Graf, J. L. and Skinner, B. J. (1970) Strength and deformation of pyrite and pyrrhotite. Ibid., **65**, 206–15.

—— Bras, J., Fagot, M., Levade, C., and Couderc, J.-J. (1981) Transmission electron microscope observation of plastic deformation in experimentally deformed pyrite. Ibid., **76**, 738–44.

Handin, J., Hager, R. V., Jr., Friedman, M., and Feather, J. N. (1963) Experimental deformation of sedimentary rocks under confining pressure: pore pressure tests. *A.A.P.G. Bull.*, **46**, 717–55.

Hobbs, B. E. (1981) The influence of metamorphic environment upon the deformation of minerals. *Tectonophysics*, **78**, 335–83.

—— (1984) Point defect chemistry of minerals under a hydrothermal environment. *J. Geophysical Res.*, **89**, 4026–38.

Hubbert, M. K. and Rubey, W. W. (1959) Role of fluid pressure in mechanics of overthrust faulting. I Mechanics of fluid-filled porous solids and its application to overthrust faulting. *Geol. Soc. Amer. Bull.*, **70**, 115–66.

Jennings, D. S. and Jilson, G. A. (1986) Geology and sulphide deposits of the Anvil Range, Yukon. In *Mineral Deposits of Northern Cordillera* (J. A. Morin, ed.) Canadian Institute Mining and Metallurgy, Special Paper 37, 319–61.

Kirby, S. H. (1984) Introduction and digest to the special issue on chemical effects of water on the deformation and strengths of rocks. *J. Geophysical Res.*, **89**, 3991–5.

—— and Kronenberg, A. K. (1987) Rheology of the lithosphere: Selected topics. *Reviews in Geophysics*, **25**, 1219–44.

McClay, K. R. (1983) Deformation of stratiform lead-zinc deposits. In *Sediment-hosted Stratiform Lead-Zinc Deposits*. Short Course Notes. Mineral. Assoc. Can. 283–307.

—— (1991) Deformation of stratiform Zn–Pb(–barite) deposits in the northern Canadian Cordillera. *Ore Geology Reviews*, **6**, 435–62.

—— and Ellis, P. G. (1983) Deformation and recrystallisation of pyrite. *Mineral. Mag.*, **47**, 527–38.

—— —— (1984) Deformation of pyrite. *Econ. Geol.*, **79**, 400–3.

Mookherjee, A. (1971) Deformation of pyrite. Ibid., **66**, 200.

—— (1976) Ores and metamorphism: Temporal and genetic relationships. In *Handbook of Stratabound and Strataform Ore Deposits* (K. H. Wolf, ed.) Elsevier, Amsterdam, 4, 203–60.

Natale, P. (1971) Prima segnalazione di struttre de deformazione plastica della pirite. *Rend. Soc. Italian Miner. Petrol.*, **27**, 539–50.

Pigage, L. C. (1990) Field guide Anvil Pb–Zn–Ag district, Yukon Territory, Canada. In *Mineral Deposits of the Northern Canadian Cordillera, Yukon-northeastern British Columbia* (J. G. Abbott and R. J. W. Turner, eds.) Geol. Sur. Canada, Open File 2169, 283–308.

—— and Anderson, R. G. (1985) The Anvil Plutonic Suite, Faro, Yukon Territory. *Can. J. Earth Sci.*, **22**, 1204–16.

—— and Jilson, G. A. (1985) Major extensional faults, Anvil Pb–Zn district, Yukon. *G.S.A., Abstracts with Programs—Cordilleran Section*, **17**, 400.

Ramdohr, P. (1969) *The Ore Minerals and Their Intergrowths*. Pergamon Press, Oxford, 1174 pp.

Smith, J. M. and Erdmer, P. (1990) The Anvil aureole, an atypical mid-Cretaceous culmination in the northern Canadian Cordillera. *Can. J. Earth Sci.*, **27**, 344–56.

Tempelman-Kluit, D. J. (1970) The relationship between sulphide grain size and metamorphic grade of host rocks in some stratbound pyrite ores. Ibid., **7**, 1339–45.

—— (1972) Geology and origin of the Faro, Vangorda and Swim concordant zinc-lead deposits, central Yukon Territory. *Geol. Sur. Canada, Bull.* 208. 73 pp.

Vokes, F. M. (1969) A review of the metamorphism of sulphide deposits. *Earth-Sci. Rev.*, **95**, 403–6.

—— (1971) Some aspects of the regional metamorphic mobilisation of preexisting sulphide deposits. *Mineral. Deposita*, **6**, 122–9.

[*Revised manuscript received 2 May 1992*]

SW

NE

Section 4+00E

E+9900

79V-308

79V-306

90V-116

79V-304

90V-115

79V-033

90V-118

79V-305

90V-108

79V-307

79V-310

E+10100

+1100m

+1000m

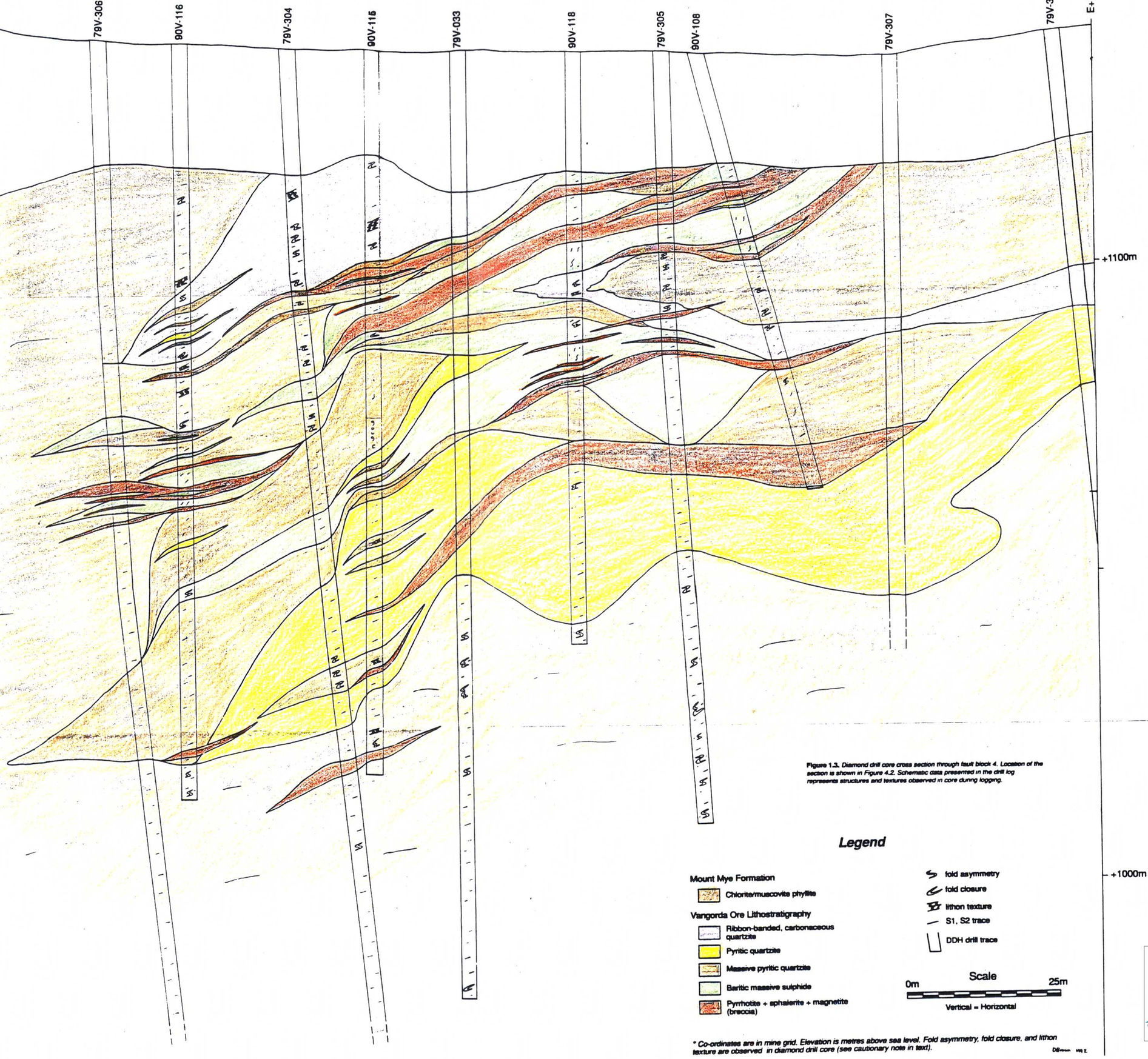

Figure 1.3. *Diamond drill core cross section through fault block 4. Location of the section is shown in Figure 4.2. Schematic data presented in the drill log represents structures and textures observed in core during logging.*

Legend

Mount Mye Formation

- Chlorite/muscovite phyllite

Vangorda Ore Lithostratigraphy

- Ribbon-banded, carbonaceous quartzite
- Pyritic quartzite
- Massive pyritic quartzite
- Baritic massive sulphide
- Pyrrhotite + sphalerite + magnetite (breccia)

- fold asymmetry
- fold closure
- lithon texture
- S1, S2 trace
- DDH drill trace

Scale

0m — 25m

Vertical = Horizontal

** Co-ordinates are in mine grid. Elevation is metres above sea level. Fold asymmetry, fold closure, and lithon texture are observed in diamond drill core (see cautionary note in text).*

DB-mon vss 2

inches

0 — 1

0 — 1 — 2

centimetres

This reference scale bar has been added to the original image. It will scale at the same rate as the image, therefore it can be used as a reference for the original size.

YUKON GEOLOGICAL SURVEY

SW

NE

Section 8+00 E

E+9900 | 79V-320 | 79V-053R | 88V-49 | 79V-302 | 87V-04 | 79V-045 | 87V-03 | 79V-303 | 90V-82 | 79V-018R | 79V-317 | E+10100

+1150m

+1100m

+1000m

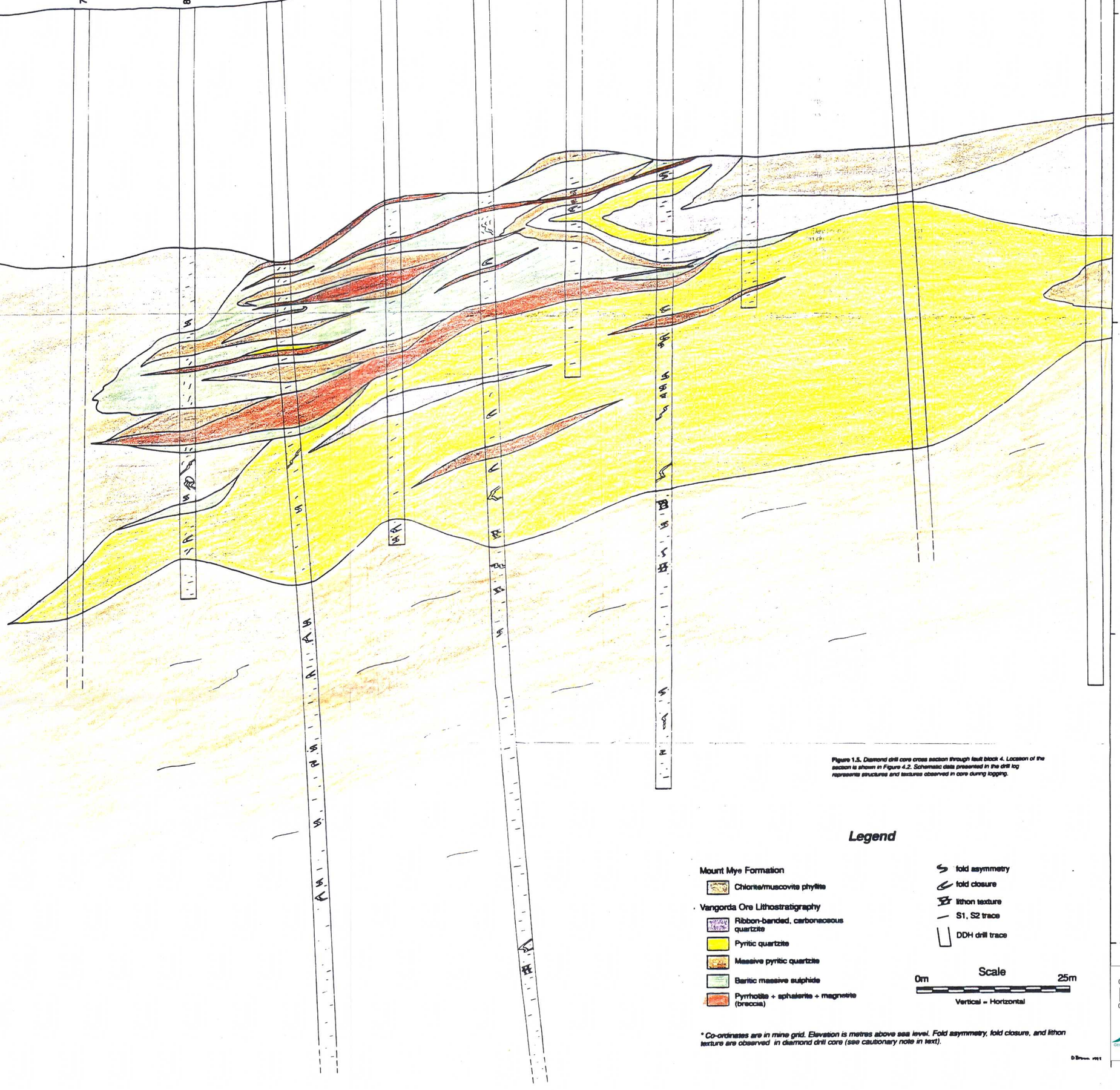

Figure 1.5. *Diamond drill core cross section through fault block 4. Location of the section is shown in Figure 4.2. Schematic dots presented in the drill log represents structures and textures observed in core during logging.*

Legend

Mount Mye Formation

- Chlorite/muscovite phyllite

Vangorda Ore Lithostratigraphy

- Ribbon-banded, carbonaceous quartzite
- Pyritic quartzite
- Massive pyritic quartzite
- Baritic massive sulphide
- Pyrrhotite + sphalerite + magnetite (breccia)

- fold asymmetry
- fold closure
- lithon texture
- S1, S2 trace
- DDH drill trace

Scale 0m 25m

Vertical = Horizontal

** Co-ordinates are in mine grid. Elevation is metres above sea level. Fold asymmetry, fold closure, and lithon texture are observed in diamond drill core (see cautionary note in text).*

D Brown 1991

inches 0 1

centimetres 0 1 2

This reference scale bar has been added to the original image. It will scale at the same rate as the image, therefore it can be used as a reference for the original size.

YUKON GEOLOGICAL SURVEY

SW

Section 6+00E

NE

E+9900
90V-67
79V-096R
79V-020R
79V-095R
79V-047R
90V-70
79V-094
90V-66
79V-035R
79V-128
E+10100

+1100m

+1000m

Figure 1.4. *Diamond drill core cross section through fault block 4. Location of the section is shown in Figure 4.2. Schematic data presented in the drill log represents structures and textures observed in core during logging.*

Legend

Mount Mye Formation

- Chlorite/muscovite phyllite

Vangorda Ore Lithostratigraphy

- Ribbon-banded, carbonaceous quartzite
- Pyritic quartzite
- Massive pyritic quartzite
- Baritic massive sulphide
- Pyrrhotite + sphalerite + magnetite (breccia)

- fold asymmetry
- fold closure
- lithon texture
- S1, S2 trace
- DDH drill trace

Scale
0m — 25m
Vertical = Horizontal

** Co-ordinates are in mine grid. Elevation is metres above sea level. Fold asymmetry, fold closure, and lithon texture are observed in diamond drill core (see cautionary note in text).*

inches
0 1
0 1 2
centimetres

This reference scale bar has been added to the original image. It will scale at the same ratio as the image, therefore it can be used as a reference for the original size.

YUKON GEOLOGICAL SURVEY

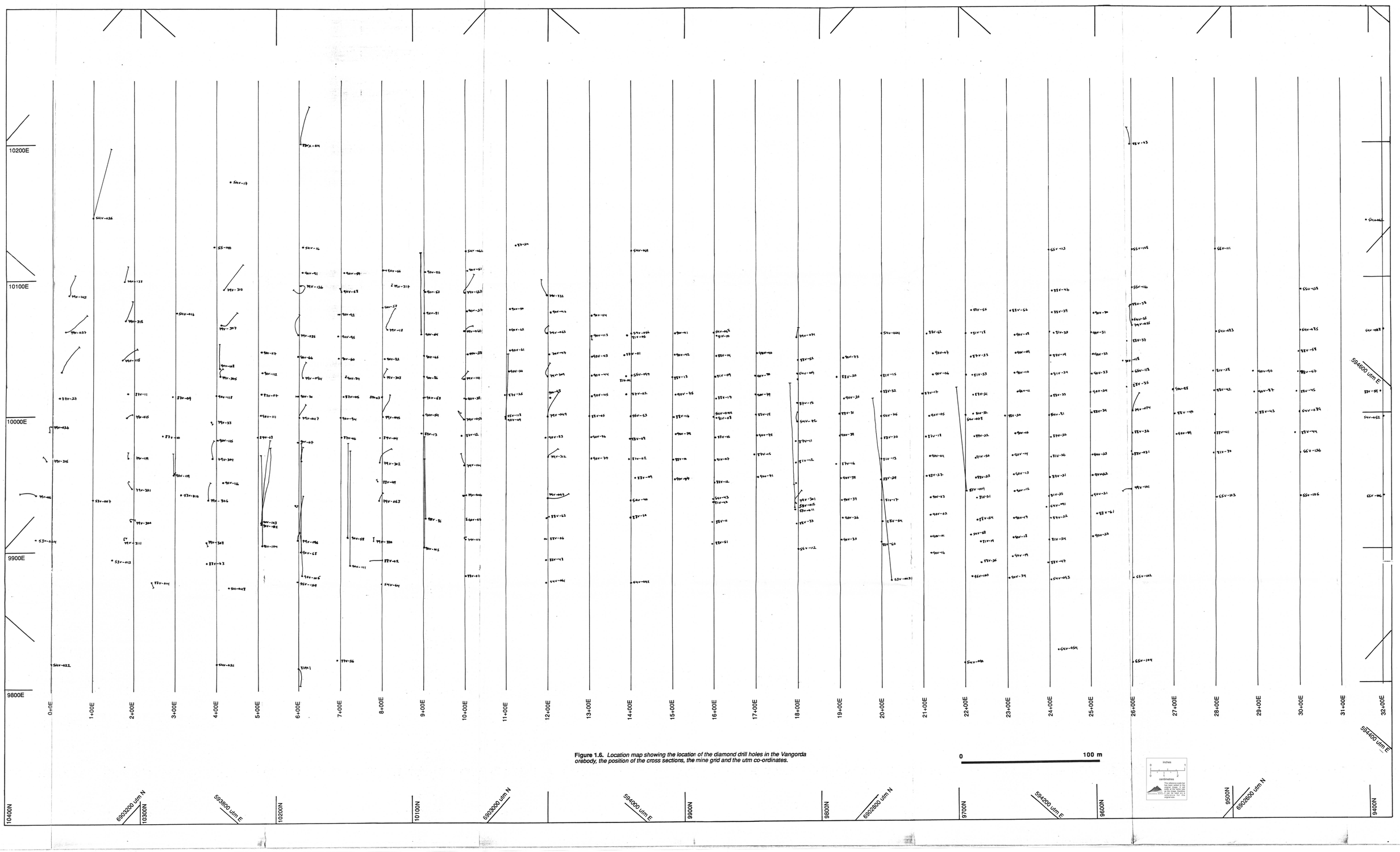

Figure 1.6. *Location map showing the location of the diamond drill holes in the Vangorda orebody, the position of the cross sections, the mine grid and the utm co-ordinates.*

Geological map of the Vangorda open pit mine

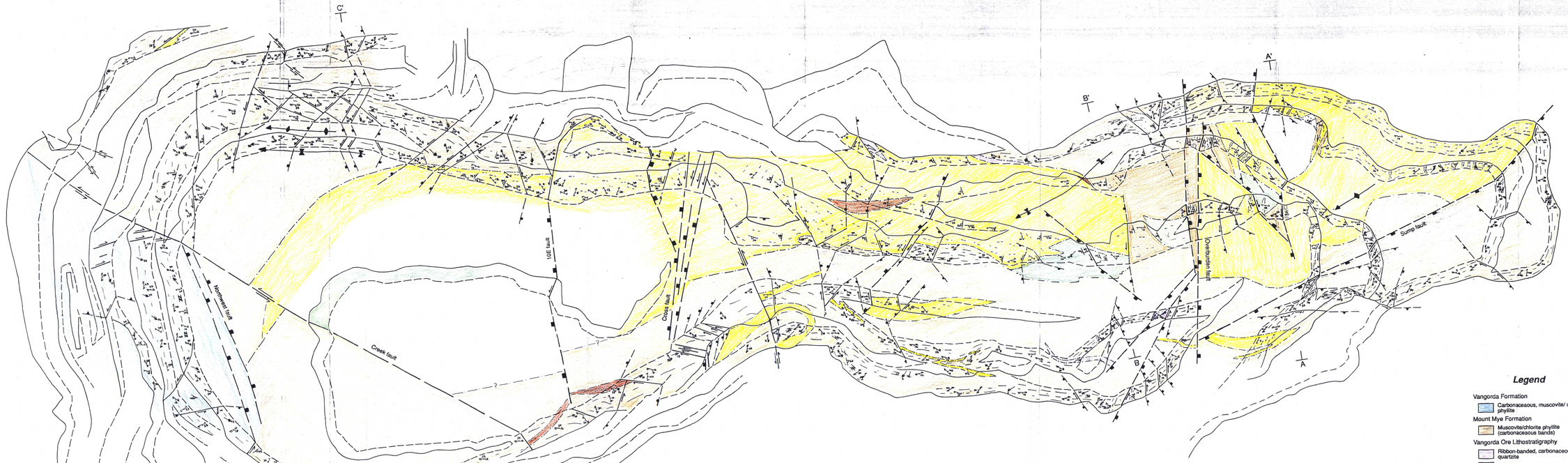

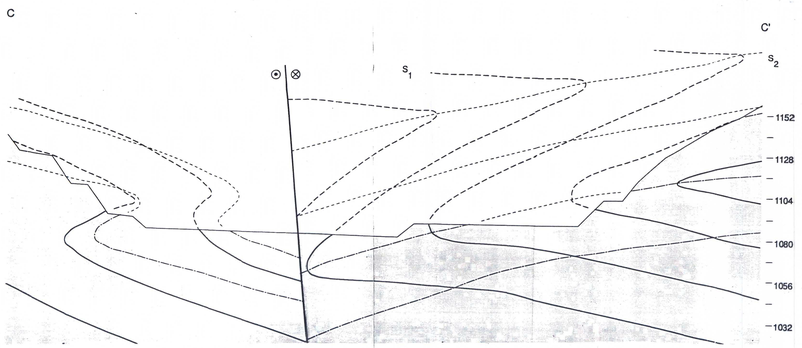

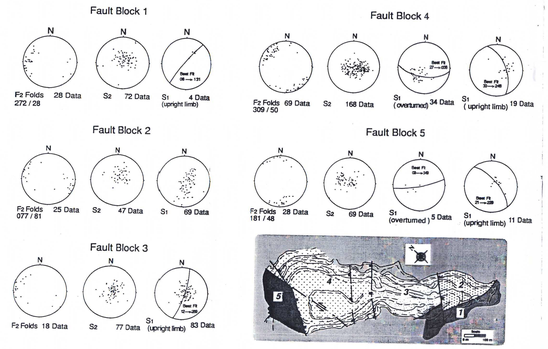

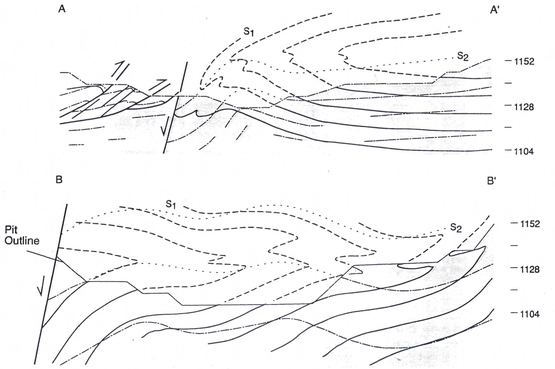

Legend

Vangorda Formation
- Carbonaceous, muscovite/ chlorite phyllite

Mount Mye Formation
- Muscovite/chlorite phyllite (carbonaceous bands)

Vangorda Ore Lithostratigraphy
- Ribbon-banded, carbonaceous quartzite
- Pyritic quartzite
- Massive pyritic quartzite
- Baritic massive sulphide
- Pyrrhotite + sphalerite + galena massive sulphide

- Bedding (S_0)
- Foliation (S_1, S_2, S_3)
- Fold axis (F_1, F_2, F_3)
- S_1 trace (in pit wall)
- S_2 trace (in pit wall)
- Fracture
- Fracture trace (in pit wall)
- Extensional Fault (> 1 m offset)
- Extensional Fault (< 1 m offset)
- Extensional Fault (in pit wall)
- Thrust Fault (defined, assumed)
- Thrust Fault (in pit wall)
- Lithofacies boundary
- Fold Asymmetry (in pit wall)
- Fold Closure (in pit wall)
- Lithon Texture (in pit wall)
- Antiformal axis
- Synformal axis

* Co-ordinates are in mine grid and UTM. Contour interval is bench toes.

0m Scale 100m

This reference scale has been reduced from the original image. It may not be accurate when used on the image, therefore it is recommended to refer to the original size.
YUKON GEOLOGICAL SURVEY

694000 utm E
6902600 utm N
9700 N
9500 N
9900 N

Figure 1.2. *Geological map of the Vanogrda open pit mine constructed from 1:200 scale mapping.*